Dissertation

Nonlinear phase-modulated spectroscopy of doped helium droplet beams and dilute gases

Lukas Bruder

Molekül- und Nanophysik
Fakultät für Mathematik und Physik
Albert-Ludwigs-Universitat Freiburg
Freiburg im Breisgau, 2017

Nonlinear phase-modulated spectroscopy of doped helium droplet beams and dilute gases

Dissertation

zur Erlangung des Doktorgrades
der Fakultät für Mathematik und Physik
der Albert-Ludwigs-Universität
Freiburg im Breisgau

vorgelegt von
Lukas Bruder
geboren in Wolfach
Freiburg im Breisgau, 2017

Dekan:	Prof. Dr. Gregor Herten
Referent:	Prof. Dr. Frank Stienkemeier
Koreferent:	Prof. Dr. Tobias Schätz
Prüfer:	Prof. Dr. Bernd von Issendorff
	Prof. Dr. Andreas Buchleitner
Tag der mündlichen Prüfung:	14.06.2017

Abstract

This dissertation focuses on the application of nonlinear time-domain spectroscopy to cold helium nanodroplet beams and dilute atomic vapors. Femtosecond pump-probe wave packet interferometry is performed to track the coherent evolution of electronic and vibronic wave packets induced in the systems. To this end, a phase modulation technique is implemented to enhance the sensitivity and resolution in the experiments. Rubidium atoms attached to helium droplets are investigated as well as rubidium-helium excimers that form on the droplet surface upon electronic excitation. In both cases a vast increase in resolution as compared to previous studies is achieved. For the first time, a highly resolved vibronic spectrum of the rubidium-helium excimer is obtained and new insight in the molecule formation process is gained. Evidence is found that the excimer forms in its rotational ground state and a novel formation channel via two-photon excitation is identified.

Furthermore, a new technique to sensitively and selectively probe multiple-quantum coherences is presented. Simultaneous, background-free detection of multiphoton excitation pathways in separate signal channels is demonstrated. The high sensitivity of this method is confirmed with measurements on highly dilute rubidium-doped helium droplet beams. In addition, this concept is applied to study the collective response of a warm atomic vapor for the D line excitation of various alkali atoms. For the first time, collective three- and four-body resonances are revealed, even at particle densities of $10^8\,\mathrm{cm}^{-3}$. A linear dependence of these signals on the ensemble density is deduced and distinct phase signatures connected to the fundamental hyperfine states in the system are observed. To elucidate the origin of these signals, the experiment is thoroughly modeled in the framework of a cooperation with the theory group of A. Eisfeld in Dresden. Based on the theoretical and experimental results, the nonlinear signals are interpreted as the collective response of dipole-coupled atoms which is superimposed with a higher-order single-atom process.

Moreover, a prospective approach to facilitate coherent nonlinear spectroscopy in the extreme ultraviolet spectral range is proposed. In a proof-of-principle study, this concept is demonstrated at ultraviolet wavelengths for linear and nonlinear excitation of alkali vapors. Contributions from second harmonic and sum-frequency light are readily dissected with the inherent quasi-continuous phase-cycling concept and the prerequisites for coherent multidimensional spectroscopy at extreme ultraviolet wavelengths are demonstrated.

Zusammenfassung

Der Fokus dieser Arbeit liegt auf der nichtlinearen Spektroskopie im Zeitraum angewandt auf kalte Helium-Nanotröpfchen-Strahlen und verdünnte Gase. Mittels Femtosekunden Pump-Probe Wellenpaketinterferometrie wird die kohärente Zeitentwicklung elektronischer und vibronischer Wellenpakete in diesen Systemen untersucht. Um die Sensitivität und Auflösung in den Experimenten zu erhöhen wird eine Phasenmodulationstechnik implementiert. Untersucht werden Rubidiumatome, die an Heliumtröpfchen gebunden sind, sowie Rubidium-Helium Exzimere, die sich auf der Tröpfchenoberfläche infolge elektronischer Anregung bilden. In beiden Fällen wird eine enorme Verbesserung der Auflösung im Vergleich zu bisherigen Studien erreicht. Erstmalig gelingt es ein hochauflösendes vibronisches Spektrum des Rubidium-Helium Exzimers zu messen und neue Einblicke in die Molekülbildung werden gewonnen. Es werden Anzeichen gefunden, dass sich das Exzimer im Rotationsgrundzustand bildet und ein Bildungsmechanismus über Zwei-Photonen-Anregung wird erstmals identifiziert.

Des Weiteren wird eine neue Technik präsentiert um Multiple-Quantenkohärenzen sensitiv und selektiv zu messen. Die simultane Detektion von Multiphotonenanregungen in separaten Signalkanälen frei von Hintergrundsignalen wird demonstriert. Mit Messungen an stark verdünnten Rubidium-dotierten Heliumtröpfchenstrahlen wird die hohe Empfindlichkeit dieser Methode bestätigt. Zudem wird dieses Konzept verwendet um die kollektive Systemantwort eines warmen atomaren Gases auf die D-Linien-Anregung verschiedener Alkalimetallatome zu untersuchen. Drei- und Vier-Körper-Resonanzen werden erstmalig beobachtet, insbesondere für Teilchendichten von nur $10^8\,\mathrm{cm}^{-3}$. Die Messungen ergeben eine lineare Abhängigkeit dieser Signale von der Ensembledichte und ausgeprägte Phasensignaturen, welche auf die fundamentalen Hyperfeinzustände des Systems zurückgehen, werden aufgedeckt. Um den Ursprung der Signale aufzuklären wird das Experiment in Zusammenarbeit mit der theoretischen Arbeitsgruppe von A. Eisfeld aus Dresden ausführlich simuliert. Basierend auf den experimentellen und theoretischen Ergebnissen werden die nichtlinearen Signale als kollektive Antwort Dipol-gekoppelter Atome interpretiert, die zudem mit einem Ein-Atom-Prozess höherer Ordnung überlagert ist.

Außerdem wird ein potenzieller Ansatz zur Realisierung der nichtlinearen kohärenten Spektroskopie im extrem ultravioletten Spektralbereich vorgeschlagen. Dieses Konzept wird in einer Prinzipstudie im ultravioletten Spektralbereich für die lineare und nichtlineare Anregung von Alkalimetall-Gasen vorgestellt. Das integrierte quasikontinuierliche Phasenvariationsschema ("phase-cycling") erlaubt es die Beiträge von Zweiter-Harmonischer- und Summenfrequenz-Lichterzeugung zu unterscheiden. Die Voraussetzungen für die multidimensionale Spektroskopie mit extrem ultravioletten Wellenlängen werden hiermit gezeigt.

Acronyms

AOM	acousto-optical modulator
APD	avalanche photo diode
BS	beam splitter
CEP	carrier envelope phase
cw	continuous wave
DQC	double-quantum coherence
FCF	Frank-Condon factor
FCW	Frank-Condon window
FWHM	full width at half maximum
FRET	Förster resonant energy transfer
GSB	ground state bleaching
HGHG	high-gain harmonic-generation
HENDI	helium nanodroplet isolation
HHG	high harmonic generation
IR	infrared
IP	ionic potential
MQC	multiple-quantum coherence
PD	photo diode
PEC	potential energy curve
PMHL	phase-modulated harmonic light
PM-MQC	phase-modulated multiple-quantum coherence
PM-WPI	phase-modulated wave packet interferometry
PMT	photo multiplier tube
QMS	quadruple mass spectrometer
RF	radio frequency
SE	stimulated emission

SHG	second harmonic generation
SQC	single-quantum coherence
TOF	time of flight
UV	ultraviolet
VMI	velocity map imaging
VIS	visible
VUV	vacuum ultraviolet
WP	wave packet
WPI	wave packet interferometry
XUV	extreme ultraviolet
ZEKE	zero electron kinetic energy
2D	two-dimensional

List of publications covered in this thesis:

[B1] **L. Bruder**, M. Mudrich, and F. Stienkemeier, *Phase-modulated electronic wave packet interferometry reveals high resolution spectra of free Rb atoms and Rb*He molecules*, Phys. Chem. Chem. Phys. **17**, 23877 (2015).

[B2] **L. Bruder**, M. Binz, and F. Stienkemeier, *Efficient isolation of multiphoton processes and detection of collective resonances in dilute samples*, Phys. Rev. A **92**, 053412 (2015).

[B3] **L. Bruder**, U. Bangert, and F. Stienkemeier, *Phase-modulated harmonic light spectroscopy*, Opt. Express **25**, 5302 (2017).

[B4] Z.-Z. Li, **L. Bruder**, F. Stienkemeier, and A. Eisfeld, *Probing weak dipole-dipole interaction using phase-modulated non-linear spectroscopy*, Phys. Rev. A (submitted).

[B5] **L. Bruder**, M. Binz and F. Stienkemeier, *Lock-in detection of strongly undersampled signals* (in preparation).

Additional publications related to the Diploma thesis:

1. V. Lyamayev, Y. Ovcharenko, R. Katzy, M. Devetta, **L. Bruder**, A. LaForge, M. Mudrich, U. Person, F. Stienkemeier, M. Krikunova, T. Möller, P. Piseri, L. Avaldi, M. Coreno, P. O'Keeffe, et. al. *A modular end-station for atomic, molecular, and cluster science at the low density matter beamline of FERMI@Elettra,* J. Phys. B: At. Mol. Opt. Phys. **46**, 164007 (2013).

Contents

1 Introduction

In spectroscopy, microscopic information about a material system is gained from the light-matter interaction. Thereby, the obtained signals and deduced matter responses are typically categorized in linear and nonlinear contributions according to their linear/nonlinear dependence on the incident light intensities. While the linear matter response provides valuable insights of fundamental properties on the atomic and molecular level, the nonlinear response naturally contains more information. In particular, the latter reveals correlations and couplings among quantum states which are key quantities to understand the complex quantum behavior of matter [1]. Furthermore, elementary processes such as molecular vibrations, chemical bond breaking or molecular charge and energy transfer, being the driving forces of numerous important chemical and biological phenomena, occur on ultrafast time scales in the picosecond to sub femtosecond regime [2]. Hence, to attain a detailed picture of the underlying dynamics and fundamental interactions of a quantum system, one of the major goals in spectroscopy is the characterization of the nonlinear matter response with both, high spectral and temporal resolution.

However, time and energy resolution are inevitably connected to each other through the Fourier transform, posing a fundamental limit for the attainable information, as for instance expressed in the famous Heisenberg uncertainty principle. Specifically in spectroscopy, temporally short optical pulses exhibit very broad spectral distributions thus providing high temporal resolution albeit at the expense of poor spectral resolution. This issue can be circumvented using ultrashort laser pulses and probing the coherent evolution of wave packets (WPs) on time scales much longer than the pulse duration. Detailed spectral information is then obtained with the Fourier transform of the acquired transient WP signals. Pioneered by Zewail and coworkers [3], this principle introduced a paradigm change in the time-resolved study of ultrafast processes [2] and has lead to the development of nonlinear time-domain spectroscopy in the optical regime [1].

A second key requirement in nonlinear spectroscopy arises from the generally small intensities of nonlinear features which are therefore often masked by prominent linear contributions. Nonlinear time-domain spectroscopy has successfully addressed this issue with the development of phase-matching and phase-cycling schemes that provide background-free detection of nonlinear signal contributions [4, 5]. In these techniques, a sequence of multiple phase-locked pulses is applied to the sample and the resulting nonlinear signals are isolated due to their specific propagation direction (phase-matching) or phase signature (phase-cycling). In this context, coherent two-dimensional (2D) spectroscopy in the optical regime has in recent years emerged as a particular powerful tool to study the nonlinear response in a variety of systems [4, 6, 7]. For instance, 2D spectroscopy has unraveled a step-wise energy transport mechanism in biological systems [8], characterized the ultrafast rearrangement dynamics of hydrogen bonds in water [9] and provided new insights into many-body physics in semiconductor nanostructures [10, 11]

and photoinduced chemical reactions [12].

While first nonlinear time-domain approaches have been applied to gas-phase samples [13], the vast majority of studies have been conducted in the condensed phase. Two reasons can be identified for this development: (i) gas phase samples, e.g. molecular beams, provide low particle densities, making the application of experimentally demanding techniques such as multidimensional spectroscopy challenging, and (ii), condensed phase experiments provide much higher flexibility in the tailored synthesis of the spectroscopic target systems. On the contrary, unambiguous interpretation of experimental as well as theoretical studies in condensed phase systems remains difficult due to the vast complexity of the surrounding environmental degrees of freedom, having lead to some controversies in the community about the interpretation of coherent beat signatures [14, 15].

Helium nanodroplet isolation (HENDI) may unite the advantages of both approaches. This technique facilitates versatile heterogeneous synthesis in a cold ($T \sim$ mK) environment with minimal perturbation from the helium bath [16]. The in this way prepared ensembles constitute well-controlled isolated gas-phase systems populated in low-energetic quantum states due to efficient evaporative cooling by the surrounding helium droplet and they enable high resolution spectroscopy [16–19]. In contrast, both properties are hard to achieve in the condensed phase. Thus, several approaches to combine coherent time-domain spectroscopy with helium nanodroplet isolation (HENDI) have been conducted in recent years [20–22]. However, a full characterization of the signal, e.g. deducing information about electronic coherences, has not been possible in these experiments, partially due to the small target densities present in doped helium droplet beams ($\sim 10^8\,\mathrm{cm}^{-3}$) [23], but also due to the high level of phase sensitivity required to probe electronic coherences [24].

One goal of the work presented in this thesis has been to overcome these constraints and to facilitate the combination of nonlinear time-domain methods with HENDI. For this purpose, a phase modulation technique has been implemented in a coherent time-domain pump-probe experiment, i.e. in electronic wave packet interferometry (WPI). Relying on the combination of acousto-optic phase modulation of the optical laser pulses combined with lock-in detection, this approach provides passive phase stabilization and particularly high sensitivity, making it ideally suitable for a combination with HENDI. Marcus and coworkers have demonstrated this principle for the first time in a WPI [25] and later in a 2D spectroscopy experiment [26]. Since then, phase modulation studies have been focused on the liquid and the solid phase, for instance, the conformation analysis of a porphyrin dimer embedded in a biological membrane [27, 28], the examination of coherent dynamics in a quantum dot sample [29] or the investigation of ultrafast charge separation in an organic solar cell [30] have been investigated. In these studies, the nonlinear signals have been exclusively deduced from fluorescence or photocurrent yields. In the scope of this PhD thesis (chapters 4 and 5), this range of applications is extended to cold molecular/cluster beam targets and the combination with photoelectron as well as mass-resolved ion detection is demonstrated [B1]. With the advantage of mass-selective ion detection, new details about the vibronic structure of the rubidium-helium (Rb*He) excimer have been revealed. In general, these experiments have successfully demonstrated all prerequisites to facilitate advanced nonlinear time-domain methods, e.g. coherent multidimensional spectroscopy, applied to dilute supersonic beams.

In spite of the great advantages of the phase modulation approach, one shortcoming is

the lacking possibility to detect multiple-quantum coherence (MQC) signals, that is the interference of WPs induced upon multiphoton transitions. These signals readily provide information about coherent dynamics in higher-lying states, which has been exploited to probe electron correlations and anharmonicities in molecular systems [31, 32], the role of higher-lying electronic states in biological relevant photo-induced processes [33] or many-body effects in semiconductor systems [10, 11] and atomic gases [34, 35]. Yet, the detection of such signals poses a general challenge in nonlinear spectroscopy, mainly due to the considerably higher phase stability required to probe MQC signals. In this context, a new method to efficiently isolate and detect MQC signals in a phase-modulated two-pulse experiment (PM-MQC detection) has been developed in the present work (chapter 6). This method stands out due to its high sensitivity, having permitted the detection of the weak response of collectively excited atoms in a highly dilute alkali-atom vapor [B2] (chapter 7). Collective two-atom excitation has been observed previously in vapors using double-quantum 2D spectroscopy [34]. With the improved sensitivity in the developed PM-MQC detection scheme, it was possible to reveal for the first time collective four-atom resonances and to observe these at vapor densities four orders of magnitude lower (down to $10^8\,\mathrm{cm}^{-3}$) than before. A thorough phase characterization of the higher order spectra in conjunction with high resolution measurements has furthermore unraveled distinct phase signatures of the multiatom resonances, that are connected to the fundamental hyperfine states in the system. A first explanation based on long-range dipole-dipole interaction has been sought in collaboration with the group of A. Eisfeld [B4].

The third theme of this dissertation covers the prospective extension of nonlinear spectroscopy schemes to high photon energies in the vacuum ultraviolet (VUV) to X-ray regime. Having, in recent years, established nonlinear time-domain spectroscopy in the THz to ultraviolet (UV) spectral range [36–39], a transfer to extreme photon energies is currently one of the main objectives in this field. This development would allow for site and chemical selectivity by addressing specific core resonances or exploiting their pronounced chemical shifts [40]. Likewise, incorporation of attosecond pulses would become feasible, thus providing unprecedented temporal resolution and opening the door to attosecond science [41]. However, at XUV wavelengths, the demands on phase stability in the optical setup increase drastically and the implementation of essential phase-matching/-cycling methods becomes intricate. Due to these challenges, only few advances in this direction have been made so far [42–45]. In this view, a promising scheme to establish coherent nonlinear all-XUV spectroscopy is proposed in this dissertation based on an extension of the phase modulation technique [B3]. A proof-of-principle study with second harmonic generation is presented in chapter 8. With this work, important insights have been gained and the general advantages of this approach have been confirmed, laying the basis for future efforts in this direction.

2 Theory

This chapter describes the basic principle of the applied phase modulation spectroscopy method and provides some general background information about nonlinear time-domain spectroscopy, dipole-dipole interaction in atomic gases and the HENDI technique.

2.1 Basic principle of coherent time-domain spectroscopy

In this thesis, a specialized phase modulation technique is incorporated to perform coherent time-domain spectroscopy on various gas-phase systems. Before discussing in detail the principle of this method, first some general aspects of nonlinear time-domain spectroscopy are discussed in this chapter. The purpose of this discussion is to clarify the basic concept of nonlinear time-domain spectroscopy and to elucidate the experimental requirements that apply in respective state-of-the-art methods. In the subsequent chapters it is then explained how the phase modulation approach specifically addresses these requirements. The discussion here is focused on the most important aspects relevant in the context of this thesis. For further details it is referred to Refs. [1, 2, 4, 46].

As outlined in the introduction, the two main goals in nonlinear spectroscopy are (i) attaining simultaneous high spectral and temporal resolution, and (ii) providing selective/background-free probing of specific nonlinear signal contributions. With the development of coherent nonlinear spectroscopy in the time domain, both aims can be achieved. Starting with (i), high spectro-temporal resolution is obtained by probing the coherent evolution of optically induced WPs in the time domain. In this context, two conceptually different methods are discussed. Both yield the desired high spectro-temporal resolution, but differ in the attainable information and experimental demands. One is measuring the rovibrational WP motion not including electronic coherences, and the other is probing interferences of electronic WPs, which is commonly termed WPI.

In the first scheme, a femtosecond pump pulse excites a rovibrational WP in some excited electronic state of a molecular system [see Fig. 2.1(a)]. Being spread in the energy space of the system, this WP corresponds to an initially sharp distribution in the nuclear coordinate space and as such can be directly related to the nuclear motion in the system [2]. The probability distribution of this non-stationary molecular state undergoes a periodic motion in the molecular potential. Thereby, dephasing and rephasing of the WP occurs according to the anharmonicity of the molecular potential. This coherent motion is probed with a second probe pulse of controllable delay τ which drives a transition through a Frank-Condon window (FCW) to the higher-lying state. In this step, the excitation probability depends on the overlap of the WP with the Franck-Condon region and therefore reflects the current state of the WP. Subsequent photoionization, stimulated emission or fluorescence detection are commonly used as observables to retrieve the

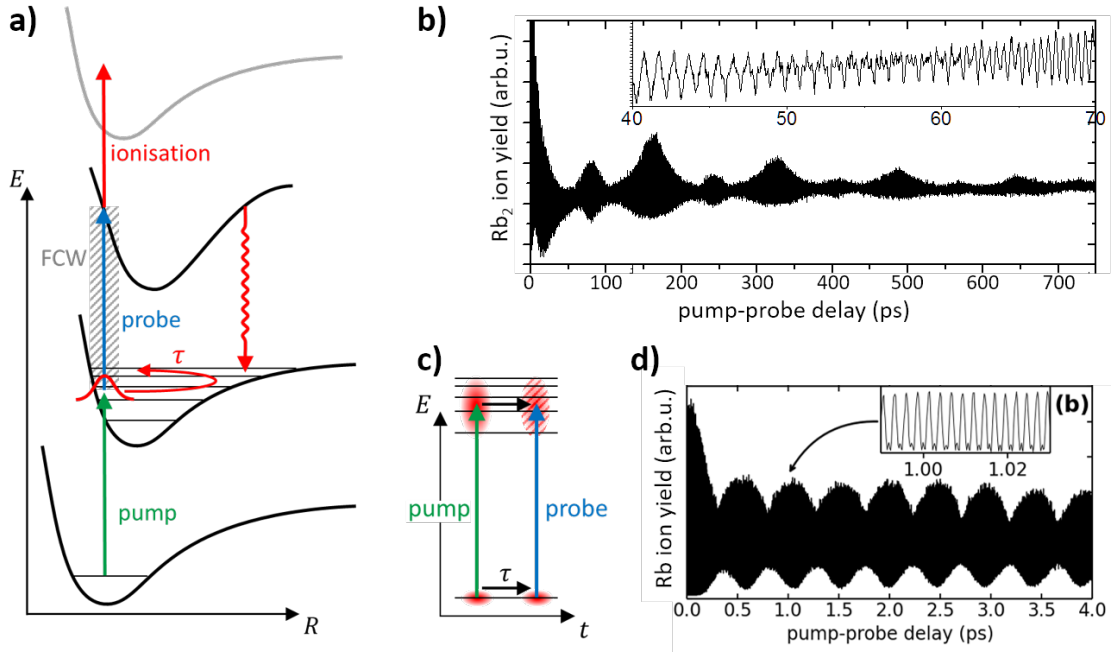

Figure 2.1: (a) Pump-probe scheme to track rovibrational WP motion in a molecular system. A first pulse (pump) excites a WP in the system which is probed after a delay time τ with a second pulse (probe). FCW denotes the Franck-Condon window and the highest lying potential (grey) indicates the ionic molecular state. (b) Respective pump-probe transient for WP propagation in a rubidium dimer. (c) WPI scheme: Pump and probe pulses each excite a rovibronic WP in the system. The interference of the two WPs gives rise to a modulation of the excited state population depending on the pump-probe delay τ. (d) Respective WPI measurement for electronic WPs excited in a rubidium atom. Note the different time scales in the measurements being in the picosecond in (b) and femtosecond range in (d). (b) and (d) are adapted from Refs. [49, B1], with permission from the PCCP Owner Societies.

WP signal [47]. The obtained signals exhibit oscillatory features which directly reflect the WP evolution with typical revivals and fractional revivals arising from the dephasing and rephasing of the WP [Fig. 2.1(b)]. Thereby, the signal frequencies correspond to the energy differences of the involved rovibrational states and thus contain the spectral information of the system. At the same time, a high temporal resolution is achieved due to the short optical pulses involved. This type of experiment has been extensively exploited in the early years of ultrafast spectroscopy [2]. As prominent examples, it enabled the first observation of bond breaking in real time [3], and, for the first time, provided real-time information about the transient intermediates in chemical reactions [48]. Both insights are not accessible in frequency-domain spectroscopy and, in this regard, they intuitively demonstrate the advantage of ultrafast time-domain spectroscopy.

While the previous scheme provides information about coherent and incoherent processes governed by the rotational and vibrational states, e.g. population relaxation and decoherence/dephasing dynamics, information about the electronic degree of freedom is vastly missing. This issue can be addressed with electronic WPI. In this case, an inter-

ferometric measurement is performed detecting the interference of two rovibronic WPs induced in the system upon weak perturbation by pump and probe pulses. In contrast to the previous case, the induced non-stationary states hence comprise of quantum states occupying different electronic states.

In more detail, pump and probe pulses each excite a superposition of the initial ground state and some excited electronic states, for instance rovibrational states in a higher-lying electronic potential [Fig. 2.1(c)]. These two WPs interfere in the quantum system as a function of the pump-probe delay τ which gives rise to a modulation of the excited state populations. Hence, the relative temporal evolution of the two WPs is encoded in the population states which are deduced from e.g. fluorescence or photoelectron/ion yields. The obtained signal then contains information about all degrees of freedom including also electronic decoherence/dephasing or rovibronic coupling. Note, that in the former scheme, the WP evolution is probed with selective excitation through a FCW, while in the WPI scheme, the WP evolution is deduced from the interference between two WPs. Hence, the latter scheme is more versatile in the choice of systems to be studied and an example for an atomic system is given in Fig. 2.1(d). Here, the signal exhibits the typical interference fringes or quantum beat oscillations due to constructive/destructive interference induced in the quantum system upon WP excitation.

However, as in both schemes the signal frequencies correspond to the energy difference of participating states [$\omega_{nm} = (E_n - E_m)/\hbar$], these frequencies are considerably larger in the case of electronic WPI. While for the pure rovibrational WPs, the signal oscillations have periods typically in the order of 10 ps to 100 fs, WPI signals involve sub 5 fs oscillation periods for electronic transitions lying in the visible (VIS) spectral range [cf. Fig. 2.1(b) and (d)]. As such, WPI experiments require a high degree of phase control which poses demands on the interferometric stability of $\lambda/50$ to $\lambda/100$ in the optical setup (λ denotes the laser center wavelength) [50]. In order to address this issue, in the past 20 years a variety of phase stabilization methods have been engineered in conjunction with the development of advanced nonlinear time-domain spectroscopy schemes. These include active stabilization with closed-loop feedback [24, 51] and passive arrangements based on diffractive [52] or birefringent optics [53], pulse shaping [54–57] or acousto-optic phase modulation [26, 58].

Coming to (ii), the enhanced information encoded in the nonlinear system response make it desirable to have spectroscopic methods being particularly sensitive to this part of the light-matter interaction. However, the nonlinear response is generally of high complexity with a vast number of different processes overlapping in the signal. Therefore, methods are necessary to select specific contributions and narrow down the system response to the relevant information. With the above mentioned stabilization methods, schemes have been developed that provide means for selective/background-free detection of the nonlinear system response and thereby also accounting for the weak nature of these nonlinear signals. These techniques rely on an extension of the WPI scheme, having lead to two methodologies termed *phase-matching* and *phase-cycling*.

The phase-matching principle is most commonly known from four-wave mixing, where three incident waves coherently interact in a nonlinear medium and generate a fourth wave propagating in a different (phase-matching) direction [59]. Similarly in nonlinear

spectroscopy, a non-collinear pulse sequence of multiple phase-locked pulses with well-defined k-vectors excite the sample. Upon the coherent interaction with the sample, a macroscopic polarization is induced of which the various linear and nonlinear contributions radiate off the sample in different directions due to momentum conservation [4, 50]. Background-free detection of individual nonlinear signals is then achieved with spatial masking. On the contraray, in phase-cycling, the phase of the optical pulses is systematically altered throughout the experiment and the desired nonlinear contributions of the system's response are identified and isolated due to their unique phase signature [5, 54]. This scheme is applied in partially collinear [56] or fully collinear geometries [54, 57] of which the latter does not rely on an ensemble interference effect, i.e. on a macroscopic polarization induced in the sample, and thus can in principle be applied to single particles.

In conclusion, the WPI method reveals generally more information than is obtained from vibrational WP propagation and can be combined with phase-matching and -cycling schemes. Therefore, this concept is commonly preferred albeit the considerably higher experimental challenges due to the increased demands on phase stability. In particular, the underlying principle of most state-of-the-art nonlinear spectroscopy types is based on the interference of optically induced WPs, i.e. on WPI [1]. Though, pulse sequences of more than two pulses, e.g. three to four pulses, are typically employed [60]. This provides a more direct access to nonlinear processes and increases the signal selectivity as well as the dimension of the deduced spectra (multidimensional spectroscopy) [4]. As such, the WPI principle is considered as the prerequisite for advanced nonlinear spectroscopy schemes and is used as a benchmark in this thesis.

2.2 Phase-modulated wave packet interferometry

As WPI relies on an interferometric measurement scheme, a high demand on the phase stability is necessary in these experiments. To account for this issue, a phase modulation technique was implemented in this PhD thesis and is combined with electronic WPI measurements. The concept of this scheme, denoted phase-modulated wave packet interferometry (PM-WPI), is explained in the current chapter. As will be outlined, the phase modulation approach considerably reduces the demands on phase stability in the WPI experiments and introduces a dynamic phase-cycling scheme that allows for signal selection. Furthermore, the sensitivity is highly improved with lock-in amplification. This makes this method particularly suitable for experiments with highly dilute samples such as helium nanodroplet beams. Some content of this chapter is adapted from Refs. [B1, B3]. More details about the phase modulation approach can be also found in Refs. [25, 26, 58, B1].

In WPI, phase-related pump and probe pulses each excite a WP in the sample, which interfere with each other depending on the relative phase between pump and probe pulses [61]. The resulting constructive and destructive WP interference is reflected as oscillations in the excited state populations. The WP interference is then monitored via incoherent processes (*action* signal) that probe the excited populations in the system. The employed optical scheme comprises of a collinear pump-probe setup [Fig 2.2(a)]. A typical Mach-Zehnder interferometer arrangement including a motorized delay stage is

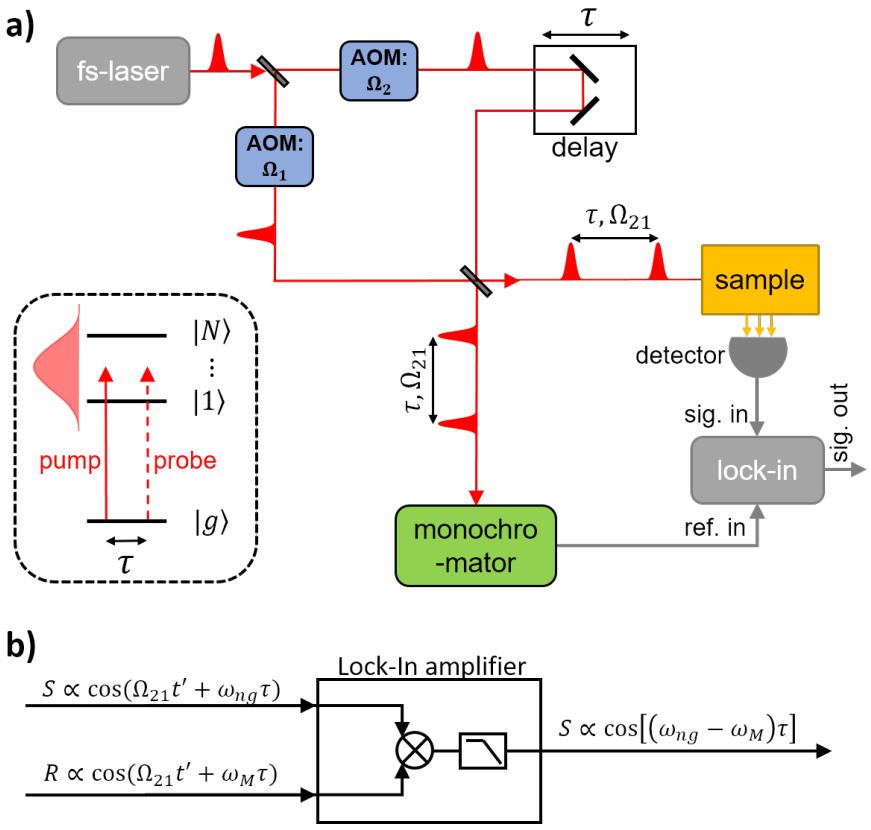

Figure 2.2: (a) Optical PM-WPI scheme. Femtosecond pump-probe pulse sequences are generated in a Mach-Zehnder interferometer. AOMs imprint a continuous phase modulation in the diffracted laser pulses. A monochromator is used to construct a reference signal for lock-in demodulation of the acquired data. This removes the phase modulation from the signal and returns the demodulated pure WP signal. The inset shows the excitation scheme in a model system. (b) Lock-in demodulation process comprised of a multiplication and subsequent low-pass filter operation which yields the frequency-downshifted WPI signal at the output.

used to generate pulses of adjustable interpulse delay τ. A simple model system consisting of few discrete energy eigenstates $|g\rangle, |1\rangle, ..., |N\rangle$, as shown in the inset of Fig. 2.2(a) is assumed. In this system, the pump and probe pulses each excite a coherent superposition of the initial state $|g\rangle$ and excited states $|n\rangle$ lying within the laser bandwidth. In the experiment, the pump-probe delay τ is systematically scanned and the WP interfernce signal is acquired. Neglecting at first the phase modulation, this yields a typical quantum beat signal [1]

$$S(\tau) = \sum_{n=1}^{N} A_n \left[1 + \beta \cos(\omega_{ng}\tau)\right] . \tag{2.1}$$

$A_n \propto |D_{ng}|^2 \tilde{E}^2(\omega_{ng})$ describes the transition probability for each $|g\rangle \rightarrow |n\rangle$ transition, with $\tilde{E}(\omega_{ng})$ being the Fourier transform of the single pulse electric field (assuming identical pump and probe pulses) evaluated at the transition frequency $\omega_{ng} = (E_n - E_g)/\hbar$ and

D_{ng} being the transition dipole moment of the relevant degrees of freedom (electronic, vibrational and rotational). The constant part in Eq. 2.1 encompasses all background signals not exhibiting a pump-probe dependence, whereas the oscillating part reflects the WP interference. The dimensionless parameter $\beta \leq 1$ determines the contrast of the quantum beat signal. Theoretically, it is $\beta = 1$, however, experimental conditions (mainly optical alignment and probing mechanism) often drastically reduce the quantum beat contrast. For simplicity, temporal overlap between pump and probe pulses has been omitted and their relative carrier-envelope phase has been set to zero. The latter is well satisfied, since pump and probe pulses originate from the same initial laser pulse split by a beam splitter. Furthermore, line broadening and decoherence effects are neglected. These will be included in the density matrix formalism presented in the successive chapter 2.3.

The WP interference in Eq.(2.1) is solely controlled by the pump-probe delay τ. However, the signal may in addition be modified by changing the relative phase of the optical pulses, as done in the phase modulation scheme. For this purpose, two acousto-optical modulators (AOMs) are placed inside the optical interferometer [Fig. 2.2(a)], that are driven with two distinct radio frequencys (RFs) denoted Ω_j (j=1,2). These bragg cells shift the frequency of the transmitted light by the applied acoustic frequency Ω_j. In case of short optical pulses (pulse duration $\Delta t \ll 1/\Omega_j$), this results in an instantaneous phase shift of $\phi_j(t') = \Omega_j t'$ for each pulse deflected by AOM j at time t'. Phase-locked driving of the AOMs then imparts a well-defined modulation of the WP signal according to $\phi_{21}(t') = \Omega_2 t' - \Omega_1 t' = \Omega_{21} t'$, yielding the PM-WPI signal

$$S(\tau, t) = \sum_{n=1}^{N} A_n \left[1 + \beta \cos(\omega_{ng}\tau - \Omega_{21} t')\right] . \tag{2.2}$$

Note, that between each laser shot, t' increments by the laser repetition time T_{rep}. In the experiment it is $\Omega_{21} \ll 1/T_{\text{rep}}$ and thus $\phi_{21}(t')$ describes a quasi-continuous modulation of the signal, while $\omega_{ng}\tau$ represents a constant phase, incremented in discrete steps throughout the pump-probe scan.

Simultaneously, replicas of the laser pulses are spectrally filtered in a monochromator resulting in a temporal elongation of the pulses, respectively. In this way, the two-pulse interference can be detected at the exit slit of the monochromator for pump-probe delays much longer than the initial pulse duration, yielding a signal of the form

$$R(\tau, t) = R_0 \left[1 + \cos(\omega_M \tau - \Omega_{21} t')\right] . \tag{2.3}$$

Here, ω_M denotes the center frequency of the monochromator's transmission function and R_0 an arbitrary amplitude. This waveform serves as reference signal for lock-in detection [Fig. 2.2(b)]. Upon lock-in demodulation the PM-WPI signal [Eq.(2.2)] is multiplied with the normalized oscillatory part of Eq.(2.3), yielding sum and difference frequency components $\propto \cos[(\omega_{ng} \pm \omega_M)\tau - (\Omega_{21} \pm \Omega_{21} t']$, respectively. A subsequent low-pass filter removes the sum frequency component resulting in an output signal of the form

$$S(\tau) = \sum_{n=1}^{N} A_n \beta \cos\left[(\omega_{ng} - \omega_M)\,\tau\right] . \tag{2.4}$$

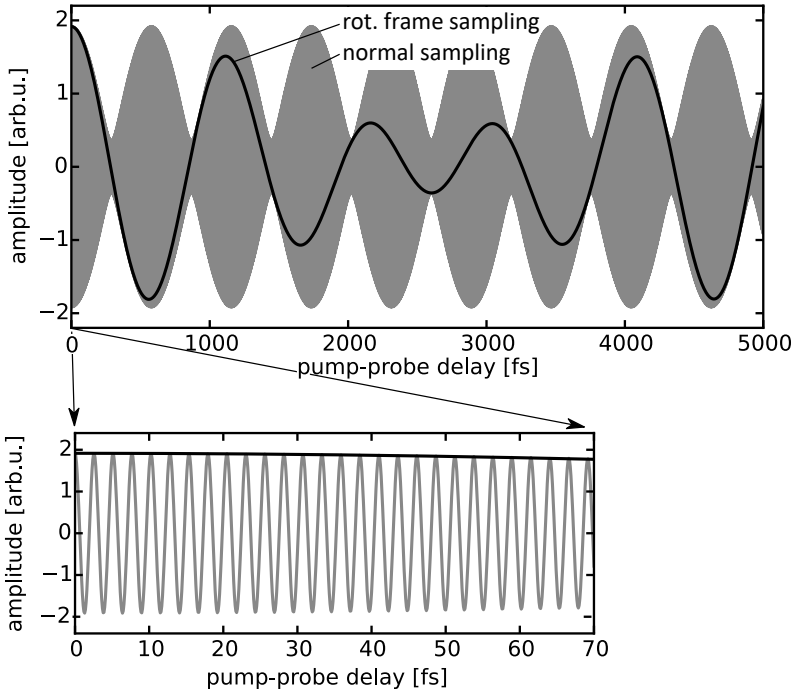

Figure 2.3: Rotating frame sampling compared with normal sampling. For visualization, Eq. (2.1) (grey) and Eq. (2.4) (black) are plotted for the D_1 and D_2 line transition of potassium. The rotating frame sampling in the phase modulation scheme leads to significantly smaller signal frequencies (see zoom of 0-70 fs pump-probe delay).

This signal oscillates with the downshifted frequency $\bar{\omega} = \omega_{ng} - \omega_M$ while the phase modulation $\phi_{21}(t') = \Omega_{21}t'$ is removed. Thus, Eq.(2.4) describes the pure WP interference signal shifted to a significantly lower frequency regime. This effect is commonly termed *rotating frame sampling* and appears also in heterodyned detection with a local oscillator field [50] and in pulse shaper based schemes [54, 55]. For visualization of the rotating frame sampling, Eq.(2.1) and (2.4) are exemplary plotted for the D_1 and D_2 line transitions of potassium in Fig. 2.3 ($\omega_M = 13011\,\mathrm{cm}^{-1}$, laser spectrum centered at $\omega_L = 13020\,\mathrm{cm}^{-1}$, full width at half maximum (FWHM) $\Delta\omega_L = 83\,\mathrm{cm}^{-1}$, Gaussian shape). As can be seen, Eq.(2.1) corresponds to normal sampling of the WP signal, whereas Eq.(2.4) describes the demodulated PM-WPI signal that corresponds to the rotating frame sampling of the WP signal. In the latter case, the amount of required sampling points is drastically reduced (in this work typically by a factor of $100 - 1000$). In contrast to optical heterodyning with a local oscillator field, in the phase modulation approach the signal is heterodyned with the electronic reference signal in the phase-synchronous lock-in demodulation. Both concepts yield amplitude and phase information and thus allow for a full reconstruction of the complex-valued system response (more details in chapter 2.3.3). However, the phase modulation approach is less intricate to implement and more robust against laser beam drifts.

Besides this aspect, considerably more important is the drastic reduction of phase noise in the demodulated signal. Any kind of fluctuations of the optical path length inside

the interferometer (e.g. vibrations of optics, fluctuation of refractive index) will cause phase/timing jitter in the signal which in conventional WPI setups severely compromises the signal. In the presented concept, this jitter, denoted $\delta\tau$, is simultaneously imprinted onto the WPI and the reference signal and is therefore efficiently removed in the lock-in demodulation process. As a result, the demodulated signal exhibits a residual phase noise of $\delta\phi = \bar{\omega}\delta\tau$ which is considerably smaller (typically a factor 100 to 1000) than in a conventional WPI setup.

In addition, the lock-in filtering introduces a selection rule, selecting only signals modulated with $\phi_{21}(t') = \Omega_{21}t'$ and thereby discriminating background signals such as stray light. This selection procedure may be regarded as dynamic phase-cycling [58] or shot-to-shot phase-cycling as commonly used in nonlinear spectroscopy [5], allowing for selective extraction of linear and, as shown in chapter 6, distinct nonlinear signals. Furthermore, the concept of lock-in amplification is generally capable of extracting signals with a known carrier frequency from large background contributions. As such, the combination of acousto-optical phase modulation and lock-in amplification provides a very efficient scheme to recover even weak WP signals and is therefore ideally suitable for the application to dilute samples.

In conclusion, PM-WPI satisfies the identified requirements of nonlinear time-domain spectroscopy, i.e. providing a passive phase stabilization scheme which reduces the demands on phase stability and providing dynamic phase-cycling that allows for selection of specific signal contributions. These properties are combined with efficient lock-in amplification, yielding particular high sensitivity, which make this method ideal for the studies conducted in this work.

2.3 Calculation of signals with the density matrix formalism

Nonlinear time-domain spectroscopy usually relies on the weak interaction of a sequence of laser pulses with a material system. Due to the weak perturbation of the system, time-dependent perturbation theory can be applied to describe the experiments. The calculations are commonly done in the wave function or density matrix formalism [1, 62]. Both approaches have individual advantages. In particular, the latter has the advantages that the inclusion of phenomenological decay rates is straight forward, and that the system's response can be represented by double-sided Feynman diagrams. These are more intuitive than loop diagrams commonly used in the wave function formalism [63]. Therefore, the density matrix description is favored in the current work. However, so far PM-WPI experiments have been exclusively described in the wave function formalism [25, 62, 64] and the purpose of the current chapter is to provide a theoretical framework based on the density matrix formalism.

To this end, exemplary the PM-WPI signal for a two-level system is derived. In particular, a diagrammatic description of the signals with double-sided Feynman diagrams is introduced. This approach is used in the discussion of experimental results in chapters 6-8. Moreover, finite pulse effects are analytically included as done in Ref. [65]. This is in contrast to most approaches describing the experiment in the impulsive limit with δ-pulses [50]. The description given in the following has the intention to provide a concise

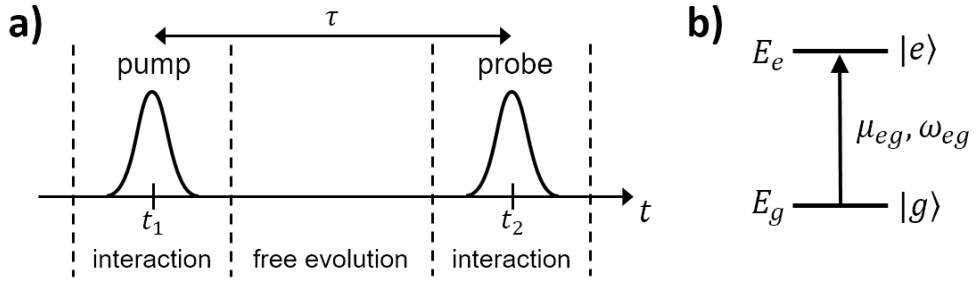

Figure 2.4: (a) Schematic representation of the time evolution in the applied pump-probe scheme. (b) Two-level model system.

summary of the theory with the focus on the most important aspects. For more details it is referred to Refs. [1, 50, 65].

2.3.1 Perturbative treatment of the light-matter interaction

In the applied pump-probe scheme, the time evolution of the system can be separated into the light-matter interaction and the free evolution of the system in between [Fig. 2.4(a)]. Thereby, the free evolution of the system can be described with the optical Bloch equations [50]. For a two-level model system [Fig. 2.4(b)] and including phenomenological decay, the Bloch equations are

$$\rho_{ee}(t) = \rho_{ee}(t_0)e^{-\frac{t-t_0}{T_1}}, \tag{2.5}$$

$$\rho_{gg}(t) = 1-\rho_{ee}(t), \tag{2.6}$$

$$\rho_{eg}(t) = i\rho_{eg}(t_0)e^{-i\omega_{eg}(t-t_0)}e^{-\frac{t-t_0}{T_2}}, \tag{2.7}$$

$$\rho_{ge}(t) = \rho^*_{eg}(t), \tag{2.8}$$

with $\omega_{ij} = (E_i - E_j)/\hbar$ and T_1, T_2 being the time constants for population relaxation and homogeneous dephasing, respectively. It is $1/T_2 = 1/(2T_1)+1/T_2^*$, with T_2^* describing the pure dephasing time. For a more compact notation, the complex resonance frequencies ξ_{ij} are introduced as

$$\xi_{ij} = \omega_{ij} - i\gamma_{ij}, \quad \text{with} \quad \gamma_{ij} = \begin{cases} \frac{1}{T_1}, & \text{for } i = j, \\ \frac{1}{2T_1} + \frac{1}{T_2^*}, & \text{for } i \neq j. \end{cases} \tag{2.9}$$

The actual light-matter interaction is treated semiclassically in the dipole approximation. The time-dependent Hamiltonian for this problem is

$$\hat{H}(t) = \hat{H}_0 + \hat{V}(t), \tag{2.10}$$

with $\hat{H}_0 = E_g\,|g\rangle\langle g| + E_e\,|e\rangle\langle e|$ being the time-independent Hamiltonian of the unperturbed system and $\hat{V}(t) = [\mu_{eg}\,|e\rangle\langle g| + h.c.]E(t)$ the time-dependent classical perturbation

of the system. It has been assumed, that the dipole moment and the electric field vector are parallel and the vector character of both parameters has been omitted. Accordingly, the Schrödinger equation is

$$i\hbar\frac{\partial}{\partial t}\hat{\rho}(t) = \left[\hat{H}_0 + \hat{V}(t)\right]\hat{\rho}(t)\,. \tag{2.11}$$

The classical electric field for pump and probe pulses (denoted with subscript $a = 1, 2$) is described with a Gaussian envelope centered at t_a with peak amplitude ϵ_a, FWHM Δt, central frequency ω_L and carrier envelope phase (CEP) ϕ_a:

$$E_a(t) = A(t - t_a)\cos\left[\omega_L(t - t_a) + \phi_a\right]\,, \quad \text{with} \quad A(t) = \epsilon_a e^{-4\log(2)\left(\frac{t-t_a}{\Delta t}\right)}\,. \tag{2.12}$$

For simplicity, the field's polarization and spatial dependence have been neglected. The combined electric field for a pump-probe sequence is

$$E(t) = \frac{1}{2}\sum_{a=1,2} E_a^+(t) + E_a^-(t)\,, \tag{2.13}$$

with $E_a^\pm(t) = A_a(t-t_a)e^{\pm i\omega_L(t-t_a)}e^{\pm i\phi_a}$. Accordingly, $\tilde{E}^\pm(\omega) = \mathrm{FT}\{E_a^\mp(t)\}$ denote the positive and negative frequency spectra of the electric fields.

While the free evolution of the system can be described with the optical Bloch equations, the light-matter interaction itself is described in a perturbative way using time-dependent perturbation theory which applies for sufficiently weak fields. The solution of the Schrödinger equation [Eq. (2.11)] is then

$$\hat{\rho}(t) = \sum_{n=0}^{\infty}\hat{\rho}^{(n)}(t)\,, \tag{2.14}$$

with $\hat{\rho}^{(0)}(t) = |g\rangle\langle g|$ and the n'th order correction in the interaciton picture is [50]

$$\begin{aligned}\hat{\rho}^{(n)}(t) \;&=\; (-\frac{i}{\hbar})^n \int_{t_0}^{t}\mathrm{d}t_n \int_{t_0}^{t_{n-1}}\mathrm{d}t_{n-1}\cdots\int_{t_0}^{t_2}\mathrm{d}t_1 \\ &\quad \underbrace{E(t_n)E(t_{n-1})\cdots E(t_1)}_{4^n\text{ terms}}\;\underbrace{\Big[\hat{\mu}(t_n),\big[\hat{\mu}(t_{n-1})\cdots,[\hat{\mu}(t_1),\hat{\rho}(t_0)]\cdots\big]\Big]}_{2^n\text{ terms}}\,.\end{aligned} \tag{2.15}$$

Note, that for a simple two-level system and a two-pulse sequence perturbing the system, Eq. (2.15) consists in second order already of 64 terms. This explains the necessity of an experimental selection process (phase-matching/-cycling), that isolates specific interaction pathways in the signal.

It is often more intuitive to write Eq. (2.15) in a recursive form:

$$\hat{\rho}^{(n)}(t) = -\frac{i}{\hbar}\int_{t_0}^{t}\mathrm{d}t_n\, E(t_n)\left[\hat{\mu}(t_n), \hat{\rho}^{(n-1)}(t_n)\right]\,. \tag{2.16}$$

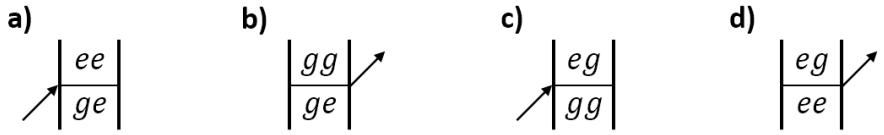

Figure 2.5: Graphical representation of Eq.(2.17)-(2.20) using double-sided Feynman diagrams. Each vortex describes a light-matter interaction $|i\rangle\langle j| \rightarrow |k\rangle\langle l|$; i.e. (a), (c) describe an absorption of the ket-side of the density matrix and (b), (d) an emission on the bra-side.

Neglecting all terms not surviving the rotating wave approximation, Eq. (2.16) reduces to four possible processes:

$$\rho_{ee}^{(n)}(t) = -\frac{i\mu_{eg}}{2\hbar}\int_{t_0}^{t} \mathrm{d}t_n\, E_a^-(t_n) e^{-i\xi_{ee}(t-t_n)} \rho_{ge}^{(n-1)}(t_n)\,, \tag{2.17}$$

$$\rho_{gg}^{(n)}(t) = +\frac{i\mu_{eg}}{2\hbar}\int_{t_0}^{t} \mathrm{d}t_n\, E_a^-(t_n) e^{-i\xi_{gg}(t-t_n)} \rho_{ge}^{(n-1)}(t_n)\,, \tag{2.18}$$

$$\rho_{eg}^{(n)}(t) = -\frac{i\mu_{eg}}{2\hbar}\int_{t_0}^{t} \mathrm{d}t_n\, E_a^-(t_n) e^{-i\xi_{eg}(t-t_n)} \rho_{gg}^{(n-1)}(t_n)\,, \tag{2.19}$$

$$\rho_{eg}^{(n)}(t) = +\frac{i\mu_{eg}}{2\hbar}\int_{t_0}^{t} \mathrm{d}t_n\, E_a^-(t_n) e^{-i\xi_{eg}(t-t_n)} \rho_{ee}^{(n-1)}(t_n)\,. \tag{2.20}$$

The physical meaning of these expressions is intuitive. Eq. (2.17), (2.19) describe an absorption process on the ket-side of the density matrix, i.e. $|g\rangle \rightarrow |e\rangle$, whereas Eq. (2.18), (2.20) describe stimulated emission on the bra-side of the density matrix, i.e. $\langle e| \rightarrow \langle g|$. Thereby, the integrand represents the transition probability as a function of t_n with highest probability at t_a where the electric field peaks and zero probability where $E_a(t_n) \approx 0$. In accordance with the Bloch equations, $e^{-i\xi_{ij}(t-t_n)}$ describes the free evolution of the system after the interaction with the external field, i.e. for the interval $[t_n, t]$. Note, that for each process a complex conjugate process/term exists which has been omitted for simplicity.

Essentially, Eq.(2.17)-(2.20) and their complex conjugate each describe one step in the light-matter interaction and subsequent free evolution of the system. With this set of equations all processes occuring in the pump-probe experiment can be calculated. Successive combination of Eq.(2.17)-(2.20) (including also complex conjugates) and summing over all possible variations ζ yields then the n'th order correction $\hat{\rho}^{(n)}(t) = \sum_\zeta \hat{\rho}_\zeta^{(n)}(t)$ of the density matrix. Thereby, each variation is subject to n field-matter interactions and may be identified as a specific interaction pathway (*Liouville pathway*). The summation of these pathways corresponds to the interference of different quantum pathways in the system, which is comparable to a Young's double-slit experiment.

2.3.2 Double-sided Feynman diagram

Each step described by Eq.(2.17)-(2.20) and respective complex conjugates, can be readily described in a graphical representation using double-sided Feynman diagrams (Fig. 2.5). In analogy to the above considerations, each n'th order contribution $\hat{\rho}_\zeta^{(n)}$ to the density

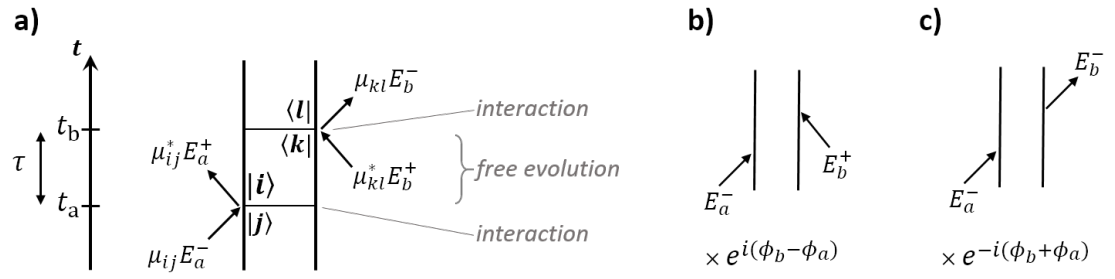

Figure 2.6: (a) General rules applying for Feynman diagrams in nonlinear spectroscopy. (b) and (c): Derivation of phase factors from the Feynman diagrams. Since each interaction with $E_a^{\pm}$ imprints a phase factor $e^{\pm i\phi_a}$, different phases accumulate in the given examples. For the specific case of PM-WPI, this phase corresponds to a quasi-continuous modulation of the signal ($\phi_a = \Omega_a t'$)

matrix can be hence constructed graphically by combining the diagrams in Fig. 2.5 (including complex conjugates). Respectively, n'th order Feynman diagrams are obtained of which each involves n vortices corresponding to n light-matter interactions. In this way, Feynman diagrams can be used as a convenient way to keep track of all possible Liouville pathways and calculate their contribution to the final state of the system based on time-dependent perturbation theory and the rotating wave approximation.

In general, several rules apply for Feynman diagrams when used in the context of nonlinear spectroscopy [1]. These are illustrated in Fig. 2.6(a) and listed in the following:

- Time increases from bottom to top.
- The left/right column corresponds to the ket-/bra-side of the density matrix.
- Arrows indicate the light-matter interaction, with inward-/outward-pointing arrows correspond to the absorption/emission of a photon.
- Right-pointing arrows correspond to $\mu_{ij}E_a^-$ interactions and left-pointing arrows to the complex conjugated interaction.
- Each diagram contributes to the density matrix with a sign according to $(-1)^l$, with l being the number of interactions on the left-hand side of the diagram.
- The mirror image of each diagram describes the complex conjugate pathway. These are typically omitted as they do not contain additional information.

As another benefit of the diagrammatic description, phase factors can be directly deduced from the diagrams for each individual contribution $\hat{\rho}_{\zeta}^{(n)}(t)$. In the coherent interaction scheme, each pulse imprints its phase onto the quantum state ρ_{ij}, which yields a factor of $e^{\pm\phi_a}$ for each $E_a^{\pm}$ interaction. Exemplary, this can be seen in Eq. (2.17)-(2.20) when pulling the constant phase factor $e^{-\phi_a}$ in front of the integral. The accumulation of all phase factors over the n interactions yields a distinct final phase signature for each

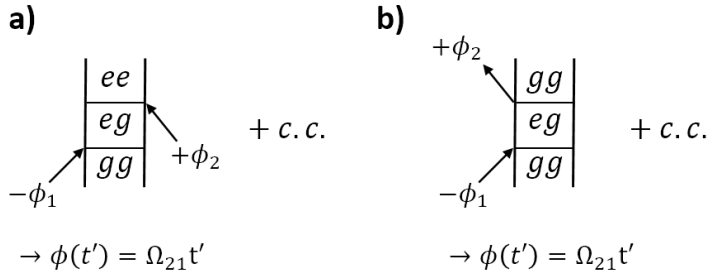

Figure 2.7: Feynman diagrams for the considered PM-WPI experiment with phase signature $\phi(t') = \Omega_{21}t'$.

pathway which can be readily derived from the Feynman diagrams using the rules above [Fig. 2.6(b),(c)].

Specifically in the phase modulation scheme, each pulse gets an instantaneous phase imprinted which is $\phi_a = \Omega_a t_m$, $t_m = t_0 + mT_{\mathrm{rep}}$. This phase is constant for the individual pulses and the resulting phase factor for each pathway can be derived as discussed. However, the imprinted phase ϕ_a increments in the experiment on a shot-to-shot basis, i.e. between each pulse launched by the laser, ϕ_a increments in discrete steps $\Delta\phi_a = \Omega_a T_{\mathrm{rep}}$ throughout the data run. Since in the experiment it is $\Omega_a \ll 1/T_{\mathrm{rep}}$, the obtained signal becomes quasi-continuously modulated, i.e. $t_m \to t'$, with t' denoting a continuous variable. Therefore, a modulation frequency can be assigned to each pathway and all pathways not yielding a modulation of $\phi(t') = \Omega_{21}t'$ are blocked in the experiment by the lock-in amplifier. In this way, certain pathways are selected due to their phase signature. Such procedure is commonly termed phase-cycling [5], as originally established in pulse shaper based experimental schemes [54].

2.3.3 Time- and frequency-domain signals

In the conducted experiments, the interference of electronic WPs imprinted in the quantum system results in a modulation of the excited state populations with respect to the relative phase between the WPs. To deduce the interference signal, observables are applied in the experiment, that are sensitive to the excited state populations. Examples are fluorescence or photoionization. As such, the signal is given by

$$S \propto \sum_e \mathrm{tr}\Big\{ P_e\, \hat{\rho}(t) \Big\}, \tag{2.21}$$

where it is summed over all excited states $|e\rangle$ and $P_e = |e\rangle\langle e|$ is the respective projection operator. The expected WP signal can be thus directly derived from the Feynman diagrams ending in excited state populations. Furthermore, for a two-pulse experiment, it is often sufficient to consider perturbation up to second order. Hence, neglecting all diagrams not yielding a modulation of $\phi(t') = \Omega_{21}t'$, only two diagrams (and their complex conjugate) remain (Fig. 2.7). This manifests a significant reduction of the initially 64 terms [Eq.(2.15)]. As can be seen, all first and second order processes with only either of the pulses interacting with the system cancel in the phase-cycling procedure, i.e. are

blocked by the lock-in amplifier. Likewise, diagram Fig. 2.7(b) does not contribute since ending in a ground state population. For the remaining diagram Fig. 2.7(a), one gets

$$\rho_{ee}^{(2)}(t,\tau) = \frac{|\mu_{eg}|^2}{4\hbar^2}\int_{t_0}^{t} \mathrm{d}t''\, E_2^+(t'')e^{-i\xi_{ee}(t-t'')}\int_{t_0}^{t''} \mathrm{d}t'\, E_1^-(t')e^{-i\xi_{eg}(t''-t')}\rho_{gg}(t_0)\,, \quad (2.22)$$

where t_1 has been set to zero and thus $\tau = t_2$ denotes the pump-probe delay.

The observables applied in the experiment map the excited state population at the time immediately after the interaction with the second pulse. This is expressed by setting $\gamma_{ee} = 0$ and performing the transition $t \to \infty$, thus the signal becomes independent of t. Likewise, it is assumed that for $t < t_0$ the system is unperturbed and in its ground state, which satisfies $t_0 \to -\infty$ and $\rho_{gg}(-\infty) = 1$. Implementing in addition the Heaviside-Theta function, denoted $\Theta(t)$, Eq. 2.22 simplifies to

$$\begin{aligned}
\rho_{ee}^{(2)}(\tau) &= \frac{|\mu_{eg}|^2}{4\hbar^2}\int_{-\infty}^{\infty} \mathrm{d}t''\, E_2^+(t'')\int_{-\infty}^{\infty} \mathrm{d}t'\, E_1^-(t')\Theta(t''-t')e^{-i\xi_{eg}(t''-t')} \qquad (2.23)\\
&= \frac{|\mu_{eg}|^2}{4\hbar^2}e^{i\phi_{21}}\int_{-\infty}^{\infty} \mathrm{d}t''\, A_2(t''-\tau)e^{i\omega_L(t''-\tau)}\\
&\qquad \times \int_{-\infty}^{\infty} \mathrm{d}t'\, A_1(t')e^{-i\omega_L t'}\Theta(t''-t')e^{-i\xi_{eg}(t''-t')}\\
&= \frac{e^{i\phi_{21}}}{4\hbar^2}\Big(E_2^- * \big(E_1^- * \mathcal{R}_{eg}\big)\Big)(\tau)
\end{aligned}$$

Here, $\mathcal{R}_{eg}(t) = |\mu_{eg}|^2\Theta(t)e^{-i\xi_{eg}t}\rho_{gg}(-\infty)$ denotes the (linear) response function of the system containing the spectroscopic information retrieved from the system. Accordingly, the time-domain signal is

$$S(\tau) \propto \frac{|\mu_{eg}|^2}{4\hbar^2}e^{-i\xi_{eg}\tau}e^{i\phi_{21}}\int_{-\infty}^{\tau} \mathrm{d}t\, \mathrm{CC}(t)e^{i\xi_{eg}t}\,, \quad (2.24)$$

where $\mathrm{CC}(t)$ denotes the cross-correlation of E_1^- and E_2^-. Outside pump-probe pulse overlap, i.e. $\tau \gg \Delta t$, the integral will yield a constant value, since $\mathrm{CC}(t \gg \Delta t) = 0$. For this case, the signal is, as expected, oscillating with ω_{eg}, decaying with γ_{eg} and phase-modulated with $\phi_{21}(t')$. During pump-probe overlap, an additional oscillation occurs due to the modulated intensity distribution of the interfering pulses. This additional contribution decays with respect to Δt and γ_{eg}.

An analytic formula for the Fourier spectrum can be obtained applying the Fourier convolution theorem, which yields

$$\begin{aligned}
S(\omega) &\propto \frac{e^{i\phi_{21}}}{4\hbar^2}\tilde{E}_1^+(\omega)\tilde{E}_2^+(\omega)\tilde{\mathcal{R}}_{eg}(\omega) \qquad (2.25)\\
&= \frac{|\mu_{eg}|^2}{4\hbar^2}e^{i\phi_{21}}\tilde{E}_1^+(\omega)\tilde{E}_2^+(\omega)\Bigg(\underbrace{\frac{\gamma_{eg}}{(\omega-\omega_{eg})^2+\gamma_{eg}^2}}_{\text{absorptive part}} + i\underbrace{\frac{\omega-\omega_{eg}}{(\omega-\omega_{eg})^2+\gamma_{eg}^2}}_{\text{dispersive part}}\Bigg)\,.
\end{aligned}$$

Here, the procedure outlined in Ref. [1] has been used to Fourier transform $\mathcal{R}_{eg}$.

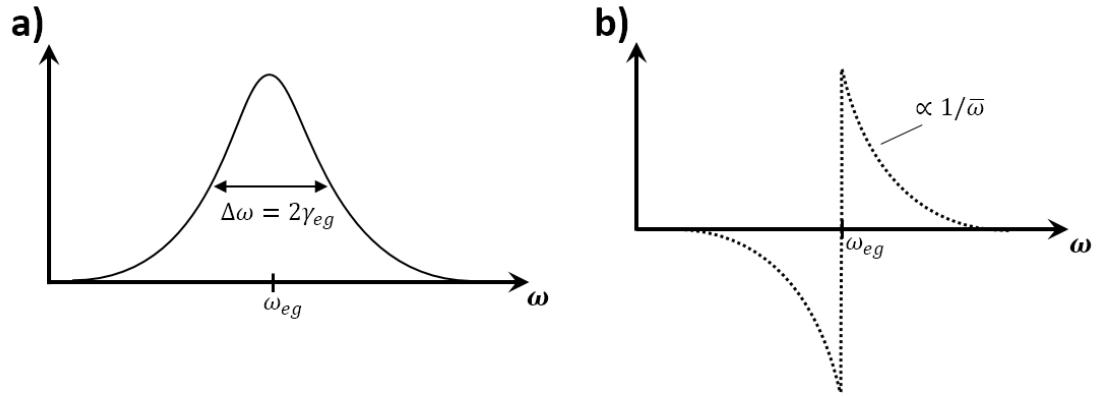

Figure 2.8: Absorptive Lorentzian (a) and dispersive hyperbolic (b) line shape of the Fourier spectrum obtained in WPI measurements. In contrast to absorption spectroscopy, the line width is determined by the decoherence in the system $\gamma_{eg} = 1/(2T_1) + 1/(T_2^*)$. In comparison to the system's susceptibility, a π-phase shift applies to the dispersive part of the Fourier spectrum.

The linear susceptibility of the system is encoded in this signal $\chi^{(1)}(\omega) = i\tilde{\mathcal{R}}_{eg}(\omega)$. Accordingly, the real part of the signal corresponds to an absorption line shape (Lorentzian) weighted with the spectral amplitudes of pump and probe pulses, while the imaginary part exhibits the characteristic hyperbolic line shape of the dispersive part of the susceptibility (Fig.2.8). In this sense, the signal is similar to a standard absorption spectrum, however, with the difference that in the WPI experiment, the linewidth corresponds to the decoherence $\gamma_{eg} = 1/(2T_1) + 1/(T_2^*)$ as opposed to pure population relaxation $1/T_1$ found in conventional absorption spectroscopy.

Furthermore, the WPI signal is independent of Doppler shifts, as opposed to absorption or emission spectroscopy. In WPI experiments, the spectral information is deduced from the phase evolution of induced coherences and therefore depends solely on the energy levels and decoherence processes in the system but not on the relative velocities between the target system and the laser pulses (absorption) or detectors (emission).

Note, that the theory discussed in this chapter relies on the assumption of weak perturbations. In case of strong perturbations, additional effects may occur, e.g. saturation, Stark shifts. The assumption of weak fields is satisfied if the excitation probability is less then 10%, i.e. $|V_{eg}| \lesssim 0.1$ [Eq.(2.11)], which leads to the following condition:

$$|V_{eg}| \approx |-\frac{i}{\hbar}\int_{-\infty}^{\infty} \mathrm{d}t\, \mu_{eg} E_a^{\pm}(t) e^{\pm i\xi_{eg}(t-t_a)}| \lesssim \frac{\mu_{eg}\epsilon_a \Delta t}{2\hbar} \lesssim 0.1\,. \tag{2.26}$$

This condition is fulfilled in the experiments for unfocused beams (typically $V_{eg} \approx 0.1$ for the D_2 line transition in rubidium).

2.4 Collective effects in dilute gases

In the presented work, an extension of the PM-WPI method was developed to selectively detect higher-order nonlinear processes with MQC signals (chapter 6). The MQC detection technique allowed for the investigation of collective resonances in dilute gas-phase

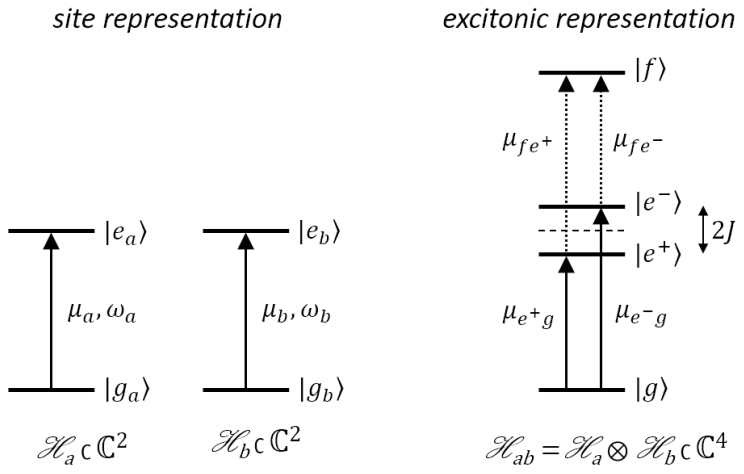

Figure 2.9: Schematic description of dipole-dipole interaction between two two-level systems, denoted with subscripts a, b.

samples (chapter 7). The observation of such signals is generally attributed to weak interparticle interactions in the system [34, 66, 67]. This interpretation is discussed in detail in chapter 7. To provide a basis for this discussion, a brief overview of interparticle interactions is given in the current chapter. Thereby, the focus lies on the long-range dipole-dipole interaction since this is considered being the dominating interaction mechanism in the studied systems. For further details it is referred to Ref. [68].

The interaction of particles in gases arise from the coulomb field of one particle acting on other particles in its vicinity. For large inter-particle distances r, the dipole-dipole interaction usually manifests the major contribution ($\propto r^{-3}$). These interactions play an important role in various systems, most prominently in the coupling among chromophores in biological systems [15] but also in semiconductors [69] or cold gases [70]. For shorter distances, the induced dipole interaction, i.e. the van der Waals interaction, becomes relevant ($\propto r^{-6}$), forming an attractive force between particles and support the formation of weakly bound complexes [71]. This interaction potential got also great attention in the studies of cold gases with the observation of the Rydberg blockade [72]. At even shorter inter-particle distances, the electron orbitals will eventually overlap, giving rise to the exchange interaction which leads to covalent binding of particles. Other interaction mechanisms may rely on collisions, which are often negligible at low particle densities. Couplings may also be induced by external light fields with wavelengths greater than the mean particle distance ($\lambda \gg \bar{r}$). Cooperative effects such as superradiance may occur, typically observed in condensed phase systems, e.g. molecular aggregates [73], but has also been in cold atomic clouds [74]. Related to this, local field effects have been observed in nonlinear spectroscopy of dense vapors ($n \approx 10^{18} cm^{-3}$) [13].

In the presented work, dilute atomic gases of densities between 10^8 to $10^{13}\,\mathrm{cm}^{-3}$ and optical excitations of low principle quantum numbers ($n < 10$) have been studied. In this regime, interactions among the particles are generally very weak, and all contributions ex-

cept for the long-range transition dipole-dipole interaction may be neglected. Exemplary, the dipole-dipole interaction for two interacting two-level systems (Fig. 2.9) is discussed in the following. This has been adapted from Refs. [50, 75].

Each two-level system may be described in its individual Hilbert space $\mathcal{H}_n \subset \mathbb{C}^2$, $n = a, b$ (site representation) or in a combined product Hilbert space $\mathcal{H}_{ab} = \mathcal{H}_a \otimes \mathcal{H}_b \subset \mathbb{C}^4$ (exciton representation). Defining the projection operators $\hat{P}_a = |e_a\rangle\langle e_a| \otimes \mathbb{1}_b$ and $\hat{P}_b$, respectively, as well as the ladder operators $\hat{\sigma}_a = |e_a\rangle\langle g_a| \otimes \mathbb{1}_b$ and $\hat{\sigma}_b$, respectively, the Hamiltonian of the coupled system can be written as

$$\hat{H} = \hbar\omega_a \hat{P}_a + \hbar\omega_b \hat{P}_b + J\left(\hat{\sigma}_a \hat{\sigma}_b^\dagger + \hat{\sigma}_a^\dagger \hat{\sigma}_b\right) . \tag{2.27}$$

Here, a bilinear coupling between the two sites has been assumed and the Heitler-London approximation was applied, which is well satisfied at low vapor densities [76]. The coupling strength J can be obtained from a multipole expansion of the Coulomb field truncated after the dipole term. For $\vec{\mu}_a || \vec{\mu}_b$ and defining r_{ab} as the inter-particle distance, one obtaines

$$J = \frac{1}{4\pi\epsilon_0} \frac{\mu_a \mu_b}{r_{ab}^3} . \tag{2.28}$$

To distinguish between strong and weak coupling, the mixing angle θ is introduced:

$$\theta = 0.5 \tan^{-1}\left(\frac{2J}{\hbar(\omega_a - \omega_b)}\right) , \tag{2.29}$$

where strong coupling can be assumed for $\omega_a \approx \omega_b$, i.e. $\theta = \pi/4$.

Diagonalization of $\hat{H}$ [Eq. (2.27)] yields the eigenstates and eigenenergies for the excitonic representation of the coupled system. For strong coupling these are

$$|g\rangle = |g_a g_b\rangle , \qquad E_0 = 0 \tag{2.30}$$

$$|e^\pm\rangle = \frac{1}{\sqrt{2}}\left(|g_a e_b\rangle \pm |e_a g_b\rangle \right) , \qquad E^\pm = \frac{\hbar(\omega_a + \omega_b)}{2} \mp J \tag{2.31}$$

$$|f\rangle = |e_a e_b\rangle , \qquad E_f = \hbar(\omega_a + \omega_b) , \tag{2.32}$$

and the transition dipole moments are

$$\mu_{e^\pm g} = \frac{1}{\sqrt{2}} (\mu_b \pm \mu_a) , \tag{2.33}$$

$$\mu_{f e^\pm} = \frac{1}{\sqrt{2}} (\mu_a \pm \mu_b) . \tag{2.34}$$

The coupling J thus lifts the energetic degeneracy of the singly excited states $|e^\pm\rangle$ [Fig. 2.9(b)]. Together with the asymmetric dipole transition moments $\mu_{e^\pm g}$, $\mu_{f e^\pm}$, the symmetry of the coupled system is distorted. This is an important point in the discussion of chapter 7.7.

In this discussion, also the case of non-interacting particles (i.e. $J = 0$) is considered. Note, that the described formalism is also valid for this case, i.e. a description in a many-body Hilbert space with collective energy eigenstates is analogous possible for an

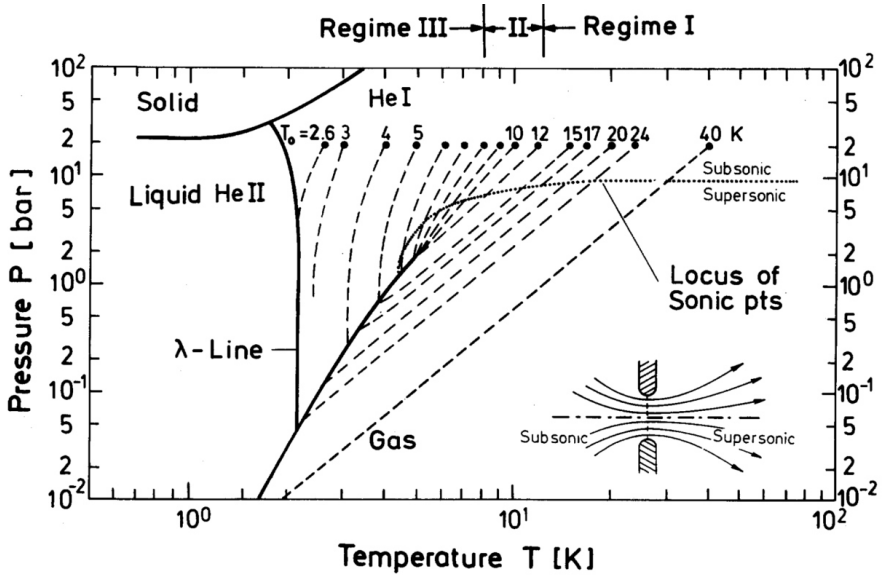

Figure 2.10: Pressure-temperature phase diagram of ^{4}He. Solid lines indicate phase transitions and dashed lines isentropes for nozzle beam expansion with different initial conditions. The areas for subcritical I, critical II and supercritical III expansion are indicated on the top of the diagram. Reproduced from Ref. [79], with the permission of AIP Publishing.

ensemble of non-interacting particles. In this case, the eigenstates of the many-body system are degenerate ($E^+ = E^-$) and the dipole moments [Eq.(2.33), (2.34)] correspond to to the dipole moments of the isolated particles. As such, an ensemble of N non-interacting two-level systems yields a 2^N-dimensional product-Hilbert space with $N+1$ energy levels. In this case, the energy level corresponding to n excited atoms would be $\binom{N}{n}$ times degenerated.

2.5 Matrix isolation with helium nanodroplets

In this chapter the most relevant characteristics of helium droplets and the HENDI technique are summarized, mostly by following Refs. [16, 23, 77]. As experiments have been exclusively carried out with the bosonic isotope ^{4}He (nuclear spin of I=0, 99.99986% natural abundance) in this work, this isotope will be meant when speaking of helium hereafter.

Being characteristic for rare gases, the atomic ground state of helium ($1s^2$) represents a closed-shell configuration which explains the small polarizability and chemical inertness of helium. Its ionic potential (IP) is at 24.6 eV and the first optical absorption ($^1S \rightarrow {}^1P$) occurs at 58 nm (21.2 eV) [78], thus helium is transparent from the far infrared (IR) to the VUV spectral range. As a unique property among all substances, helium is missing a triple point and remains liquid at saturated vapor pressures down to absolute zero temperature. As such, bulk helium undergoes a first order phase transition from the gas phase to the ordinary liquid phase I at 4.2 K temperature and atmospheric pressure and a second order phase transition occurs at the lambda line to the superfluid phase II (see

Fig. 2.10). The latter represents a distinct state of matter with unique properties such as zero viscosity and very high thermal conductance.

In view of matrix isolation spectroscopy experiments, the liquid nature of helium at low temperatures manifests an important advantage over solid hydrogen or other rare gas matrices. In solid matrices an inhomogeneous broadening due to different conformation states of the matrix with the embedded impurity can occur, which is missing in helium. Likewise, lineshifts are typically factor $10 - 100$ larger in sold matrices than in liquid helium. On the contrary, the small to vanishing viscosity of helium causes also the inevitable agglomeration of substances embedded in the matrix or the adsorption to the container walls in which the liquid helium is kept.

This can be circumvented when forming well separated units of bulk helium, i.e. small helium droplets in the gas phase. As will be explained below, these droplets are produced in an adiabatic expansion into a vacuum chamber. Further cooling is achieved by evaporation of helium atoms, leading to sub Kelvin temperatures (370 mK) of the droplets and embedded species. This is in contrast to seeded molecular beam experiments, where low translational temperatures can be achieved ($\sim 1\,\mathrm{K}$) but the internal degrees of freedom (vibrational, rotational) of expanded molecules are not efficiently cooled (typically $1 - 100\,\mathrm{K}$) [80]. Furthermore, the compatibility with molecular substances is limited in this technique. The needed stagnation pressure in the beam expansion require strong heating of the substances without causing fragmentation and the synthesis of more advanced (heterogeneous) complexes is limited. Both issues are circumvented in HENDI with (sequential) doping of the droplets at low vapor pressures subsequent to the adiabatic expansion. In this sense, helium nanodroplets are commonly termed as the *ideal* spectroscopic matrix, uniquely combining the benefits of matrix isolation and molecular beam techniques.

Note, that the discussed advantages of helium nanodroplets depend on the doping mechanism. In particular, alkali atoms do not immerse into the droplets and reside on the surface, as will be discussed below. In this case considerable broadening of the alkali absorption lines occurs ($\sim 100\,\mathrm{cm}^{-1}$). Hence, in these systems the focus lies on studying interaction effects between the dopant and the matrix.

2.5.1 Helium droplet formation

Helium nanodroplets are produced in a free jet expansion, as first demonstrated by Becker et al. in 1961 [81]. Typically, a cooled helium gas ($T_0 = 4 - 20\,\mathrm{K}$) is expanded from a high pressure reservoir ($p_0 = 20 - 100\,\mathrm{bar}$) through a small nozzle ($\varnothing = 5\,\mu\mathrm{m}$) into a vacuum chamber. Thereby, depending on the initial temperature and pressure of the expansion, the process of droplet formation is categorized in three regimes, that is the subcritical I, critical II and supercritical regime III [79] (see Fig. 2.10). In the experiments conducted in the presented work, expansion conditions were such, that the helium droplets were formed in the subcritical regime ($T_0 = 17\,\mathrm{K}$, $p_0 = 50\,\mathrm{bar}$). In this case, the helium jet is cooled through the adiabatic transition from the gaseous to liquid phase along the isentropes shown in the phase diagram Fig. 2.10. Due to the helium condensation, the aggregation of van der Waals bound liquid droplets is initiated and depending on the initial subcritical expansion conditions, droplets of the order of $10^3 - 10^4$ atoms are formed (Fig. 2.11).

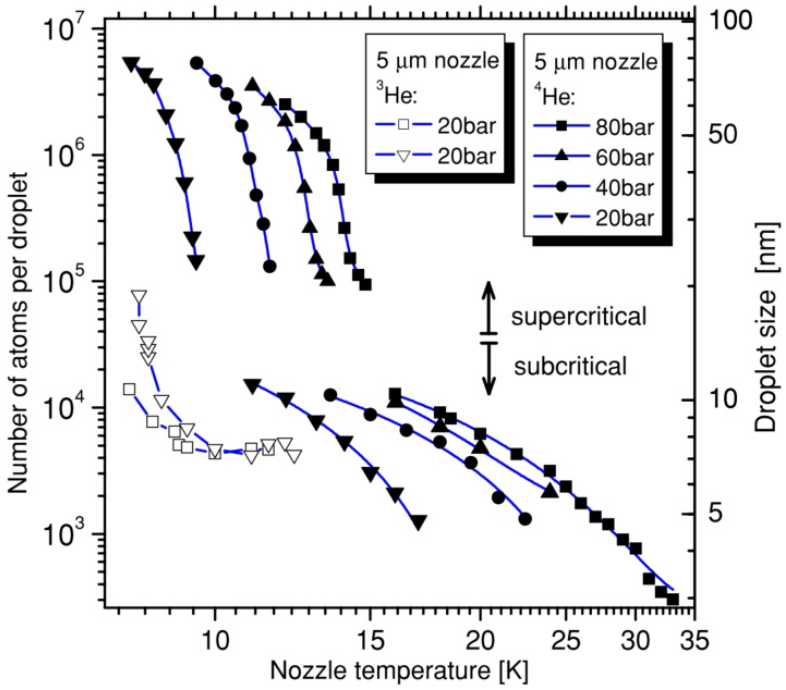

Figure 2.11: Mean droplet size $\langle N \rangle$ as a function of the expansion conditions that are stagnation pressure, nozze temperature and diameter. It is distinguished between sub- and supercritical expansion and between the isotopes ^{3}He and ^{4}He. Reproduced from Ref. [23], with permission from IOP Publishing.

Thereby the resulting droplet size statistic follows a log-normal distribution [82]. For the experimental parameters chosen in the presented experiments, a mean droplet size of $\langle N \rangle \approx 7000$ atoms is estimated [23]. Assuming spherical symmetric droplets, the corresponding mean droplet diameter is 3.8 nm, which explains the term *nano*-droplets. As typical for log-normal distributions, the droplet size distribution is very broad (FWHM $\Delta N \approx 7000$), which however has not a significant influence in the type of experiments conducted in this work. As a consequence of the adiabatic cooling, the velocity distribution of the formed helium nanodroplets becomes very narrow ($\Delta v/v \approx 0.01 - 0.03$) with a mean beam velocity of $v = 200 - 400\, m/s$.

2.5.2 Properties of helium nanodroplets

Due to the rare gas configuration, helium interacts only weakly with other substances via van der Waals interaction, being generally an advantage in matrix isolation. As an example, the helium dimer exhibits a binding energy of only $9 \times 10^{-4}\,\mathrm{cm}^{-1}$. This binding energy increases with increasing number of binding partners, i.e. with increasing number of helium atoms in a cluster/droplet, reaching a constant value of $5\,\mathrm{cm}^{-1}$ for bulk helium of more than 10^4 atoms. Accordingly, in a helium droplet system excess energy is efficiently dissipated by evaporation of helium atoms. Thereby, the evaporative cooling rate of droplets decreases exponentially after the droplet formation leading after roughly

100 µs to an equilibrium temperature of $T = 370\,\mathrm{mK}$ of the droplets.

Regarding the dispersion relation of bulk superfluid helium, two fundamental collective excitations can be assigned, which are phonons and rotons [16, 83]. A momentum transfer to an individual helium atom is in this system not possible. As a consequence, a critical velocity (*Landau critical velocity* $v_c \approx 60\,\mathrm{m/s}$) exists below which scattering particles do not interact with the superfluid and thus travel frictionless through the medium. These properties also apply to helium nanodroplets. However, due to the finite size of the droplet system, collective surface modes, so called ripplons, occur in addition. Moreover, the energy of rotons ($\sim 10\,\mathrm{K}$), phonons ($\sim 1\,\mathrm{K}$) and ripplons ($\sim 0.1\,\mathrm{K}$) differ roughly by a factor of ten and depend on the droplet size, e.g. for a typical size of 7000 atoms, rotons and phonons are not excited at 370 mK and only low energetic ripplon modes are occupied [16, 83].

2.5.3 Doping of helium nanodroplets

Helium droplets may be doped with particles in a pick-up process through inelastic collisions. This pick-up process follows a Poisson statistic determined by the particle density of the dopant ρ, the length of the doping cell l and the cross section of the droplets σ. Accordingly, the probability to dope a helium droplet with k particles is in first approximation given by [84]

$$P_k(l, \rho, \sigma) = \frac{(l\rho\sigma)^k}{k!} e^{-l\rho\sigma} \,. \tag{2.35}$$

Upon the inelastic collision, the dopant transfers its kinetic energy to the droplets and subsequently forms van der Waals bonds with the surrounding helium atoms. Furthermore, the dopant may contain internal energy which is quickly dissipated into the droplet environment due to the fine quantization of phonons and ripplons [85], thus providing efficient cooling of the internal degrees of freedom of the dopant. The kinetic excess energy, the binding energy of the dopant with the droplet and the internal energy of the dopant is then dissipated from the system by evaporation of helium atoms. In this context, the helium droplets are often referred to as personal nanocryostats providing efficient cooling of the individual dopants' internal degrees of freedom down to the vibrational ground state and low lying rotational states, thus providing well-defined initial states for spectroscopic analysis.

Despite the generally weak interaction of the helium matrix with the embedded species, pronounced matrix-induced effects may occur, resulting spectroscopic line shifts and broadening [cf. Fig. 2.12(b)]. Due to the binding of the embedded species with the matrix environment, the electronic states of the dopant are downshifted to lower energies. Since these shifts differ for individual electronic states, a blue or red shift of the transitions can be caused, depending on the structure of the embedded particle. For instance, the absorption D_1 and D_2 lines of alkali atoms are typically blue shifted by roughly 5-50 cm^{-1} [86]. Furthermore, upon excitation of the dopant, internal modes of the helium environment may be excited in conjunction, giving rise to pronounced phonon wings in the spectra [19].

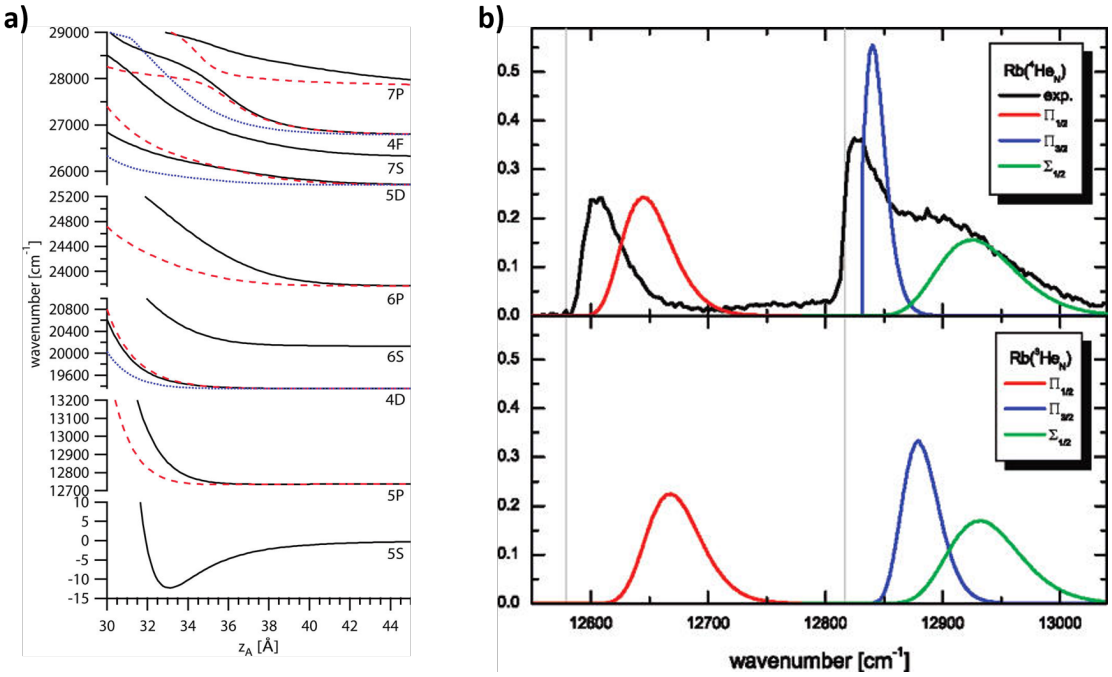

Figure 2.12: (a) Potential curves for the pseudo-diatomic molecule $RbHe_N$, calculated for $N = 2000$. Shown are the Σ- (solid black), Π- (dashed red) and Δ-states (dotted blue) for asymptotic atomic states as indicated by the labels. (b) Absorption profiles for the excitation to the $\Pi_{1/2,3/2}$ and $\Sigma_{1/2}$ potentials obtained from narrow bandwidth laser excitation and calculations based on the model developed in Ref. [86]. The grey vertical lines show the gas phase transition frequencies. (a) is reproduced from Ref. [87], Copyright 2011 American Chemical Society. (b) is reproduced from Ref. [86], Copyright 2007 American Chemical Society.

In general, the binding energy of the dopant with the helium matrix can be calculated using density functional theory [88]. Due to the strong Pauli repulsion of the closed s-shell of helium atoms, helium nanodroplets are electron repellent. As a consequence not all substances immerse into the droplet. In particular alkali atoms reside on the surface of the droplet in shallow dimples due to their weakly bound valence electron [19, 87]. This situation can be theoretically described with a pseudo-diatomic molecule model [86, 89–91]. In this model, the system is described as a diatomic molecule with the helium droplet being a giant quasi-atom that is bound to the alkali atom. For quantitative calculatoins, the alkali-helium pair potential is summed over the droplet density which does well reproduce the spectra for excitation to the first elecronic states of the bound alkali atoms [86]. A refinement of this model has been recently published to accurately include higher-lying electronic states [Fig. 2.12(a)] [87]. These models predict a weakly bound configuration for the pseudo-molecular ground state ($\approx 10\,\mathrm{cm}^{-1}$) and repulsive excited states, giving rise to significantly broadened absorption spectra for the alkali atoms attached to the helium nanodroplets as compared to the gas phase spectra [86] (see also Fig. 2.12).

2.5.4 Droplet-induced and desorption dynamics

In contrast to studies in the gas phase, doped helium nanopdroplets provide the opportunity to study system-bath interactions in a controlled way. As such, a variety of photo-induced dynamics can be observed in these systems from which details about the guest-host interaction can be deduced. First time-resolved measurements of helium nanodroplet systems involved time-correlated single photon counting [92, 93] and femtosecond pump-probe spectroscopy [20]. With these methods, the molecule formation and structure of alkali-helium excimers has been extensively studied [21, 22, 92–95].

While the majority of the conducted experiments have not been sensitive to coherent dynamics, few have been dedicated to probe the coherent evolution of vibrational wave packets in small alkali molecules (dimers and trimers) [49, 96–99] with the pump-probe scheme outlined in Fig. 2.1(a). These molecules have been formed on the helium droplet surface and due to the interaction with the helium environment, distinct decoherence and dissipation dynamics of the excited WPs on the picosecond to nanosecond time scale have been observed, which is in contrast to observations in the gas phase. Supported by theoretical models, details about the coupling mechanism with the helium bath have been deduced and a hint for the existence of the Landau critical velocity has been found [100].

While these studies have been sensitive to the surface properties of the helium nanodroplets, a recent attempt has been dedicated to probe coherent dynamics of a LiI molecule fully solvated in the helium droplet. As opposed to the free gas phase LiI system, no coherent dynamics have been observed in the doped droplet system, suggesting very efficient and thus very rapid energy transfer from the dopant to the droplet environment within few femtoseconds [101]. However, before a conclusion can be drawn whether these types of experiments are generally not feasible, more studies with different species have to be conducted. For instance, in Ref. [77] it has been suggested that larger organic molecules may maintain electronic coherence for longer times inside a helium droplet and studies of other species in rare gas matrices revealed electronic decoherence of WP signals on more feasible time scales, e.g. hundrets of femtoseconds [102].

Another important class of dynamics observed in doped helium droplet systems is the desorption of alkali atoms off the helium droplet surface upon electronic excitation. These dynamics have been first studied in the frequency domain with nanosecond lasers combined with velocity map imaging (VMI) of photoelectrons and ions [91, 103, 104] and later with time-resolved femtosecond pump-probe measurements [105, 106]. Depending which excited state potential of the pseudo-diatomic molecule is excited [e.g. see Fig. 2.12(a)], different desorption times are obtained. Related to the presented PhD thesis is the $5p\Pi_{3/2}$ excitation of a rubidium-helium-droplet pseudo-diatomic molecule (Rb-He$_N$), for which the corresponding desorption times are $< 100\,\mathrm{ps}$ [106].

As a competing process to the desorption of the excited alkali atoms, the pair-wise attraction between the excited alkali atom and individual helium atoms can lead to the formation of bound alkali-helium exciplexes. These molecules may desorb off the droplet as well, albeit presumably on different, much longer time scales. As hinted by previous experimental observations [95] and theoretical studies [107], the RbHe exciplex may reside on the droplet surface for more than one nanosecond. A similar behavior has also been observed for alkali dimer and trimer molecules [49, 99, 108, 109] and RbHe$_N$ excited on

the red wing of the $5p\Pi_{1/2}$ transition [110].

Other dynamics involve the direct excitation of the droplet itself, giving rise to nanoplasma formation and collective energy and charge transport effects, as summarized in the review Ref. [77]. These studies are however not relevant in the scope of this work and are therefore not further discussed.

3 Experimental methods

The basic principle of the phase modulation technique and some general aspects about helium nanodroplets were discussed in the preceding chapter. The intention of the current chapter is to complement technical details.

3.1 Optical setup

Fig. 3.1 shows the optical setup used for the experiments cunducted in the present work. A similar setup has been extensively described in Ref. [64]. Therefore, only a summary with the focus on new aspects is provided here. Femtosecond laser pulses are split with a first beam splitter (BS) and focused with a common lens (f=200 mm) into the AOMs placed in each arm of a Mach-Zehnder type interferometer. This lense has been slightly tilted to avoid direct back reflection into the laser cavity. The AOMs are phase-locked driven with RFs Ω_1=155.0 MHz and Ω_2=155.005 MHz, respectively yielding a difference frequency of Ω_{21}=5 kHz. After the AOMs, the first diffraction order of the dispersed beam is selected with pinholes (PHs) and collimated (f=200 mm). One beam is delayed with a motorized translation stage (200 mm travel range, 1 µm minimal incremental motion, 0.5 µm resolution) and afterwards collinearily superimposed with the second beam in a beam splitter. After recombination, one part of the co-propagating pulses is fed into a monochromator whereas the other part is used to excite the spectroscopic sample. A lens (f=30 mm) mounted on a xyz-translation stage is used to match the aperture ratio of the monochromator (focal length 500 mm, aperture ratio f/6.9, slitwidth 10 µm , nominal resolution 0.03 nm) ensuring optimal illumination of the optics. An avalanche photo diode (APD) is used to acquire the refernce signal (S_{ref}) which is bandpass filtered (transmission at 3-11 kHz) and amplified (factor 100) before fed into the lock-in amplifiers.

As samples serve effusive atomic or doped helium droplet beams (HENDI apparatus) and alternatively a heated vapor cell. The fluorescence (S_{fluor}) of the vapor cell is mapped perpendicularly to the laser propagation with a 4f-lens arrangement (f=20 mm) onto a photo diode (PD). For transitions in the UV spectral range (chapter 8), a photo multiplier tube (PMT) has been employed instead, to provide sufficient sensitivity at these wavelengths. In some measurements a lens (f=150 mm) is in addition used to focus the laser beam into the vapor cell. Moreover, the spectroscopic cell and photo detector are enclosed in a housing to avoid saturation of the detector by ambient light. For experiments with the atomic/droplet beam, the laser pulses are focused into the vacuum apparatus with a lens (f=150 mm). To align the overlap of the laser focus with the droplet beam, this lens is mounted on a xyz-translation stage. In the vacuum chamber, photoelectrons/-ions ($S_{\mathrm{el/ion}}$) are detected as explained below. The respective signals $S_{\mathrm{el/ion}}$, S_{fluor} are fed into the lock-in amplifiers for demodulation with the reference signal S_{ref}.

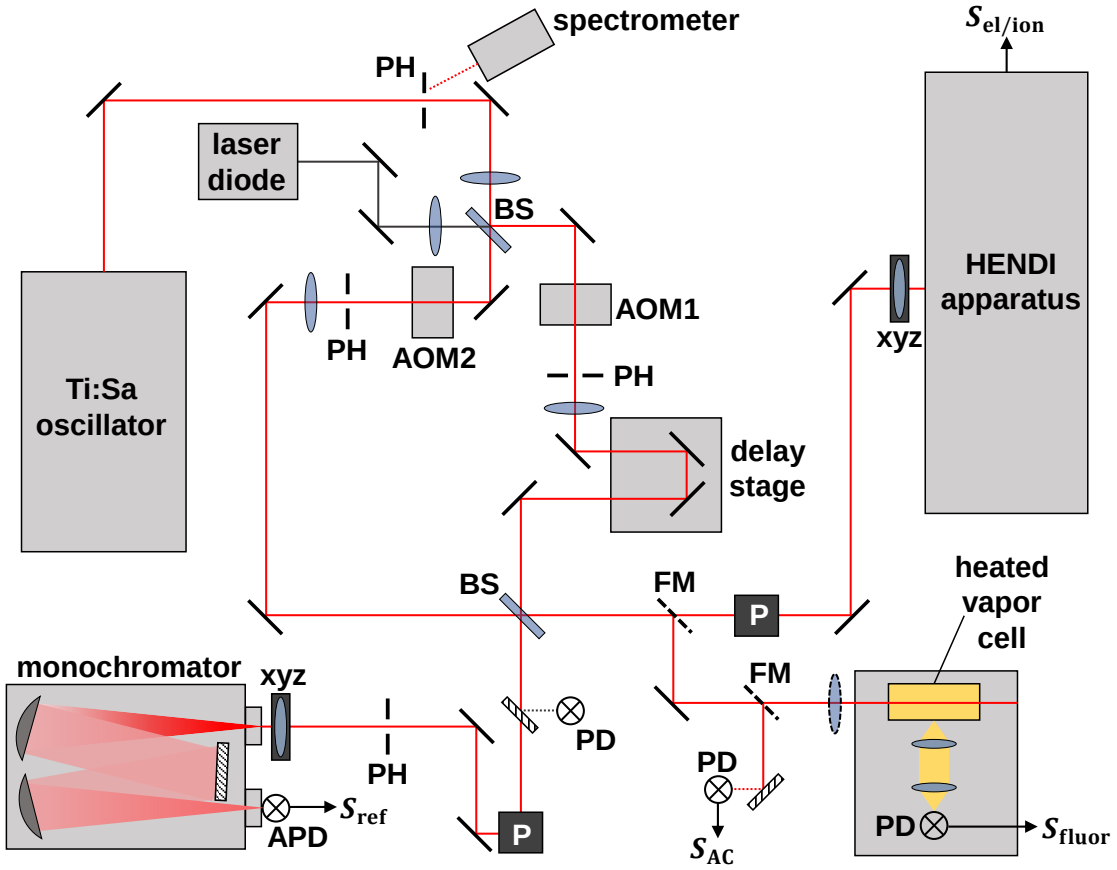

Figure 3.1: Optical PM-WPI setup. P denotes periscope and FM flip mirror. All other abbreviations are explained in the text.

Due to the 40/60 ratio of the employed beam splitters, pump and probe pulses exhibit an intensity ratio of 1:3 (pump/probe). Typical values of pulse energies and intensities for the conducted experiments are given in Tab. 3.1. To estimate the laser intensity, the beam diameter at the sample position has been characterized from which the spatially averaged peak intensity (averaged over beam cross section) has been calculated

$$I_{\mathrm{peak}} = \sqrt{\frac{4\log(2)}{\pi}}\frac{\bar{P}T_{\mathrm{rep}}}{\pi r^2 \Delta t}\,, \tag{3.1}$$

with $\bar{P}$ denoting the average laser power and Δt the FWHM pulse duration.

For pulse characterization, the pump-probe autocorrelation signal S_{AC} has been regularly evaluated and pulse spectra have been acquired with a fiber spectrometer (0.8 nm resolution) detecting a diffuse reflection off the first pinhole used to block back reflections of the beam splitter.

For high resolution measurements, i.e. scanning the pump-probe delay up to 1 ns, the monochromator signal is not suitable. Instead a continuous wave (cw) laser diode [(LD),

Experiment	Power [mW]	Energy [nJ]	I_{peak} [MW/cm^2]	$I_{\mathrm{peak,f}}$ [GW/cm^2]
Fluorescence	200	2.5	0.7	1.0
Photoelectr./-ions	240	3.0	0.9	1.2
Mass-res. ions	136	1.7	0.5	0.7

Table 3.1: Typical average power, energy and peak intensity listed for the pump pulse. The respective values for the probe pulse are a factor of 3 larger. I_{peak}, $I_{\mathrm{peak,f}}$ correspond to unfocused and focused (f=150 mm) laser beams with beam diameters ø=1.5 mm and ø = 40 µm , respectively.

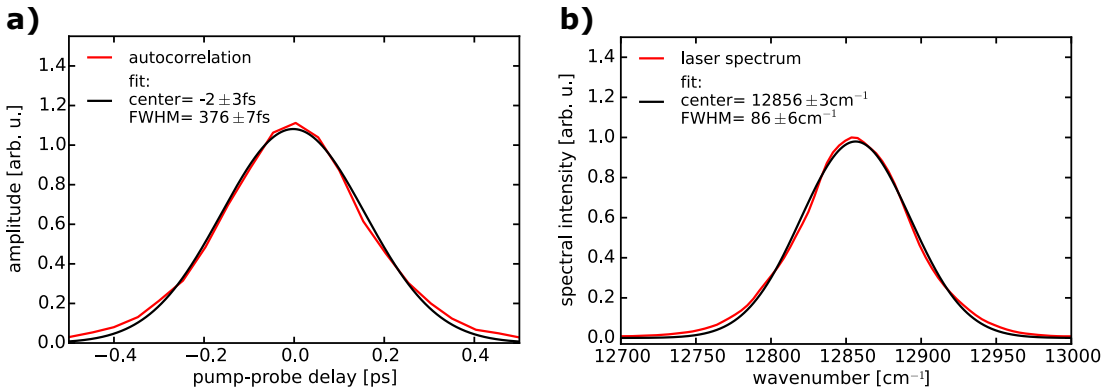

Figure 3.2: Pump-probe autocorrelation in (a) and laser spectrum in (b), both acquired for a laser wavelength of 778 nm. Gaussian fits yield a pulse length of $\Delta t = 188 \pm 4$ fs (FWHM of intensity) and spectral width of $\Delta\nu = 86 \pm 6\,\mathrm{cm}^{-1}$.

780 nm[1]] has been coupled into the interferometer at the first beam splitter and superimposed with the femtosecond pulses with a slight vertical offset. After the interferometer, the auxiliary laser is blocked in the sample arm to avoid interference with the experiment and deflected onto a photo diode in the reference arm yielding the reference signal for lock-in demodulation.

As femtosecond laser source serves a titanium:sapphire oscillator delivering optical pulses with repetition rate $1/T_{\mathrm{rep}}$=80 MHz, average power $\bar{P}$=2-3 W, pulse duration $\Delta t \approx$190 fs (FWHM value of intensity profile) and spectral width $\Delta\nu \approx$85 cm^{-1}(FWHM value of power spectral density) being typical values for the predominantly used laser wavelengths of 770-780 nm. Exemplary, a pump-probe autocorrelation trace and a laser spectrum for a laser wavelength of 778 nm are shown in Fig. 3.2. Since the laser spectrum is fairly narrow, small fluctuations in the laser spectrum may change the spectral overlap of the laser pulses with the resonances in the system being studied. In the conducted experiments, this effect is in the $\approx 5\,\%$ range. An example is given in Fig. 3.3. Additional amplitude fluctuations of the laser are typically below 3 %.

The AOMs consist of a TeO_2 crystal ($l = 6$ mm) with the acoustic wave traveling along the laser beam propagation (longitudinal mode). To provide phase-locked driving of the devices, a custom-built driver is used, described in Ref. [64]. Due to the applied RF power (1 W), considerable heating of the AOMs occurs, typically 30°C for a lab temperature of

[1]In this thesis, air wavelengths are meant if not otherwise specified.

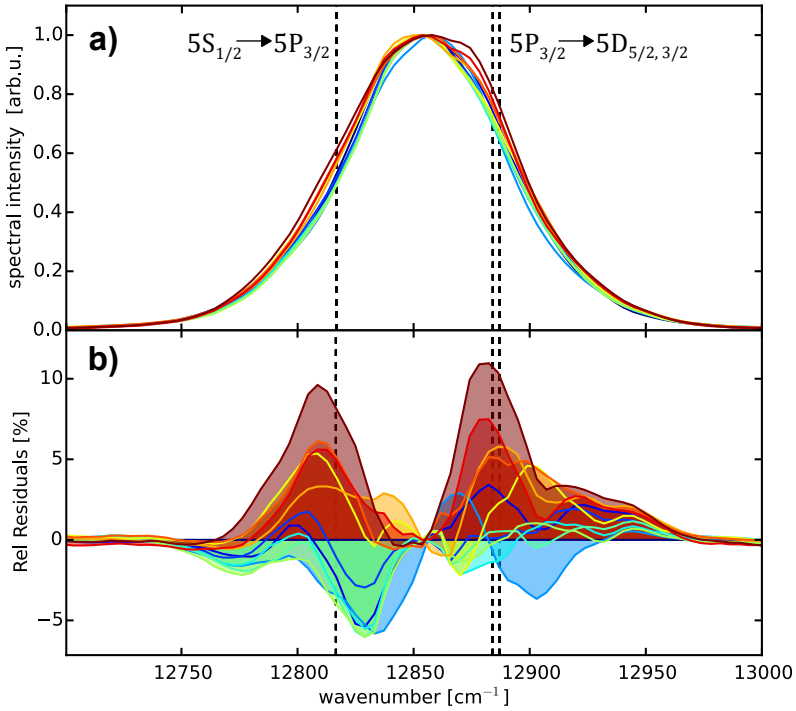

Figure 3.3: Fluctuations of the laser spectrum and effect on the transitions excited in the sample. (a) shows 9 spectra acquired over a period of 8 h at a wavelegnth of 778 nm. (b) shows the spectral fluctuations in a residual plot relative to the first spectrum. Vertical dashed lines indicate the position of relevant resonances in rubidium.

21°C. Hence, to avoid de-adjustment of the interferometer, it is important to keep the RF power permanently switched on.

The performance of the optical setup sensitively depends on the alignment of the interferometer, which is typically done by optimizing the interference contrast of the recombined beams after the interferometer. This procedure has been improved in the scope of this dissertation utilizing a position sensitive CCD sensor to find the optimal beam overlap. Since not relying on interference fringes, pre-knowledge of the temporal pump-probe overlap (i.e. zero delay position) is not necessary in this approach and application in two-color experiments is possible. However, to insure correct alignment, it is essential to eliminate distortions in the beam profiles that lead to ambiguities in estimating the beam center position (Fig. 3.4). For this purpose, the pinhole after AOM1 is adjusted accordingly (Fig. 3.1).

As the performance of the employed monochromator has been significantly below the specifications, an alignment of the instrument has been performed in the scope of this PhD thesis. With this, a resolution of 0.14 nm and a (unidirectional) reproducibility of ±0.1 nm has been achieved, corresponding to a frequency uncertainty of 1.6 cm^{-1}at 780 nm. Furthermore, since a collimated light source is used in the actual experiments, the instrument performance sensitively depends on the incident angle of the laser beam. Therefore, an alignment procedure has been developed in this PhD thesis. Briefly, the

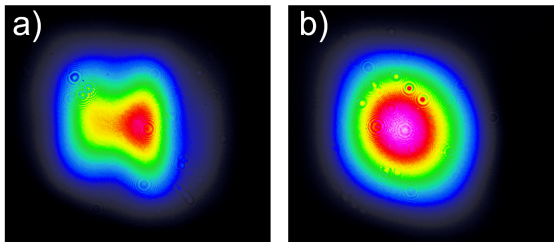

Figure 3.4: Laser beam profile captured at 4 m distance after the interferometer. (a) shows the originally distorted profile and (b) shows the profile after blocking reflexes with a iris diaphragm, which reduced the laser power by 1%.

Species	K	Rb	Cs
Density [cm^{-3}]	$(9.4 \pm 1.6) \times 10^9$	$(1.4 \pm 0.2) \times 10^{11}$	$(4.6 \pm 0.7) \times 10^{11}$

Table 3.2: Estimated densities in the vapor cell for different alkali atom species and a cell temperature of $T = 50°\mathrm{C}$.

monochromator is set to zero wavelength, where the grating deflects in zero order, thus functioning as an ordinary mirror. A bright isotropic light source is placed at the exit slit illuminating the monochromtor in reverse direction. Due to the isotropic spreading of the light, the monochromator optics are optimally illuminated independent of the position/incident angle of the light source. The light cone leaving the instrument at the entrance slit is then used to align a pinhole placed in 150 mm distance (Fig. 3.1). Eventually, the laser is coupled into the monochromator by aligning it through the pinhole and entrance slit. In summary, with these steps, the performance of the monochromator could be improved to obtain feasible reference signals for pump-probe scans of ± 130 ps.

For longer pump-probe scans, the reference signal has been generated with a laser diode. The employed DFB (distributed feedback) laser diode (80 mW typical power, 2 MHz linewidth, 780 nm wavelength) has been temperature stabilized to reduce frequency drifts to less than ± 500 MHz.

The vapor cell contains a mixture of potassium, rubidium and cesium. The temperature of the gas, and thus its density, is defined by the coldest spot in the cell (cold finger). A thermocouple attached to this position is used to determine the temperature T of the gas. The particle density of the individual atomic species inside the spectroscopic cell is calculated using the empirical formula $p(T) = 10^{3+a+b/T}$ [111] and applying the ideal gas law. The parameters a, b are: $a = 4.402$, $b = -4453$ (K); $a = 4.312$, $b = -4040$ (Rb) ; $a = 4.165$, $b = -3830$ (Cs). Most experiments have been conducted with a cell temperature of 50°C for which the calculated density values are given in Tab. 3.2. The errors are due to a ± 2 K temperature uncertainty.

3.2 Vacuum apparatus

The HENDI apparatus employed in this work has been described in detail in Refs. [112, 113]. A similar apparatus acompanied with a comprehensive characterization of helium

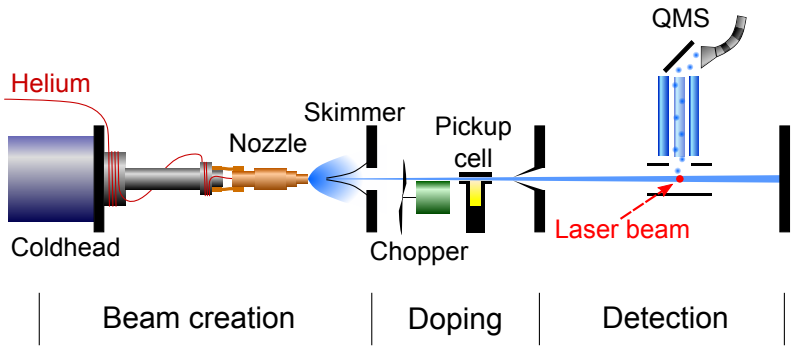

Figure 3.5: HENDI apparatus used in this work. In the detection chamber, the laser beam intersects perpendicularly with the droplet beam. In one part of the experiments, the QMS has been replaced by an integral ion/electron detector as explained in the text.

Chamber	Source	Oven	VMI	TOF
Pressure [mbar]	1.8×10^{-4}	1.4×10^{-6}	1.8×10^{-8}	1.6×10^{-8}

Table 3.3: Chamber pressure readings for nozzle temperature $T_{\text{nozzle}} = 17\,\text{K}$, stagnation pressure $p_{\text{nozzle}} = 50\,\text{bar}$ and oven temperature $T_{\text{oven}} = 85°\text{C}$.

droplet beam generation and the doping process is described in Ref. [114]. Therefore, only a brief description of this part of the experiment is given here.

The relevant part of the vacuum apparatus comprises of three chambers (Fig. 3.5), that are the source chamber for the production of the helium nanodroplet beam, the oven chamber for doping the droplets and a detection chamber where the droplet/effusive beam interacts with the laser and photoelectrons or -ions are detected. In the actual setup, two successional chambers have been connected to the detection chamber [VMI and time of flight (TOF)] which however have not been used in this work and are therefore not shown. Typical values for the pressure readings in these chambers are given in Tab 3.3. A pressure gauge has not been installed in the detection chamber. Therefore this pressure has to be inferred from adjacent chambers that are the oven and VMI chamber. Note, that in this thesis, pressure readings are meant when speaking of chamber pressures. To obtain the actual chamber pressures, correction factors have to be applied depending on the employed pressure gauges and the type of background gas that is detected. For the installed cold cathode pressure gauges (Pfeiffer, IKR 270) a correction factor of 5.9 for helium and of 1.0 for air applies.

The helium droplets are produced in a supersonic expansion with following expansion parameters: nozzle diameter $ø = 5\,\mu\text{m}$, nozzle temperature $T_{\text{nozzle}} = 17\,\text{K}$ and stagnation pressure $p_{\text{nozzle}} = 50\,\text{bar}$ leading to a mean droplet size of $\langle N \rangle \approx 7000$ [23]. At a distance of 13 mm behind the nozzle, a nickle skimmer ($ø = 400\,\mu\text{m}$) is installed. This reduces the pressure in the succeeding chamber and thus avoids destruction of the droplet beam by shock waves [115]. Differential measurements with/without the droplet beam is performed with a mechanical chopper placed in the subsequent oven chamber. Beam characterization has been done with the following steps: (i) A sufficient helium flow through the nozzle has been insured by checking the pressure increase in the source chamber when increasing the

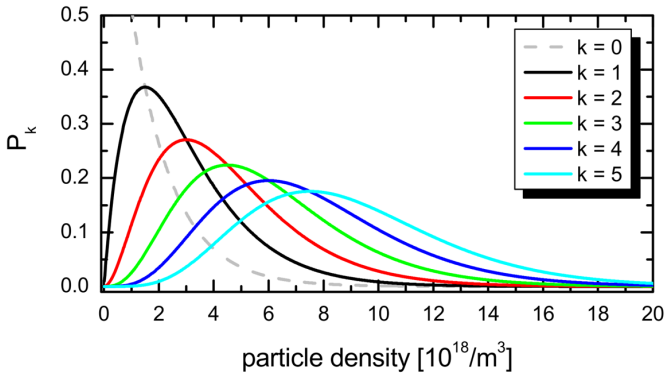

Figure 3.6: Doping probability as a function of the dopant (particle) density in the doping volume (oven). Distributions are shown for doping helium droplets with k particles, calculated for doping cell length $l = 10mm$ and droplet size of $N = 5000$ atoms. Reproduced from Ref [84], Copyright 2011 Springer-Verlag.

stagnation pressure and cooling down the nozzle. In the used apparatus, a decent helium flow corresponded to a pressure increase of $\Delta p_{\text{source}} = 1.8 \times 10^{-4}$ mbar for $T_{\text{nozzle}} = 17$ K, and $p_{\text{nozzle}} = 50$ bar. (ii) As a second criteria served the pressure increase in the VMI chamber for unblocked versus blocked droplet beam which has been $\Delta p = 1.4 \times 10^{-8}$ mbar. To assure, that this pressure increase is not simply due to gaseous helium, in addition the pressure increase for $T_{\text{nozzle}} = 294$ K and $T_{\text{nozzle}} = 17$ K (both for $p_{\text{nozzle}} = 50$ bar) has been compared. If a helium droplet beam is produced and not destroyed on the way, the cold nozzle yields a factor of 2 larger pressure increase in the VMI chamber.

Doping is done by evaporating rubidium in a doping cell (oven) which is crossed by the droplet beam, thereby picking up the rubidium atoms by inelastic scattering. This process may be described with a Poisson statistic [Eq.(2.35)] with relevant parameters being the partial pressure of the dopant, the length of the doping cell ($l = 10$ mm) and the droplet size. The droplet cross section can be estimated by $0.15N^{2/3}$ nm^2 [23]. Exemplary, the Poisson statistic for a droplet size of $N = 5000$ and $l = 10$ mm is plotted in Fig. 3.6 from which the optimal partial pressure for monomer doping can be deduced. For a larger droplet size, as used in the conducted experiments, the distributions shift to slightly smaller dopant pressures, respectively. The evaporation of rubidium also produces an effusive atomic beam in the apparatus which generates a significant background signal. Therefore, the optimal doped-droplet/effusive beam signal ratio has to be individually determined in the experiment, which has been found for an oven temperature of 84°C, to which the oven has been stabilized in the experiments. At this setting the droplet beam extinction constituted roughly 10 % (inferred from pressure increase in the VMI chamber).

In the conducted experiments, the droplet/effusive signal ratio has been typically 2:1 (depending on the wavelength) for ionization of the Rb atoms with a single laser pulse and 1:1 in WPI measurements. One reason for this difference could be molecular contributions (Rb_n and $RbHe_n$) adding to the droplet signal in the first case but are spectrally discriminated in the second case. At the prevailing experimental conditions, these contri-

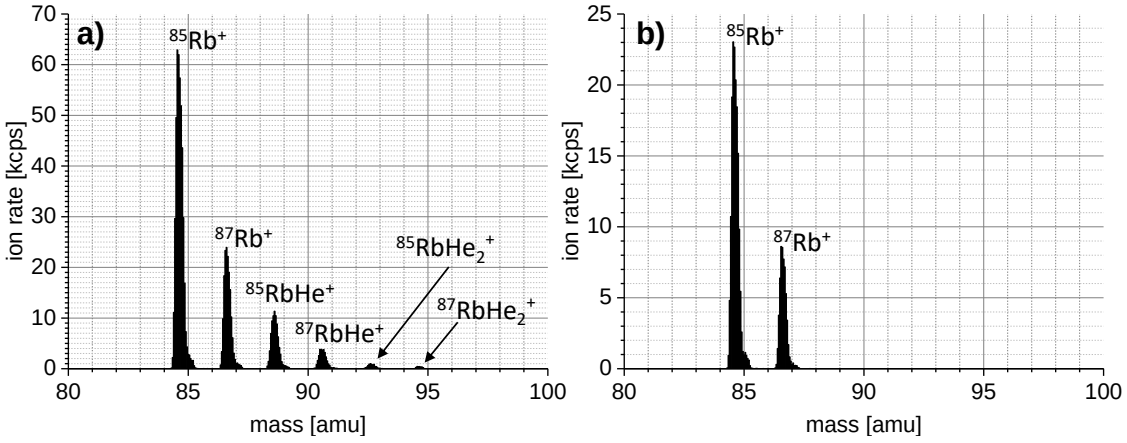

Figure 3.7: Mass spectra for photoionization at a laser wavelength of 775 nm. (a) Mass distribution for unblocked helium droplet beam and (b) for a blocked droplet beam revealing the formation of RbHe and $RbHe_2$ molecules in the doped droplet beam. The unit kcps denotes kilo counts per second.

Particles	Repeller [V]	Extractor [V]	Channeltron [V]
Electrons	-2950	-1790	-1700
Ions	2990	-1720	-1760

Table 3.4: Voltages applied to the electron/ion detector for photoelectron/-ion detection, respectively.

butions are however too small [98] to explain the observation. Another explanation might be given by a fast decoherence process in the doped droplet system that decreases the WPI pump-probe signal but not the droplet signal for ionization with a single pulse.

Upon interaction with the laser pulses, Rb atoms and $RbHe_n$ molecules desorb off the droplet and are subsequently ionized by absorbing further photons. Thereby, the ionization probability reflects the WP signal and thus exhibits the Ω_{21}-modulation imprinted by the acousto-optic phase modulation. The photoions and -electrons are detected in the experiment employing two detection schemes. For a first series of experiments, a commercial quadruple mass spectrometer (QMS) (Extrel MAX-1000) has been installed in the detection chamber. The QMS serves as a mass gate, selecting ions of a certain charge/mass ratio, which are then detected with a channeltron. The channeltron signal is amplified and fed into the lock-in amplifier for demodulation of the Ω_{21}-modulation. For characterization purposes, photoion mass-spectra have been recorded by scanning the QMS mass filter and applying (unmodulated) probe pulses without a pump pulse. Example mass-spectra are shown in Fig. 3.7 for blocked and unblocked helium droplet beam, respectively, clearly revealing the bare Rb^+ ions as well as the formation of $RbHe_n$ molecules. In a second series of experiments, photoelectron and -ion detection has been performed with a simple two-electrode arrangement comprised of a repeller, an extractor electrode and a channeltron amplifying the integral electron or ion signal. This signal has been further amplified and demodulated with a lock-in amplifier. Applied voltages

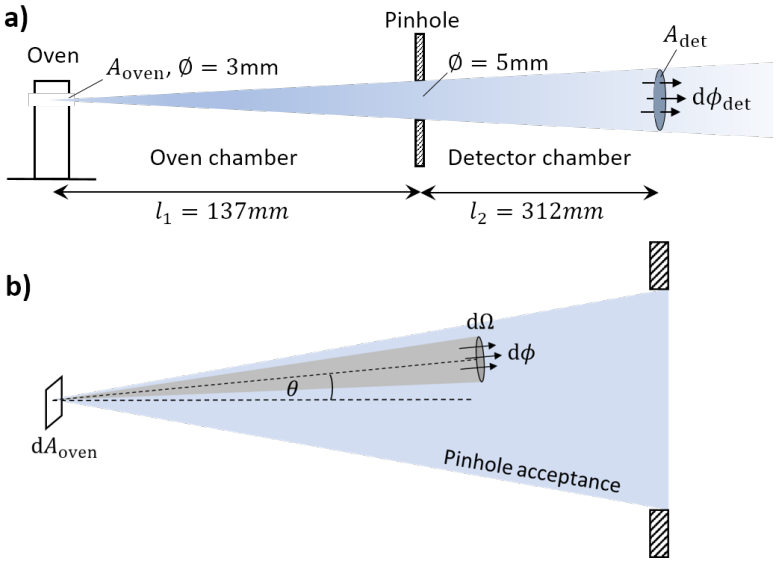

Figure 3.8: Schematic of effusive beam propagation in (a) as assumed for density estimation of effusive atoms in the detection volume. (b) shows a schematic for the atom flux emitted by the oven.

for photoelectron and -ion detection, respectively, are shown in Tab. 3.4. Note that these voltages are nontypical for such detector arrangements, however yielded the best results in the conducted experiments.

For the experiments conducted in this work, an estimate of the sample densities in the ionization and fluorescence measurements is desirable. For monomer doping, the number density of doped helium droplets at the interaction volume in the detection chamber is estimated to be $\approx 10^8\,\mathrm{cm}^{-3}$ [23]. The density of the effusive atom beam at the detector position is evaluated as follows: The Rb atoms are emitted from the oven cell opening (denoted A_{oven}) into the vacuum chamber [Fig.3.8(a)]. Thereby, the flux of atoms emitted by the surface element $\mathrm{d}A_{\text{oven}}$ with velocities $[v, v+\mathrm{d}v]$ into the solid angle $\mathrm{d}\Omega$ [Fig.3.8(b)] is given by [116]

$$\phi(\theta, v) = \rho_{\text{oven}}\, v f(v) \mathrm{d}v\, \frac{\mathrm{d}\Omega}{4\pi} \cos(\theta) \mathrm{d}A_{\text{oven}}\,. \tag{3.2}$$

Here, $f(v)$ denotes the Maxwell-Boltzmann velocity distribution. A pinhole separates the oven from the detector chamber, which restricts the acceptance angle θ to small values. This allows a separation of the integration over $\mathrm{d}\Omega$ and $\mathrm{d}A_{\text{oven}}$. Executing these integrations as well as the integration over v, yields an effective atom flux in the detection chamber of

$$\phi_{\text{det}} = \rho_{\text{oven}} \gamma A_{\text{oven}} \bar{v}\,, \tag{3.3}$$

where $\gamma = 8.3 \times 10^{-5}$ represents the fraction of emitted atoms into the detection chamber, and $\bar{v}$ the atom's mean velocity. With the equality $\phi_{\text{det}} = \rho_{\text{det}} A_{\text{det}} \bar{v}$ it follows

$$\rho_{\text{det}} = \rho_{\text{oven}} \gamma \frac{A_{\text{oven}}}{A_{\text{det}}} = 1.7 \times 10^{-5} \rho_{\text{oven}}\,. \tag{3.4}$$

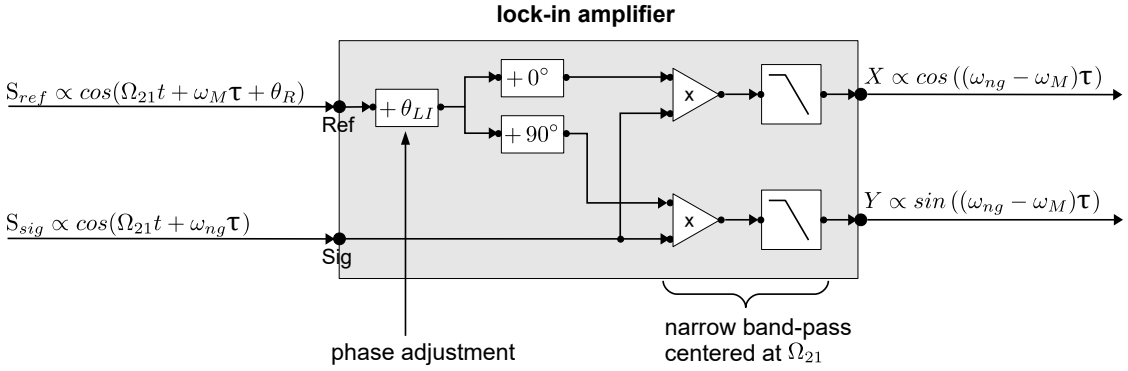

Figure 3.9: The employed digital lock-in amplifier performs synchronous demodulation with two reference signals shifted by 90°. This yields demodulated in-phase (X) and in-quadrature (Y) components of the applied input signal S_{sig}.

For an oven temperature of $T = 84°\mathrm{C}$, this yields an effusive beam density of $\rho_{\mathrm{det}}(84°\mathrm{C}) = (3.4 \pm 0.7) \times 10^7\,\mathrm{cm}^{-3}$ (temperature error of $\pm 2\,\mathrm{K}$ has been assumed). This value is approximately a factor of 2 smaller than the density of the doped droplet beam and thus explains the observed droplet/effusive signal ratio of 2:1. Hence, at the typical experimental conditions, the target densities in the HENDI experiments are a factor of $\approx 10^4$ smaller than in the vapor cell.

3.3 Data acquisition and analysis

A LabVIEW program has been written to control the data acquisition routine which is outlined in the following. Time-domain WP interference signals are recorded as a function of the pump-probe delay τ, sampled in discrete equidistant steps chosen as integer multiples of the translation stage's minimum incremental motion, i.e. $\Delta\tau = n \cdot 3.34\,\mathrm{fs}$. The monochromator frequency is set to the center of resonance frequencies of the spectroscopic target. This ensures strong downsampling of the WP signal. Respectively, delay steps of $\Delta\tau \sim 15 - 80\,\mathrm{fs}$ are usually sufficient to fully sample the oscillatory features in the recorded pump-probe transients. The reference signal is fed together with the WPI signal into a lock-in amplifier for demodulation of the Ω_{21}-beat note. The low bandwidth output signal of the lock-in amplifier is analog-digital converted (10 kHz sampling rate) in the acquisition computer. Thereby, for each delay value τ averaging is performed for $50 - 1500$ ms depending on the signal quality. Between each delay step, data acquisition is paused to account for the settling time of the delay stage ($\approx 40\,\mathrm{ms}$), the locking time of the lock-in amplifier to lock to the reference signal (typical 40 ms) and the settling time of the lock-in low pass filter ($150 - 270\,\mathrm{ms}$). The latter value depends on the lock-in filter settings. Typically, a filter time constant (RC-filter) of 30 ms and a roll-off of $6 - 18\,\mathrm{dB}$ is used, corresponding to a filter bandwidth of $3 - 8\,\mathrm{Hz}$ (FWHM).

Dual phase demodulation in the lock-in process yields in-phase $X(\tau)$ and in-quadrature $Y(\tau)$ components of the pump-probe signal (Fig.3.9). Furthermore, the lock-in amplifier

provides an adjustable phase θ_{LI} to compensate phase offsets between the references and the WPI signal. In the here conducted experiments, this phase is set to zero and instead corrected in the post processing (see chapter 6.4).

To calibrate the pump-probe delay axis, the zero delay point is regularly determined in pump-probe autocorrelation scans. To this end, the signal $R = \sqrt{X^2 + Y^2}$ is constructed which corresponds to the envelope function of the autocorrelation trace. In this way ambiguities arising from incorrect phase correction is omitted [117]. The zero delay point is determined with a Guassian fit. Furthermore, for each pump-probe scan, a laser spectrum is acquired for diagnostic purposes.

For data analysis, the in-phase and in-quadrature signals are used to construct the complex-valued signal $Z = X + iY$. For time-domain analysis, usually the real part of Z is plotted. For spectral analysis, a Gaussian window and zero padding is applied before performing a discrete Fourier transform of Z. The window function is chosen such, that it is centered at the center of the time-domain data set and decays to 5% of its peak amplitude at the endpoint of the data set. This ensures smoothing of Fourier artifacts caused by the finite length of the data set. Furthermore, the amplitude of the obtained Fourier spectrum is scaled to the window length of the time-domain data set to obtain spectral amplitudes that are independent of the length of the time-domain data set.

In the experiment, the signal is sampled at the downshifted frequencies $\bar{\omega} = \omega_{\mathrm{sig}} - \omega_{\mathrm{M}}$. Therefore, the obtained Fourier spectrum $\tilde{Z}$ is shifted by $+\omega_{\mathrm{M}}$ to recover the original resonance frequencies ω_{sig}. For the narrow absorption lines of the gas phase alkali transitions ($< 10\,\mathrm{MHz}$), the calibration uncertainty of the monochromator is insufficient. Therefore, ω_{M} is corrected in the post processing by calibrating the Fourier axis with a known resonance. For this purpose, values are taken from Ref. [78] and an uncertainty of $\pm 0.1\,\mathrm{cm}^{-1}$on the frequency axis is achieved.

In most cases, it is sufficient to analyze the absolute value of the spectrum, however, if phase information is desired, a separation into absorptive and dispersive parts is done. According to the Kramers-Kronig relation, $Re\{\tilde{Z}\}$ corresponds to the absorptive part of the spectrum and $-Im\{\tilde{Z}\}$ to the dispersive part, respecitvely [25]. To achieve correct separation, the Gaussian window function must in these cases be centered at $\tau = 0\,\mathrm{fs}$ and spectral phase corrections are applied as outlined in chapter 6.4.

For the analysis of spectral peaks, a Gaussian function with fixed offset is fitted, i.e. $f(\omega) = Ae^{-[(\omega-\omega_{\mathrm{peak}})/\sigma]^2}$. For spectrally overlapping peaks, a sum of Gaussians is fitted, respectively. To obtain a realistic error on the fit, the noise floor of the spectrum is evaluated and taken as error on the individual data points used for the fit.

To extract the pure droplet signal in the helium droplet beam experiments, a differential measurement is performed. A chopper wheel implemented in the vacuum apparatus is blocking and unblocking the droplet beam and the difference signal is obtained with a lock-in amplifier. In this case, the signal is modulated with the chopping frequency $\Omega_{\mathrm{Ch}} = 20\,\mathrm{Hz}$ and the phase modulation $\Omega_{21} = 5\,\mathrm{kHz}$, thus requiring a dual lock-in demodulation comprised of two lock-in amplifiers connected in series. The Ω_{21}-modulation is demodulated with the first lock-in amplifier. Here, a short filter time (3 ms) is used, corresponding to a filter width of 42 Hz, and thus providing sufficient bandwidth to transmit the chopper modulation. The second lock-in amplifier is referenced to the slow chopper frequency therefore operated in sync-mode and a time constant of 100 ms (1.3 Hz band-

width) is used to efficiently remove residual noise from the signal. In this dual lock-in measurement only the in-phase component of the demodulated droplet signal is obtained.

4 Phase-modulated wave packet interferometry applied to doped helium nanodroplets

With the preceding chapters, the first part of this PhD thesis was presented, in which the basic theoretical and experimental principles relevant in this work were explained. The current and successive chapters will now present the experimental results.

In a first series of experiments, PM-WPI is combined with mass-resolved ion detection and the application to rubidium-doped helium nanodroplets is investigated. Thereby, the feasibility of this combination in view of future studies with mutidimensional spectroscopy and more advanced target systems is demonstrated. Some content of this chapter is adapted from Ref. [B1].

4.1 Background

As high phase stability is required to resolve the interference of electronic WPs, stabilization methods are cruicial in these experiments. The first successful demonstration of fully resolved electronic coherence has been thus reported by Scherer et. al. in 1991 employing an active feedback stabilization [24]. A number of studies on gas phase samples followed, mainly with the focus on coherent control applications [25, 118–125]. Ohmori et. al. have pointed out the advantage of using cold molecular beams in conjunction with WPI experiments to improve the interference contrast and refining data interpretation [125]. Their experiments on a HgAr van der Waals complex have been, however, so far the only successful implementation of such an approach. While studies have been performed in the IR to UV spectral range, recent approaches focus on experiments in the extreme ultraviolet (XUV) regime [42]. However, due to the limited phase control, only the low frequency beat corresponding to the envelope of the averaged interference fringes of electronic WPs have been resolved. The same applies to attempts studying electronic WPI in doped helium droplet beams [20, 22]. In the HENDI experiments, two issues can be identified. These are on the one hand, insufficient phase control in the optical setup, and on the other hand, the low density of the droplet beam commonly compromising the signal quality. A new attempt has been thus conducted in the present work using the phase modulation approach.

4.2 Excitation scheme and experimental results

In the PM-WPI experiments, the interference of electronic WPs induced in rubidium atoms attached to helium droplets is studied. To this end, spectrally identical pump

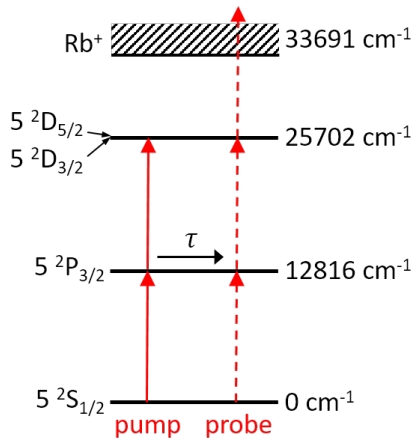

Figure 4.1: Excitation scheme for electronic WPI in a rubidium atom. Pump and probe pulses each excite a WP consisting of the ground state $5S_{1/2}$ and the excited states $5P_{3/2}$, $5D_{5/3,3/2}$. Subsequent ionization maps the WP interference onto the ion yield. Energy values are taken from [78].

and probe pulses excite each an electronic WP in the rubidium system comprised of the $5S_{1/2}$ ground and higher-lying $5P_{3/2}$ and $5D_{5/3,3/2}$ states [(Fig. 4.1)][1]. The corresponding $5S_{1/2} \rightarrow 5P_{3/2}$ and $5P_{3/2} \rightarrow 5D_{5/2,3/2}$ transitions are separated by $70.40\,\mathrm{cm}^{-1}$ and $67.44\,\mathrm{cm}^{-1}$, respectively, thus fall into the bandwidth of the femtosecond pulses. The interference of the two coherently excited WPs is mapped onto the ion yield by subsequent ionization of the sample with an additional photon from the probe pulse or by absorbing photons from consecutive pulses.

For sample preparation, helium droplets are produced in a supersonic jet expansion using the parameters specified in chapter 3.2. Monomer doping is achieved by heating rubidium to 84.5°C in the pick-up cell. Mass-resolved detection is done with a QMS. Since the alkali atoms tend to desorb off the droplet upon electronic excitaiton [105], the photo-ionized atoms can be detected in the gas phase at the bare atomic masses using the mass spectrometer set to the ^{85}Rb isotope mass. In the optical setup, the monochromator is set to $12897.78\,\mathrm{cm}^{-1}$ and the laser center frequency is $12903\,\mathrm{cm}^{-1}$. Pulse energies are 1.7 nJ (pump) and 5.2 nJ (probe) before entering the vacuum apparatus. The laser beam is focused with a lens (f=150 mm), resulting in a beam diameter of 40 µm at the interaction volume (see also Tab. 3.1). Time-domain interferograms are acquired by sampling the pump-probe delay in 50 fs steps from 0 to 50 ps while demodulated data are averaged for 1 s for each delay position.

Fig. 4.2(a) and (c) show the time- and frequency domain representation of the acquired data. For comparison (b) and (d) show data obtained in a conventional (without phase modulation) WPI measurement previously conducted in the Stienkemeier group with similar equipment and under comparable experimental conditions [126]. While in the time-domain, only a section of the first 4 ps is shown, the frequency spectra correspond to a Fourier transform of the entire pump-probe scan.

[1] In a more precise description, the pseudo-diatomic energy levels of $RbHe_N$ would be considered instead of the atomic system. This is however omitted for simplicity.

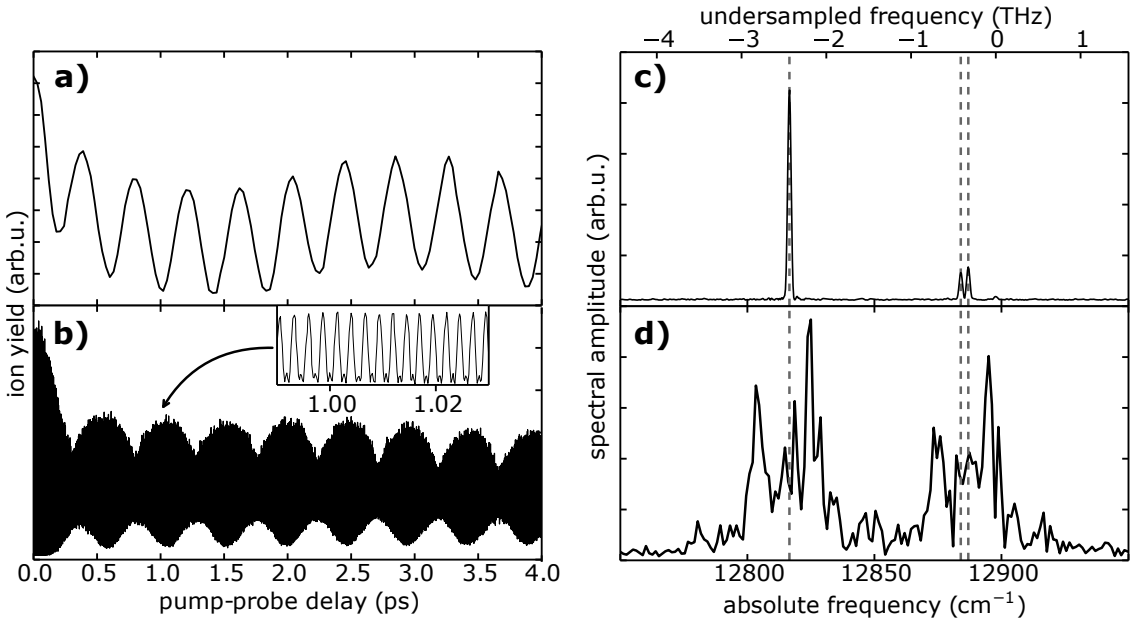

Figure 4.2: Electronic WPI measurements of Rb atoms attached to He droplets. (a) Rb^+ ion yield as a function of the pump-probe delay obtained from a PM-WPI measurement (in-phase component). (b) Respective data obtained in a conventional WPI experiment. (c) and (d): Corresponding discrete Fourier transforms of the pump-probe transients. The absolute frequencies given by the bottom scale of (d) are common to both spectra. The scale at the top of (c) shows the downshifted frequencies at which the pump-probe transient is detected in the phase modulation scheme before being shifted by the monochromator frequency in the post processing. Vertical dashed lines indicate the atomic Rb transition frequencies. Graphs are reproduced from Ref. [B1].

4.3 Discussion

Some distinct properties can be identified in the two data sets. In the conventional WPI experiment (b), the WP interference is fully sampled, leading to fast oscillations in the sub 5 fs regime, as shown in the inset. This is in contrast to the pump-probe transients shown in (a), which is, although also fully sampled, measured in the rotating frame of the monochromator signal and thus downshifted from ≈380 THz to below 3 THz [refer to the top frequency scale in (c)]. This reduces the amount of data points required to obtain the same information: the PM-WPI data set (0-50 ps pump-probe delay, 50 fs step size) comprises only 1.6 % of the sampling points acquired in the fully sampled case (0-63 ps pump-probe delay, 0.6 fs step size). As a common feature in both experiments, both time-domain signals exhibit a transient increase at zero pump-probe delay. This is caused by additional ionization pathways occurring during temporal overlap of pump and probe pulses.

A discrete Fourier transform [shown in (c) and (d)] provides the spectral representation of the pump-probe data, revealing a drastic improvement of the signal quality in the phase modulation case. The sharp spectral resonances observed in (c) correspond precisely to the expected $5S_{1/2} \rightarrow 5P_{3/2}$ and $5P_{3/2} \rightarrow 5D_{5/2,3/2}$ transitions (shown as vertical dashed lines). Here even the spin-orbit splitting of the 5D state (Δ=2.96cm^{-1}) is resolved. This

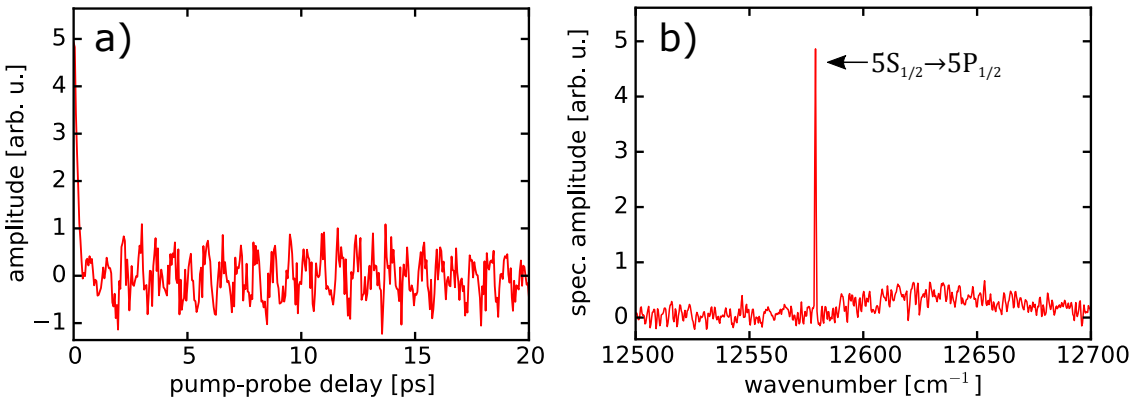

Figure 4.3: D_1 excitation of Rb atoms attached to helium nanodroplets. (a) Time-domain data. Shown are the first 20 ps pump-probe delay. (b) Fourier spectrum of the pump-probe signal. The broad peak centered at 12625 cm^{-1}originates from the transient signal enhancement in the pump-probe overlap region.

stands in contrast to the spectrum shown in (d), where transition frequencies can be identified only qualitatively and the splitting of the 5D state is not resolved. Note, that in principle also a peak at the transition frequency $5S_{1/2} \rightarrow 5D_{5/2,3/2}$ should occur (not within the plotted wavenumber range). In the phase modulation measurement, this signal is however detected in a separate demodulation process as explained in chapter 6.

Two effects are responsible for this significant improvement of signal quality. On the one hand, phase noise, typically caused by instabilities in the optical interferometer, is imprinted onto the excited WPs and therefore strongly compromises the interferometric signal. In the conventional WPI experiment, these phase errors have been partially compensated by tracking the interferogram of a HeNe laser while scanning the pump-probe delay. In the phase modulation scheme, the phase noise is simultaneously tracked in the reference signal and cancels to a large extend in the lock-in demodulation, thus providing a real-time phase correction. This efficiently reduces the demands on phase stability resulting in a drastic improvement in resolution and an excellent signal-to-noise ratio. On the other hand, imprinting a well-defined modulation onto the WPI signal, allows incorporating efficient lock-in detection to extract weak signals from very large background contributions. This advantage of the phase modulation method is particularly important when investigating highly dilute samples. In helium droplet beam experiments, target densities are estimated to fall below $10^8\,cm^{-3}$ [23] which usually puts a severe constraint to the achievable signal-to-noise ratio; the lock-in demodulation, however, provides great background suppression.

Besides the shown experiment, PM-WPI signals were obtained for the rubidium D_1 ($5S_{1/2} \rightarrow 5P_{1/2}$) and cesium D_1 ($6S_{1/2} \rightarrow 6P_{1/2}$) transitions. In both cases, no resonant intermediate state (as the 5D state in rubidium) lies within the bandwidth of the laser to support resonance-enhanced two-photon ionization. As such, signal amplitudes were three orders of magnitude smaller but a reasonable signal quality could be still achieved, thus confirming not only the improved phase noise characteristics but also the enhanced sensitivity due to lock-in amplification. An example for the rubidium D_1 excitaiton is

shown in Fig.4.3. In this measurement, the pump-probe delay is scanned for 0-50 ps, the laser center wavenumber is 12625 $cm^{-1}$and the monochromator is set to 12625 cm^{-1}.

Another benefit of the phase modulation approach is the quasi phase-cycling routine inherent in this scheme. As outlined above (chapter 2.2 and 2.3.2) only excitation pathways that lead to an Ω_{21}-modulation of the signal will be amplified in the lock-in detection. All other processes, such as pathways involving interactions with either of the pump or probe pulses; or ions/electrons generated from stray light, being often a problem in photoelectron spectroscopy, are strongly suppressed. In more general, phase-cycling, as it is commonly used in multidimensional spectroscopy [5, 54, 57], can be used to reduce a complex (nonlinear) system response to the most relevant contributions, which is often a crucial capability to unfold weak signals and allow clear data interpretation. An example of this aspect using the phase modulation technique will be given in chapter 6, where weak multiphoton transitions are sensitively extracted from the system response. The demonstration of phase-cycling and phase stabilization in the presented electronic WPI experiment combined with HENDI shows thus all prerequisites for advanced nonlinear spectroscopy schemes such as coherent multidimensional spectroscopy applied to helium droplet systems. In this sense, the attained signal quality for the rubidium model system confirms the feasibility of such an approach.

As explained in the pseudo-diatomic model (chapter 2.5.3) considerable line shifts and broadening effects occur for the alkali resonances when attached to a helium droplet. Likewise, various droplet-induced desorption and relaxation dynamics have been observed in a number of atomic and molecular alkali systems. As such, the gain in resolution in the current experiment should reveal such interactions of the alkali atom with the helium host. Yet, the observed sharp resonances neither exhibit shifts nor broadening with respect to the gas phase lines and WP interference fringes have been observed for pump-probe delays of up to 100 ps (not shown), suggesting negligible guest-host interaction in this system. An explanation may be given by the desorption of rubidium atoms off the droplet surface upon electronic excitation, happening typically within < 100 ps [106]. Other studies have reported that in some cases rubidium atoms remain attached to the droplet when excited at the red edge of the absorption spectrum [110]. The observations in the current experiment suggest that the atoms desorb upon interaction with a first pump-probe pulse pair and are then probed in the gas phase with a consecutive pulse pair leading to the same results as in gas phase experiments. With a droplet beam velocity of ≤ 400 m/s, a laser focus diameter of 40 µm and a laser repetition rate of 80 MHz, ≈ 8 pump-probe cycles may interact with a droplet or the respective desorbed atom before it has migrated out of the laser focus, making this a likely explanation for the reported observations. This scenario has been also discussed in Ref. [112].

4.4 Conclusion

In conclusion, electronic WPs were induced in rubidium atoms attached to helium droplets using the phase modulation approach. The WP interference signals where deduced from mass-resolved photoion yields acquired with a QMS. A direct Fourier transform of the fully resolved quantum beat signals revealed high resolution spectra for the Rb $5S_{1/2} \rightarrow$

$5P_{3/2}$ and $5P_{3/2} \rightarrow 5D_{5/2,3/2}$ transitions. A drastic improvement in resolution and signal-to-noise ratio was obtained as compared to previous WPI studies on the same system. Good signal quality was also obtained for the rubidium and cesium D_1 excitation, where ionization cross sections are much smaller.

The deduced spectra for the alkali-helium system lack any matrix-induced effects (line broadening/shifts) and resemble respective gas-phase spectra. This is explained by the desorption of the alkali atoms off the droplet surface upon electronic excitation. A final answer to this question may be given in future studies of doped helium nanodroplets, in which low repetition rate lasers are used in conjunction with the improved signal quality and resolution of the phase modulation approach.

While the alkali atoms served here as a model system, the obtained results confirm in general the feasibility of combining phase-modulated nonlinear time-domain spectroscopy with HENDI. In particular, the prerequisite for an extension to 2D electronic spectroscopy has been demonstrated with these experiments.

5 Rubidium-helium exciplexes

In a second study, the phase modulation technique is applied to a molecular system, that is the RbHe exciplex. As will be shown, the improved resolution reveals new details of the vibrational structure beyond that of current models and information about dynamics can be inferred. These experiments have been carried out in conjunction with the measurements described in the previous chapter. Thus the same equipment has been used. Some parts of this chapter have been adapted from Ref. [B1].

5.1 Background

RbHe diatomic molecules lack a stable ground state configuration and are therefore referred to as exciplexes (excited complex) or excimers. First studies of the RbHe exciplex involved dispersed emission spectroscopy [90], but as the ground state potential is strongly repulsive, broad lines are obtained and accurate information about the vibrational structure of bound states have not been retrieved. A conventional WPI experiment with femtoseond pulses for the first time provided access to the vibrational energies of excited electronic states [22]. However, only differences between individual modes have been accessible and the assignment of vibrational states could not be done rigorously. In particular the role of higher-lying electronic states correlating to the 5D atomic asymptote had not been included. Later, femtosecond pump - picosecond probe experiments have probed the dynamics of individual vibronic levels [95]. These measurements confirmed the previous rough assignment; however the spectral resolution stayed behind the one achieved using the WPI technique. Recently, zero electron kinetic energy (ZEKE) studies have been demonstrated as an interesting alternative to probe the structure of Na*He exciplexes [127], which yielded a resolution comparable with the previous WPI experiment on the RbHe species. By employing the phase modulation approach in the here presented work, a new experimental approach is demonstrated to study the vibronic structure of the unstable molecule, yielding a vastly enhanced resolution compared to the mentioned previous studies. In this way the involved potentials can be accurately tested on a level beyond that of current ab initio calculations.

5.2 The RbHe potentials

As the alkali-helium quasi-molecules consist of only one helium atom with two electrons in a closed-shell configuration and an alkali atom with closed-shell electrons except of one weakly bound valence electron, these molecules are of fairly simple structure and have attracted interest from theorists as a benchmark system for new modeling approaches. Several ab initio calculations have been conducted [128–132] and density

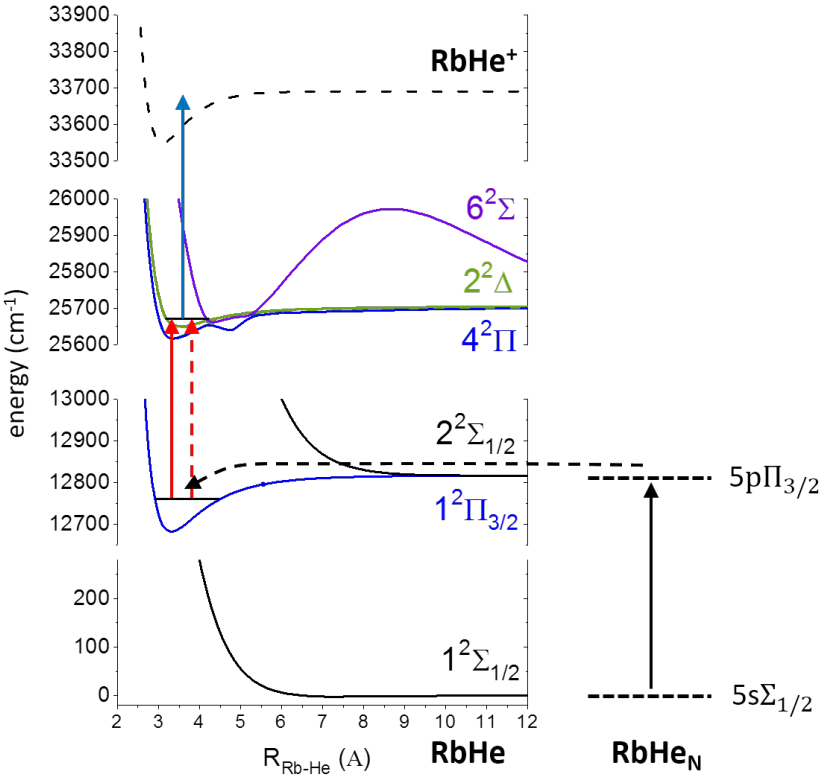

Figure 5.1: Exciplex formation and probing mechanism. An excitation of the $RbHe_N$ pseudo diatom (black arrow) is followed by a tunneling and relaxation into the $1^2\Pi_{3/2}$ bound Rb*He exciplex state (dashed arrow). Upon rovibronic excitation, electronic WPs are induced by pump and probe pulses (red arrows) and probed subsequently via ionization (blue arrow). Only relevant states for the RbHe pair potentials are shown. $RbHe_N$ states are shown schematically.

functional theory [133] and pathintegral Monte Carlo methods [107, 134] have been applied. Furthermore, a semi-empirical pair potential model has been proposed by Pascale [135]. In this approach, the three-body problem is solved comprising of the closed-shell alkali-ion and helium atom as well as the free valence electron being shared among the two cores. Thereby, the interaction of the free electron with either of the two constituents is deduced from collision experiments. Despite of their age (1983), the obtained pseudo pair potentials still seem to yield most wide spread agreement with experiments [22, 86, 90, 92, 93, 95, 127]. In particular, the recent high resolution ZEKE results were in much better accordance with the Pascale PECs than with state-of-the-art ab initio calculations [127]. Furthermore, Pascale's model has been so far the only one including molecular states correlating to the 5D asymptote of the atomic Rb states, which are however crucial for the interpretation of electronic WPI experiments. For these reasons, the semi-empiric pair potentials of Pascale have been used in the current work.

The initial work of Pascale did not include spin-orbit couplings. Jakubek and Takami

have introduced a procedure to account for the spin-orbit coupling in Ag*He exciplex potentials [136] which has been later transferred to Rb*He exciplexes to calculate the excited state potentials correlating to the 5P asymptote [90, 93]. An extension to the higher-lying electronic states correlating to the 5D asymptote has been performed by Giese et. al. [95, 99] and their data are used in the present work. Fig. 5.1 shows the respective potentials. As can be seen, the ground state of the pair potential is repulsive, whereas bound configurations exist for excited electronic states which may be intuitively explained by a missing Pauli repulsion in the nodal region of extended rubidium electron orbitals having angular momentum of $l > 0$. Furthermore, the electronic state correlating to the $5P_{3/2}$ asymptotic atomic state comprises of only one bound configuration, that is the $1^2\Pi_{3/2}$ potential energy curve (PEC). On the contrary, the higher-lying electronic states correlating to the 5D asymptote comprise of 5 bound configurations ($4^2\Pi_{3/2,1/2}$, $2^2\Delta_{3/2,1/2}$, $6^2\Sigma_{1/2}$), thus forming a rather complex excited state manifold.

5.3 Exciplex formation and probing mechanism

Formation and dissociation of molecular bonds are among the fundamental processes in chemistry. As such, the alkali-helium exciplex formation is an intriguing aspect that can be readily investigated in the alkali-doped helium droplet system. Upon excitation to the lowest excited P state, the enhanced interaction to helium leads to the formation of alkali-helium exciplex molecules which desorb off the droplet and can be probed in the gas phase [21, 22, 92, 94, 95]. The formation dynamics has been discussed for different alkali exciplexes (Na*He [92], K*He [94] , Rb*He [90, 95, 103]). Moreover, comperative studies using He droplets formed of the fermionic isotope ^{3}He have been performed in order to probe the influence of superfluidity of the droplets [21]. However, a complete understanding of the formation and desorption process of metal-helium exciplexes on helium droplets is still missing mainly due to the rather complicated interplay between the attractive Rb*He pair potential and the repulsive Rb*He$_N$ pseudo-diatomic states (Fig. 5.1).

Different models have been discussed in order to interpret the formation of alkali-helium exciplexes and the measured time-dependent signals. Tunneling processes have been modeled [93, 127, 137] and direct laser-excitation of bound states in the excited pair potential has been suggested [103, 104, 135, 138]. For the case of the Rb*He exciplex, the tunneling model has predicted formation times of 42 ps for initial excitation to the $5p\Pi_{3/2}$ state of the pseudo-diatomic molecule [93]. This stands in contrast to experimental observations with femtosecond pump-probe techniques yielding values of ≈ 8.5 ps [21, 22] and $\lesssim 10$ ps [95], thus hinting rather to the faster direct photoassociation-like mechanism. A recent study combining angular resolved photoelectron spectroscopy with femtosecond pump-probe techniques, however, rises doubts on the previously interpreted formation times [106], which indicates that the formation process may be still not fully elucidated.

In the scope of the presented phase modulation experiments, the formation and probing of the exciplex molecule is associated with three steps (Fig. 5.1): (i) the excitation of the RbHe$_N$ pseudo-diatomic molecule to the $5p\Pi_{3/2}$ PEC followed by a tunneling process into the $1^2\Pi_{3/2}$ exciplex state; (ii) the excitation of WPs comprising of superpositions

of states from the $1^2\Pi_{3/2}$ with the higher-lying $4^2\Pi_{3/2,1/2}$, $2^2\Delta_{3/2,1/2}$, $6^2\Sigma_{1/2}$ PECs; and (iii) the detection of the WP interference via photoionization of the molecule. Note, that a formation via the 5D atomic asymptote is at first not considered, as this mechanism has so far not been discussed in the literature. It will be shown below, that the conducted phase modulation experiments provide hints for this formation channel and a detailed discussion is provided in section 5.7. Detection of the $RbHe^+$ ions is done with a QMS set to the ^{85}RbHe mass. A typical mass spectrum is shown in Fig. 3.7(a). As can be seen, the mass resolution is sufficient to clearly separate the $^{85}RbHe^+$ and $^{87}RbHe^+$ isotopes and respective $RbHe_2^+$ contributions. Larger $RbHe_n$ ($n > 2$) complexes are not observed that would indicate helium snowball formation around the ionic cores [105] . Hence, it is concluded that desorbed gas phase ions are detected in the experiment.

Eventually, a brief discussion of alternative formation and probing mechanisms is given. As discussed, a direct photoassociation-like excitation from the $RbHe_N$ ground into bound Rb*He states may be also a valid formation mechanism (not shown in Fig. 5.1). This scenario would support the direct preparation of electronic WPs in the Rb*He molecule with the first pulse inducing electronic coherences between the $1^2\Pi_{3/2}$ PEC and the PECs correlating to the 5D asymptote. Alternatively, for both suggested scenarios it would be possible that the molecule formation is induced with a preceding pump-probe pulse pair and the WPI experiment is then performed on the already formed and desorbed Rb*He molecule in the gas phase, equivalent to the considerations outlined in the previous chapter. This mechanism would be likely as the lifetime of the exciplex ($1^2\Pi_{3/2}$ state) is estimated to be $\approx 15 - 25$ ns [129, 130, 132], thus longer than the separation between pulse pairs of 12.5 ns.

5.4 High resolution exciplex spectra

In the applied PM-WPI scheme, rovibronic transitions between the $1^2\Pi_{3/2}$ PEC correlating to the $5P_{3/2}$ and the $2^2\Pi$, $4^2\Delta$, $6^2\Sigma$ PECs correlating to the $5D_{5/2,3/2}$ atomic Rb states are probed (cf. Fig. 5.1). Due to the phase-cycling procedure inherent in the phase modulation scheme, pure (ro)vibrational WP propagation in these PECs [cf. Fig.2.1(a)] is not detected as this scheme does not result in a Ω_{21}-modulation of the signal.

The same equipment has been used as in the PM-WPI measurements on rubidium atoms attached to the droplet presented in the preceding chapter. However, in the exciplex measurements, demodulated signal strengths have been generally a factor of 20 smaller. Reasonable WPI signals where obtained in the laser wavelength range of $769 - 781$ nm with a maximum in the ion yield at 774 nm. At this wavelength, high resolution measurements have been performed with a delay ranging from -100 to 120 ps. An example time-domain signal is shown in Fig. 5.2, with the inset showing the beat signatures that reflect the WP interference. A strong enhancement of the ion yield during temporal pump-probe overlap is observed (narrow spike at 0 ps), which yields a broad spectral feature in the Fourier domain. Since this feature does not contain eligible information, it is removed from the pump-probe transients before performing the Fourier transform, analogous to the procedure applied in Ref. [24].

Fig. 5.3 shows the respective Fourier spectrum, revealing a fully resolved vibronic spec-

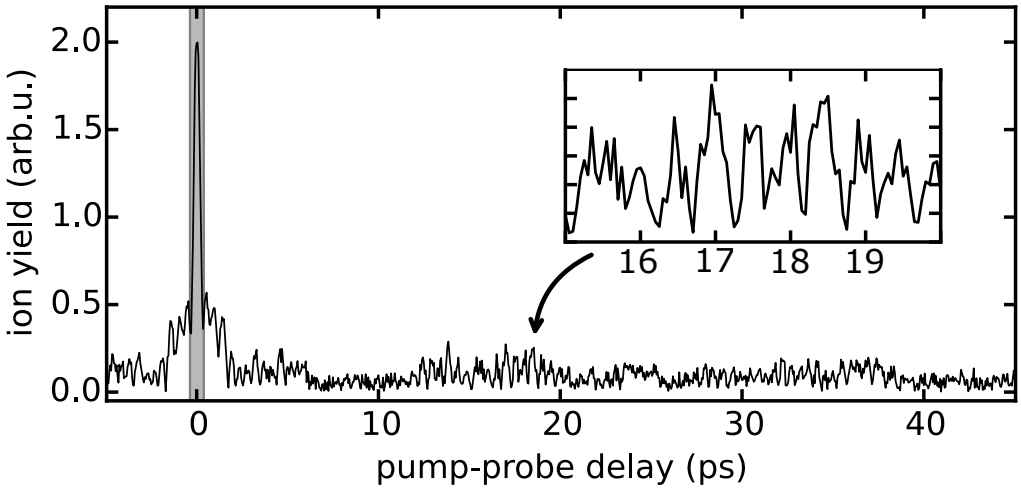

Figure 5.2: Rb*He exciplex time-domain data for a pump-probe scan at 774 nm. Plotted is the absolute value of the signal $R = \sqrt{X^2 + Y^2}$ which reveals the beats of involved oscillations. The grey vertical bar indicates the pump-probe overlap region corresponding to a decay of the pump-probe autocorrelation function to 6 % of its peak amplitude.

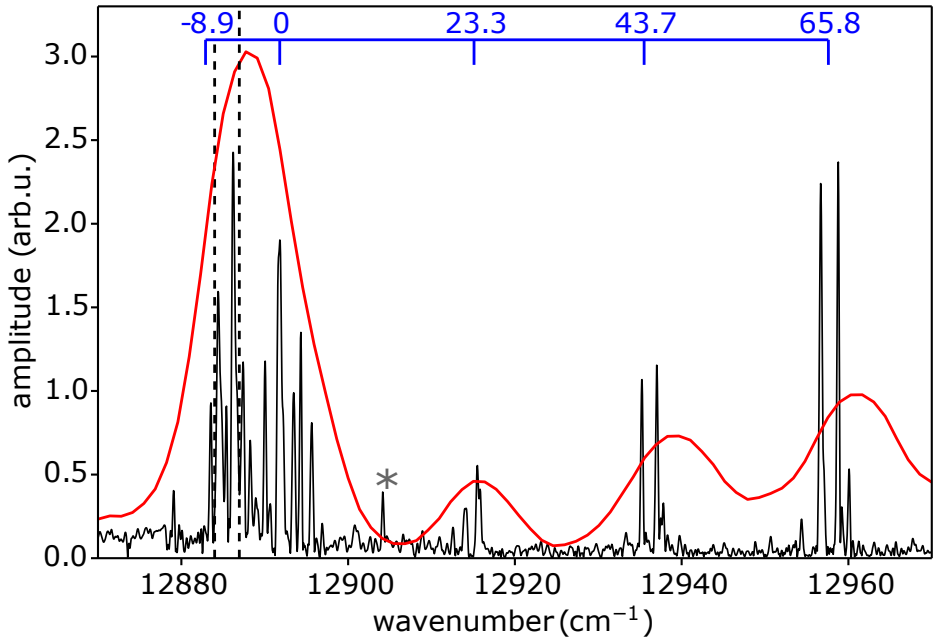

Figure 5.3: Rb*He exciplex spectrum obtained from PM-WPI (black) and femtosecond pump - picosecond probe (red) measurements [95]. Relative transition frequencies inferred from conventional WPI [22] are also shown (blue scale on top). Black dashed lines indicate the $5P_{3/2} \rightarrow 5D_{5/2,\,3/2}$ atomic Rb transitions. Reproduced from Ref [B1].

trum of the exciplex molecule with a spectral resolution of $0.3\,\mathrm{cm}^{-1}$ (FWHM). An intuitive interpretation of the observed spectral features can be inferred. Comparing the spectral lines with the position of the $5P_{3/2} \rightarrow 5D_{5/2,\,3/2}$ atomic Rb transitions (vertical dashed lines), the following coarse assignment may be done: the closely spaced spectral lines in the vicinity of the atomic transitions involve mainly vibrational modes energetically close to the dissociation limits. Lines at larger frequencies correspond to transitions of lower lying vibrational modes in the $1^2\Pi_{3/2}$ electronic state and the line splitting originates from the congestion of the higher-lying PECs. The marked peak (asterisk) in the spectrum corresponds to residual low-frequency noise of the demodulated signal, thus appearing at the monochromator wavenumber ($12904.15\,\mathrm{cm}^{-1}$) in the Fourier spectrum. This contribution is caused by a coarse sensitivity setting of the lock-in amplifier being not optimized to the signal amplitude which is in the exciplex measurements impeded by the strong signal increase at zero pump-probe delay. Accordingly, this feature is suppressed in all other data shown in this PhD thesis.

For comparison, results from previous photoionization studies of the Rb*He exciplex are also shown in Fig. 5.3. In a conventional WPI experiment [22] the signal quality was not sufficient to deduce the absolute transition frequencies through a direct Fourier analysis; relative distances between vibrational levels were deduced instead. To compare with the phase modulation experiment, an assignment of the relative frequencies obtained in Ref. [22] to the distances between spectral features in the current study is shown (blue scale on top). Good agreement is found, albeit the phase modulation data exhibit a factor of 10 better resolution and allows for a more unambiguous interpretation. A different approach for achieving vibrationally resolved data on Rb*He exciplex molecules has been pursued in a femtosecond pump - picosecond probe experiment [95]. This study allowed to deduce absolute transition frequencies although at the cost of resolution which is factor 30 lower than achieved in the current phase modulation experiment. After applying a red shift of $2\,\mathrm{cm}^{-1}$ to the corresponding data (red spectrum) good agreement is obtained despite the different measurement schemes. The systematic shift can be attributed to coarse calibration of the pulse shaper that was used to generate the picosecond probe pulses. Calibration errors in the phase modulation data can be excluded since calibration measurements with a rubidium vapor cell have been carried out regularly during the measurements.

5.5 Comparison with theory

To calculate the WPI spectrum, Frank-Condon factors (FCFs) for transitions between the $1^2\Pi_{3/2}$ lower potential and the $4^2\Pi_{3/2,1/2}$, $2^2\Delta_{3/2,1/2}$, $6^2\Sigma_{1/2}$ upper PECs are evaluated employing the LEVEL 8.0 code of LeRoy [139]. This code calculates for the given Pascale potential all bound states and evaluates the wave function overlap to determine the FCFs, yielding in total 140 contributions of which a large number exhibits, however, negligible amplitudes. Adiabatic vibronic couplings have been neglected, i.e. electronic dipole moments have been assumed to be independent of the nuclear coordinate. Furthermore, weighting of amplitudes with the laser spectrum and probing step (photoionization) have been omitted and equal initial populations in the $1^2\Pi_{3/2}$ have been assumed. Moreover,

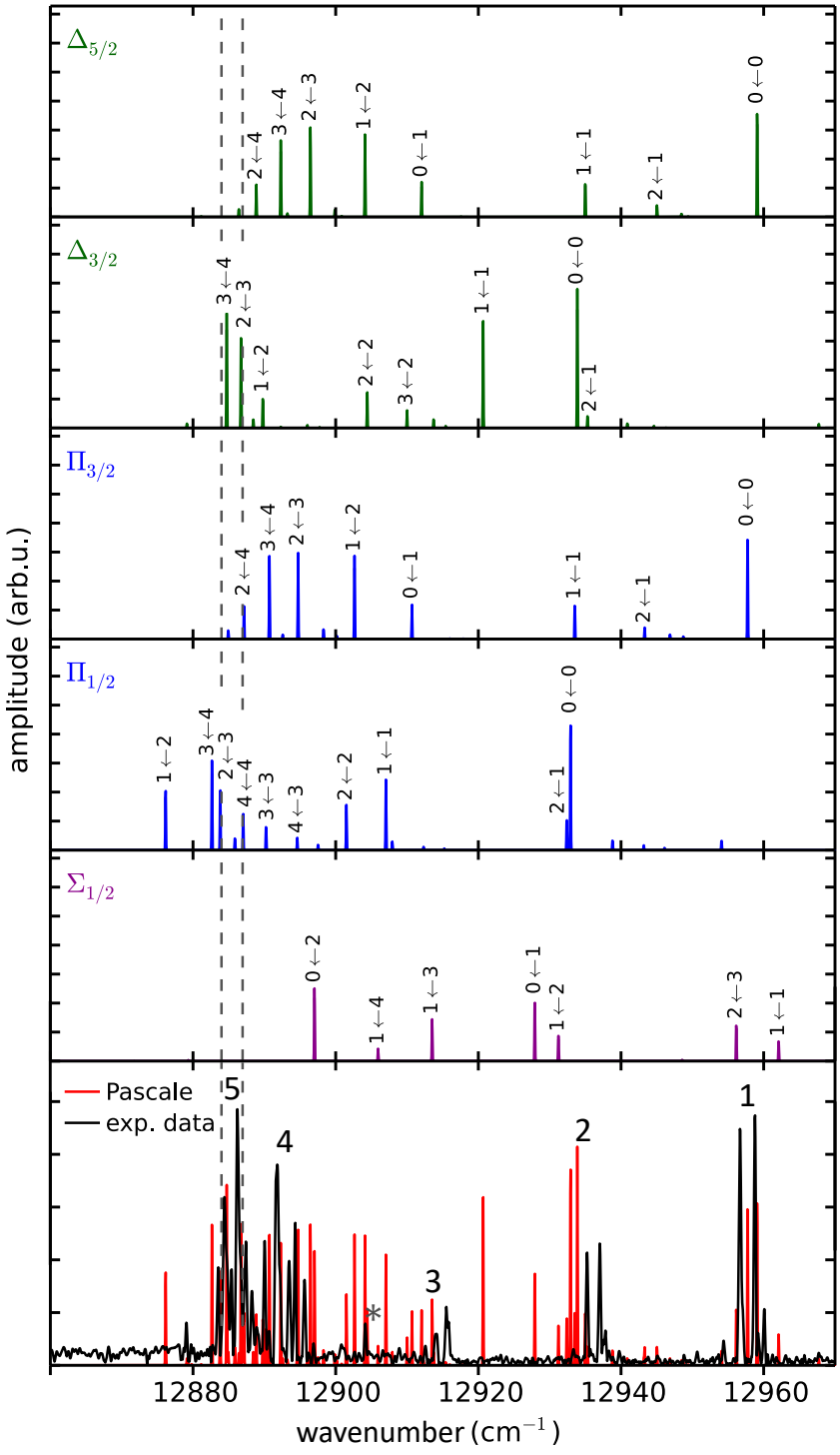

Figure 5.4: Experimental Rb*He exciplex spectrum compared with calculations based on the potentials by Pascale [135]. The five upper panels show the calculated FCFs (blue shifted by $4\,\mathrm{cm}^{-1}$) for transitions from the $1^2\Pi_{3/2}$ lower potential to each higher-lying potential, separately (label). Adding up all five spectra yields the red spectrum in the bottom panel which is compared to the experimental data (black). Five features can be identified in the experimental spectrum (labels) as discussed in the text. For simplicity only most prominent vibronic transitions are labeled. Adapted from Ref. [B1].

a systematic blue shift of $4\,\mathrm{cm}^{-1}$ has been applied, which seems a reasonable adjustment for such type of numeric models.

The resulting spectrum is shown in Fig. 5.4 together with the experimental data. A semi-quantitative agreement between experiment and theory is found, i.e. the essential structure of the experimental spectrum is reproduced. Considering the degree of detail revealed in the experimental data and the high experimental resolution which certainly exceeds the precision of the Pascale PECs, this agreement is quite satisfactory.

For a comparison of observed spectral lines with individual vibronic transitions, the calculated transitions from the $1^2\Pi_{3/2}$ intermediate PEC to the individual upper potentials are separately shown in five sub panels with labels indicating the upper PECs. This allows a more precise interpretation of the exciplex spectrum than was possible in previous studies [22, 95]. Five distinct features are identified as labeled in the lowest panel. Since the Franck-Condon overlap of modes from the $1^2\Pi_{3/2}$ PEC with hot states of the upper PECs is small, mainly lower vibrational modes ($\nu = 1 - 3$) of the higher-lying PECs contribute. Furthermore, the quantum numbers of vibrational modes in the lower molecular $1^2\Pi_{3/2}$ state generally increase from feature 1 towards feature 5. However, in contrast to the previous interpretation [22], the doublets 1 and 2 correspond primarily to $0 \rightarrow 0$ transitions and thus do not reflect the vibrational ladder of the $1^2\Pi_{3/2}$ potential. Moreover, features 4 and 5 correspond to transitions from the $1^2\Pi_{3/2}$ $\nu = 3, 4$ modes to different higher-lying PECs. Feature 4 represents dominantly transitions to the upper $\Pi_{3/2}$ and $\Delta_{5/2}$ states, whereas feature 5 primarily to the $\Pi_{1/2}$ and $\Delta_{3/2}$ PECs. This difference provides information about the molecule formation process, as will be discussed further below.

The exciplex spectrum has also been calculated including rotational transitions. The equilibrium nuclear distance in the Pascale potentials (neglecting the $6^2\Sigma_{1/2}$ state) is $R_e \approx 3.5\,\mathring{A}$ [135], which corresponds to a rotational constant of $B_e \approx 0.4\,\mathrm{cm}^{-1}$for the ^{85}Rb isotope. Therefore, at a droplet temperature of 370 K, Boltzmann factors for rotational states $J > 0$ are below a value of 0.2 and for simplicity only initial states with $J = 0$ have been considered. The rotational splittings and Hönl-London factors for the respective $J'' = 0 \rightarrow J' = 0, 1$ transitions have been calculated using the Level 8.0 code. From the estimated rotational constant, splittings of roughly $0.8\,\mathrm{cm}^{-1}$(P- and R-branch) are expected in the spectrum and should be well resolved within the experimental resolution of $0.3\,\mathrm{cm}^{-1}$.

Fig. 5.5 shows a comparison for the deduced spectra excluding rotations in (a) and including them in (b). In this case, the calculated stick spectra have been convoluted with the experimental resolution of $0.3\,\mathrm{cm}^{-1}$(FWHM of Gaussian) for a more realistic comparison with the experimentally obtained features. As revealed in (b), rotational lines are clearly separated within the experimental resolution, which matches with the predictions. The additional lines, however, lead to less agreement with the experimental data. In contrast, in (a), the number of lines in the calculated and experimental spectrum seem to match fairly well. The experimental data do not indicate, that spectral lines are missing in the theoretical model. From this observation, it is concluded that rotational features are not observed in the measurement. Data were also acquired for the ^{87}Rb*He isotope. However, since the effective mass of both exciplex isotopes differ only by 0.1%,

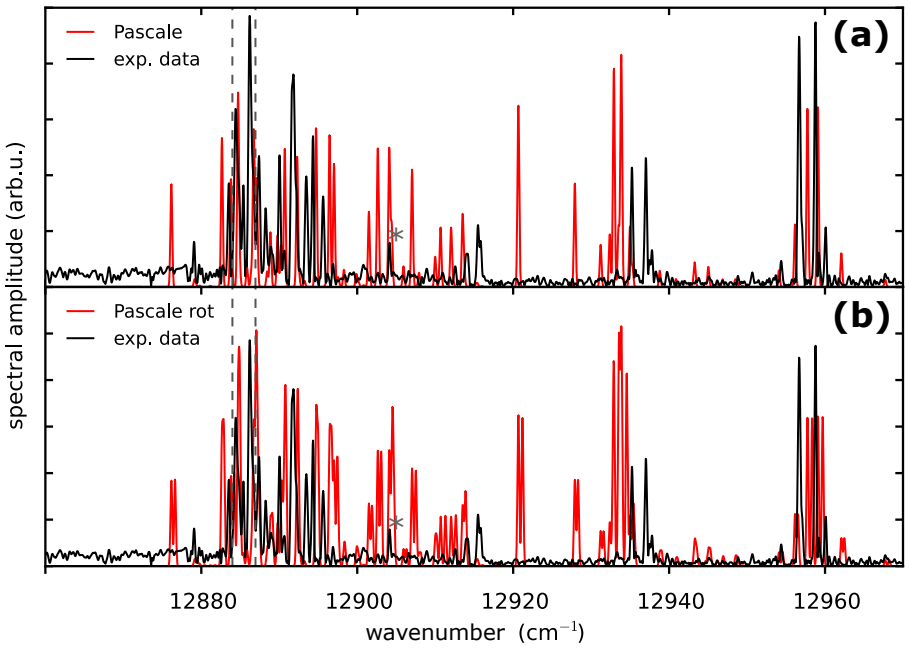

Figure 5.5: Simulation of Rb*He exciplex spectra excluding (a) and including (b) rotational transitions $J'' = 0 \rightarrow J' = 0, 1$. The calculated stick spectra (red) have been convoluted with a Gaussian of 0.3 cm^{-1}FWHM to account for the resolution in the experimental data (black).

isotope effects cannot be resolved within the experimental resolution and is thus not feasible to identify rotational lines in the spectrum.

The absence of rotational features is explained within the formation process of the molecule. In the experiment, the Rb*He exciplex forms upon excitation with the pump pulse. This step should not induce a rotation of the molecule as the exciplex is formed directly on the surface of the droplet. As a consequence, the WPs induced by the pump pulse do not include excited rotational states. The probe pulse, on the contrary, may excite rotational states in the system. However, only states with $J = 0$ will interfere with the WP excited by the pump pulse. As such, only these states yield an interference signal and are detected in the WPI measurement. Hence, in this particular constellation, the measurement procedure is insensitive to rotational excitation which explains the absence of rotational features in the data.

Eventually, the experimental data were compared to other models. To this end, the $1^2\Pi_{3/2}$ potential by Pascale has been exchanged with an ab initio model of Yabuzaki and coworkers [128]. In a second attempt, it was assumed that the five main features identified in the experimental data (Fig. 5.4) reflect the vibrational ladder of the $1^2\Pi_{3/2}$ potential and a Morse potential was fitted to replace the potential by Pascale. Both approaches yielded less agreement with the experimental data and were therfore not considered.

5.6 Formation and relaxation dynamics

Previously, two types of dynamics have been observed in the Rb*He exciplex system involving a fast process attributed to the molecule formation occurring within a few picoseconds, on the one hand, and a slow relaxation of vibrational modes on the nanosecond time scale, on the other hand. Different formation mechanisms have been proposed for the Rb*He exciplex as already discussed above. Recent, experimental observations suggest a fast photoassociation-like formation [21, 22, 95, 103]. In this case, the molecule would be initially prepared predominantly in the highest bound state $1^2\Pi_{3/2}$ ($\nu = 4$) followed by a rapid redistribution to lower lying states ($\nu = 2, 3$) stabilizing the molecule within approximately 15 ps [22, 95]. Giese et. al. observed further relaxation on time scales up to 1.7 ns, suggesting that the Rb*He molecules reside on the droplet for long times after its formation [95]. This is in accordance with experimental evidence of an indirect desorption process due to vibrational relaxation [107, 140]. Furthermore, for alkali dimers and trimers attached to the surface of helium droplets, a similar behavior of fast redistribution of population into different modes followed by slow relaxation has been observed [49, 99, 108]. In this context, possible observations of dynamics within the improved signal quality of the current experiments shall be briefly discussed.

Fig. 5.2 shows a pump-probe transient of the Rb*He measurements. Signal interpretation for times smaller than the pulse duration is commonly omitted and the pump-probe overlap has been marked accordingly by a grey vertical bar. Yet, outside of this region, a fast decay of the ion yield within 1.7 ps is clearly visible. This fast process may indicate formation dynamics corresponding to a time scale being approximately in accordance with previously observed formation and redistribution dynamics [22]. For a spectral analysis of this feature, a Fourier transform for a delay range of ± 1.7 ps is shown in Fig. 5.6. This spectrum is compared with the high resolution exciplex spectrum obtained from a pump-probe scan of -100 to 120 ps. To this end, the latter has been convoluted with a Gaussian to match the low resolution obtained for the short-time Fourier transform of the ± 1.7 ps time interval. As can be seen, both spectra coincide qualitatively. The pronounced spectral feature at $12880 - 12900\,\mathrm{cm}^{-1}$and the two doublets ($12936\,\mathrm{cm}^{-1}$, $12958\,\mathrm{cm}^{-1}$) involve different vibrational modes (Fig. 5.4). Therefore, a rearrangement of vibrational populations in the system would lead to a change in spectral amplitudes of these features. From this, it can be concluded that no signs for a rearrangement process within these first few picoseconds can be observed.

On the contrary, rotational dephasing, as discussed for instance in Refs. [24, 141, 142], may cause the observed rapid drop of signal amplitude in Fig. 5.2. A remarkable resemblance can be found with the electronic WPI signal obtained for gas-phase I_2 molecules [24] for which environmental-induced decoherence can be excluded and a detailed theoretical analysis confirmed a rotational dephasing effect [141]. This effect originates from closely spaced rotational modes which results in a revival structure in the pump-probe signal with large revival time constants (in the hundred picosencond to nanosecond range). Thus, at zero pump-probe delay, all modes are initially in phase and quickly dephase, giving rise to a rapid drop in the signal amplitude. Revivals and fractional revivals occur then at much longer pump-probe delays which would be presumable outside the accessible pump-probe range in the PM-WPI experiment. Yet, this interpretation contradicts with the

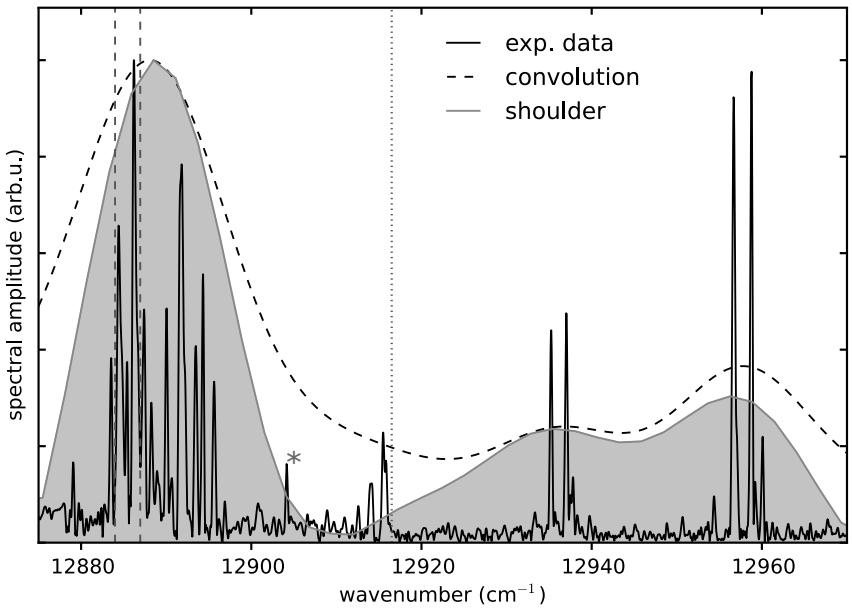

Figure 5.6: Fourier transform for a pump-probe delay range of ±1.7 ps (gray spectrum) yields a spectral analysis of the rapid decay (shoulder), observed in Fig. 5.2. For comparison, the high resolution exciplex spectrum (black spectrum) is convoluted with a Gaussian (black dashed spectrum). Vertical dashed lines indicate the $5P_{3/2} \rightarrow 5D_{5/2,\,3/2}$ atomic Rb transitions. The vertical dotted line shows the laser center frequency.

previous conclusion that rotational excitation is missing in the performed experiments. In the Rb*He molecule, the closely spaced vibrational modes of the congested upper PECs ($4^2\Pi_{3/2,1/2}$, $2^2\Delta_{3/2,1/2}$, $6^2\Sigma_{1/2}$) should, however, lead to a rapid dephasing of the signal in analogy to closely spaced rotational lines. Therefore, the rapid decay of amplitude within 1.7 ps observed in Fig. 5.2 is attributed to fast dephasing due to the closely spaced vibronic transitions appearing in the spectral range of $12880 - 12900\,\mathrm{cm}^{-1}$(vibronic bands 4 and 5 in Fig. 5.4).

In order to make the time evolution of the most prominent spectral features directly accessible, in addition a spectrogram representation of the time-domain data obtained by short-time Fourier analysis (Gaussian window function of 4 ps FWHM, 0.5 ps step size) is shown in Fig. 5.7. The five distinct spectral features identified above (Fig. 5.4) are recognizable in the spectrogram (labels). Due to the closely spaced lines, clear beat notes can be observed in the spectrogram. This is in principle in analogy to the above discussed rapid dephasing observable in the time-domain data. For the doublets 1 and 2, where only two major lines interfere, a periodic revival structure occurs, allowing for a quantitative analysis. Obtained revival time constants are 15.8 ps (doublet 1) and 19.2 ps (doublet 2) which correspond well to the line splitting of $2.1\,\mathrm{cm}^{-1}$(doublet 1) and $1.8\,\mathrm{cm}^{-1}$(doublet 2). In feature 3, three lines overlap, of which two differ by less than $0.3\,\mathrm{cm}^{-1}$(experimental resolution). This corresponds to a revival time constant of 111 ps and a faint feature can be identified at the end of the pump-probe scan (108 ps). With smaller spectral spacings, revival times increase and the reoccurrence of some features are expected to lie outside

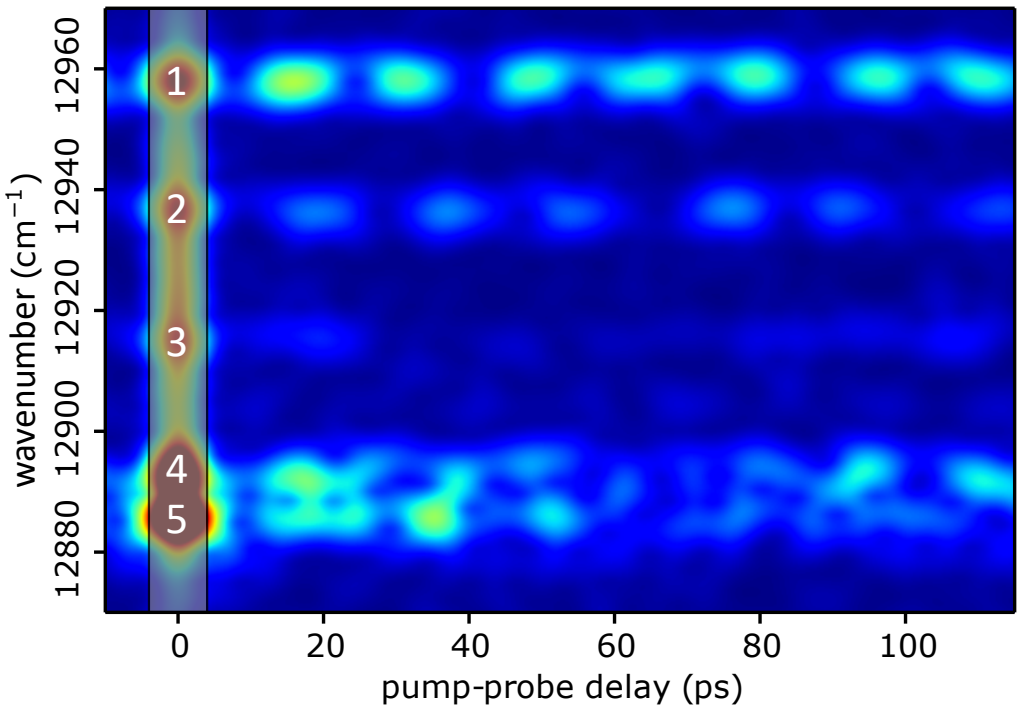

Figure 5.7: Spectrogram representation of the Rb*He data obtained by short-time Fourier transform of the pump-probe transient for a Gaussian window function (4 ps FWHM) slided over the data (5 ps step size). The pump-probe overlap region has been marked with a vertical bar. Most prominent spectral features are labeled.

of the accessible delay range. This case applies for the vibronic bands 4 and 5, where a large number of spectral lines are closely spaced and revival features are missing.

Traces along the observed beat structures indicate a slow relaxation presumably on the nanosecond time scale (not shown) which seems in accordance with the results of Ref. [95]. However, the accessible time window in the phase modulation experiments is too small for a reliable conclusion and the observed amplitude decrease are rather interpreted as slow beats among closely spaced lines. The latter assumption is supported by recent measurements of desorption times of the Rb*He exciplex formed via excitation to the $1^2\Pi_{3/2}$ PEC being in the < 100 ps range [143].

The above discussed rapid amplitude decay within the first 1.7 ps is also observed in the spectrogram, however, the short-time Fourier transform results in a temporal blurring, which makes this feature less pronounced. Nonetheless, outside the pump-probe overlap region (vertical bar), a fast decay of the lowest lying vibronic band (5) is observable. This is in accordance with the previous WPI study in Ref. [22], where a spectrogram for the first 20 ps was analyzed. Both spectrograms match well in the first 20 ps. In the previous study, a rearrangement of vibrational energy from feature 5 to doublet 1 has been interpreted. With the longer delay range accessible in the current spectrogram and the identification of periodic revivals, a different interpretation is more evident: Based on the current experiment, the in Ref.[22] observed increase of the doublet 1 at about

17 ps is assigned to the first revival (15.8 ps) of the initial doublet 1 amplitude. Likewise, the decay of amplitude in feature 5 is explained by a dephasing as discussed above, and the corresponding revival lies outside the accessible delay range. Hence, in contrast to the previous interpretation in Ref. [22], a rearrangement dynamic is not observed in the exciplex data.

The absence of transient features in the data that reflect the molecule formation dynamics may have two reasons. On the one hand, the formation dynamics are too fast to be resolved with the femtosecond pulses. On the other hand, the detected signal may arise from multiple pump-probe pulse pairs interacting with the system, as discussed above. In this case, the molecule is formed with a first pulse pair. Thus, the exciplex is already formed and relaxed to its equilibrium state when the WPs are induced with a second pulse pair. This would explain the absence of formation dynamics. Nonetheless, (static) information about different formation mechanisms/channels can be deduced in the PM-WPI experiments, as is discussed in the successive section.

5.7 Exciplex formation upon two-photon excitation

In previous studies, it has been assumed, that the Rb*He molecule forms upon a one-photon excitation of the $RbHe_N$ system [21, 22, 90, 95]. The femtosecond pulses employed in the experiment provide however sufficient intensity to drive two-photon transitions. In this context, a possible two-photon excitation process leading to exciplex formation, is investigated.

For this purpose, exciplex signals have been recorded for $\tau = 0-40$ ps and different laser wavelengths ranging from $769.5 - 781.3$ nm to reveal the signal dependence on the laser wavelength (Fig. 5.8). A general increase of spectral amplitudes is observed when tuning the laser from the red (781.3 nm) to the blue (773.8 nm). Two local maxima of the spectral amplitudes are found around 777 nm (12870 cm^{-1}) and 774 nm (12920 cm^{-1}), respectively. These wavelengths coincide with the calculated Franck-Condon factors in Ref. [86] for the $1^2\Sigma \rightarrow 1^2\Pi_{3/2}$ (peak at 12828 cm^{-1}), $2^2\Sigma_{1/2}$ (peak at 12851 cm^{-1}) excitations in the $RbHe_N$ system [cf. Fig. 2.12(b)]. Moreover, a previous study combining absorption and emission spectroscopy revealed, that the Rb*He exciplex forms primarily upon the excitation through the $1^2\Sigma \rightarrow 1^2\Pi_{3/2}$ Franck-Condon window while the excitation to the $2^2\Sigma_{1/2}$ leads to fast desorption of the rubidium atom without exciplex formation [90]. Therefore, it is concluded that the fist maximum at 777 nm reflects a peak in the formation probability of the exciplex via the $RbHe_N$ $1^2\Sigma \rightarrow 1^2\Pi_{3/2}$ one-photon excitation. In the following, the second maximum occurring at 774 nm is discussed in more detail.

Besides the molecule formation, the recorded signals also reflect the probability to induce the vibronic WPs in the molecule and the final photoionization step to deduce the WP interference signal. The latter can be neglected in the current discussion as a constant ionization cross section is expected over the probed laser wavelength range. The excitation of vibronic WPs in the system becomes more likely for laser wavelengths between 777 and 774 nm, where the spectral overlap between the laser and the vibronic transitions increases. This explains the increase in amplitude of the three doublets, labeled 1-3 for shorter laser wavelengths. However, the vibronic bands labeled 4 and 5 increase as well,

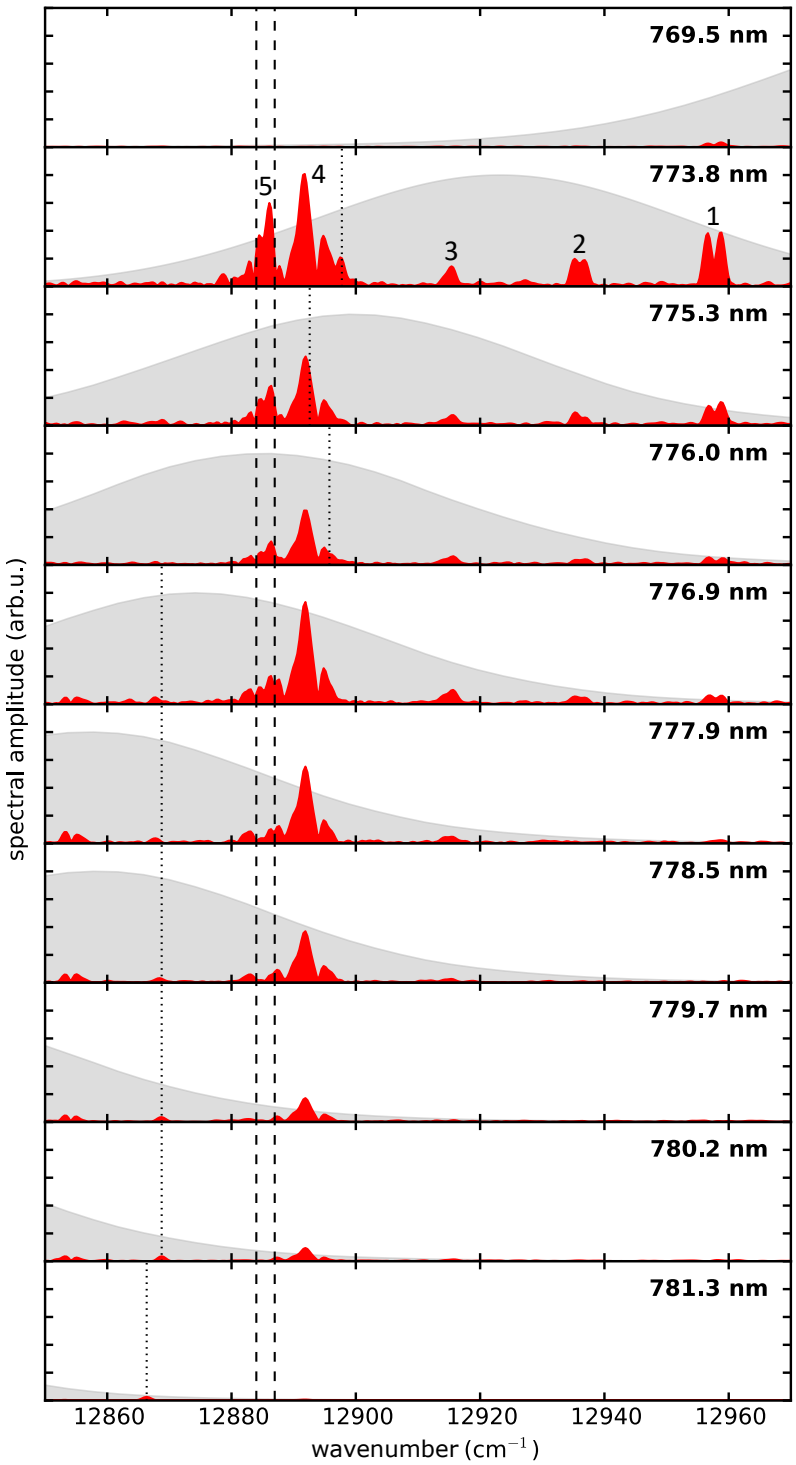

Figure 5.8: Rb*He Fourier spectra (red) for different laser wavelengths. Corresponding laser spectra are shown in grey for wavelengths as labeled. Vertical dashed lines indicate the $5P_{3/2} \rightarrow 5D_{5/2,3/2}$ atomic Rb transitions and dotted lines the applied monochromator frequency. The main spectral features are labeled in analogy to Fig. 5.4.

despite being less resonant with the laser spectrum. Furthermore, feature 5 increases relative to feature 4. This behavior can only be explained by a shift of initial populations of the vibrational states in the molecule. As both bands involve transitions from the same vibrational modes ($\nu = 3, 4$) of the lower $1^2\Pi_{3/2}$ potential, a change in population of these modes should not explain the observed effects. On the contrary, transitions to different higher-lying PECs are involved in the two bands (Fig. 5.4). Band 4 primarily involves transitions to the upper $\Pi_{3/2}$ and $\Delta_{5/2}$ PECs, whereas band 5 corresponds to transitions to the $\Pi_{1/2}$ and $\Delta_{3/2}$ PECs. Thus, it is concluded, that a change in the initial populations of the higher-lying potentials occurs at laser wavelengths approaching 774 nm.

This hints an additional formation mechanism that directly populates the higher-lying electronic states. Upon two-photon excitation, higher-lying $RbHe_N$ states correlating to the rubidium 5D asymptote may be populated from where the Rb*He molecule is formed via a tunneling process. Likewise, exciplex formation through a direct excitation from the $RbHe_N$ ground state to the $4^2\Pi_{3/2,1/2}$, $2^2\Delta_{3/2,1/2}$, $6^2\Sigma_{1/2}$ PECs of Rb*He could be possible. In analogy, for one-photon excitation similar tunneling [93, 127, 137] and photoassociation-like [21, 22, 95, 103] pathways have been proposed for various alkali-helium exciplexes.

In gas-phase rubidium atoms, two-photon transitions to the 5D states are weak (1% of the D_2 line strength, cf. Fig. 7.13). This suggest, that the two-photon excitation pathway should be negligible. However, in the $RbHe_N$ system, corresponding two-photon processes are presumably stronger since the intermediate electronic states exhibit much broader absorption profiles [Fig. 2.12(b)] which favors resonant enhanced two-photon transitions. Furthermore, the found maximum in exciplex yield at a laser wavelength of $\approx 774\,\mathrm{nm}$ ($12920\,\mathrm{cm}^{-1}$) fits to a two-photon excitation ($25840\,\mathrm{cm}^{-1}$) to the $5\mathrm{d}\,\Pi$, Δ, Σ manifold of the $RbHe_N$ system, which is blue shifted with respect to the atomic rubidium transition [87]. This supports the hypothesis of exciplex formation through a tunneling process from these states. On the contrary, for a direct photoassociation-like mechanism, the two-photon energy is too large to yield reasonable spectral overlap with vibrational modes of the higher-lying states. Thus, a direct photoassociation process seems less likely.

Another experimental observation supports the hypothesis of a two-photon exciplex formation pathway. In the PM-WPI scheme, a two-photon excitation leads to a modulation of the signal at the second harmonic of the acoustic beat frequency (i.e. $\phi(t) = 2\Omega_{21}t$). This signature can be used to identify two-photon transitions, as will be explained in detail in the successive chapter. In the exciplex measurements, a $2\Omega_{21}$-modulation was identified in the Rb^*He^+ ion yield, indicating a two-photon process. This signal decayed rapidly within the pump-probe overlap time which fits with the hypothesis of a fast exciplex formation process via two-photon excitation.

Alternatively, the increase in spectral amplitudes for excitation wavelengths around 774 nm may be explained with a different approach. It has been discussed above, that the exciplex signal may arise from the interaction with more than one pump-probe pulse pair. In this case, the first pulse pair initiates the exciplex formation via a one-photon excitation (pump pulse) and excites the molecule (partially) to the higher-lying states (probe pulse). A successive pulse pair then induces the WP interferences that lead to the detected signals, now for molecules that are initially populated in the $1^2\Pi_{3/2}$ as well as in the higher-lying PECs. However, this mechanism does not explain the increase of the

vibronic bands 4 and 5 in Fig. 5.8 when tuning the laser away from these resonances to the blue, where less spectral overlap is obtained with the vibronic transitions. Therefore, this approach is not considered. Other processes, such as saturation of specfic spectral lines, are also omitted since they did not fit with the observed dependence on the laser wavelength in Fig. 5.8.

With this, it is concluded, that a second formation mechanism/channel exists to form the Rb*He exciplex via two-photon excitation. This process should be primarily induced with intense femtosecond laser pulses that provide sufficient intensity and spectral width to drive a (resonant enhanced) two-photon excitation in the system that forms the exciplex in electronic states correlating to the 5D atomic asymptote. Experiments with a UV laser to directly address the formation channel with a one-photon process may yield further insights into this process.

5.8 Conclusion

In conclusion, the presented work has demonstrated for the first time the applicability of PM-WPI to a molecular sample in the gas phase at very low particle densities and milikelvin temperatures. The investigated Rb*He diatomic molecule forms upon electronic excitation of a rubidium atom residing on the surface of a helium nanodroplet. Electronic WPs were induced between the bound states of the $1^2\Pi_{3/2}$ PEC and the higher-lying $4^2\Pi_{3/2,1/2}$, $2^2\Delta_{5/2,3/2}$, $6^2\Sigma_{1/2}$ PECs. The WP interferences were detected in the ^{85}Rb*He$^+$ ion yield upon photoionization. Highly resolved vibronic spectra with a resolution of $0.3\,\mathrm{cm}^{-1}$(FWHM) were obtained revealing new details about the energetic structure of the exciplex. Good agreement with previous studies [22, 95] was found, albeit with an improvement in resolution of a factor of 10 and 30, respectively. Furthermore, comparing the achieved resolution with recent high resolution ZEKE studies on the Na*He exciplex, an improvement of a factor of 17 was achieved.

A particular challenge in the analysis of the Rb*He system constitutes of the high congestion of higher-lying electronic states where many vibrational modes are closely spaced. A comparison with theory allowed for a dissection of the individual contributions. To this end, the exciplex spectrum was modeled based on the pair potentials by Pascale [135], which yielded a semi-quantitative agreement and confirmed that the novel experimental approach is suitable to test fine details of pair interaction potentials. An assignment of individual lines allowed for a refined interpretation of the spectral features, as compared to the previous studies on the exciplex. Furthermore, with the high signal quality and spectral resolution, for the first time, an additional exciplex formation channel via two-photon excitation was identified. This is in contrast to previous experimental [21, 22, 90, 95] and theoretical [93, 95, 107] studies, where only the Rb*He formation through one-photon excitation was considered. Moreover, evidence was found, that the exciplex is initially formed in its rotational ground state. This is concluded from the fact, that the WPI spectra lack signatures of rotational excitation despite the sufficient experimental resolution to reveal those.

Besides the high temporal resolution, the applied femtosecond pump-probe scheme provides also high temporal resolution which allowed to study the formation and relaxation

dynamics of the molecule. Previously, slow vibrational relaxation on a nanosecond time scale has been found in the Rb*He system subsequent to the molecule formation [95]. The PM-WPI data do not contradict with this observation, however, a quantitative analysis of this aspect was not possible within the accessible pump-probe delay range of 120 ps. Moreover, fast formation and rearangment dynamics within less than 20 ps have been reported for the Rb*He molecule [22]. The improved signal quality in the current study allowed for a refined interpretation. As such, the previous observations were now interpreted as reoccurring revivals of initial populations rather than a shift of populations to lower-lying vibrational states. Hence, information about the formation dynamics are not found in the PM-WPI data. One reason might be, that the dynamics are smeared out by preceding laser pulses that prepare the exciplex in an equilibrium state before the dynamics are actually probed with subsequent pulses. An insufficient time resolution in the experiment might be another explanation for the lack of formation dynamics in the data.

6 Detection of multiple-quantum coherences

In the preceding chapters, the PM-WPI method was used to reveal one-photon resonances in the studied atomic and molecular systems. In the scope of this dissertation, a new method has been developed which extends the phase modulation technique to allow in addition for the selective detection of multiphoton processes. The basic principle of this scheme is presented in the current chapter. In conjunction, one- and two-photon excitation in the rubidium-doped helium droplet system is investigated. Parts of this method have been recently published in Ref. [B2] and some content of this chapter is adapted therefrom.

6.1 Background

Nonlinear time-domain spectroscopy measures the nonlinear response of a system subject to the interaction with a sequence of multiple (≥ 2) phase-locked femtosecond pulses. The established state-of-the-art methods rely on probing the interference of WPs to deduce temporally and spectrally resolved information about populations and coherences in the system [4]. This is achieved by inducing single-quantum coherences (SQCs) in the system, that are WPs induced upon one-photon excitations. While these techniques are being constantly refined [60], deducing information about higher-lying states remains yet challenging.

In recent years, nonlinear methods have been extended to address this issue by probing MQCs, that are quantum coherences induced upon multiphoton transitions [5, 10, 32, 144, 145]. Experiments can be designed to allow for background-free detection of MQC signals, being a significant advantage in detecting the generally weak multiphoton processes. Furthermore, MQCs provide the information about higher-lying states relative to the ground state, instead of referencing excited state signals to intermediate states, thus facilitating data interpretation considerably. As examples, MQC signals have allowed to characterize the influence of electron correlations in molecular systems [31], probing the anharmonicity of molecular potentials [32], elucidating the role of higher-lying electronic states in ultrafast photoinduced processes [33] or unraveling congested electronic spectra of fluorescent proteins [146]. Furthermore, many-body effects in semiconductor nanostructures [10, 11, 145, 147] and in atomic gases [34, 35] have been revealed.

However, monitoring the phase evolution of MQCs manifests a particular experimental challenge. As the interference of WPs induced upon multiphoton excitations evolves roughly at multiplies of the excitation frequency, demands on phase stability in the optical setup are particular high in these experiments; and despite the background-free detection scheme, MQC signals remain challenging to acquire since high sensitivities are required

to extract the commonly weak multiphoton processes. Therefore, only few MQC studies have been conducted in which manly the (low-order) double-quantum coherence (DQC) signals have been detected [10, 31–33, 144–146, 148]. As an exception, one experimental apparatus has been reported capable of detecting higher-order ($n > 2$) quantum coherences [11, 55].

The phase modulation approach seems in this context ideal to tackle these challenges, but so far MQC signals have not been accessible within this method. In the presented PhD thesis, a phase-modulated multiple-quantum coherence (PM-MQC) detection scheme has been thus developed. This novel approach can circumvent the discussed issues by performing systematic downsampling of MQC quantum beats and incorporating lock-in detection for signal enhancement. The established method stands out by its high sensitivity, a simple two-pulse setup and the ability to acquire arbitrary high-order MQC signals in a single measurement, while demands on phase stability are hardly increasing for higher-order quantum coherence signals.

6.2 Multiple-quantum coherence detection method

Generally, verifying multiphoton pathways can be difficult: identification can be done via the power law of the excitation intensity which is a cumbersome routine; or from emission spectra that are often compromised by multistep relaxation pathways or dark relaxation channels. An alternative approach has been demonstrated by Tian and Warren measuring the static two-photon absorption in a molecular system with two phase-modulated laser beams, resulting in a signal modulated at twice the acoustic frequency [149]. Later, this concept has been adapted for the development of photoacoustic multiphoton microscopy [150] and recently incorporated to disentangle contributions in second harmonic generation (SHG) [151] and molecular relaxation processes [152]. While these examples focus on time-averaged absorption and emission rates, in the current work, a variant of this principle has been implemented in nonlinear time-domain spectroscopy, i.e. in multiphoton WPI experiments.

The developed phase-modulated multiple-quantum coherence (PM-MQC) detection scheme deploys the same pump-probe setup as before [see also Fig. 6.1(b)]. Considering a model system with ground state $|g\rangle$, first excited state $|e\rangle$ and a high-lying state $|n\rangle$ [Fig. 6.1(a)], electronic WPs may be induced via one- and n-photon excitation pathways, respectively [examples given in Fig. 6.1(c), (d)]. In the phase modulation experiment, pump and probe pulses each get an individual phase ϕ_a imprinted by the acousto-optic bragg cells. Upon interaction with the sample, these phase signatures are inscribed into the quantum pathways, resulting in the accumulation of different phase factors for the one- and n-photon pathways as can be derived from time-dependent perturbation theory or directly from the shown Feynman diagrams. A linear sweep of the phase $\phi_a(t) = \Omega_a t$ on a shot-to-shot basis yields a quasi-continuous modulation of the signal components and in analogy to the PM-WPI theory given above, the n-photon signal is

$$S_n(t,\tau) = A_n \left[1 + \beta^n \cos\left(\omega_{ng}\tau - n\Omega_{21}t\right)\right] . \tag{6.1}$$

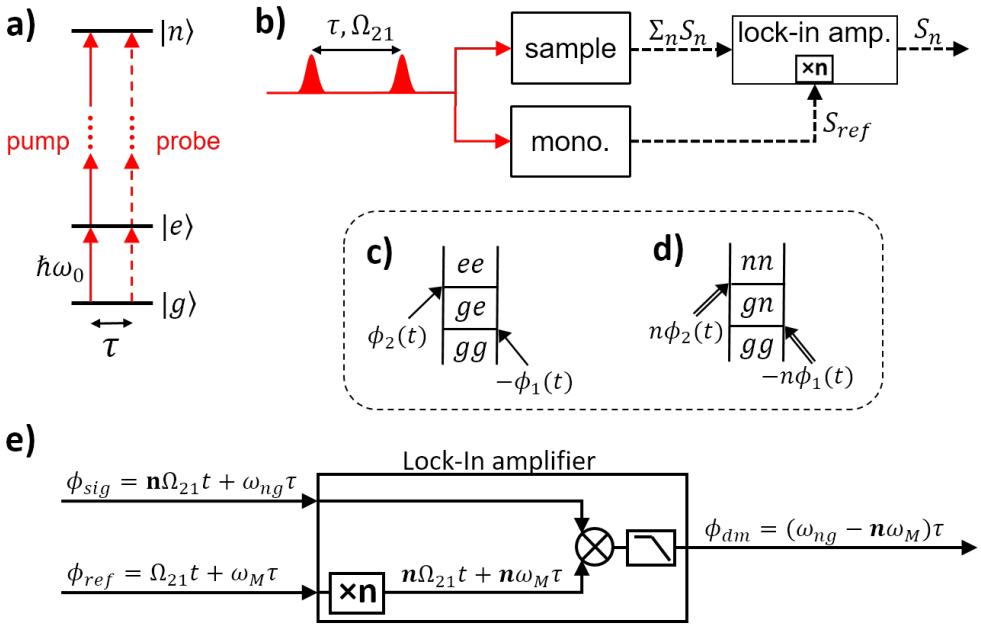

Figure 6.1: (a) Pump-probe WP excitation in a model system for an n-photon excitation. (b) Schematic diagram of the PM-MQC detection scheme. (c) and (d): Respective double-sided Feynman diagrams for one- and n-photon excitation. (e) Harmonic lock-in detection using an external reference signal. For simplicity only the phase terms of the signal (ϕ_{sig}), reference (ϕ_{ref}) and demodulated signal (ϕ_{dm}) are shown.

To detect the n-quantum coherence signal S_n, harmonic lock-in demodulation is applied [Fig. 6.1(e)]. To this end, an external reference signal is applied to the lock-in amplifier, which is an important difference to the work of Tian and Warren. The reference signal is constructed with a monochromator as done in the previous phase modulation studies. Upon harmonic demodulation, $R(\tau, t)$ is digitized and its n'th harmonic is generated yielding a normalized waveform

$$R_n(t, \tau) = \cos(n\omega_M\tau - n\Omega_{21}t)\,. \tag{6.2}$$

Performing this crucial step with digital electronics ensures low noise characteristics and small harmonic impurities in the reference signal, which is a key property to achieve the high performance, as shown below. $R_n(t, \tau)$ exhibits a modulation at n-times the acoustic beat frequency Ω_{21}, resulting in a demodulation of the n-photon MQC signal, while at the same time signals exhibiting different modulation frequencies (e.g. SQC signal) are discriminated. As a crucial characteristic, the pump-probe delay dependent phase term $\omega_M\tau$ is preserved and shifted by factor n. Due to this, the n-photon WP oscillations are detected in the rotating frame of n-times the reference frequency which results in a demodulated signal of the form

$$S_n(\tau) = A_n\beta^n \cos\left[(\omega_{ng} - n\omega_M)\tau\right]\,. \tag{6.3}$$

Similar to the previous PM-WPI measurements for SQC detection, the here detected MQC signal oscillates at the downshifted frequency $\bar{\omega}_n = \omega_{ng} - n\omega_M$. Hence, even for high-order multiphoton transitions lying in the deep UV spectral range, quantum beats are downsampled to low frequencies. As a crucial feature, demands on phase stability remain low for all harmonics which is in contrast to phase-matching based MQC detection schemes [60]. In general, the introduced PM-MQC scheme extends the quasi phase-cycling concept inherent in the phase modulation technique to access nonlinear signals in a pump-probe experiment, thus allowing to study higher order effects without the need of modifying the optical setup. Furthermore, simultaneous isolation of different MQC signals is possible in a single measurement by employing multiple lock-in amplifiers connected in parallel. This is in contrast to phase-cycling pulse shaper based nonlinear experiments. While rotating frame sampling at higher harmonics can be implemented there as well [5], simultaneous downsampling of different n-photon quantum coherences is not possible and must be done in separate data runs.

6.3 Application to helium nanodroplets

To demonstrate the PM-MQC detection scheme, measurements are performed on rubidium-doped helium droplets in the same helium droplet beam machine as has been used in the previous WPI measurements. Rubidium is in this context an ideal model system as it provides only few resonant well-defined energy levels but supports already one- and two-photon transitions to test the proposed scheme.

Sample preparation was done with the same parameters as used before. Pump-probe scans have been conducted for $0 - 50\,\mathrm{ps}$ and $\Delta\tau = 50\,\mathrm{fs}$ step size. Acquired QMS and monochromator signals have been split and fed into two lock-in amplifiers connected in parallel. Simultaneous acquisition of SQC (first harmonic demodulation) and DQC (second harmonic demodulation) signals was performed by referencing the devices to the first and second harmonic of the monochromator signal $\phi_{ref} = n\Omega_{21}t - n\omega_M\tau,\ n = 1, 2$. Respective demodulated interferograms of the mass-selected Rb^+ photoion yield are shown in Fig. 6.2. Here, the monochromator was set to $12898\,\mathrm{cm}^{-1}$and the laser to $12904\,\mathrm{cm}^{-1}$, enabling the resonant excitation of both the $5^2P_{3/2}$ and the $5^2D_{3/2,5/2}$ states (cf. Fig. 6.3a), and subsequent ionization with 3 photons in total. As revealed by the time-domain interferograms, the downshifting by ω_M and $2\omega_M$, respectively, results in similar signal frequencies for both pump-probe transients, being $< 3\,\mathrm{THz}$.

The Fourier transformed spectra are shown in Fig. 6.3(b), (c), confirming a clear separation of one-photon transitions, denoted $\omega_{1,2,3}$ (b) and two-photon transitions, denoted $\omega_{4,5}$ in (c). In this sense, the quasi phase-cycling scheme is demonstrated, i.e. selective detection of linear and nonlinear signal contributions in different demodulation channels is achieved. Furthermore, the first harmonic spectrum (b) provides information about the one-photon coherences between the ground and first excited state as well as between first and second excited state; whereas the second harmonic spectrum (c) directly reveals the coherence between ground and second excited state. Thus, the latter signal provides information about dynamics in higher-lying states correlated to the ground state. This characteristic is beneficial when probing for instance the vibrational structure of unknown

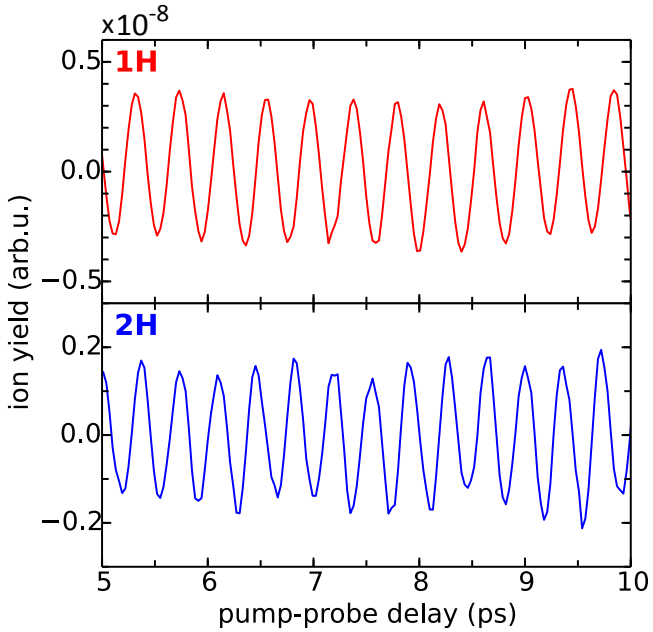

Figure 6.2: Interferograms recorded in a single measurement referenced to the first and second harmonic of $\phi_{ref} = \Omega_{21}t - \omega_M\tau$, labeled 1H and 2H, respectively. The SQC (red) and DQC signals (blue) are obtained in the first/second harmonic demodulation channels, respectively. The downshifting by ω_M and $2\omega_M$, results in similar signal frequencies for both pump-probe transients. Reproduced from Ref. [B2].

higher-lying molecular potentials excited via a resonant intermediate level. In such case, SQC signals would provide vibronic energies relative to the intermediate potential leading to a large number of possible combinations. The DQC signal, in contrast, would yield the vibronic energies directly correlated to the initial (ground) state, thus facilitating data interpretation significantly.

As another aspect, the high sensitivity of the PM-MQC method is demonstrated with data for a non-resonant two-photon transition to the Rb $7^2S_{1/2}$ state (ω_6). Here, the laser center wavenumber was set to $13182\,\mathrm{cm}^{-1}$ and the monochromator setting was $13134\,\mathrm{cm}^{-1}$. Signal amplitudes are roughly two orders of magnitude smaller as compared to the resonant two-photon excitation to the 5D states. Nonetheless, an excellent signal quality is obtained, confirming the high sensitivity of the method, even for mass-selected ions of particle densities $\lesssim 10^8\,\mathrm{cm}^{-3}$.

The same signals have been observed with fluorescence detection in a vapor cell (Fig. 7.5); however, two-photon signals are augmented by the enhanced photoionization cross section of the higher-lying final states. As such, the ratio between the $5^2S_{1/2} \rightarrow 5^2P_{3/2}$ (D_2) transition and the $5^2S_{1/2} \rightarrow 5^2D_{5/2}$ transition is roughly 1000:1 in the fluorescence measurement. In this context, another advantage of the PM-MQC detection method becomes apparent. The noise level in the fluorescence data is 1.3×10^{-7} (1H), 2.3×10^{-9} (2H), 7.1×10^{-10} (3H) and 4.6×10^{-10} (4H). Hence, the noise decreases with higher-order detection and the $5^2S_{1/2} \rightarrow 5^2D_{5/2}$ resonance (1.7×10^{-8} peak amplitude) would be buried in the noise floor, if this feature was recorded in the first harmonic demodulation channel.

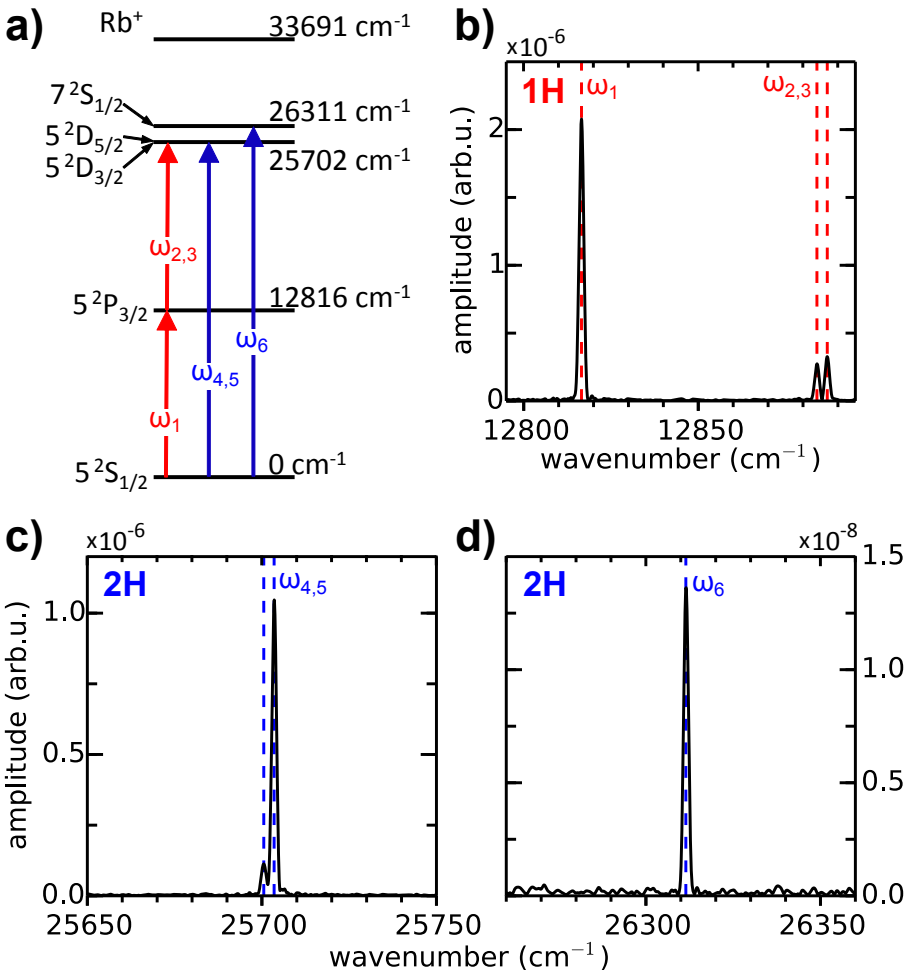

Figure 6.3: (a) Level diagram of the involved Rb electronic states. (b)-(d): Fourier transformed spectra of the measured pump-probe data referenced to ω_M (1H) and $2\omega_M$ (2H). Dashed vertical lines show the tabulated transitions [78]. Reproduced from Ref. [B2].

6.4 Phasing of detected signals

In nonlinear time-domain spectroscopy, heterodyne detection is implemented to retrieve amplitude and phase of the signal in order to access the full information encoded in the system response. In most nonlinear spectroscopy schemes characterizing the signal phase is intricate and different phasing routines have been developed [50]. In the phase modulation approach, heterodyne detection is automatically given by the phase-synchronous lock-in demodulation with an external reference signal constructed from the optical pulses. As an advantage over other techniques, the demodulated data are inherently phased [25, 26], which applies for the first harmonic demodulation. However for

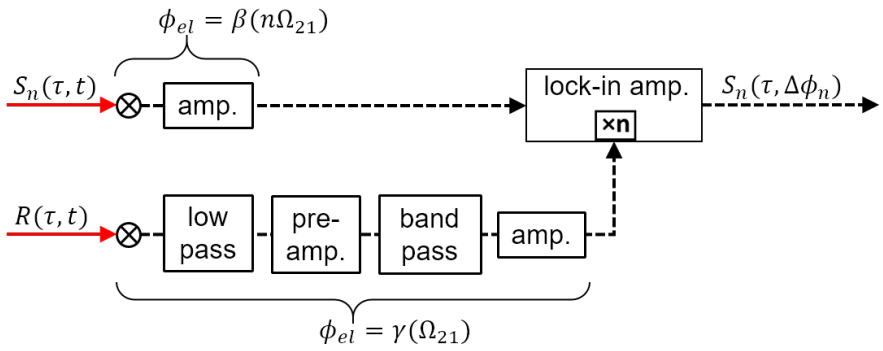

Figure 6.4: Phase shifts ϕ_{el} induced in the signal and reference detection, respectively. $\beta(\omega)$ and $\gamma(\omega)$ denote the frequency functions of the electronic circuit parts and $\Delta\phi_n$ denotes the resulting phase offset in the n'th harmonic demodulated signal.

higher order demodulation, a phasing concept had to be developed, which has been implemented in the scope of a Master thesis [153] supervised by the author. Here, a brief summary is given, details can be found in Ref. [153].

In the experimental setup, analog electronics induce a phase shift ϕ_{el} on the phase-modulated signal and reference prior to the lock-in demodulation (Fig. 6.4). The frequency-dependent accumulated phase shift, denoted $\beta(\omega)$ and $\gamma(\omega)$ for the signal and reference electronics, respectively, depends on the applied modulation frequency Ω_{21}. As such, higher-order signal components S_n as obtained in the PM-MQC detection, yield a different phase shift $\beta(n\Omega_{21})$ than one-photon processes with $\beta(\Omega_{21})$. Accordingly, the signals used by the lock-in amplifier for n'th harmonic demodulation are

$$S_n(\tau, t) \quad \propto \quad \cos\left[\omega_{ng}\tau + \alpha_n + n\Omega_{21}t + \beta(n\Omega_{21})\right] , \tag{6.4}$$

$$R_n(\tau, t) \quad \propto \quad \cos\left[n\omega_M\tau + n\Omega_{21}t + n\gamma(\Omega_{21})\right] , \tag{6.5}$$

where α_n represents the pure signal phase of the n'th order system response, thus representing the physical relevant phase information. Note, that β and γ are evaluated at different frequencies, thus using identical electronic parts for the signal and reference would not level out the accumulated phase factors. A characterization of the absolute values of β and γ is in the given experimental setup difficult, and the relative phase function

$$\Delta\beta_n(\Omega_{21}) := \beta(n\Omega_{21}) - \beta(\Omega_{21}) \tag{6.6}$$

has been determined instead. Furthermore, phase-resolved data have been acquired exclusively for $\Omega_{21} = 5\,\mathrm{kHz}$ in the presented work. Hence, to simplify notation the following definitions are used in the remainder of this chapter: $\beta(\Omega_{21}) =: \beta_1$, $\Delta\beta_n(\Omega_{21}) =: \Delta\beta_n$, and $\gamma(\Omega_{21}) =: \gamma_1$.

In case of first harmonic lock-in detection, the demodulated signal is

$$S_1^{\mathrm{dm}}(\tau) \propto \cos\left[\bar{\omega}_1\tau + \alpha_1 + (\beta_1 - \gamma_1)\right] . \tag{6.7}$$

Phasing of this signal is done by adapting the common routine for phase modulation experiments [25, 26]. To this end, it is assumed $\alpha_1 = 0$, as only linear processes are

expected to contribute to S_1^{dm}, and a global phase factor $\phi_1^{\mathrm{corr}} = -(\beta_1 - \gamma_1)$ is applied to the signal. ϕ_1^{corr} corresponds to a zero-order spectral phase correction which can be performed prior to the data run in the time domain using the adjustable phase θ_{LI} of the lock-in amplifier, or in the post processing setting $\theta_{\mathrm{LI}} = 0$. The latter generally yields higher accuracy ($\delta\phi_1^{\mathrm{corr}} = \pm 2.5°$) in particular for noisy data, and has been thus applied in the present work. In addition, first order spectral phase correction has been performed to account for timing errors ($\delta\tau \neq 0$) as described in Ref.[154] (uncertainty $< \pm 15°$). The fairly large error in the latter case is due to the coarse step size of the employed translation stage, suggesting a hardware upgrade for future studies.

In case of n-order harmonic lock-in detection, the demodulated signal is

$$S_n^{\mathrm{dm}}(\tau) \propto \cos\left[\bar{\omega}_n\tau + \alpha_n + (\beta_n - n\gamma_1)\right], \tag{6.8}$$

and the respective first-order correction phase is for this signal

$$\phi_n^{\mathrm{corr}} = -\left[\Delta\beta_n + \phi_1^{\mathrm{corr}} - (n-1)\gamma_1\right]. \tag{6.9}$$

This correction requires knowledge of γ_1 which is determined with a distinct WPI measurement for calibration, as described in Ref. [153]. In-between measurements, γ_1 appeared to vary significantly (in the range of $55° - 90°$) and frequent calibration was necessary. This behavior is attributed to a broken component in the reference signal circuit identified only after data acquisition for this thesis was completed. Furthermore, α_1 appeared to be intensity dependent, indicating that at larger intensities nonlinear effects (saturation) add to the first-order WPI signals (cf. Ref. [122]), which complicated data interpretation. In total, these factors result in a fairly large uncertainty of the determined phase, which has been within an acceptable range for the simple systems studied in the scope of this PhD thesis; however, the phasing routine will require improvement in accuracy for future studies of more complex systems.

Besides the phase correction of higher-order signals, also amplitude correction was done. To this end, the amplitude-frequency function of the signal detection electronics was determined by characterizing the signal amplitude as a function of the modulation frequency Ω_{21}. Corresponding correction factors for frequencies $n\Omega_{21}$ have been applied to the respective n'th harmonic signal in the data analysis.

6.5 Conclusion

A new method, termed PM-MQC detection, has been developed to sensitively and selectively detect multiphoton processes. This scheme is based on tracking the coherent time evolution of MQCs, which are electronic WPs induced in the system upon multiphoton excitation. From this, information about coherences and populations of higher-lying states is readily deduced with high spectro-temporal resolution.

The PM-MQC principle has been demonstrated for one- and two-photon excitation in the rubidium-doped helium droplet system. WP interferences were separately detected in different demodulation channels for the $5S_{1/2} \rightarrow 5P_{3/2}$ (D_2 line), the $5S_{1/2} \rightarrow 5D_{5/2,3/2}$ and the $5S_{1/2} \rightarrow 7S_{1/2}$ transition, yielding high quality interference fringes in the pump-probe transients and sharp resonances with excellent signal-to-noise ratios in the Fourier

transforms spectra, even for the non-resonant two-photon transition to the 7S state. As an advantage, the multiphoton WP signal of the 5D state is directly correlated to the ground state and not to intermediate states as typical in resonant enhanced multiphoton excitation. This generally facilitates data interpretation, which is in particular beneficial when more complex and congested spectra are analyzed. In addition, a phase calibration procedure has been developed to phase the higher-order signals. This allows to deduce, besides amplitude information, also the phase of the WP signals and thus provides access to the full information encoded in the nonlinear response.

As unique advantages of the PM-MQC method, demands on phase stability remain low for arbitrary high order multiphoton excitation processes. One- and multiphoton signals are acquired simultaneously and can be directly correlated in a single measurement. The MQC signals are sensitively detected with harmonic lock-in detection yielding background-free detection in separate demodulation channels with reduced noise characteristics for the higher-order signals. An example was given, where this characteristic enabled the detection of two-photon fluorescence signals, that would have been otherwise covered by the noise in the one-photon signal spectrum. As such, the established method demonstrates a unique ability to unravel weak nonlinear signals.

7 Collective resonances in dilute samples

In this chapter, the nonlinear response of collectively excited particles in highly dilute systems is investigated by employing the developed PM-MQC detection scheme. Some experiments presented here have been conducted by two graduate students (Ulrich Bangert, Marcel Binz) under the supervision of the author.

7.1 Background

Many-body interactions play a key role in a wide variety of quantum systems. Delocalized excitons occur in taylor-made molecular aggregates [155–160] but also in biological systems such as light harvesting antennas and reaction centers [15, 161–164], and multiexcitonic states have been observed in semiconductor materials [10, 11, 69, 145, 147, 165]. In these systems, inter-particle distances are typically small which gives rise to strong couplings and pronounced effects, e.g. line shifts and broadening of excitonic energies or the occurence of cooperative spontaneous emission (superradiance) [73, 166]. Due to the long-range nature of the dipole-dipole interaction, a variety of many-body phenomena have been observed in cold gases as well [167, 168]. Examples are the Rydberg blockade [70, 72], photoassociation of cold molecules [168, 169], Förster resonant energy transfer (FRET) between Rydberg atoms [170–172] or superradiance in a Bose-Einstein condensate [74].

Among the accessible systems, vapors may be of special interest as they provide a simplified system to study many-body effects. While cold gases are more confined in the relevant parameter space, warm ensembles represent more realistic model systems for natural processes in chemistry and biology. In this regard, experiments with warm vapors may complement studies in ultracold clouds to gain a more complete understanding of the observed interaction mechanisms. However, in warm gases, typical experimental observables for many-body interactions (line shifts and broadening) are masked by much stronger broadening mechanisms due to the higher thermal energy and density of the ensemble, requiring thus specialized nonlinear optics methods to extract the subtle effects [76]. As such, nonlinear frequency- [173–175] and time-domain [13, 176–179] spectroscopy methods have been successfully applied to reveal dipole-dipole interactions and local field effects in gases of high particle densities ($\rho \gtrsim 10^{15}\,\mathrm{cm}^{-3}$). At lower densities, these methods do not provide sufficient sensitivity. However, the long-range potential of the dipole-dipole interaction suggests that cooperative effects may be also relevant in such regimes.

Among the nonlinear time-domain methods, recently developed MQC detection schemes have gained particular interest as they can significantly enhance the sensitivity to probe many-body effects. It has been shown theoretically that in such experiments the collective nonlinear response only appears in the signal if an interaction lifts the degeneracy of the excitonic states [66, 180], thus the mere presence of a MQC signal indicates the

existence of an interaction in the system. As such, these methods uniquely provide a sensitive background-free probe of many-body phenomena not requiring to resolve line shifts or dissecting broadening mechanisms [34, 66]. This approach has first been exploited to study bi- and higher-order excitons in semiconductor nanostructures [10, 11, 145] which facilitated the deduction of binding energies and dephasing rates of the observed quasiparticles. In atomic vapors, DQC signals revealed delocalized excitonic states [34, 35] which suggests that the long range transition dipole-dipole interaction is relevant at densities as low as $\rho \sim 10^{12}\,\mathrm{cm}^{-3}$. The here employed method relies on 2D spectroscopy combined with a distinct phase-matching geometry to reveal the DQC signals [32]. Although having significantly enhanced the sensitivity to probe many-body processes in dilute samples, these methods are restricted in two aspects: they cannot be applied to much lower ensemble densities than the ones demonstrated; and an extension to probe n-body ($n > 2$) phenomena requires very sophisticated setups [55].

On the contrary, the developed PM-MQC detection relies on a simple two-pulse scheme and stands out by its high sensitivity. This has permitted, in the scope of the presented work, the investigation of collective effects in atomic gases and doped helium droplet systems at much lower densities. As a novelty, multiatom resonances have been observed at densities of $\rho \leq 10^{8}\,\mathrm{cm}^{-3}$ and ambient temperature, which is four orders of magnitude lower than previously reported. Furthermore, for the first time collective four-atom excitation has been observed in these systems. However, considering the small dipole-dipole interaction strength ($J/\hbar = 100\,\mathrm{Hz}$ at $\rho = 10^{8}\,\mathrm{cm}^{-3}$) in the studied systems, these results are surprising and it is discussed whether the observed collective excitations necessarily require an interparticle interaction to occur in the PM-MQC experiments. As will be shown below, the achieved experimental results combined with theoretical modeling lead to the conclusion that the weak dipole-dipole interaction is the origin of the observed multiatom resonances. Though, the signals are in addition superimposed with a higher-order single-atom signal arising from the interaction of one atom with multiple pump-probe pulse cycles.

7.2 Observation of collective resonances in dilute vapors

7.2.1 Collective resonances in a potassium vapor

As a first example, the collective excitation in a potassium vapor is presented. A fraction of these results has been published in Ref. [B2] and some content shown here is adapted therefrom.

The potassium sample is prepared in a heated alkali vapor cell ($\rho \approx 10^{10}\,\mathrm{cm}^{-3}$) and fluorescence signals are recorded. D_1 and D_2 lines are excited simultaneously with the unfocused pump-probe pulses tuned to $13005\,\mathrm{cm}^{-1}$. Fig. 7.1(a) shows the relevant energy levels of potassium. In this system, multiphoton transitions to higher-lying states in the single potassium atom are not present when excited with the employed femtosecond pulses having a bandwidth of $89\,\mathrm{cm}^{-1}$ FWHM. Thus, the energy landscape of the potassium atom can be reduced to an effective three-level system and higher-order MQC signals should not be observed in this system. However, if considering an ensemble of atoms described in a product basis (excitonic representation), one can assign new collective

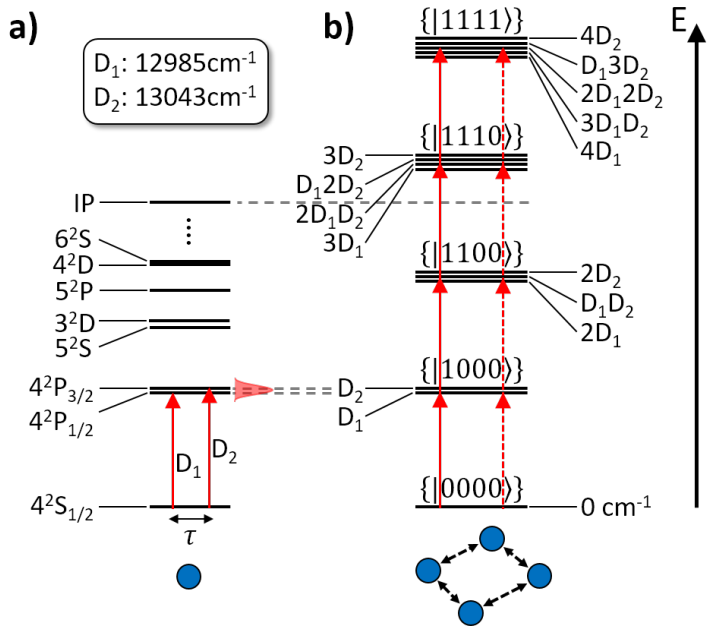

Figure 7.1: (a) Level diagram for atomic potassium and wavenumbers for the excited D_1 and D_2 lines [78]. (b) Corresponding collective energy states for an ensemble of four potassium atoms described in a product basis. For clearer visualization in (a), states lying between the 6^2S and the ionic potential (IP) are not shown. Since the laser is only resonant to the D_1 and D_2 line transitions, only these excitations are considered for the collective energy levels. Adapted from Ref. [B2].

energy states which yields a ladder-type energy structure as exemplary shown for an ensemble of four atoms in Fig. 7.1(b). The higher-lying collective energy levels may be probed by inducing MQCs in the system, that is in this case the superposition of multiple many-body wave functions. The time evolution of such quantum coherences then occurs at harmonics of the single-atom resonances and can be clearly identified well separated from the single-atom frequencies in the Fourier spectra.

Example data are shown in Fig. 7.2. The pump-probe transients have been recorded simultaneously for first- to fourth-order harmonic demodulation employing four lock-in amplifiers connected in parallel. Clear quantum beats are observed in all demodulated signals. The corresponding Fourier spectra (Fig. 7.3) reveal sharp peaks centered at the predicted multiatom resonances. The individual resonances exhibit different phases (shifted by multiples of π), which results in positive and negative features, as will be discussed in more detail further below. With each harmonic, the signal amplitude (Fig. 7.2) decreases by about one order of magnitude. Nonetheless, a very good signal quality is obtained for all spectra which demonstrates the high sensitivity of the applied method. The highest collective energy that is detected ($4D_2$) would correspond to an excitation wavelength of 190 nm which in general indicates sufficient phase stability to perform electronic WPI at VUV wavelengths. Furthermore, clear collective four-body signals are obtained down to vapor densities of $10^8\,\mathrm{cm}^{-3}$.

So far, in vapors only second-order collective resonances have been observed using 2D spectroscopy [34, 35]. As these experiments probe a macroscopic polarization induced in the sample, they lack sensitivity for highly dilute samples. In comparison, the PM-MQC approach is more universal as it relies on an 'action' signal for detection (e.g. single photons, electrons or ions) and arbitrary high-order MQC signals can be retrieved without

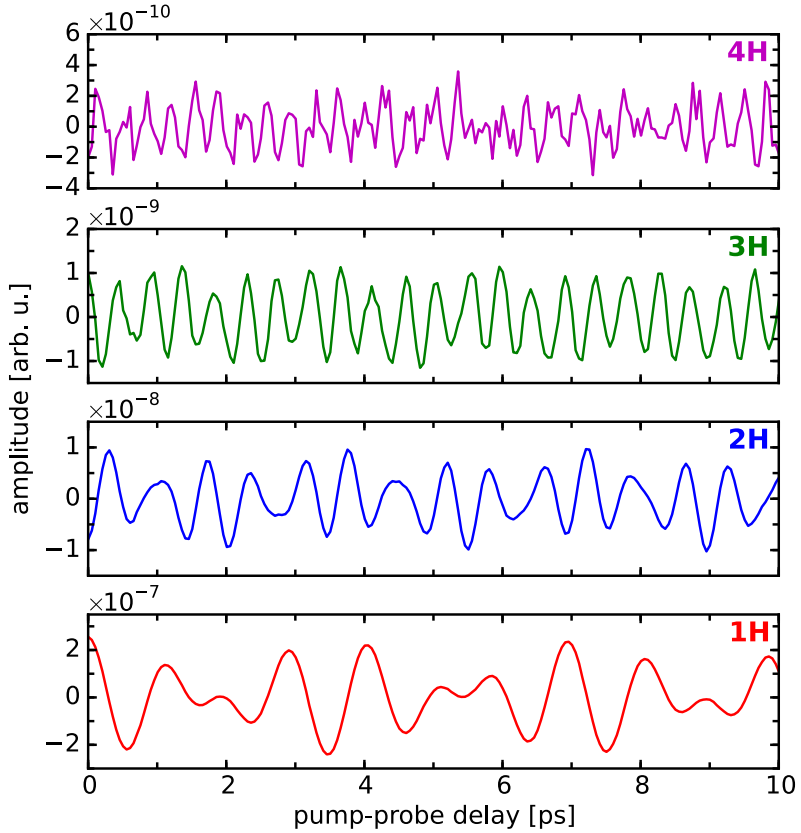

Figure 7.2: Time-domain interferograms of collective excitations in a potassium vapor, detected with first to fourth harmonic lock-in demodulation (labeled 1H-4H). The 1H signal corresponds to the single-atom response, whereas the 2H-4H signals reflect the interference of multiphoton WPs (MQC signals) revealing the multiatom response of the system.

modifying the setup. As such, the presented data show for the first time, that collective multiatom excitation is possible at densities ($10^8\,\mathrm{cm}^{-3}$) four orders of magnitude lower than previously demonstrated ($10^{12}\,\mathrm{cm}^{-3}$).

Likewise, collective three- and four-body excitation has not been observed in warm vapors before. Yet, many-body interactions have been observed in cold Rydberg clouds [172]. These systems exhibit knowingly strong couplings and a four-body FRET process could be detected for a density of excited Rydberg atoms of $\rho \approx 10^{10}\,\mathrm{cm}^{-3}$. In the current experiment, transition dipole moments are much weaker and the excitation probability of $\approx 10\,\%$ yields a density of excited atoms roughly three orders of magnitude lower. Furthermore, hints for a three-body process in a rubidium vapor at ambient temperature have been reported [181] which however could be traced back to single-atom processes with overlapping Doppler effects. As a strength of the current method, signals are intrinsically Doppler-free as the evolution of coherences in the system is probed rather than spectral profiles of absorption or emission lines (chapter 2.3.3). This allows to extract subtle effects even in warm vapors. Further note, that collisions between particles are omitted in the applied scheme since probing times (i.e. pump-probe delays being $< 1\,\mathrm{ns}$)

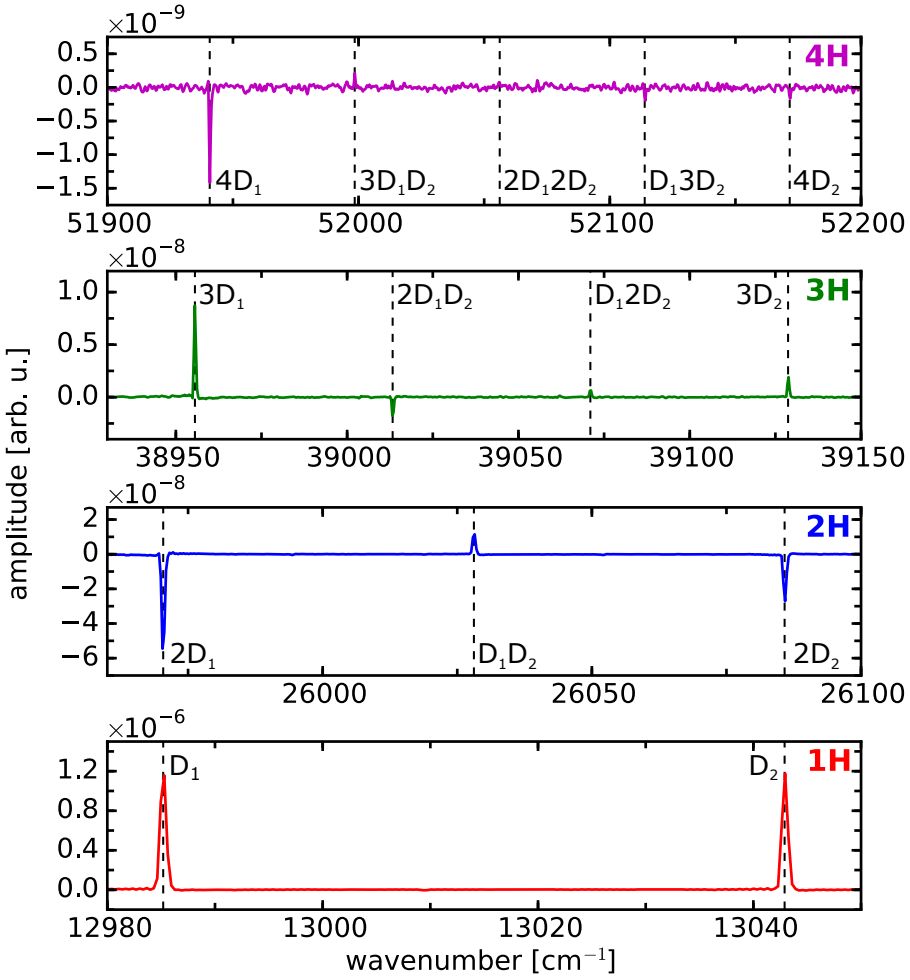

Figure 7.3: Fourier spectra (real part) of the potassium measurement of Fig. 7.2, revealing collective resonances in the potassium vapor. Vertical dashed lines indicate the predicted energies of the collective states. Their labels correspond to the notation introduced in Fig. 7.1.

are 5 orders of magnitude smaller than the average time between collisions ($T_{\mathrm{col}} \sim 100\,\mu\mathrm{s}$, cf. Tab. 7.1). This is in contrast to studies typically conducted in the ultracold community where probing times are usully much larger [167, 168].

However, in the investigated sample the dipole-dipole interaction strength of the D line excitations are estimated being $J/\hbar \approx 20\,\mathrm{kHz}$ (T=50°C) [Eq.(2.28)]. This rises doubts that the observed collective signals can be interpreted as an indicator for interactions among the atoms. In principle, any ensemble may be described in a many-body Hilbert space and collective energy states can be assigned independently of an interaction. As such, it might be argued that in the presented experiments the atoms are primarily coupled via the external light field (A more detailed discussion will be given below).

To access the full information encoded in the collective signals, the absorptive part (instead of the absolute value) of the complex-valued Fourier spectra ($Re\{\tilde{Z}\}$) are analyzed which is in contrast to the data shown in the preceding chapters. For this purpose, data

sets have been phase-calibrated as described in chapter 6.4. As an incisive feature, the resulting absorptive spectrum in Fig. 7.3 reveals distinct phase signatures for the individual many-body resonances. For simplification, the terms *diagonal* and *cross* peak are introduced in this context. Diagonal peaks refer to collective excitations where atoms are excited via identical transition whereas cross peaks refer to collective excitations of atoms excited via different transitions. E.g. in the 2H spectrum, two diagonal peaks appear for two atoms collectively excited via the D_1/D_2 transition (labeled $2D_1$,$2D_2$) and one cross peak appears for either of the atom excited via D_1 and the other via the D_2 transition (labeled D_1D_2). A phase shift of $(n-1)\pi$ of the diagonal peaks relative to the single-atom transition is observed (n is the number of atoms collectively excited). For cross peaks the phase behavior seems less consistent. In the 2H spectrum, the cross peak exhibits a π-phase shift relative to the diagonal peaks. In the 3H and 4H spectrum one cross peak is in-phase with the diagonal peaks while the other is out-of-phase. Note, that qualitatively this phase dependence is also revealed in the time-domain data Fig 7.2, where the 1H and 3H interferograms start with a positive amplitude whereas the 2H and 4H signals start with negative amplitudes, corresponding to a π-phase shift. A quantitative assignment and differentiation between diagonal and cross peaks is however only possible in the frequency-domain where in-phase and in-quadrature signal components are needed to reconstruct the signal phase. This shows the advantage of heterodyned (phase-synchronous) detection allowing to retrieve both signal components to construct the complex-valued Fourier transform.

The observed phase signatures show a dependence on the laser intensity. For weak fields, i.e. weak perturbation of the system, the peak phases are as shown in Fig. 7.3. For strong perturbation, i.e. focusing the laser beam with a lens, the detected resonances undergo a continuous phase rotation approaching as asymptotic value a phase shifted by π with respect to the initial phase. This behavior is attributed to a strong field effect and it appears that this laser intensity dependent phase behavior indicates saturation effects more sensitively than peak amplitudes do.

Besides the phase signatures, peak amplitudes also reveal a distinct characteristic. In Fig. 7.3, the ratio of D_1/D_2 peak amplitudes is $A_{D1}/A_{D2} = 0.99$ which does not correspond to the expected ratio of

$$\frac{A_{D1}}{A_{D2}} = \left(\frac{|\mu_{D1}|\tilde{E}(\omega_{D1})}{|\mu_{D2}|\tilde{E}(\omega_{D2})} \right)^2 = 0.87\,. \tag{7.1}$$

This discrepancy originates from the Fourier transform of a finite amount of data points. The resonances $4^2S_{1/2} \rightarrow 4^2P_{1/2,3/2}$ involve a substructure of closely spaced hyperfine transitions ($\Delta\nu \sim 20 - 450\,\mathrm{MHz}$). These cause slow beats in the time domain of which only fractions of a cycle are sampled in the pump-probe scan (0-40 ps). This results in a wrong estimate of the spectral amplitude of the frequency components. Larger amplitude discrepancies can be found for other species (Rb, Cs) for a variation of the pump-probe delay window, confirming this dependency. A precise description of the experiment requires thus the inclusion of hyperfine sublevels even in very simple spectra such as the single-atom response of gas-phase alkali atoms. Likewise, the amplitude ratio of collective diagonal and cross peaks strongly depend on the hyperfine sublevels as will

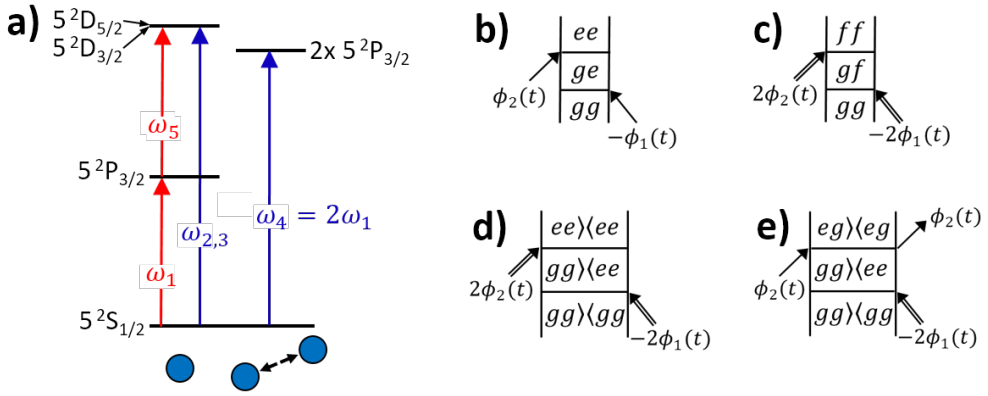

Figure 7.4: (a) Level diagram for atomic rubidium. Shown are the one- (ω_1) and two-photon transitions ($\omega_{2,3}$) in a single rubidium atom (left side) and the two-photon transition (ω_4) for collective excitation of two atoms (right side). The one-photon transition (ω_5) is too weak to be observed in the fluorescence measurements. (b), (c): One- and two-photon excitation pathways in a single atom. (d), (e): Pathways for a collective two-atom excitation. $|g\rangle$, $|e\rangle$ and $|f\rangle$ correspond to the atomic states $5^2S_{1/2}$, $5^2P_{3/2}$ and $5^2D_{5/2,3/2}$, respectively. Only examples for Feynman diagrams are given. A complete list involving different time-ordering of excitations is omitted.

be further discussed below.

7.2.2 Direct comparison of the one- and two-atom response

As a complication in the PM-MQC scheme, each laser pulse is involved in more than one field-matter interaction, i.e. the n'th harmonic Fourier spectrum shows processes induced by $2n$ field-matter interactions or n interactions with each laser pulse, respectively. This may complicate the interpretation of the experiment in contrast to nonlinear multidimensional spectroscopy experiments where each pulse interacts only once with the system. Thus, to exclude possible ambiguities investigations have been focused on atomic rubidium where a direct comparison of the single- and multiatom response in the same harmonic spectrum is possible. In this system, a two-photon excitation occurs in a single atom as well as in the combined two-atom system [Fig. 7.4(a)]. Both processes are of fourth order in the field-matter interaction [Fig. 7.4(c)-(e)] and appear in the second-harmonic demodulation.

To elucidate the origin of the observed phase signatures and amplitude ratios the potassium measurements have been thus complemented with experiments on rubidium. Fig. 7.5 shows a phase-resolved measurement for a laser wavelength of 12858 cm^{-1}. As discussed, the two-atom response ($2\times 5S_{1/2} \rightarrow 5P_{5/2}$) can be directly correlated to the single-atom response ($5S_{1/2} \rightarrow 5D_{5/2}$) in the second-harmonic demodulation channel, which reveals a clear phase difference between the two processes (2H spectrum). The latter is in phase with the one-photon single-atom response ($5S_{1/2} \rightarrow 5P_{3/2}$, 1H spectrum). However, the collective two-atom resonance is shifted by π, which is in accordance with the potassium results above. From this, it can be concluded, that the observed phase shift is a unique property of the many-body process. Another confirmation of this phase

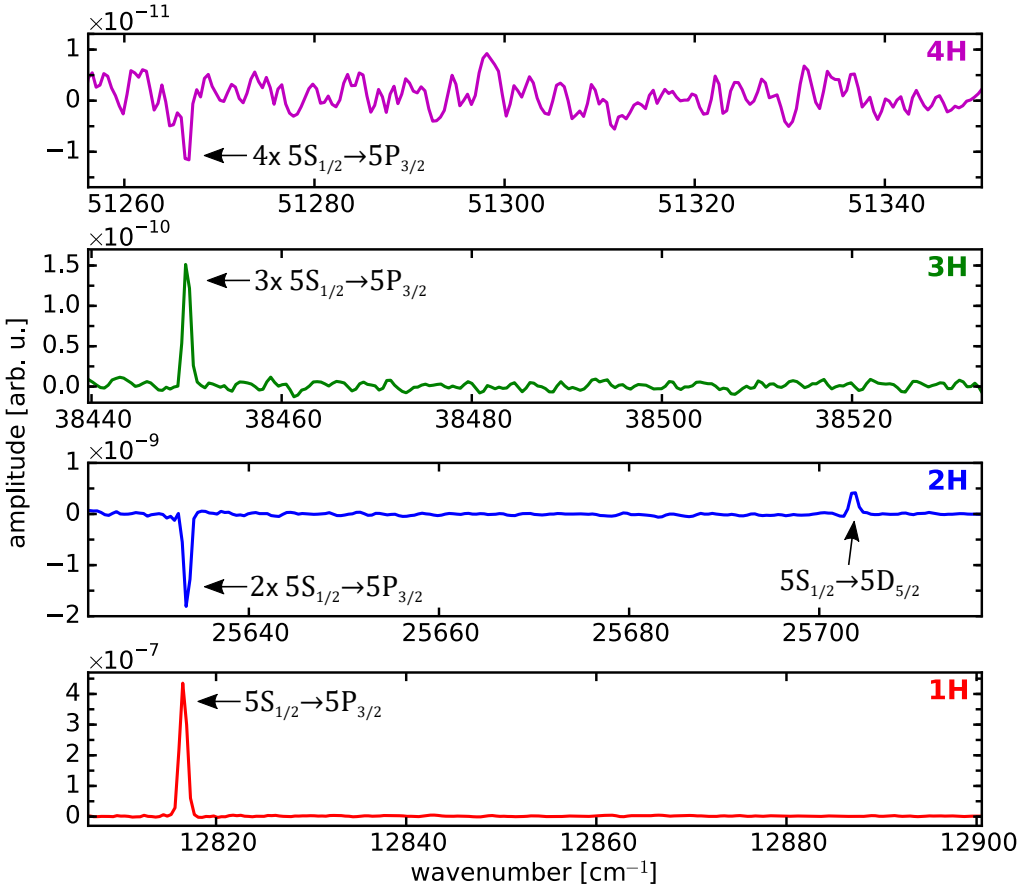

Figure 7.5: Low resolution spectrum of rubidium. The single-atom transitions $5S_{1/2} \rightarrow 5P_{3/2}$ and $5S_{1/2} \rightarrow 5D_{5/2}$ are detected in the 1H and 2H spectrum, respectively. The multi-atom response of the $5S_{1/2} \rightarrow 5P_{3/2}$ transition is detected in the 2H-4H spectra.

behavior is given in the successive chapter 8.4.

In addition, Fig. 7.6 shows collective resonances observed in the rubidium-doped helium droplet system. Instead of mass-resolved ion detection with a QMS, the integral photoion yield was acquired in the droplet experiment. Background contributions from molecular species (e.g. RbHe exciplexes) can be distinguished due to well separated resonances in the highly resolved Fourier spectra. Observations show, that their contributions to the integral ion spectrum are negligible weak and hidden in the noise floor. A focusing lens (f=150 mm) was implemented and the absolute value of the Fourier transform is plotted for time-domain traces of 40 ps length. The laser center wavenumber was set to 12930 cm^{-1}. Only first and second harmonic data have been recorded in this data run.

In contrast to the fluorescence measurements, an additional single-atom resonance ($5P_{3/2} \rightarrow 5D_{5/2}$) appears in the 1H spectrum. This is due to the increased photoionization cross section of the higher-lying 5D states, which results in an enhancement of pathways ending in a 5D population. Likewise, besides the $2 \times 5S_{1/2} \rightarrow 5P_{3/2}$ two-atom resonance already observed in the fluorescence measurements, a second collective reso-

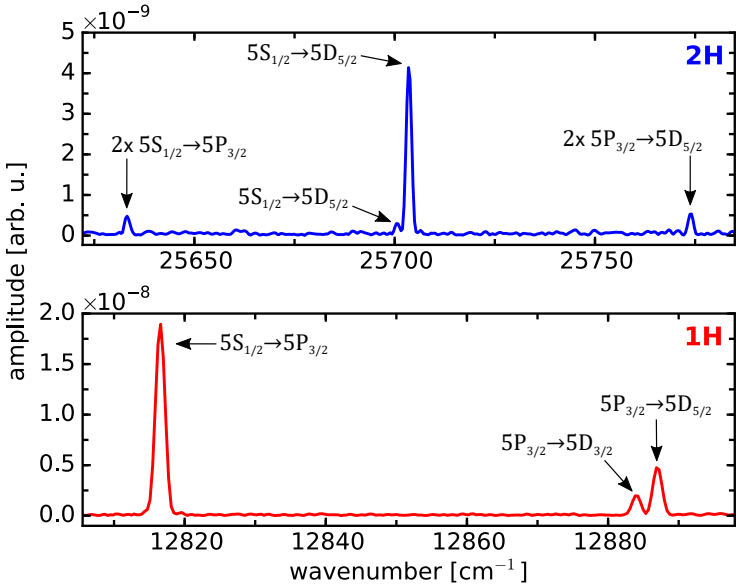

Figure 7.6: Collective resonances in the rubidium-doped helium droplet system obtained from integral photoion detection. Two-atom resonances for the $5S_{1/2} \rightarrow 5P_{3/2}$ and $5P_{3/2} \rightarrow 5D_{5/2}$ excitation are revealed. Here, the absolute values of the Fourier spectra are shown.

nance $2 \times 5P_{3/2} \rightarrow 5D_{5/2}$ is revealed in the 2H spectrum. These many-body resonances have been also observed in the droplet measurements discussed in the preceding chapter (Fig. 6.3, outside the shown wavenumber range) but have not been sown as the focus there was on the single-atom processes.

7.3 Hyperfine-resolved measurements

The high stability in the phase modulation setup allows for high precision measurements, realized by delay scans reaching out into nanosecond delay times. To this end, a cw auxiliary laser was superimposed with the optical path of the femtosecond pulses to generate a well-defined narrow-band reference signal at 12805.58 cm^{-1}. The femtosecond laser was set to 12858 $cm^{-1}$and the pump-probe delay was scanned for $\tau = 0 - 1$ ns in 80 fs increments. The same data set was used for the low resolution representation of the rubidium spectrum shown above, where only the first 35 ps of the pump-probe transient were evaluated. A direct comparison of the low- and high resolution representation of the data is thus possible.

Fig. 7.7 shows the high resolution spectrum for a pump-probe scan of 1 ns, yielding a nominal resolution of $\Delta\nu = 900$ MHz (FWHM). The peak substructure observable in the 1H spectrum corresponds to the hyperfine splitting of the ^{85}Rb and ^{87}Rb isotopes (Fig. 7.8). Since this substructure is dominated by the splitting in the $5S_{1/2}$ atomic ground state, the same pattern appears in the $5S_{1/2} \rightarrow 5D_{5/2}$ transition. In contrast, the collective two-atom response reveals a substructure consisting of peaks with different phases. This might be explained by the involvement of various diagonal and cross peaks

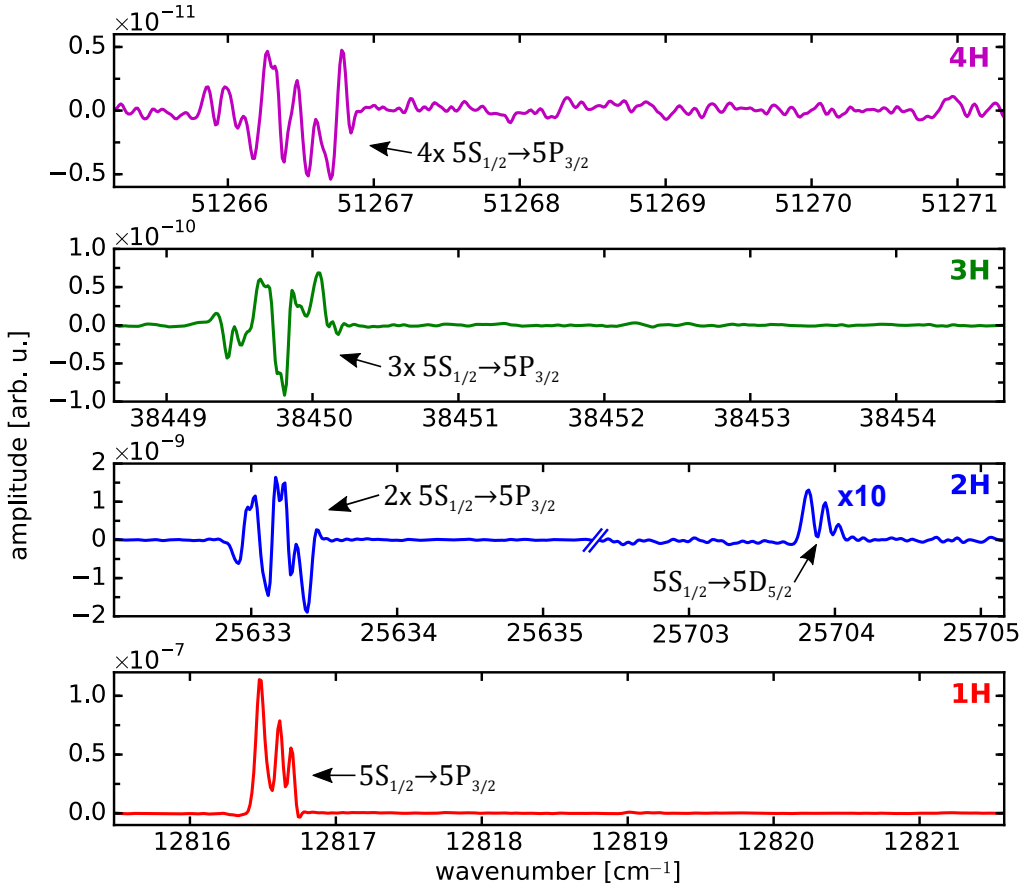

Figure 7.7: High resolution spectrum of rubidium. The $5S_{1/2} \rightarrow 5D_{5/2}$ has been scaled by a factor of 10.

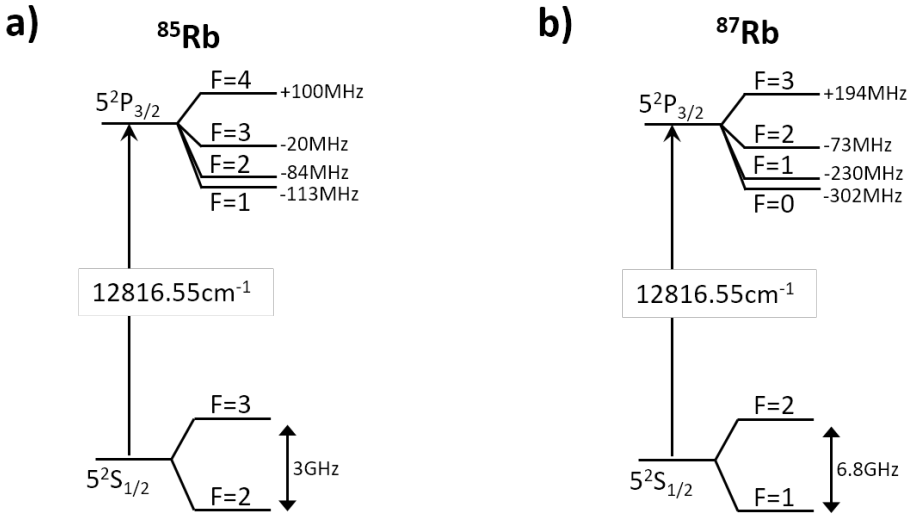

Figure 7.8: Hyperfine levels of the two rubidium isotopes, values taken from [182, 183].

of the hyperfine transitions exhibiting phases that differ by a π phase shift, as observed in the potassium measurement. The same characteristic is revealed in the higher-order collective resonances. Note that the four-atom resonance is now revealed much clearer than in the low resolution case (Fig. 7.5).

As the multi-atom responses comprise of many negative and positive cross and diagonal hyperfine peaks, it is not obvious that the average of this substructure yields the peak shapes observed in the low resolution spectrum of Fig. 7.5. Therefore, the high resolution spectrum was convoluted with a Gaussian distribution to match the resolution of the low resolution data in Fig. 7.5 (not shown). The averaged peaks match well with the low resolution representation of the spectrum, yielding a negative net peak for the two- and four-atom resonance and a positive net peak for the three-atom resonance. Hence, the two Fourier spectra (low/high resolution) are in accordance with each other and it is concluded, that the distinct phase signatures observed in the low resolution spectrum essentially originate from the collective hyperfine substructure components of the individual peaks.

Furthermore, a drastic increase of collective amplitudes is observed in the high resolution spectrum (Fig. 7.7) as compared to the low resolution case (Fig. 7.5). The increase in peak amplitudes becomes obvious when comparing the $2 \times 5S_{1/2} \rightarrow 5P_{3/2}$ with the $5S_{1/2} \rightarrow 5D_{5/2}$ transition. The latter feature has been scaled by a factor of 10 in the high resolution spectrum. Note, that the Fourier transform are scaled to the pump-probe delay window length, therefore this increase in amplitude may not be apparent from the y-scales of Fig. 7.5 and Fig. 7.7. Hence, the averaged net peaks in the low resolution spectrum exhibit smaller amplitudes than the underlying hyperfine components, due to the destructive interference of hyperfine cross and diagonal features. The real magnitude of the peaks can be thus only estimated in the resolved high resolution spectrum.

This insight may be transferred to the potassium measurement above (Fig. 7.3) where hyperfine sublevels have not been accessible. In analogy to the rubidium measurement, in the potassium spectrum diagonal peaks may be dominated by diagonal hyperfine contributions and therefore the net peaks exhibit negative amplitudes. Whereas the substructures of the cross peaks solely consist of hyperfine cross peaks, therefore the net peak purely reflects the phase of the underlying cross peak contributions yielding a positive net amplitude. In the 3H spectrum the cases might be distinguished where three atoms all undergo different hyperfine transitions (cross peak); two undergo the same transition (semi-cross peak); and all three undergo the same transition (diagonal peak). The interplay of these contributions may explain the different phases of $2D_1D_2$, D_12D_2 cross peaks. Analogous considerations may apply to the 4H spectrum. A quantitative simulation to confirm this hypothesis has been omitted for the reasons outlined below.

7.3.1 Qunatitative analysis

The discussed examples indicate a simple behavior for diagonal and cross peaks, i.e. both differ in phase by a factor of π and for each additional atom in the many-body resonance an additional global phase shift of π applies. To evidence this hypothesis, a coarse simulation was performed for the D_1 excitation in cesium. In contrast to the rubidium D_2 excitation, no isotope effect occurs in cesium (100% natural abundance of ^{133}Cs),

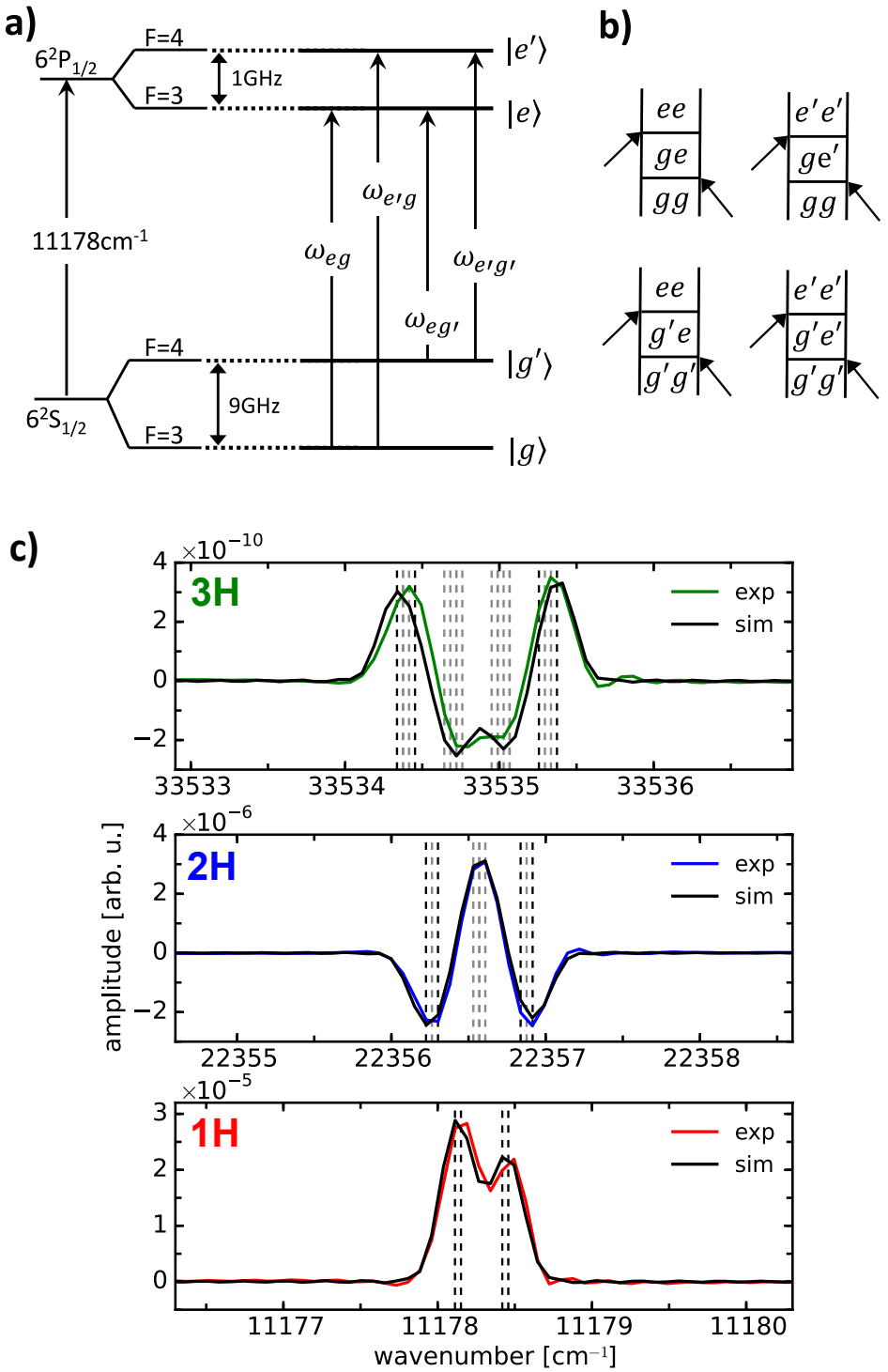

Figure 7.9: (a) Hyperfine energy levels of the D_1 transition of ^{133}Cs. (b) Respective single-atom excitation pathways. (c) Fourier spectra of experimental and simulated data of the D_1 excitation in cesium. Transition frequencies are indicated by black dashed lines (1H spectrum). In the 2H, 3H spectrum black/grey dashed lines indicate the diagonal/cross peaks, respectively. Values are taken from Ref. [184].

only four hyperfine transitions exist and hyperfine levels are well separated in ground and excited states [Fig. 7.9(a)]. Experimental data for a 0-125 ps scan are shown in Fig. 7.9(c). The 1H spectrum shows the D_1 resonance with the peak substructure revealing the four hyperfine transitions. The 2H and 3H spectrum show the respective two- and three-atom resonances involving various combinations of hyperfine diagonal and cross peaks. In the multiatom responses it becomes clear, that hyperfine diagonal peaks are shifted by π relative to hyperfine cross peaks giving rise to negative and positive features in the higher-order spectra. This confirms the above hypothesis that diagonal/cross peaks exhibit different spectral phases. Furthermore, diagonal peak amplitudes have larger amplitudes. Otherwise the larger number of cross peak contributions would dominate the spectra and no mixture of positive and negative features would appear in the 2H and 3H spectra. The interplay between out-of-phase diagonal and cross peak contributions also explains that the center of the net peaks deviate slightly from theoretical transition frequencies.

The data are simulated based on time-dependent perturbation theory (chapter 2.3). For fluorescence probing one obtains four pathways for the single-atom excitation [Fig. 7.9(b)]. In the experiment, the cesium vapor has a temperature of 330 K, hence the $6S_{1/2}$, F=3,4 ground states are equally populated and all four Liouville pathways contribute equally. For the transition dipole moments a weighting factor to account for the degenerate Zeeman states is applied [184]. A phenomenological decay is neglected as lifetimes in the system are much larger than the scanned time window. Likewise, δ-pulses are assumed as the pulse duration is much shorter than the dynamics in the system and the scanned time window. To calculate the two- and three-atom response, diagonal and cross peak contributions are phase shifted by multiplies of π as discussed above. A differentiation in the three-atom response for cross and semi-cross peaks as discussed above is omitted. Eventually, the amplitude ratio of diagonal and cross peak contributions is fitted[1], yielding a ratio of diagonal/cross peak amplitudes of 1.67 (two-atom response) and 0.45 (three-atom response).

The single- and two-atom response is well described by the simulation [Fig. 7.9(c)]. Also the spectral shift of the net peaks relative to the calculated transition frequencies is well reproduced in the 2H spectrum. Slightly less agreement is observed for the three-atom response, indicating that the applied model may not be sufficient to reproduce all details of the experiment.

In addition, a high resolution measurement (0-1 ns) was performed with a vapor cell containing the selected isotope ^{87}Rb. The time-domain interferograms and Fourier spectra are shown in Fig. 7.10 and Fig 7.11, respectively. In this case the vapor was kept at room temperature. Therefore, the $5S_{1/2} \rightarrow 5D_{5/2}$ resonances could not be observed. The data are simulated applying the same procedure as above. In this system, considerably more transitions exist for the many-body excitations: 21 combinations of hyperfine transitions occur for the two-atom excitation and 61 for the three-atom case. Best fitting diagonal/cross peak ratios are obtained for values of 1.03 and 4.0 for the two- and

[1] The absolute value of the Fourier transforms have been fitted to avoid phase ambiguities in the experimental data. For a fit of the real part of the spectrum, a deviation of 10-20% of the peak ratios has been obtained.

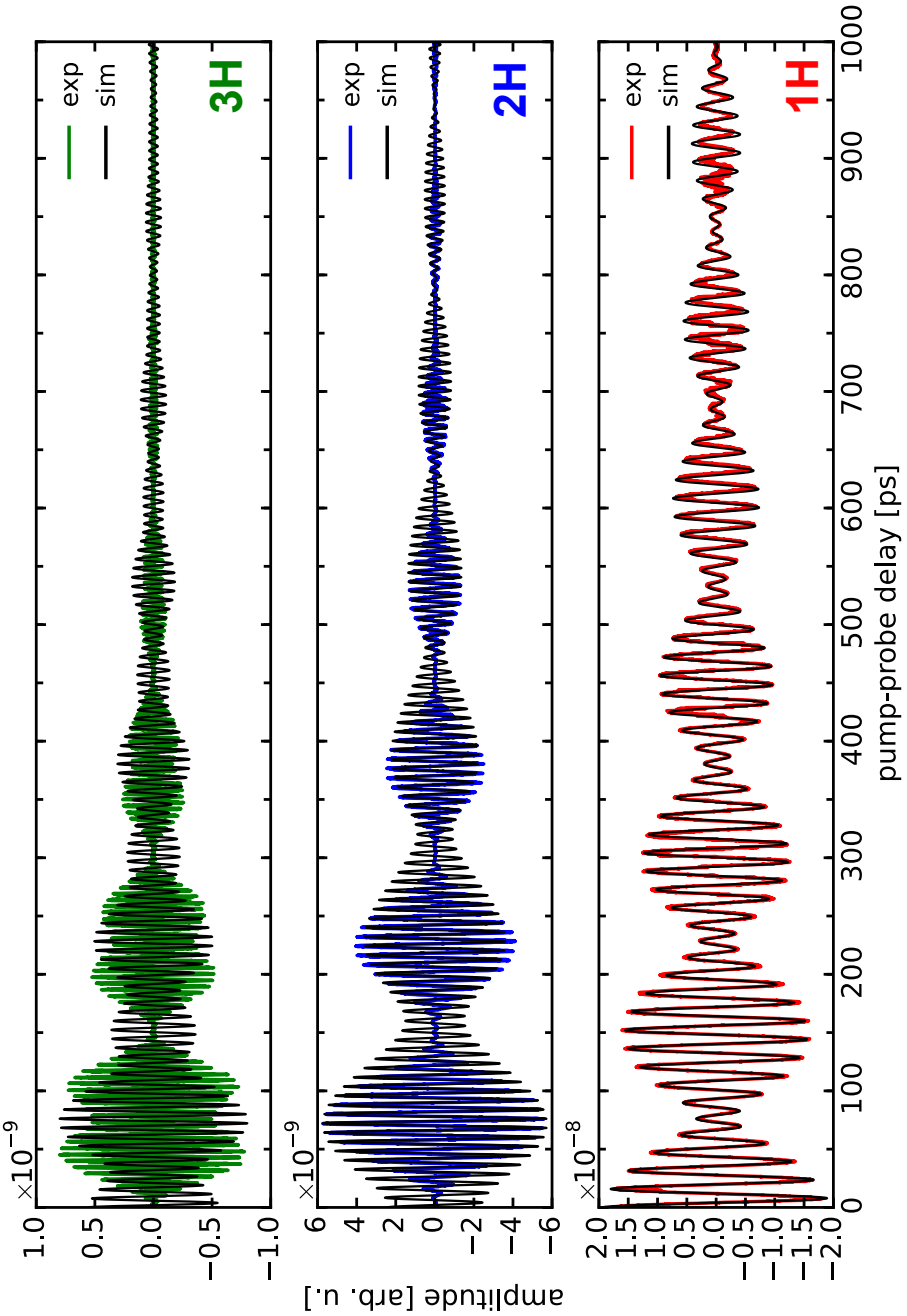

Figure 7.10: WP interference signals of ^{87}Rb in a vapor cell at room temperature. Single- to collective three-atom excitations are detected in the first harmonic to third harmonic demodulation channels (labeled 1H-3H). Experimental and simulated data are shown as labeled.

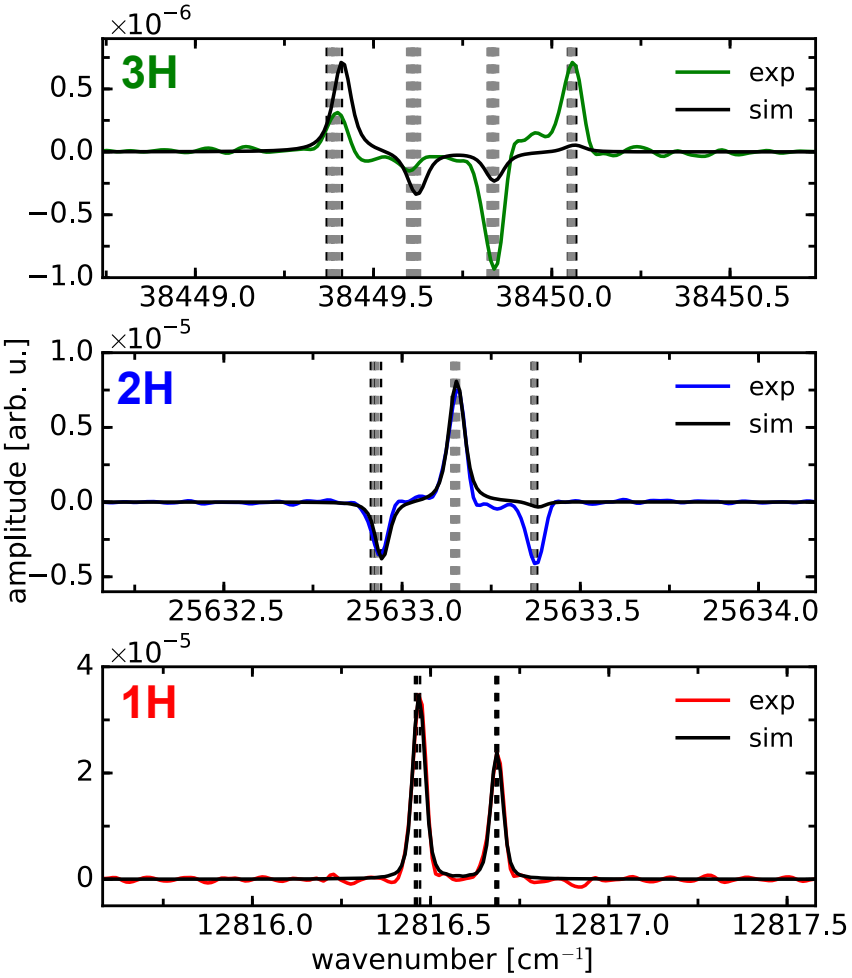

Figure 7.11: Fourier spectra of experimental and simulated data for D_2 excitation in ^{87}Rb. Transition frequencies are indicated by black dashed lines (1H spectrum). In the 2H, 3H spectrum black/grey dashed lines indicate the collective diagonal/cross peaks, respectively. Values are taken from Ref. [183].

three-atom response, respectively. A saturation of 15% is assumed for the F=2→F'=3 transition to match the single-atom signal. Since this transition has a factor of ≥ 3 larger oscillator strength than all other transitions, this assumption seems reasonable. Furthermore, a phenomenological decay factor of $\exp(-n\gamma\tau)$ is applied to fit the data, with $\gamma = 1.4\,\mathrm{GHz}$ and n being the number of collectively excited atoms. This decay rate is a factor of 10 larger than expected from the lifetime of the excited states. Inhomogeneous Doppler broadening is excluded since the applied probing scheme is insensitive to this effect and self-broadening is estimated being only $\sim 20\,\mathrm{kHz}$ (cf. Tab. 7.1). Moreover, the following experimental reasons were considered: (i) Laser beam divergence reducing the probe pulse intensity at 1 ns pump-probe delay. However, the divergence of the laser beam is certainly too small to result in a reduction of laser intensity of 75% on a travel range of the beam of 30 cm and therefore this case is excluded. (ii) Misalignment of the transla-

tion stage. This case is excluded as the delay stage alignment procedure with a position sensitive CCD sensor (chapter 3) would reveal a misalignment of such magnitude. (iii) The finite bandwidth of the auxiliary laser. This introduces a spectral broadening in the frequency-domain. Accordingly a corresponding signal decay in the time-domain would be expected. However, in the phase-synchronous lock-in detection, frequency fluctuations in the reference signal result in phase fluctuations in the demodulated time-domain signal and not in an decrease of the amplitude. As such, this case is excluded as well.

Fig. 7.10 and 7.11 show the time- and frequency-domain data together with the simulation. The single-atom data show excellent agreement with the simulation (1H), which indicates, that in general the WPI experiments can be well described and no hidden effects are present. In particular, the near-perfect agreement of the time-domain interfergram for delay times up to 1 ns indicates a well-controlled measurement process and experimental artifacts can be excluded. The good agreement with the applied decay factor strengthens the hypothesis that a decoherence effect is present in the system that results in a single exponential decay on a time scale of 714 ps. With the above considerations, this decay mechanism is attributed to an unassigned decoherence effect. Moreover, the good agreement in the 1H frequency spectrum shows that peak amplitudes can be well reproduced by the model. This confirms the above given hypothesis for the potassium measurements where peak amplitudes deviate from expected values due to insufficient long pump-probe delay scans.

Considering the higher-order signals (2H, 3H), however a clear deviation between simulation and experiment is found. While in the cesium example, reasonable agreement was achieved for the collective many-body response, this is not the case for the rubidium data. From this, it is concluded that the collective resonances generally involve a more complex behavior than assumed in the simulation.

In summary, from the presented high-resolution studies it can be concluded that the collective multiatom resonances exhibit a phase shift relative to the single-atom processes which depends on the number of atoms being collectively excited. This phase signature is connected to the fundamental hyperfine states in the system and different phase factors apply for collective diagonal and cross peaks. In addition, a quantitative analysis revealed, that the underlying mechanism is more involved than apparent from the low resolution data. A systematic that explains all details revealed by the high resolution measurements could not be found within the applied assumptions although the single-atom response was successfully modeled to a high degree of precision. The latter excludes experimental uncertainties and confirms the high quality of the experimental data. Furthermore, an exponential decay of the induced quantum coherences with a decoherence rate of $\gamma^{(n)} = n1.4\,\mathrm{GHz}$ of the n-atom response was determined.

7.4 Laser intensity and wavelength dependence

As the collective excitation of multiple atoms involves higher-order excitation pathways, these signals should exhibit a clear nonlinear dependence on the laser intensity. For this purpose, rubidium was investigated in the vapor cell for pump-probe scans of 0-30 ps. The laser was tuned to $12852\,\mathrm{cm}^{-1}$, focused with a f=200 mm lens and systematically

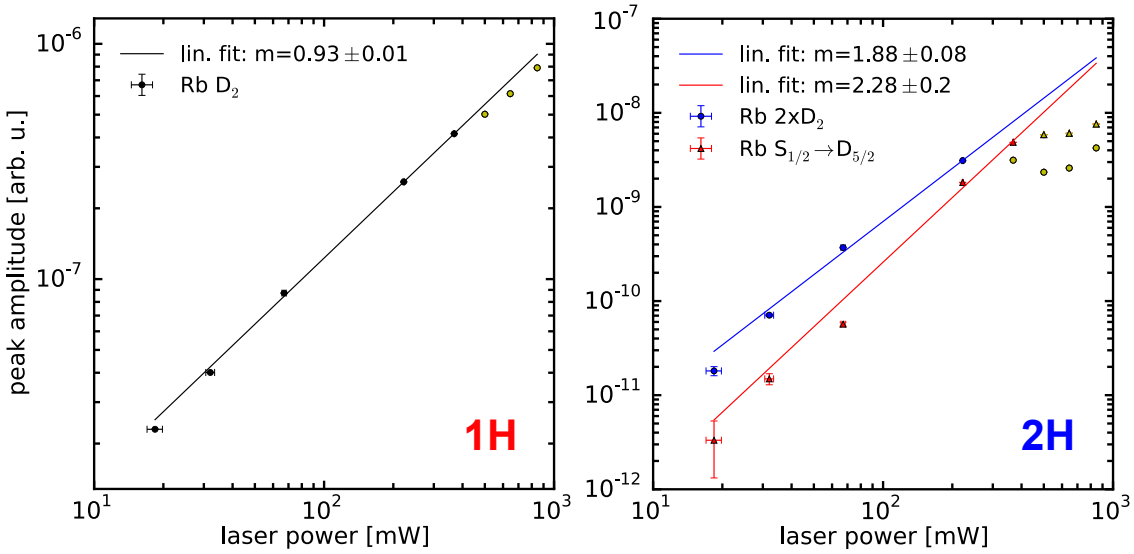

Figure 7.12: Excitation of a rubidium vapor as a function of the laser power. Shown are the peak amplitudes of the single-atom D_2 (1H) and $5S_{1/2} \rightarrow 5D_{5/2}$ (2H) excitations and the collective two-atom excitation $2\times D_2$ (2H). Linear fits reveal the power law in the log-log plots. Saturated points (yellow) are excluded from the fits.

attenuated with neutral density filters. Peak amplitudes as a function of the laser power are shown in Fig. 7.12. Here the one- and two-photon excitation in a single atom can be directly compared to the collective two-atom amplitude. A linear fit in a log-log scale readily reveals the power law for the individual signals. The one-photon excitation (D_2 excitation) shows a linear dependency and can be clearly distinguished from the two-photon excitations ($2\times D_2$, $5S_{1/2} \rightarrow 5D_{5/2}$) showing a quadratic behavior within the uncertainties. This quadratic behavior is further more confirmed when comparing this measurement with the fluorescence attenuation measurement discussed below (section 7.6). Errorbars are due to the uncertainties in the laser power measurements (horizontal) and peak fit errors (vertical). Furthermore, higher-order collective excitations of atoms show qualitatively a steeper slope, thus confirming a higher-order power dependence as expected. However, for these resonances not enough data points can be obtained to perform a reasonable fit: at low laser intensities, peak amplitudes are too small for evaluation since the higher-order processes require more laser intensity; and for high laser intensities, saturation compromises the measurement. Therefore a quantitative evaluation was omitted for these signals. In summary, the shown examples confirm a correct laser intensity dependence of single- and multiatom signals.

In addition, the dependence on the laser (center) wavelength is investigated in Fig. 7.13. Plotted are the peak amplitudes of the D_2, $2\times D_2$ and $5S_{1/2} \rightarrow 5D_{5/2}$ transitions. A focusing lens (f=150 mm) was implemented and a saturation of 30 % of the $5S_{1/2} \rightarrow 5D_{5/2}$ transition was assumed. Vertical error bars originate from the fit error of the spectral peaks for individual resonances. Horizontal errors come from the fit error on the laser spectra, acquired for each measurement.

The data are modeled by convoluting the narrow absorption lines with the broad laser

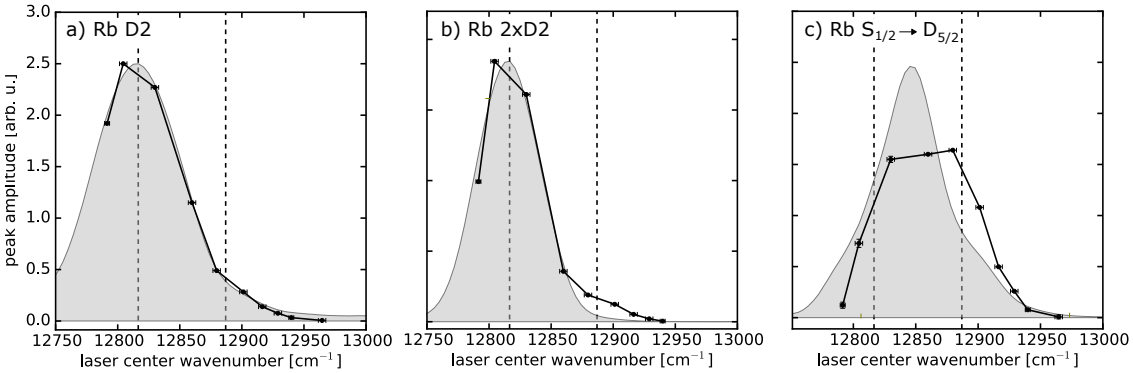

Figure 7.13: Laser wavelength dependence of individual resonances in rubidium. (a) and (c): Single-atom D_2 and $5S_{1/2} \rightarrow 5D_{5/2}$ excitation. (b) Two-atom $2\times D_2$ excitation. Theoretical curves are shown in grey. Vertical dashed lines mark the D_2 and $5P_{3/2} \rightarrow 5D_{5/2}$ transition frequencies.

spectrum. This is straight forward for the D_2 resonance. For the $2\times D_2$ resonance the line shape is squared. The $5S_{1/2} \rightarrow 5D_{5/2}$ resonance are modeled as a purely resonant two-photon transition, i.e. the absorption profiles of the $5S_{1/2} \rightarrow 5P_{3/2}$ and $5P_{3/2} \rightarrow 5D_{5/2}$ are multiplied. The latter transition is weighted with a factor of 0.1 to account for the conditional probability of the second transition as a function of the first transition. This factor corresponds to a 10% excitation probability as being typical for the employed pump-probe setup.

Good agreement between theoretical curves and the fluorescence data is found for the D_2 and $2\times D_2$ resonances which confirms the above shown laser power dependence for these processes. For the $5S_{1/2} \rightarrow 5D_{5/2}$ transition, a blue shift in the absorption profile towards the $5P_{3/2} \rightarrow 5D_{5/2}$ resonance is observed. Here, less but still acceptable agreement between experiment and theory is found. The discrepancy may be explained by the crude model which does not include non-resonant two-photon excitation pathways. The laser wavelength dependence has also been measured for the rubidium-doped droplet system, where all absorption profiles are shifted more towards the $5P_{3/2} \rightarrow 5D_{5/2}$ resonance since this transition is involved in the resonant enhanced two-photon ionization.

In summary, the laser intensity has been varied over almost two orders of magnitude and a linear and a quadratic behavior was quantitatively determined for the collective two-atom response. This was further confirmed with the comparison to single-atom one- and two-photon processes showing a linear and quadratic behavior, respectively. Higher-order collective resonances showed qualitatively the respective higher-order power law. Furthermore, the laser wavelength dependence was systematically investigated, which revealed the expected absorption profiles for all investigated resonances and additionally confirmed the quadratic laser intensity dependence of the two-atom resonance.

7.5 Density effects

In a series of measurements, the density dependence of the collective resonances was determined. To this end, the photoelectron yield of excited rubidium atoms in an effusive beam was detected. The effusive beam was generated with the doping oven in the HENDI apparatus. The density of the effusive beam was controlled with the oven temperature which allowed a density variation of two orders of magnitude. The target density at the position of the photoelectron detector was calculated as outlined in chapter 3.2. At high temperatures, however, this estimate for the beam density was inaccurate due to the heat inertia of the radiatively heated oven. Therefore, the density was calibrated with a linear fit of the $5S_{1/2} \rightarrow 5D_{5/2}$ signal. A linear density dependence is expected for this single-atom resonance and can be thus used for the calibration of the density axis. The laser wavelength was set to $12890\,\mathrm{cm}^{-1}$and pump-probe scans were performed for 0-15 ps. Fig. 7.14 shows the obtained data. Since excitation pathways ending in the 5D level are augmented by the larger photoionization cross section, a larger array of collective resonances can be observed in these measurements. A very clear linear density dependence is obtained (slope of 1 in log-log plot) for the single- and multiatom resonances. This is an important result which is discussed in detail further below. Furthermore, the collective two-atom signal can be compared to a recent 2D spectroscopy experiment where two-body resonances were investigated in a potassium vapor [34]. Here, a linear density dependence was found which is hence in accordance with the results of this PhD thesis.

The density dependence is also investigated for atoms prepared in the heated vapor cell (Fig. 7.15). Here, a higher variation of the density can be achieved, however, as can be seen, the measured curves are superimposed with a second effect: in the vapor cell, the fluorescence is mapped from a volume in the center of the cell (5 cm cell length) and the laser beam is thus significantly attenuated while propagating through the medium (Beer-Lambert law). This causes the attenuation of the signal with increasing vapor density. The $5S_{1/2} \rightarrow 5D_{5/2}$ is mostly unaffected by this attenuation effect, since much fewer light is absorbed at the two-photon resonance while propagating through the medium. The laser attenuation in the gas cell has been calculated to verify the observed signal decrease, which qualitatively confirmed the observed decay. However, to exclude additional effects besides the laser attenuation, quantitative modeling is necessary. This measurement shows thus the advantage of using an effusive beam of small diameter ($\varnothing = 6.5\,\mathrm{mm}$) to elucidate the density dependence.

Furthermore, the collective signal curves exhibit an outlier at $\rho = 4.5 \times 10^{11}\,\mathrm{cm}^{-3}$, which does not occur in the single-atom signals. Since the single- and multiatom signals are measured simultaneously in the same measurement, it is concluded, that these outlier points are not due to experimental fluctuations. Moreover, the collective signals undergo a phase transition (phase of spectral peaks rotates) around these outlier points. These effects have not been further investigated in this thesis.[2]

In conclusion, the dependence of the multiatom responses on the particle density was compared to the single-atom signals in an effusive beam over a density range of $\rho =$

[2] An investigation was not possible due to logistic reasons (lab refurbishment) followed by a break down of the laser.

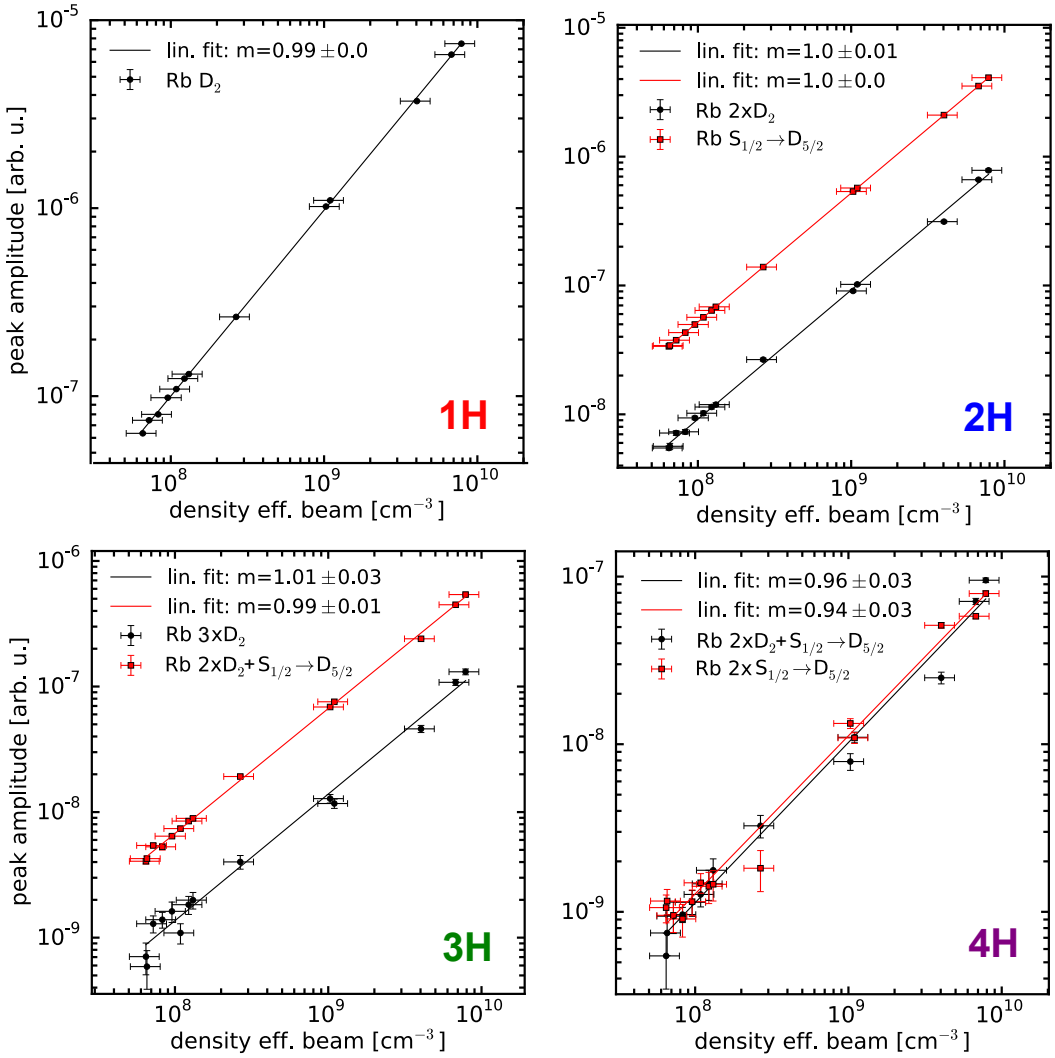

Figure 7.14: Density dependence of single- and multiatom resonances measured in an effusive rubidium atom beam. A linear fit in the log-log plot reveals the power law. The $5S_{1/2} \rightarrow 5D_{5/2}$ transition was used to calibrate the density axis and the fit result for this peak is therefore redundant.

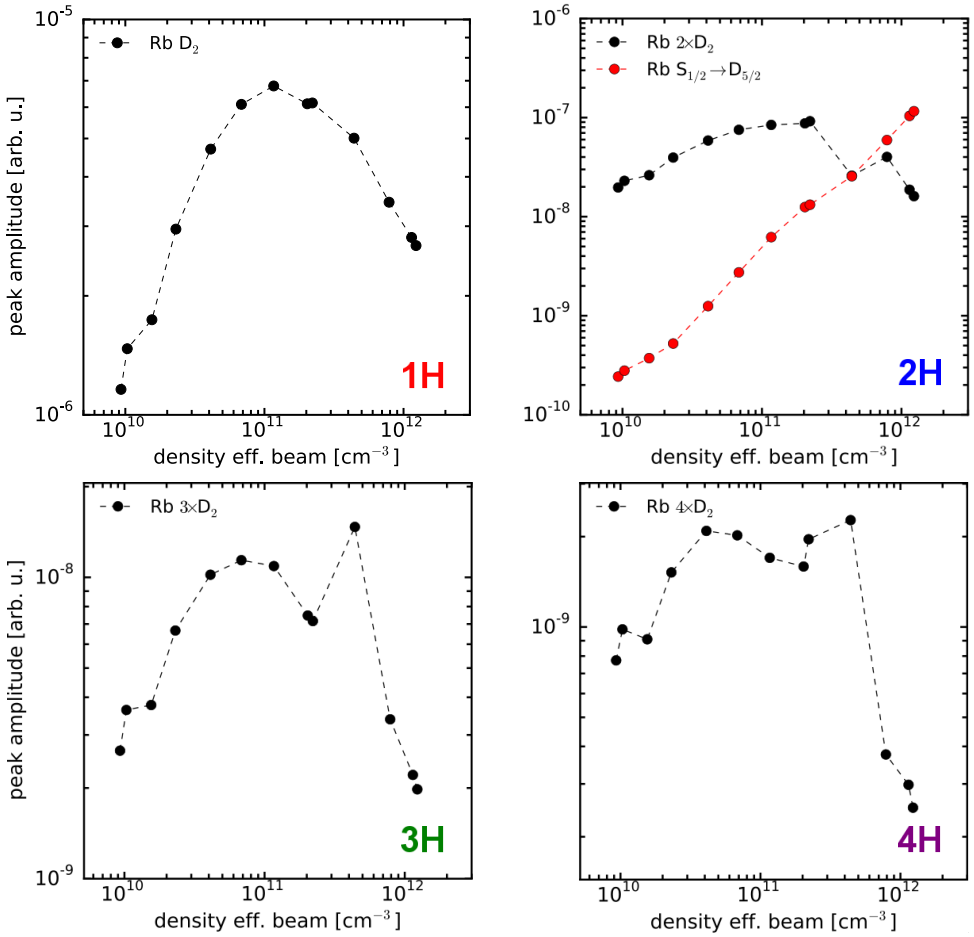

Figure 7.15: Density dependence of single- and multiatom resonances of rubidium measured in an a vapor cell of 5 cm length. With increasing vapor density the laser power is attenuated due to absorption along the beam path in the vapor cell. This reduces the signal amplitudes.

$6.5 \times 10^7 - 8 \times 10^9\,\mathrm{cm}^{-3}$. For all signals a clear linear dependence on the ensemble density was found. A characterization was also done in a vapor cell, however, there the density dependence was compromised by laser attenuation in the vapor leading to a significant decay of the signal.

7.6 Discussion of experimental ambiguities

To elucidate the origin of the observed collective resonances, the dependence on various experimental parameters (hyperfine substructure, laser power/wavelength, particle density) was systematically investigated as presented above. To complement these studies, a discussion about possible experimental ambiguities is given in the following. These involve rediffraction of photons in the acousto-optic bragg cells, nonlinearities in the detectors, saturation of detection electronics and pile-up effects due to the high repetition

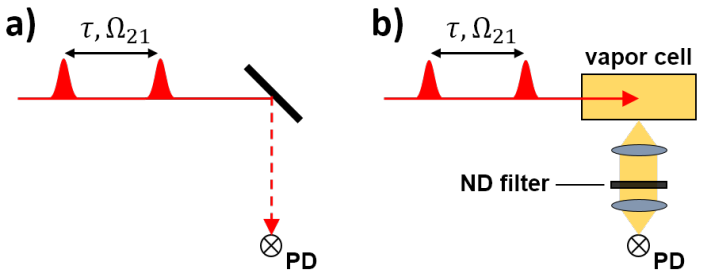

Figure 7.16: Measurement procedures to investigate harmonic impurities in the detection electronics. (a) The fluorescence photo detector (PD) is illuminated with the laser beam being deflected off a diffuse surface (peace of paper) which produced sufficient signal to cause saturation of detection electronics. (b) The fluorescence of the vapor cell was detected and the photon flux was systematically attenuated with neutral density (ND) filters.

rate of the laser.

Rediffraction in acousto-optical devices has been interpreted previously as a source for harmonic impurities [150, 185]. This effect was not observed in the conducted phase modulation experiments. Demodulated signals would appear far outside of the accessible spectral range of the laser and corresponding aliasing frequencies have been regularly checked.

Nonlinearities in the detection such as two-photon absorption was investigated in conjunction with the phase modulation approach [151]. This would produce spurious harmonic signals that might be misinterpreted as collective signals. Due to the low fluorescence intensities in the experiment this effect can be excluded. This is also confirmed by the saturation tests discussed below. Likewise, overlapping photoelectron/-ion pulses may produce higher harmonic signals. However, electron/ion count rates ($< 70\,\mathrm{kHz}$, cf. Fig. 3.7) are too low in the experiments to produce overlapping pulses (MHz bandwidth of detection electronics).

Saturation of detection electronics may result in higher harmonic signals being deceptively similar to the observed collective signals. To exclude saturation effects, two tests were conducted. First, saturation was simulated in the experimental setup by directly illuminating the fluorescence photo detector with the interfering pump-probe pulses [Fig. 7.16(a)] which causes saturation of the detection circuit. This was confirmed by a spectral analysis of the detector signal, revealing contributions at higher harmonics of the acoustic beat frequency damped by $\geq 50\,\mathrm{dB}$. Harmonic lock-in demodulation of these signals yield spurious features in the higher-harmonic Fourier spectra of the pump-probe transients. With systematic investigations, it was found, that these saturation signals are typically more than a factor of 100 smaller than the observed collective resonances. In addition, these spurious signals exhibit phase signatures which differ from the distinct phases of the collective signals. Since these observations were obtained for a very high photon flux incident on the fluorescence detector, signal amplitudes are expected to be even smaller in the actual WPI experiments where fluorescence yields are orders of magnitude smaller.

As a second test, a series of PM-MQC measurements were conducted as a function

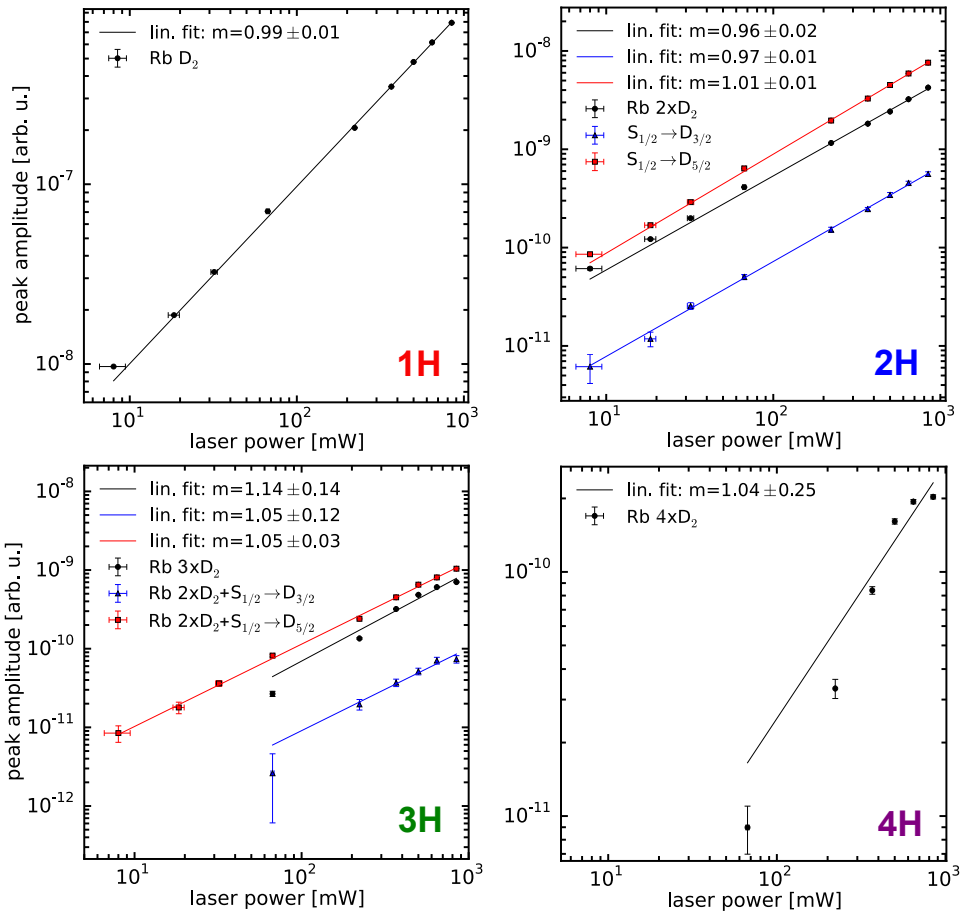

Figure 7.17: Signal dependence on the fluorescence flux on the photo detector. PM-MQC measurements with a rubidium vapor has been performed and the fluorescence yield has been attenuated with neutral density filters placed in front of the detector. A linear fit in the log-log plots reveals the power law. Note the different slope in the 2H signal as compared to laser power attenuation shown in Fig. 7.12.

of the photon flux on the fluorescence detector. To this end, the fluorescence yield was systematically attenuated with neutral density filters [Fig. 7.16(b)]. Pump-probe scans were performed for 0-30 ps and the laser was tuned to 12852 $cm^{-1}$to excite the rubidium atoms in the vapor cell. A lens (f=200 mm) was used to focus into the vapor cell to obtain a larger array of collective signals. Fig. 7.17 shows a clear linear dependence for all single- and multiatom resonances. Note the difference to the laser power dependence shown in Fig. 7.12. This linear behavior excludes saturation in the photo detector as well as any subsequent electronic parts.

Other arguments that exclude saturation effects are the anomalous amplitude behavior observed for the collective signals. As discussed above, collective cross and diagonal peaks exhibit different amplitudes which is in contradiction to saturation processes. E.g. in the potassium measurement (Fig. 7.3) the cross peak of the two-atom response should in case of saturation have an amplitude equal to the geometric mean of the two diagonal peaks,

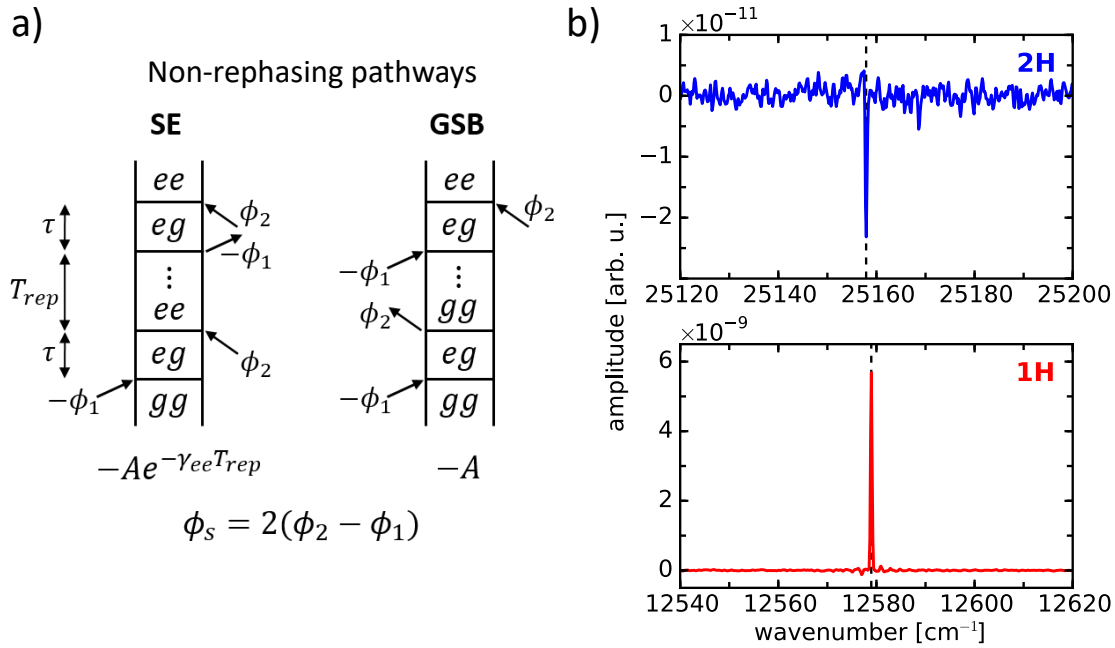

Figure 7.18: (a) Non-rephasing stimulated emission (SE) and ground state bleaching (GSB) pathways induced by two consecutive pump-probe pulse pairs. $|g\rangle$, $|e\rangle$ denote the ground and excited electronic state of the system. Both pathways yield a phase modulation of $\phi(t) = 2\Omega_{21}t$ and are thus detected in the second harmonic demodulation. (b) D_1 line excitation in a rubidium vapor. The PM-MQC measurement was performed with a low repetition rate laser system ($1/T_{\mathrm{rep}} = 5\,\mathrm{kHz}$).

which is not the case.

Harmonic impurities in the reference signal used for the lock-in demodulation may occur. For harmonic lock-in demodulation, a specific harmonic of the reference signal is generated in the lock-in amplifier electronics. If the settling time in-between pump-probe delay steps is too short, portions of the fundamental frequency component are not completely removed after the harmonic generation, which leads to spurious signals in the lock-in demodulation process. This effect is attributed to a filter in the lock-in electronics which requires a certain settling time to efficiently damp the fundamental frequency components in the reference signal. The resulting spurious demodulated signals appear at frequencies $\omega' = \omega_{1\mathrm{phot}} - n\omega_{\mathrm{M}}$ in the n'th harmonic Fourier spectra, where $\omega_{1\mathrm{phot}}$ denotes a one-photon excitation normally detected in the first-harmonic spectrum. Hence, one-photon signals can leak into higher harmonic spectra (therefore termed *leak* peaks in this work). For sufficiently long waiting times, these leak signals vanish and are therefore usually of no concern.

Multiple pump-probe pulse pairs may interact with a single atom and produce higher harmonic signals [152]. Pathways that involve multiple laser cycles would be likely in the experiments since the lifetime of atoms ($T \sim 25\,\mathrm{ns}$) is a factor of two greater than the laser repetition time ($T_{\mathrm{rep}} = 12.5\,\mathrm{ns}$). Exemplary, the case of two consecutive pump-probe pulse pairs interacting with a single atom is considered. This case can be compared

with a four-pulse 2D spectroscopy experiment, leading to stimulated emission (SE) and ground state bleaching (GSB) pathways [28]. In the 2D spectroscopy experiment, rephasing and non-rephasing signals are relevant and detected separately. In contrast, in the four-pulse PM-WPI experiment, rephasing pathways yield only a constant demodulated signal and are therefore not considered. The remaining non-rephasing pathways are shown in Fig. 7.18(a).

Both pathways comprise of two consecutive pump-probe interactions separated by the laser repetition time T_{rep} and end in an excited state population ρ_{ee}. In between the pulse pairs, the atom is in the excited state ρ_{ee} (SE pathway) or in the ground state ρ_{gg} (GSB pathway). This explains the additional damping term ($e^{-\gamma_{ee}T_{\mathrm{rep}}}$) in the SE pathway which arises from the decay of the excited state population during the time interval T_{rep}. Furthermore, the pathway amplitudes are negative with respect to the single pump-probe signal [Eq. (2.24)]. This phase shift of π (minus sign) arises from the Raman-like process induced by the first/second pulse pair in the GSB/SE pathways respectively. Moreover, the SE and GSB signals are proportional to $\cos(2\omega_{eg}\tau - 2\Omega_{21}t)$ as they essentially involve the squared contribution of the single pump-probe signal which is proportional to $\cos(\omega_{eg}\tau - \Omega_{21}t)$. As such, they yield a resonance at $2\omega_{eg}$ which is equal to the collective two-atom resonances observed in the experiments. Thus, these single-atom signals may be misinterpreted as collective contributions. However, respective cross peak pathways (not shown) contribute with the same phase factor to the second harmonic signal. This is in contrast to the shown measurements where the phase of collective cross and diagonal peaks differs by π . Thus, multiple laser cycle pathways cannot explain the observed phase behavior for collective cross and diagonal peaks. Analog multiple laser cycle pathways are obtained for respective higher-order processes that involve more than two consecutive pump-probe pulse pair interactions.

In the experiment, the multiple laser cycle contributions can be omitted using a low repetition rate laser ($T_{\mathrm{rep}} \gg 1/\gamma_{ee}$). After the first pump-probe interaction, the SE pathway yields an excited state population $\rho_{ee}(\tau) \propto \cos(\omega_{eg}\tau - \Omega_{21}t)e^{-\gamma_{ee}t}$ and the GSB pathway an complementary ground state population $\rho_{gg}(\tau) = 1 - \rho_{ee}(\tau)$. For $T_{\mathrm{rep}} \gg 1/\gamma_{ee}$, all atoms are relaxed to the ground state and SE as well as GSB pathways become irrelevant. Therefore, measurements have been performed with a laser repetition rate of $T_{\mathrm{rep}} = 200\,\mu\mathrm{s}$.[3] Fig. 7.18(b) shows an example for the D_1 excitation of rubidium in the vapor cell. In this particular example, the phase calibration is performed relative to a pronounced leak peak appearing in the 2H spectrum (outside shown wavenumber range). A clear collective two-atom excitation is observed exhibiting a phase signature in accordance with measurements shown above. Recently, measurements have been also preformed with a new laser system ($T_{\mathrm{rep}} = 5\,\mu\mathrm{s}$) which yielded a better signal quality and confirmed the measurement shown in Fig. 7.18(b). With this laser system collective signals were also observed for the rubidium D_2 and the potassium D_1, D_2 lines. This evidences the existence of a collective signal independent of the laser repetition rate. Yet, it is not excluded that in the measurements performed with the high repetition rate laser, signals from multiple laser cycles superimpose with the observed collective signals.

[3] A separate laser system was implemented for this purpose.

Dipole interaction ($2J/\hbar$)	190 kHz
Doppler broadening ($\Delta\omega_{\mathrm{FWHM}}$)	3.4 GHz
Self-broadening ($\Delta\omega_{\mathrm{FWHM}}$)	16 kHz
Natural linewidth ($\Delta\omega_{\mathrm{FWHM}}$)	38 MHz
Exp. resolution ($\Delta\omega_{\mathrm{FWHM}}$)	1 GHz

Table 7.1: Comparison of the dipole interaction with typical broadening mechanisms in a vapor. Values have been calculated for the rubidium D_2 transition, a vapor temperature of $T = 50°\mathrm{C}$ (corresponds to $\rho = 1.4 \times 10^{11}\,\mathrm{cm}^{-3}$), and a pump-probe scan of 0-1 ns. The self-broadening was estimated from the rubidium D_1 line, value taken from Ref. [186].

7.7 Comparison with theory and interpreation of results

Eventually, an interpretation of the experimental results is sought by comparing them to different theories.

In the investigated systems, transition dipole-dipole interactions are very small. Tab. 7.1 compares the dipole interaction J with other effects in the experiment. As can be seen, typical broadening mechanisms are much greater than the multiatom interaction. In this regard, the PM-MQC detection scheme provides a very sensitive method to unravel these subtle effects even in warm gases. Yet, the very small interaction strength suggests that the atomic ensembles should be treated as non-interacting particles. In this case, the appearance of collective signals may be explained by a coupling induced with the intense external light fields. However, it has been theoretically proven that in a non-interacting ensemble a collective absorption can only be induced with entangeled photons while with classical light collective excitation pathways generally cancel [67].

This argument has been exploited in 2D spectroscopy studies. Exemplary, a model system consisting of two coupled two-level systems is considered (cf. chapter 2.4) which gives rise to an excitonic four-level system [Fig. 7.19(a)]. Phase-matching is used to isolate the two collective excitation pathways shown in Fig. 7.19(b) (and analogous pathways where $|e\rangle$ and $|e'\rangle$ are permuted, which are not shown for simplicity). These pathways yield the same amplitude with a phase shift of π and therefore a signal is only measured if interactions among the atoms break the symmetry between the otherwise destructively interfering pathways; thus providing a sensitive probe for even very weak interactions as present in dilute vapors [34, 66, 180]. A similar argument applies for the performed PM-MQC measurements. This case has been analyzed in detail in cooperation with the group of A. Eisfeld from the Max-Planck-Institute for the Physics of Complex Systems, Dresden. These results are briefly discussed in the following. For details it is referred to Ref. [B4].

In the theoretical study, an atomic gas with nearest-neighbor dipole-dipole interaction of variable strength is considered and the collective two-atom response was calculated. In this case, the two pathways in Fig. 7.19(b) essentially split into three equivalent pathways shown in (c). One pathway ends in a f-population which corresponds to two excited atoms as opposed to the pathways ending in a e-population corresponding to one excited atom. Therefore, the first pathway exhibits a factor of two in the amplitude and in analogy to the argument above the net signal cancels if the degeneracy in the system is not lifted by an

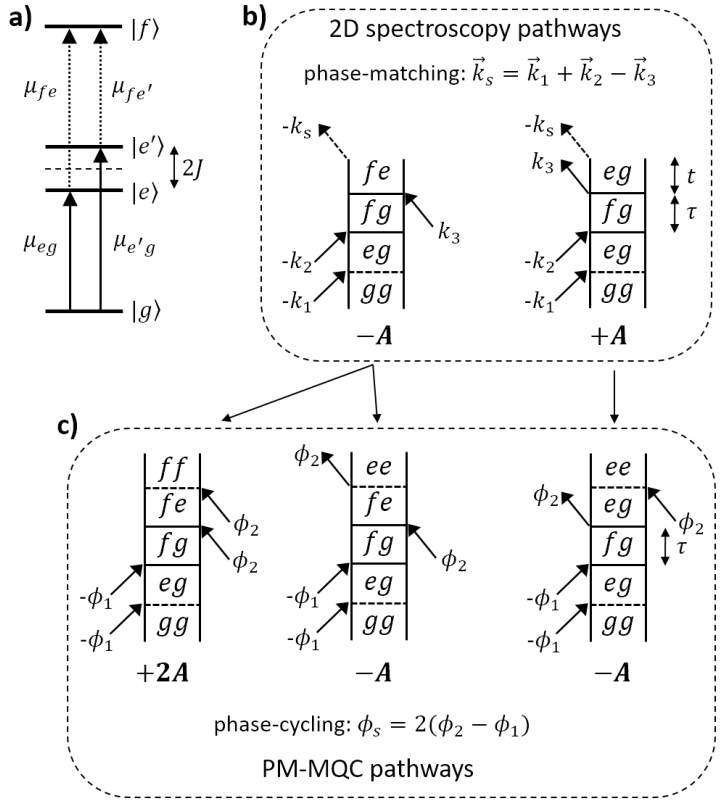

Figure 7.19: (a) Level diagram for two coupled two-level systems. (b) and (c): Corresponding DQC pathways as probed in 2D spectroscopy and PM-MQC experiments, respectively. Interactions occurring at the same time are separated by horizontal dashed lines. Amplitudes of the individual pathways are indicated underneath.

interaction. As such, the experimentally observed collective signals would uniquely imply the existence of weak dipole-dipole interactions in the system. This important result was confirmed by semi-numerical simulations including finite pulse effects. The latter effect has been recently identified as a source of artifacts in DQC signals [187], which indicates the importance of including finite pulse widths in the simulations of the experiment. In addition, the experimental procedure involving the phase modulation and signal isolation with harmonic lock-in detection was included in the simulation to realistically reproduce the measurement procedure.

The simulation result shows a linear dependency of the two-atom signal on the dipole interaction strength J. For $J = 0$ vanishes the collective signal which implies that the PM-MQC measurement provides a sensitive probe for an interaction in the system. A quadratic dependence of the two-atom response on the laser power is found, which is in accordance with the experimental observation (Fig. 7.12). Furthermore, the two-atom signal scales linearly with the ensemble density. This can be understood as follows: In the N atom ensemble, the peak value of the nearest-neighbor distribution $\bar{r}$ scales with the atomic density ρ as $\bar{r} \propto 1/\rho^{1/3}$. With the the dipole-dipole interaction J scaling as $J \propto 1/\bar{r}^3$, it hence follows $J \propto \rho$. Thus, the linear dependence on the dipole interaction strength implies a linear dependence on the ensemble density, which is in accordance with the experimental results (Fig. 7.14). So far, only the collective excitation of two-atoms has been simulated and information about the laser power and density dependence of the

higher-order ($n > 2$) collective signals has not been retrieved, yet.

In general, the simulation results have shown, that due to the long-range nature of the dipole-dipole interaction collective signals can occur even in highly dilute atomic vapors. The main features of the collective two-atom excitation observed in the experiments (diagonal and cross peaks) as well as laser power and density dependencies have been reproduced. Furthermore, a mechanism that can in principle explain the experimentally observed phase signatures has been proposed in the theoretical study. Yet, the simulation results yield significantly lower signal strengths than obtained in the experiment. Realistic parameters were used in the simulations and the observed discrepancy cannot be explained by experimental uncertainties. However, an extensive theoretical description of atomic vapors remains challenging due to the statistical nature of these ensembles involving relatively broad distributions of interatomic distances, relative orientation of dipole moments and kinetic energies of the constituents. The discrepancy may be thus explained by the crude approximations in the theoretical model. In particular, the inclusion of interactions beyond the nearest-neighbor approximation may improve the agreement as was the case in similar gas-phase studies [35, 179]. In addition, the experimentally observed decoherence of the WP signals with a time constant of 714 ps (Fig. 7.10) may indicate, that the interaction in the atomic system is actually stronger than assumed in the model which would be another explanation for the obtained discrepancy.

Having considered the dipole-dipole interaction as a possible mechanism for the occurrence of multiatom resonances in the studied systems, it will be now discussed whether alternative mechanisms can explain the observed signals for the assumption of non-interacting particles. In principle, collective excitation in non-interacting ensembles should not exist as generally argued in Ref. [67]. However, the observed resonances could originate from the response of single atoms. This might be caused by experimental artifacts (e.g. saturation of detectors and electronic signals) as discussed and vastly excluded above. An exception occurs for the interaction of multiple laser cycles interacting with a single atom. In this case, signals can be produced that exhibit the collective frequencies. The laser intensity and density dependence of this effect is in accordance with the experimental results, making this a likely explanation for the observed signals. However, the experimentally revealed distinct phase signatures of collective cross and diagonal peaks cannot be explained with this theory. Moreover, the multiatom resonances are also detected for low laser repetition rates, which excludes the contribution of multiple laser cycle pathways.

Furthermore, it has been argued, that the higher-order signals may arise from the single-atom response as an intrinsic effect in the particular detection method that is applied [188]. This is based on the assumption that the applied lock-in demodulation reduces the experimental observable to an effective many-particle operator. As a consequence, the detected signals can be expressed as a function of the single-atom response which excludes the necessity of an interaction to observe the higher-order signals in the experiment. In this case, the higher-order signals scale with the laser intensity as measured in the experiment. However, this approach predicts a non-linear dependence of the higher-order signals on the ensemble density which contradicts with the experimentally observed density dependence. Furthermore, the experimentally observed phase signatures cannot be explained within this theory.

Another explanation may be given by Floquet theory [189]. This is however excluded since the experimentally applied fields are too weak to induce a significant effect. Furthermore, cascading and local field effects have been discussed [1, 13, 190], which however should not be relevant at the low particle densities in the present experiments. Eventually, contributions of dimer and trimer formation in warm gases have been discussed as well [181], but these contributions are negligible at ambient temperatures and could be clearly spectrally distinguished with the given experimental resolution.

In summary, the theoretical results based on dipole-dipole interaction are in accordance with the observed laser power and density dependence for the two-atom resonance. For a comparison of the higher-order collective resonances, the simulations have to be extended. Furthermore, the experimentally observed distinct phase signatures of individual peaks might be explained by the relative orientation of the transition dipole moments induced in the sample. On the contrary, the interaction of multiple laser cycles with a single atom results also in higher-order signals. This mechanism is in accordance with the experimentally determined laser power and density dependence for all higher-order signals. However, clearly no explanation can be found to explain the observed phase characteristic of collective diagonal and cross peaks. In addition, tests with lower laser repetition rates exclude this effect as the sole reason for the observed higher-order signatures. All others possible mechanisms are excluded as they are in less accordance with the experimental results. As such, the higher-order resonances are interpreted as a superposition of two signals: one originating from the long-range dipole-dipole interaction present in the system; the other originating from multiple laser cycles interacting with a single atom. While in the first case, the signals reflect the collective excitation of multiple atoms, in the latter case, the signals stem from the non-cooperative excitation of single atoms in the system. Thus, the observed higher-order resonances reflect a composition of the single- and collective multiatom response of the system.

7.8 Conclusion

By applying the PM-MQC detection method to dilute atomic systems, clear signatures of higher-order resonances were revealed. These resonances appear at the collective energies corresponding to multiple atoms simultaneously excited in the system. Results were obtained for different systems (atomic vapors and doped helium droplet beam), several alkali atom species (K, Rb, Cs), a variation of laser intensities as well as ensemble densities and for different laser repetition rates. In particular, it was found that the n'th-order resonances scale with the n'th power of the laser intensity. Furthermore, all signals exhibit a linear dependence on the ensemble density. As a striking characteristic, distinct phase signatures were observed for the higher-order diagonal and cross peaks, that differ by a phase of π. In this context, diagonal/cross peaks refer to multiple atoms excited via the same/different transitions. High resolution measurements ($\Delta\omega_{\mathrm{FWHM}} = 1\,\mathrm{GHz}$) revealed that this phase characteristic is connected to the fundamental hyperfine states in the system. Such phase signatures have not been observed before which shows the advantage of the phase sensitive detection scheme and the attainable high spectral resolution. As another novelty, collective three- and four-body excitation was revealed in thermalized

atomic gases, which were observed down to particle densities of $\rho \sim 10^8\,\mathrm{cm}^{-3}$and in the doped droplet beam system.

In the literature, it has been proven under general circumstances, that an interaction among the particles is necessary to induce collective multiatom excitations in a system [67]. As such, the obtained results are surprising since the mean interaction strength is particularly weak in the studied systems ($J/\hbar \approx 100\,\mathrm{Hz}$ at $\rho \sim 10^8\,\mathrm{cm}^{-3}$). In this context, different mechanisms were discussed that may produce the observed higher-order signals. These include experimental ambiguities as well as theories based on single-atom but also collective multiatom excitation. The experimental data exclude almost all proposed mechanisms, which leaves two processes as the most likely interpretation for the observed higher-order signals. One of these processes constitutes the interaction of multiple pump-probe pulse cycles with a single atom. This mechanism can explain most experimental observations (i.e. laser intensity and ensemble density dependence), but does not reproduce the observed phase signatures. Furthermore, tests involving lower laser repetition rates revealed that this mechanism is not the solely contribution to the higher-order signals. The second process represents the collective multiatom excitation of dipole-coupled atoms. A thorough simulation of the studied system and experimental procedure confirmed this as a probable mechanism. The main experimental features are reproduced (laser intensity and ensemble density dependence) and the revealed phase signatures of collective peaks might be explained within this theory. However, the simulation results predicted signal amplitudes that are orders of magnitude smaller than retrieved in the experiment. This discrepancy is attributed to the applied coarse model, which does not account for the complexity of the investigated gas-phase systems.

In summary, the observed signals are attributed to a superposition of two processes, that are the single-atom response arising from the interaction with multiple pump-probe pulse cycles, and the collective multiatom excitation due to dipole-dipole interaction.

8 Phase-modulated harmonic light spectroscopy

The results shown in the preceding chapter indicate that the combination of phase modulation with harmonic lock-in detection is a promising method to facilitate nonlinear spectroscopy in the deep UV to XUV spectral range. This is explored in the current chapter. The experimental work of this project was mostly carried out by a graduate student (Ulrich Bangert) supervised by the author of this PhD thesis. Simulations and data analysis has been performed by the author. Some content of this chapter is adapted from Ref. [B3] and complementary information can be also found in Ref. [153].

8.1 Background

Progress in spectroscopy has been always tremendously stimulated by the development of new coherent light sources, e.g. from the realization of the first operating laser [191], to the incorporation of coherent femtosecond pulses [1, 2, 46] and recently the extension to coherent light sources in the VUV to X-ray regime [192–196]. Likewise, engineering and applying ever new spectroscopic methods has greatly improved our understanding of matter [1, 4, 6, 7, 40, 186, 197]. Among these, in particular coherent time-domain methods in the optical regime, most prominently multidimensional spectroscopy, have in recent years emerged as particular powerful and versatile tools to study complex processes on ultrafast time scales [1, 4, 7]. With the recent development of XUV and X-ray laser sources, a transfer of these spectroscopic techniques to high photon energies may become feasible. This development would provide attosecond temporal resolution [41] and facilitate site/chemical-selectivity by addressing specific core resonances and/or exploiting their pronounced chemical shifts [40], thus manifesting a fundamentally improved spectroscopic toolkit with unprecedented temporal and spatial resolution. In particular, several application examples have been proposed by theorists [40, 198–201] and recently first experimental demonstrations towards all-XUV pump-probe studies have been conducted [42–45].

However, this advancement requires solving some major technical difficulties and a general experimental solution has not emerged, yet. While current XUV light sources are capable of providing spatial and temporal coherence and high photon flux [193, 202], generating XUV pulse sequences with sufficient phase stability remains a major challenge. Numerous phase stabilization methods have been developed to facilitate pump-probe and multidimensional spectroscopy in the IR, VIS and UV spectral range [26, 51–55, 203, 204]. Yet, with shorter wavelengths in the VUV to X-ray regime, much higher phase stability is required and the desirable transfer of established stabilization methods to the new

wavelength regime is challenging, mainly due to the unavailability of commercial optics necessary for the implementation.

Several methods aiming to solve this issue have been developed. Direct pulse manipulation in the XUV is achieved with wavefront division optics [42, 43, 205–207]. However, fundamentally limited by mechanical instabilities, this approach may not provide a general solution at extremely short wavelengths. For free electron lasers (FELs), manipulation of the electron pulse has been exploited, e.g. by shifting the phase of the electron bunches in a retardation unit. Recently, this lead to the first demonstration of coherent control with FEL light, confirming the ability to generate phase-locked pulses [45]. However, this technique seems intricate and less flexible in view of designing advanced multidimensional schemes. Another approach is based on the driving/seeding laser, transfering its coherent properties onto the XUV pulses as demonstrated for high harmonic generation (HHG) sources as well as for seeded FELs [208, 209]. By applying phase-locked pulse sequences in the driving laser, the generation of phase-stable XUV pulses with HHG sources [210–212] and seeded FELs [44] has been achieved. While pulse manipulation on the fundamental frequency is much easier than in the XUV and phase stability in the driving field can be achieved with very high precision, the stability might still be insufficient for upscaling to extremly short wavelengths. In addition, phase jitter inherent to the conversion process or amplified thereupon, may compromize the phase stability of the XUV pulses.

As an interesting aspect, the latter approach may facilitate an implementation of the phase modulation concept. This would reduce demands on phase stability by orders of magnitude and introduce a phase-cycling scheme which allows background-free detection of nonlinear signals in collinear beam geometries. As such, this approach may represent a general solution to overcome current challenges of facilitating nonlinear time-domain spectroscopy in the XUV. In this view, the principle of phase-modulated harmonic light (PMHL) spectroscopy has been established which combines the phase modulation technique with harmonic light generation to perform spectroscopy with harmonics of the phase-modulated fundamental light. In the following this concept is demonstrated in a proof-of-principle study which combines the PM-MQC method with SHG to perform electronic WPI in the 400 nm wavelength range.

8.2 Experimental method

8.2.1 Optical setup and detection scheme

In the proposed concept of PMHL spectroscopy, harmonics of the fundamental light are generated subsequent to the optical interferometer (Fig. 8.1). In the demonstrated example, a nonlinear crystal is used to produce second order harmonics, but in principle HHG and high-gain harmonic-generation (HGHG) processes may be incorporated instead, yielding much higher harmonics. Upon harmonic generation of the individual pulses, their phase is shifted to integer multiples $\phi_i(t) = n\Omega_i t$, with n being the number of the harmonic. This relationship has been experimentally confirmed for SHG in nonlinear crystals [149–151, 185], higher harmonics in HHG sources [208] and for the HGHG process in a seeded FEL [209]. Driving a one-photon transition $|g\rangle \rightarrow |n\rangle$ (inset of Fig. 8.1) with the n'th harmonic light will then yield a WPI signal modulated with $\phi_{21}(t) = n\Omega_{21}t$.

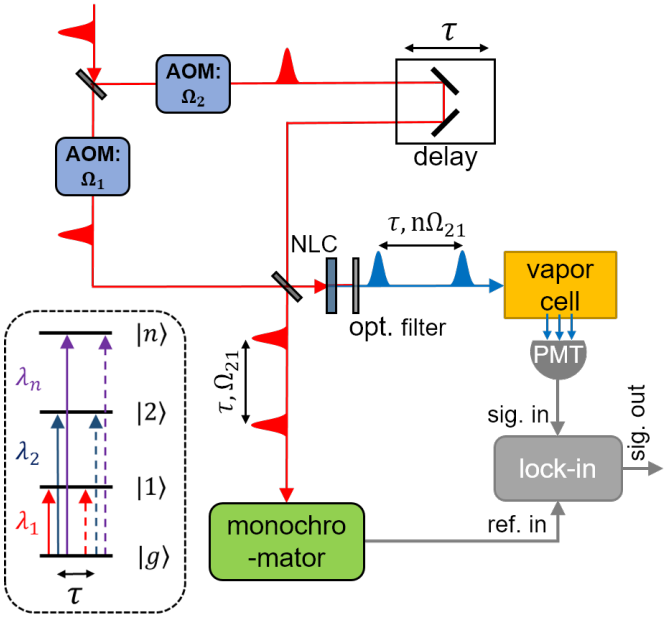

Figure 8.1: Schematic diagram of the optical setup for PMHL spectroscopy. The previous PM-WPI setup has been extended to UV wavelengths. A nonlinear crystal (NLC) followed by an optical filter is placed behind the interferometer to generate collinear second harmonic pulses that are phase modulated by the harmonic of the acoustic frequencies ($n\Omega_i$, i=1,2) applied at the AOMs. A monochromator is used to construct the reference signal from the fundamental laser pulses. Harmonic lock-in detection is performed to demodulate the fluorescence signal. The inset shows schematically simultaneous WP excitation with different harmonic wavelengths.

At the same time, a portion of the phase-modulated pulses is branched off before the HG process to generate the reference signal for lock-in demodulation in the monochromator, yielding a reference signal modulated at the fundamental acoustic beat frequency $\phi_{\mathrm{ref}}(t) = \Omega_{21}t$. In analogy to the previous PM-MQC scheme, the individual harmonic signal contributions can be extracted with harmonic lock-in demodulation. Hence, for a one-photon WP excitation with n'th harmonic light, the demodulated signal is

$$S_n(\tau) = A_n\beta\cos\left[(\omega_{ng} - n\omega_{\mathrm{M}})\tau\right] . \tag{8.1}$$

As this procedure is analogous to the PM-MQC scheme, all advantages discussed for that method also apply to the PMHL spectroscopy technique. In particular, phase fluctuations ($\delta\tau$) in the optical interferometer are traced with the fundamental pulses before the beam recombination and harmonic light generation occurs. This phase noise is transferred onto the harmonic light pulses in the harmonic generation process. The same harmonic transfer is performed in the reference signal, however not optically but electronically in the lock-in amplifier electronics. Performing this crucial step with in the digital lock-in amplifier electronics ensures low noise characteristics and small harmonic impurities. Residual noise in the demodulated signal then scales only with the down-shifted WP interference frequencies $\bar{\omega}_n\delta\tau$. Note, that on the contrary uncorrelated noise appearing in the signal or reference beam will be amplified linearly with the order of the harmonic. Experimental observations, however, have confirmed that this source of noise is negligible for harmonic demodulation up to fourth order.

As a second important property, phase-cycling is introduced in the harmonic beam line. By performing phase modulation on the fundamental pulses where standard acousto-optics are available, nonlinear signal contributions (e.g. MQC signals) can be selectively detected and background signals such as stray light are efficiently suppressed. This will

be of particular advantage for experiments with high photon energies in the VUV spectral range and beyond, where stray light and background photoions/-electrons typically pose severe challenges.

The apparatus employed for the experiments presented below is the same as used in the previous studies. In addition, to generate the SHG pulses, the laser beam is focused onto a betha barium borate crystal (2 mm thickness) with a f=40 mm lens. Afterwards, the beam is collimated (f=50 mm) and the fundamental light is blocked with two dielectric mirrors (Thorlabs E01-coating) and an optical short pass filter (Edmund Optics 84-712) yielding pulses around 400 nm and 0.2 nJ (pump), 2 nJ (probe) pulse energies. These enter the heated vapor cell (324 K) and the fluorescence is detected using a photo-multiplier tube (Hamamatsu H10721-20) combined with a commercial preamplifier. Fluorescence and reference signals are split and fed into four digital lock-in amplifiers. Corresponding to the fundamental acoustic beat frequency of $\Omega_{21} = 5$ kHz, higher harmonic contributions are modulated with 10, 15 and 20 kHz, respectively. According to the frequency characteristics of employed detection electronics, signal amplitudes and phases were corrected in the data analysis as discussed above.

8.2.2 Signal contributions for linear and nonlinear excitation

To study the effects of linear and nonlinear excitation, exemplary a model system is considered that supports one- and two-photon transitions [Fig. 8.2(a)] and corresponding SQC and DQC signal contributions will be briefly derived. In conjunction the effects of additional pulse contributions occurring for temporal overlap of fundamental pump and probe pulses [Fig. 8.2(b)] are investigated in detail.

In the experiment, the phase-modulated electric fields of the fundamental pump and probe pulses can be expressed as (chapter 2.3.1) :

$$E_1(t,t') = A_1 g(t-t',\,\Delta t)\cos\left[\omega_0(t-t')+\Omega_1 t'\right], \tag{8.2}$$

$$E_2(t,t',\tau) = A_2 g(t-t'-\tau,\,\Delta t)\cos\left[\omega_0(t-t'-\tau)+\Omega_2 t'\right]. \tag{8.3}$$

Here, $t' = t_0 + mT_{\mathrm{rep}}$ denotes the quasi-continuous time variable incrementing each laser cycle by T_{rep}. ω_0 denotes the frequency of the fundamental light, $A_i\,, i = 1, 2$ are the pulse amplitudes and $g(t,\Delta t) = e^{-4\ln 2(t/\Delta t)^2}$ describes the Gaussian pulse envelope function with Δt being its FWHM value.

The UV pulses result from the second order polarization induced in the nonlinear crystal:

$$P^{(2)}(t,t',\tau) \propto \left[E_1(t,t')+E_2(t,t',\tau)\right]^2 \tag{8.4}$$

$$= \text{const.} + E_{\mathrm{SHG1}} + E_{\mathrm{SHG2}} + E_{\mathrm{SFG}} + E_{\mathrm{DFG}}\,. \tag{8.5}$$

Constant and slowly varying contributions to the polarization due to optical rectification and difference frequency generation (E_{DFG}) will be omitted since these fields are not relevant for the experiment. The remaining contributions describe three UV pulses [Fig. 8.2(b)] which correspond to the SHG of individual pump and probe pulses, denoted

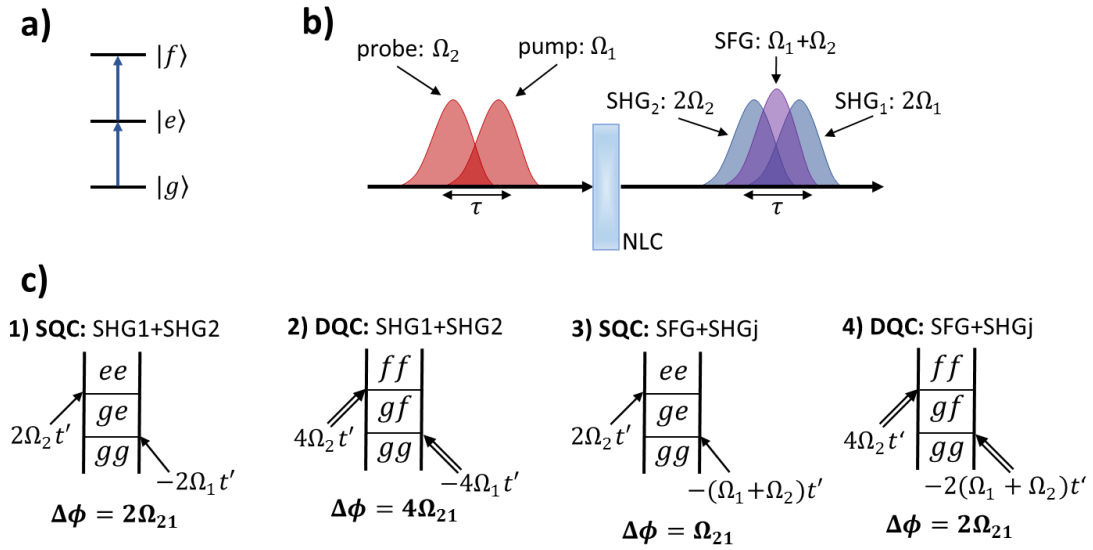

Figure 8.2: (a) Model three-level system with one- and two-photon transition. (b) Collinear pump-probe pulses induce SH pulses in a nonlinear crystal (NLC). SHG1 and SHG2 denote the SHG pulses of individual incident pump and probe pulses and SFG denotes the SFG pulse occurring during pump-probe overlap. (c) Double-sided Feynman diagrams for SQC and DQC pathways involving interactions with one SHG pump and probe pulse (1 and 2) and for interactions with the SFG and either of the SHG pulses (3 and 4). Reproduced from Ref. [B3].

E_{SHG1} and E_{SHG2}, respectively, as well as the sum frequency generation (SFG) of the incident pump and probe pulses, denoted E_{SFG}:

$$E_{\mathrm{SHG1}}(t,t') = \frac{A_1^2}{2} g(t-t', \frac{\Delta t}{\sqrt{2}}) \cos\left[2\omega_0(t-t') + 2\Omega_1 t'\right] , \tag{8.6}$$

$$E_{\mathrm{SHG2}}(t,t',\tau) = \frac{A_2^2}{2} g(t-t'-\tau, \frac{\Delta t}{\sqrt{2}}) \cos\left[2\omega_0(t-t'-\tau) + 2\Omega_2 t'\right] , \tag{8.7}$$

$$\begin{aligned} E_{\mathrm{SFG}}(t,t',\tau) &= A_1 A_2 g(\tau, \sqrt{2}\Delta t) g(t-t'-\frac{\tau}{2}, \frac{\Delta t}{\sqrt{2}}) \\ &\quad \times \cos\left[2\omega_0(t-t'-\frac{\tau}{2}) + (\Omega_1+\Omega_2)t'\right] . \end{aligned} \tag{8.8}$$

All three pulses have the same temporal envelope function. However, the SFG pulse, as it occurs only during temporal pump-probe overlap, exhibits an additional τ-dependent Gaussian amplitude function.

Exciting the three-level system with this pulse sequence gives rise to a number of signals. Due to the individual phase modulation of the incident pulses their contributions to the detected signal can be isolated with harmonic lock-in demodulation. Disregarding all diagrams which do not yield a modulation $\Delta\phi = n\Omega_{21}t'$, $n \in N$, four types of processes are identified as major contributions to the signal. Examples are given in Fig. 8.2(c): diagrams 1 and 2 show SQC and DQC pathways induced upon interactions with a SHG pump and probe pulse, whereas diagrams 3 and 4 show the same processes for interactions

with the SFG pulse and either of the two SHG pulses. Note that only representative examples of Feynman diagrams are shown. A complete set of diagrams including different time-ordering during pulse overlap is omitted. Furthermore, processes represented by diagrams 1 and 3 appear in the second harmonic (2H) lock-in demodulation ($\Delta\phi = 2\Omega_{21}t'$), diagram 2 in the fourth harmonic (4H) ($\Delta\phi = 4\Omega_{21}t'$) and diagram 3 in the first harmonic (1H) ($\Delta\phi = \Omega_{21}t'$). Hence, we get a mixing of SQC and DQC processes in the 2H demodulation whenever SFG pulses are involved.

From the Feynman diagrams, semi-quantitative expressions for the individual signal contributions are derived:

$$S_{\mathrm{1QSHG}} \propto \frac{|\mu_{eg}|^2}{\hbar^2}\tilde{E}^2(\omega_{eg})\cos\left(\omega_{eg}\tau - 2\Omega_{21}t'\right), \tag{8.9}$$

$$S_{\mathrm{2QSHG}} \propto \frac{|\mu_{eg}|^2|\mu_{fe}|^2}{\hbar^4}\tilde{E}^2(\omega_{eg})\tilde{E}^2(\omega_{fe})\cos\left(\omega_{fg}\tau - 4\Omega_{21}t'\right), \tag{8.10}$$

$$S_{\mathrm{1QSFG}} \propto \frac{|\mu_{eg}|^2}{\hbar^2}g\left(\tau, \sqrt{2}\Delta t\right)\tilde{E}^2(\omega_{eg})\cos\left(\omega_{eg}\tau/2 - \Omega_{21}t'\right), \tag{8.11}$$

$$S_{\mathrm{2QSFG}} \propto \frac{|\mu_{eg}|^2|\mu_{fe}|^2}{\hbar^4}g\left(\tau, \Delta t\right)\tilde{E}^2(\omega_{eg})\tilde{E}^2(\omega_{fe})\cos\left(\omega_{fg}\tau/2 - 2\Omega_{21}t'\right). \tag{8.12}$$

Here, a phenomenological decay has been neglected for simplicity. S_{1QSHG} and S_{2QSHG} describe the SQC/DQC signals from interactions with the SHG1 and SHG2 pulses, represented by diagrams 1 and 2, whereas S_{1QSFG} and S_{2QSFG} describe the SQC/DQC signals from interactions with the SFG and SHG1/SHG2 pulses, represented by diagrams 3 and 4. For simplicity we have assumed all pulse envelopes to be Gaussian, denoted $g(t, \Delta t)$, where Δt being the FWHM width of the fundamental pulses. $\tilde{E}(\omega)$ denotes the pulse spectrum. We neglected chirp and treated $|e\rangle$ as a resonant intermediate level enabling resonant two-photon excitations and μ_{ij} denote the transition dipole moments.

The behavior of these signals is intuitive. Eq. (8.9) and (8.10) represent ordinary phase-modulated SQC and DQC signals, however modulated at twice the phase modulation frequency due to the SHG process prior to the light-matter interaction. Eqs. 8.11 and 8.12 describe essentially the same SQC and DQC pathways, however involving interactions with a SFG pulse. Therefore, these signals occur only for a short delay window as apparent from the τ-dependent envelope functions inherited by the SFG pulse. Further, these signals exhibit a $\tau/2$-delay dependence, which is self-evident considering that the delay between SFG and SHG pulses increases only by $\Delta\tau/2$ for each $\Delta\tau$ increment [Fig. 8.2(b)]. As a consequence, these signals appear at half the downshifted WP oscillation frequencies.

These expressions are used for a crude simulation of the experimental data. In addition, stray light effects are included. The majority of stray light is efficiently eliminated upon lock-in demodulation since it does not exhibit a well-defined modulation frequency. However, during temporal pump-probe overlap, a portion of stray light reflects the pump-probe pulse interference, i.e. the interferometric quadratic autocorrelation, denoted S_{ACquad}. It is

$$S_{\mathrm{ACquad}}(\tau, t') = \int_{-\infty}^{\infty} \mid P^{(2)}(t, t', \tau) \mid^2 \mathrm{d}t = S_0 + S_{\mathrm{CC}} + S_{\mathrm{AC}}\,. \tag{8.13}$$

Here, S_0 corresponds to an intensity correlation, which does not exhibit a phase modulation and is thus not detected. S_{CC} represents the low-frequency cross-correlation of

SHG and SFG pulses and S_{AC} represents the high-frequency autocorrelation of two SHG pulses:

$$S_{\mathrm{CC}}(\tau, t') = (A_1^3 A_2 + A_1 A_2^3)\sqrt{\frac{\pi}{4\ln 2}}\Delta t g\left(\tau, \frac{2}{\sqrt{3}}\Delta t\right)\cos\left[\omega_0\tau - \Omega_{21}t'\right], \quad (8.14)$$

$$S_{\mathrm{AC}}(\tau, t') = \frac{A_1^2 A_2^2}{2}\sqrt{\frac{\pi}{4\ln 2}}\Delta t g\left(\tau, \Delta t\right)\cos\left[2\omega_0\tau - 2\Omega_{21}t'\right]. \quad (8.15)$$

S_{CC} and S_{AC} exhibit a well-defined phase modulation and therefore add to the demodulated signal whenever stray light is detected in the experiment.

8.3 Linear excitation and spectroscopy with multiple harmonic light

At first, PMHL spectroscopic data for linear excitation in the vapor cell are presented. As the vapor cell contains a mixture of potassium, rubidium and cesium the ability to perform simultaneous spectroscopy with multiple harmonics of the laser light exciting the sample, can be demonstrated as well. The fundamental laser wavelength is tuned to 774.5 nm (12912 cm^{-1}) and the monochromator set to 774.4 nm (12913.9 cm^{-1}). No spectral filtering is done after the nonlinear crystal, hence the sample is excited with portions of the first and second harmonic light simultaneously. In rubidium and potassium, D line transitions are excited with the fundamental light and in cesium the $\Delta n = 2$ transition $6\mathrm{S}_{1/2} \rightarrow 8\mathrm{P}_{3/2}$ is excited with second harmonic light [cf. Fig. 8.3(a)]. The respective data obtained from a ±30 ps pump-probe scan for 1H and 2H demodulation is shown in Fig. 8.3(b) to (e). In the time domain, clean high quality interferograms can be observed with oscillation frequencies strongly downshifted due to rotating frame sampling upon lock-in demodulation. This drastically reduces the amount of required data points and the influence of phase noise picked up in the optical setup as discussed above. Correspondingly, sharp resonances and an excellent signal-to-noise ratio is obtained in the respective Fourier spectra, for excitation with the fundamental as well as second harmonic light.

During pump-probe overlap of fundamental pulses in the nonlinear crystal, more UV output is obtained and intuitively a transient exaggeration of the cesium signal around zero pulse delay should be expected, which is in contrast to the measured second-harmonic time-domain data [Fig. 8.3(b)]. However, the increased UV yield during pulse overlap is actually contained in the SFG pulse, which contributes to the first-harmonic signal. Accordingly, a pronounced signal increase around zero delay is observed there [Fig. 8.3(c)] and a broad spectral feature appears in the respective Fourier spectrum [Fig. 8.3(e)] which is centered at half the frequency of the $6\mathrm{S}_{1/2} \rightarrow 8\mathrm{P}_{3/2}$ transition of cesium. This is in accordance with the theory discussed above.

The applied phase modulation thus allows for a clear separation of the light-matter response for different harmonics in the light field. An exception occurs during temporal overlap of pulses where due to SFG pulse generation some UV light contribution leaks into the 1H signal channel. As a consequence, pulse overlap effects are minimized in the 2H signal channel and a constant amplitude is obtained there. The UV light contribu-

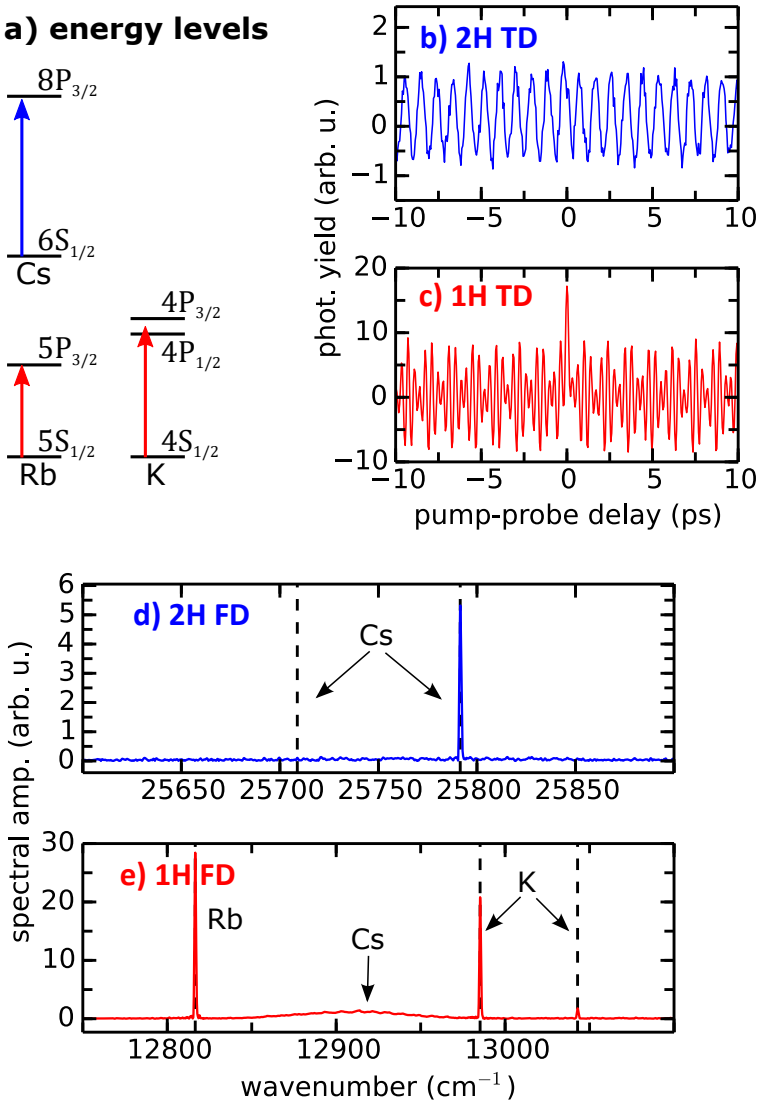

Figure 8.3: Obtained signals for first and second harmonic laser pulses exciting an alkali-metal vapor mixture containing potassium (K), rubidium (Rb) and cesium (Cs). (a) shows the relevant near IR and UV transitions in the alkali atoms. (b)-(e) show the first and second harmonic time- and frequency-domain data, denoted 1H, 2H TD and 1H, 2H FD, respectively. Vertical dashed lines indicate transitions frequencies taken from [78]. Reproduced from Ref. [B3].

tions to the first-harmonic signal exhibit specific broad line shapes and can be therefore clearly distinguished from other processes whenever pulse durations are shorter than the dynamics in the system.

Note that in molecular systems, transitions may be driven either with a one-photon excitation from one of the harmonics of the laser light or with a multi-photon excitation of a respective lower harmonic. Both processes would appear in the same harmonic spectra. Differentiating these processes must be done on a case by case basis. This scenario,

however, does not play a role in the experiments shown here.

8.4 Nonlinear excitation and stray light effects

As a second example, data for the $5S_{1/2} \rightarrow 6P_{3/2,1/2}$ transitions in rubidium are presented. Here the laser was focused with a f=150 mm lens into the vapor cell and the delay was scanned for $0 - 40$ ps. Fundamental light was blocked from entering the vapor cell using an optical filter. Data for the second harmonic pulses tuned to 420.8 nm (20825 cm^{-1}) and the monochromator set to 840.6 nm (11897.0 cm^{-1}) is shown in Fig. 8.4.

In this example, signal contributions are obtained in the 1H, 2H and 4H demodulation channel, whereas the 3H demodulation channel returned only noise. In the 2H demodulation channel, a high resolution signal for the $5S_{1/2} \rightarrow 6P_{3/2,1/2}$ resonances is retrieved [Fig. 8.4(c) and (d)]. In the 1H demodulation channel, only processes involving SFG pulses are contributing since the fundamental light is blocked in this experiment. Accordingly, a short transient is detected here, decaying on a time scale determined by the pulse length, yielding a respective broad peak in the Fourier domain [Fig. 8.4(e) and (f)]. In the 4H demodulation channel, clear resonances can be observed [Fig. 8.4(b)] which are attributed to the collective excitation of two rubidium atoms via the $5S_{1/2} \rightarrow 6P_{3/2,1/2}$ transitions. The rubidium system thus supports one- and two-photon transitions and therefore serves here as a model system to study nonlinear effects. A corresponding excitation scheme is shown in Fig. 8.4(a). This observation is in accordance with the results of the previous chapter as the detected collective two-atom response exhibits a phase shift of π (collective diagonal peaks) relative to the respective single-atom resonances [Fig. 8.4(d)]. A collective cross peak is not observed in this case. This contribution is hidden in the noise.

As a unique feature of the 2H signal, a distinct depletion of the pump-probe transient around zero pulse delay occurs [Fig. 8.4(c)]. To elucidate the nature of this feature, measurements for different laser wavelengths are shown in Fig. 8.5. The 2H time-domain data [Fig. 8.5(a)] indicate that two effects are superimposed at the time origin leading to a signal enhancement if the laser is rather off-resonant and a signal decrease if the laser is more resonant. For the 2H frequency spectra shown in Fig. 8.5(b), only a small time-domain window is Fourier transformed in order to make the transient features more pronounced. In these spectra, a positive broad peak centered at the laser wavelength occurs which is identified with the autocorrelation of SHG pulses [Eq. (8.15)] originating from stray light scattered into the detector. This feature becomes less pronounced when being more resonant to the atomic transitions. Here, broad negative peaks centered at the $5S_{1/2} \rightarrow 6P_{3/2,1/2}$ transition frequencies become evident instead.

This effect can be understood when considering the collective two-atom resonance detected in the 4H spectrum. While this signal originates from the collective excitation with SHG pump and probe pulses, the analog process appears in the 2H spectrum for interactions with an SFG and either of the two SHG pulses [cf. Feynman pathways in Fig. 8.2(c)]. As discussed above, these signals appear at half the transition frequency and only contribute to the signal during pump-probe overlap. Furthermore, the collective signals in the 4H [Fig. 8.4(b)] and 2H [Fig. 8.5(b)] spectra exhibit the same phase signature

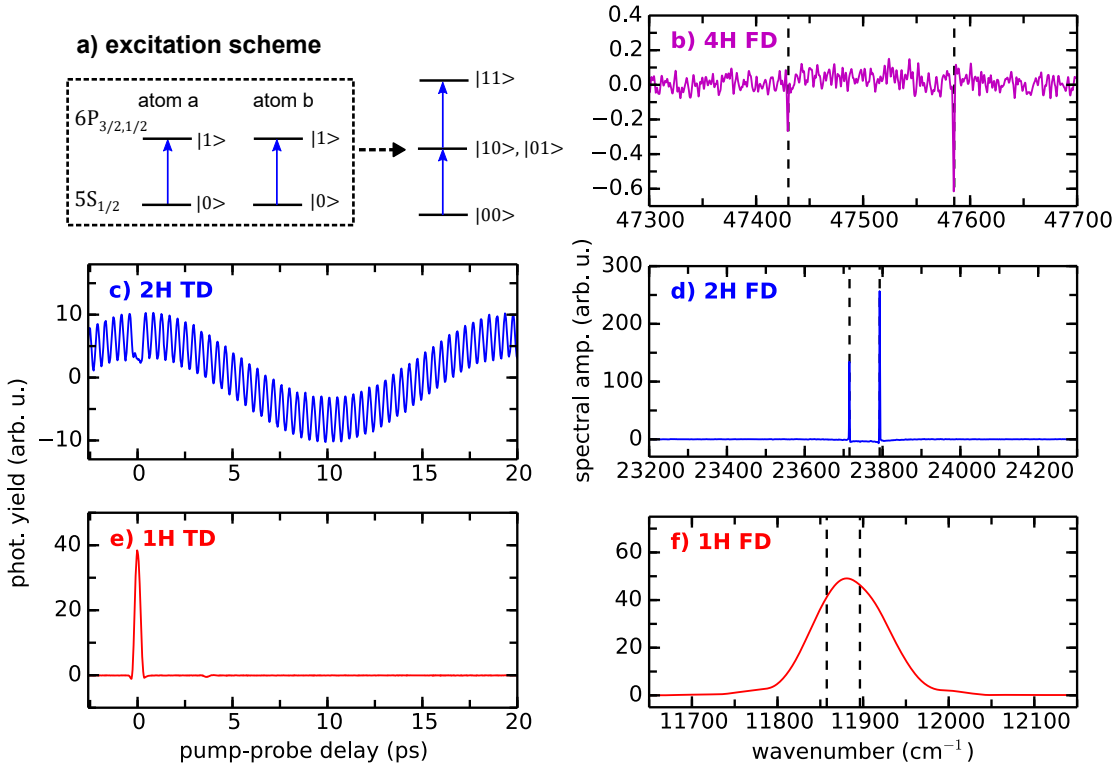

Figure 8.4: Excitation of the $5S_{1/2} \rightarrow 6P_{3/2,1/2}$ transitions in a rubidium vapor for the laser wavelength 420.8 nm (23764 cm^{-1}). The excitation scheme is shown in (a). (c), (e) show the time-domain data for 2H and 1H lock-in demodulation and (b), (d), (f) the discrete Fourier transforms of 4H, 2H and 1H signals. In (b) the collective excitation $5S_{1/2} \rightarrow 6P_{3/2}$ and $5S_{1/2} \rightarrow 6P_{1/2}$ is hidden in the noise floor. Vertical dashed lines show transition frequencies taken from [78]. Reproduced from Ref. [B3].

and appear as negative peaks with respect to the single-atom resonances. This phase signature explains the depletion of the pump-probe signal around zero delay. The depletion depth also matches with predictions derived from the amplitudes of the 4H peaks. In general, this case provides another confirmation of the phase assignment of collective resonances discussed in the previous chapter.

Furthermore, this interpretation is consistent with observations in the 1H signal [Fig. 8.5(c)]. Similar to the 2H signal, two transient processes are superimposing here for small pulse delays. One contribution comes from the the $5S_{1/2} \rightarrow 6P_{3/2,1/2}$ excitation involving a SFG pulse interaction. The other contribution is due to stray light reflecting the cross-correlation of SHG and SFG pulses [Eq. (8.14)]. Note that both effects produce interference fringes in the time domain, however being not directly apparent in the data since oscillation frequencies are strongly downshifted due to rotating frame detection.

A comparison of the 1H signal with a simulation confirms the discussed assignment for the different signal contributions. For the simulation, Eq. (8.11) and (8.14) with experimentally obtained pulse parameters are used. The relative amplitudes between

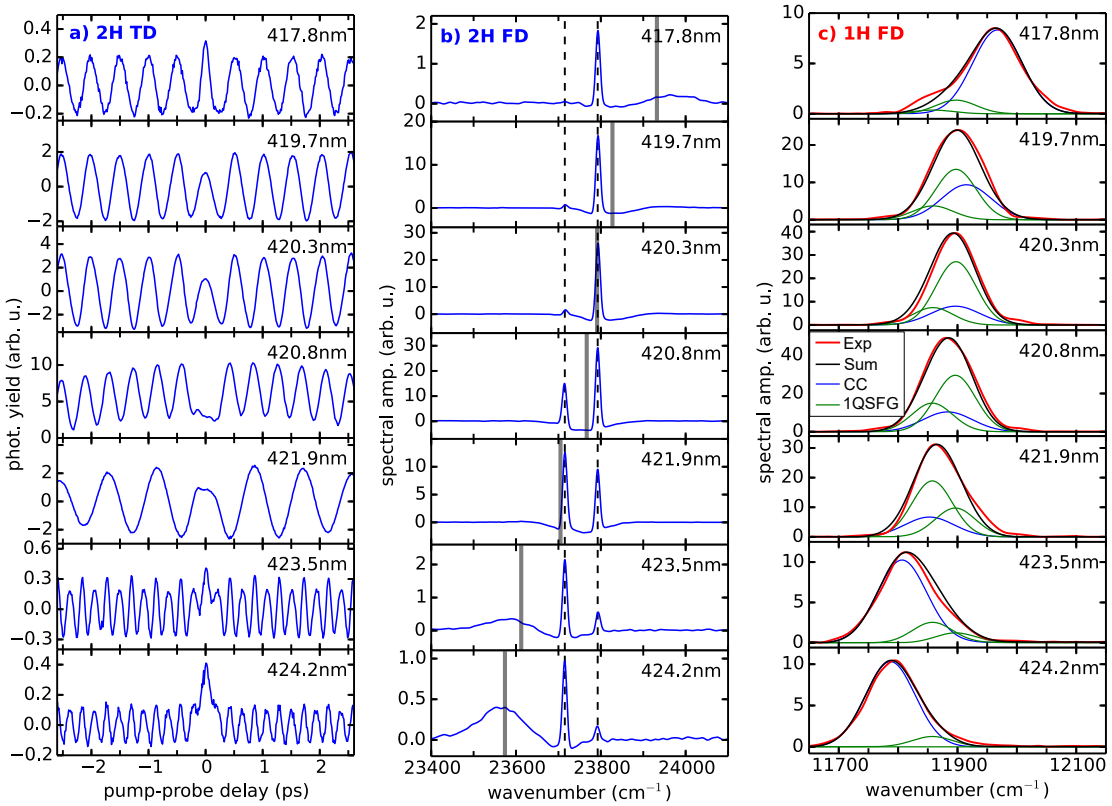

Figure 8.5: Excitation of the $5S_{1/2} \rightarrow 6P_{3/2,1/2}$ transitions in a rubidium vapor for laser center wavelengths between 417.8 and 424.2 nm. (a) shows the second harmonic time-domain (2H TD) data and (b) and (c) show the second (2H FD) and first harmonic (1H FD) frequency-domain spectra. In (a), oscillation frequencies differ among data runs which is due to changes of the monochromator wavelength. In (c), simulated signals are included as discussed in the text. Gray vertical lines indicate the laser center frequency and black dashed lines show transition frequencies taken from [78]. Reproduced from Ref. [B3].

the $5S_{1/2} \rightarrow 6P_{3/2,1/2}$ transitions have been set to the peak ratios taken from the 2H signal [Fig. 8.5(b)], whereas the ratio between this signal and the cross-correlation was a free parameter. The Fourier transform of simulated data is shown together with the experimental data in Fig. 8.5(c). Good agreement between simulations and experimental data is obtained and the two underlying signal contributions can be clearly identified. For simplicity, no spectral chirp was included in the theoretical model and deviations between experiment and simulation are attributed to spectral chirp of the UV pulses due to the relatively long nonlinear crystal employed for the frequency conversion.

In conclusion, rubidium served here as a simple model system to study nonlinear electronic excitation with the concept of PMHL spectroscopy. Since the phase modulation

method allows for phase-sensitive detection, the weak collective features can be identified by their phase shift with respect to single-atom and stray light contributions. If scanning longer delays, the collective peaks leaking into the 2H spectra as well as the stray light peak are negligible since these effects decay rapidly with increasing pump-probe delay [cf. Fig. 8.4(d)].

8.5 Prospective extension to high harmonic light sources

In view of an application to high harmonic light sources some general aspects are briefly discussed. The conducted experiments demonstrate the ability to track the coherent time evolution of electronic WPs for linear and nonlinear optical excitation. In particular DQC signals have been isolated and interpreted as collective two-atom excitations. In view of future XUV studies, DQC signals may yield valuable insight into double-core excitations and related many-body correlations [200]. Furthermore, simultaneous spectroscopy with different harmonics of the light field can be readily performed and direct correlation of different harmonic signal contributions is possible. In this sense, XUV experiments with multiple harmonics simultaneously exciting a sample might be a feasible application and optical isolation of specific harmonics normally causing power losses and pulse dispersion could be omitted. Likewise, the presented time-domain spectroscopy approach might be very beneficial to achieve high spectral resolution with broadband high harmonic pulses independent of the detector resolution. In time-domain methods the spectral resolution is solely determined by the Fourier transform of pump-probe traces and thus a resolution in the low μeV regime is feasible as demonstrated with the high resolution measurement in the previous chapter.

The employed collinear beam geometry is a significant advantage for the implementation in XUV beam lines. However, in collinear experiments, the typically highly convoluted nonlinear system response is very challenging to disentangle. Therefore, phase-cycling becomes crucial to narrow down the signal to the most relevant contributions. As this relies on a precise phase manipulation of the optical pulses, phase-cycling is hard to achieve in the XUV. In the proposed approach, a solution is provided by manipulating the pulses solely on the fundamental frequency. This is combined with high resolution pump-probe scans and phase-sensitive detection, having allowed to disentangle the detected system response containing several overlapping contributions, i.e. from linear and nonlinear excitation of the spectroscopic sample as well as from interaction with different harmonic light including fundamental, SHG and SFG pulses. Thereby, a particular focus lay on possible ambiguities occurring during temporal overlap of pulses. A precise understanding of this part of the experiment may help to reliably extract information about particularly fast dynamics [213]. At short pump-probe delays, an overlap of different signals in the same harmonic demodulation channel occurs due to the generation of SFG pulses. No additional information is contained in the SFG signal contributions. However, they may complicate data interpretation if more advanced systems will be studied.

The efficiency of the proposed scheme relies on the high purity of the acousto-optically induced phase modulation, performed on a shot-to-shot basis. Other modulation techniques based on modulating the pulse delay [24, 214], e.g. with piezo mirrors, may also

operate with high repetition rate lasers on a shot-to-shot basis, but typically introduce pronounced harmonic sidebands. Pulse shaper based setups would allow for a linear phase modulation, but not with high repetition rates and the achievable pulse delay is restricted to the low picosecond regime [57]. However, lock-in amplification is most efficient at high modulation frequencies and it has been initially pointed out that the phase modulation scheme may not work with low repetition rate laser systems [25, 26], which is in contradiction to most state-of-the-art coherent high harmonic light sources operating at low repetition rates ($\lesssim 1\,\mathrm{kHz}$). This issue has been solved in the scope of this PhD thesis in cooperation with a graduate student (Marcel Binz) [B5]. The developed scheme relies on a fully sampled reference signal produced with a cw auxiliary laser (as used in chapter 7.3). In the phase-synchronous lock-in detection, the undersampled PM-WPI signal is then compared to the fully sampled reference waveform. This concept correctly reconstructs the demodulated WPI signal even for large undersampling factors (tested up to a factor of 160) while maintaining the high signal-to-noise ratio typical for the phase modulation approach. Details can be found in Ref. [117].

In the phase modulation scheme demands on phase stability are generally reduced by orders of magnitude. With harmonic lock-in detection, this concept is transferred to the respective harmonic of the fundamental light, therefore allowing electronic WP interference measurements even at very short wavelengths, possibly down to the VUV and XUV regime. Combined with the fully integrated lock-in amplification, the optimal stray light suppression and the compatibility with detectors preferable for ultra high vacuum detection, e.g. photoionization or any kind of depletion signal, make the approach ideal for VUV to XUV applications.

The presented concept can also be extended to multidimensional spectroscopy in a straightforward way [26]. Similarly, a pulse shaper based two-dimensional spectroscopy setup has been transferred to shorter wavelengths [185]. Alternatively, a two-dimensional spectroscopy setup was transferred to the UV by placing nonlinear crystals inside each arm of the optical interferometers. This omits the SFG contributions in the signal, albeit being considerably more intricate than the proposed approach, especially in view of HHG or HGHG applications.

8.6 Conclusion

As a novel approach PMHL spectroscopy has been introduced in a proof-of-principle study using second harmonic light generation. This concept relies on an extension of the PM-WPI method, however, after modulating the femtosecond pump and probe pulses at their fundamental wavelength, the laser light is transferred to shorter wavelengths in a coherent process, e.g. in SHG. This is combined with harmonic lock-in detection to extract the WPI signal now modulated at higher harmonics of the acoustic beat frequency. In this way, all advantages of the phase modulation technique are transferred to shorter laser wavelengths.

Specifically, WPI was performed in the UV spectral range ($\sim 400\,\mathrm{nm}$), probing respective transitions in gas-phase rubidium ($5S_{1/2} \rightarrow 6P_{3/2,1/2}$) and cesium atoms ($6S_{1/2} \rightarrow 8P_{3/2}$). One- and two-photon excitation pathways induced by interactions with SHG and

SFG pump-probe pulses were readily dissected with the inherent phase-cycling scheme. Furthermore, simultaneous spectroscopy with multiple harmonic light was demonstrated. Due to the collinear beam geometry and the high sensitivity and robustness of the method, a transfer to VUV and XUV wavelengths should be feasible and the prerequisites for all-XUV 2D electronic spectroscopy have been demonstrated.

9 Summary

In this dissertation, phase-modulated nonlinear time-domain spectroscopy was implemented and applied to dilute gas-phase samples which involved on the one hand doped helium nanodroplet beams and on the other hand warm atomic gases. Electronic WPs were induced in the samples and their coherent time evolution was studied with high precision in interferometric measurements, i.e. in WPI. These experiments provided access to the coherent dynamics of the system with simultaneous high temporal and spectral resolution. In this scope, the employed phase modulation technique was for the first time applied to a cold ($\approx 370\,\mathrm{mK}$) supersonic beam target of low density ($\sim 10^8\,\mathrm{cm}^{-3}$) and the compatibility with mass-resolved ion detection was demonstrated [B1]. The passive phase stabilization and high sensitivity of the applied method resulted in a drastic improvement in signal quality as compared to previous studies [22, 126].

Specifically, rubidium atoms attached to helium nanodroplets (RbHe_N) were investigated. The enhanced resolution in these experiments revealed sharp spectral lines that resemble gas-phase rubidium resonances. This is explained by the desorption of the atoms off the droplets upon electronic excitation. In a competing process, Rb*He excimer molecules form to a small extend on the droplet surface. Mass-selective detection allowed to isolate these contributions and a highly resolved vibronic spectrum ($\Delta\omega_{\mathrm{FWHM}} = 0.3\,\mathrm{cm}^{-1}$) for transitions between the bound states of the $1^2\Pi_{3/2}$ and the higher-lying $2^2\Delta$, $4^2\Pi$, $6^2\Sigma$ PECs was retrieved [B1]. A comparison with theory allowed to dissect the various contributions of the convoluted upper electronic states and enabled a refined assignment of spectral features as compared to previous studies [22, 95]. This permitted two novel conclusions: Evidence was found that the exciplex is formed in its rotational ground state, and an additional formation channel of the molecule via two-photon excitation was revealed. The femtosecond time resolution of the experiment furthermore allowed to study the dynamics of the formation process which enabled a refinement of previous interpretations. Solely dephasing and rephasing of vibronic WPs was found and the absence of formation dynamics in the presented and previous studies is attributed to the ambiguities caused by the high repetition rate of the employed laser.

The formation dynamics of the exciplexes still eludes from an accurate description and future studies using a low repetition rate laser provide a promising approach to resolve this process. Different formation channels (e.g. via the 5P, 5D and 6P atomic asymptotes) would provide complementary data to test formation models. An extension of the optical setup to 2D sepctroscopy would reveal in detail energy relaxation pathways that lead to the stabilization of the initially hot molecule. Moreover, the high level of detail and resolution retrieved for the exciplex spectrum may stimulate the development of new models and provide a benchmark system for current ab initio techniques. In general, the novel combination of phase-modulated nonlinear spectroscopy applied to molecular samples isolated on the surface or inside helium nanodroplets provides a plethora of

applications in future studies, involving, for instance, the investigation of intra- and intermolecular dynamics in isolated heterogeneous complexes or the characterization of decoherence effects induced by a well-controlled environment, e.g. by the helium matrix or individual embedded solvent molecules (*microsolvation*).

Furthermore, a new method was developed [B2] to sensitively and selectively detect the temporal evolution of MQCs, that are electronic coherences induced upon multiphoton transitions. With this method (termed PM-MQC detection), the coherent dynamics of high-lying states become readily accessible and are directly correlated to the ground state, thus facilitating data interpretation. To reveal the full information content of the quantum coherence signals, i.e. deducing amplitude and phase information, a concept was established to calibrate the phase of the higher-order signals. The PM-MQC scheme was tested in alkali vapors and rubidium-doped helium droplets where simultaneous detection of one- and two-photon transitions in separate signal channels was demonstrated. This background-free detection provides reduced noise characteristics which constitutes a clear advantage for the detection of commonly weak nonlinear signals. Future applications may focus on more advanced molecular systems embedded in helium droplets, attached to rare gas clusters or dissolved in liquids. Matrix/solvent-induced effects on high-lying states can be readily studied with the established technique and the role of these states in inter- and intramolecular dynamics can be elucidated. The attainable high resolution will allow to disentangle convoluted Rydberg states and autoionization mechanisms occurring in highly excited states. The established concept may as well have impact on current phase-modulated 2D spectroscopy experiments where MQC signals have been so far not accessed.

In addition, the developed method was used to study the collective response of a warm atomic vapor for the D line excitation in potassium, rubidium and cesium atoms. The particular high sensitivity of the experimental scheme revealed for the first time three- and four-body resonances at particle densities down to $\rho \sim 10^8\,\mathrm{cm}^{-3}$. Thereby, a linear dependence on the ensemble density and a nonlinear scaling with the laser intensity was found. As a unique property, the employed setup enables high resolution measurements ($\Delta\omega_{\mathrm{FWHM}} = 1\,\mathrm{GHz}$) which revealed distinct phase signatures of the multiatom resonances that are connected to the fundamental hyperfine states of the system. The experiment was simulated for a nearest-neighbor dipole-dipole coupling model in collaboration with the group of A. Eisfeld [B4]. The main features of the detected signals were reproduced, albeit a quantitative agreement was not achieved which is attributed to the crude approximations in the model. In addition, a single-atom process that involves the interaction with multiple consecutive pump-probe pulse pairs was identified as a second mechanism that contributes to the observed higher-order signals. Based on these findings, the higher-order signals are interpreted as the collective response of dipole-coupled atoms which is in addition superimposed with a higher-order single-atom process.

The presented results reveal a complex behavior for the collective excitation of even highly dilute atomic ensembles which is expected to stimulate further theoretical advances towards more elaborate models and to have an impact on other fields, e.g. the ultracold community. Future PM-MQC studies could test the hypothesis of dipolar coupling with s-orbital excitations. State-selective preparation of atoms e.g. with optical pumping or by exploiting the low helium droplet temperature will provide further insights. Rydberg

excitations in warm/cold vapors could be studied where an enhancement of interaction phenomena is expected and complementary information to the extensive studies of cold Rydberg ensembles could be gained. Besides the investigation of dilute samples, where the applied method clearly had proven its advantages due to its particular high sensitivity, investigations of strongly correlated (molecular) ensembles are as well intriguing. Typical target systems would be thin films [73], quantum dot assemblies [215] or biomolecular aggregates [15, 164]. Recently, cooperative effects were also observed in highly doped rare gas clusters [166, 216]. These systems are of interest as they bridge the gap between thin films and the liquid phase. The PM-MQC approach would add a new perspective to these studies by providing femtosecond temporal resolution and the access to coherent properties. In addition, an incorporation in multidimensional spectroscopy promises great potential as indicated in Ref. [11].

Eventually, a novel approach to facilitate all-XUV nonlinear spectroscopy was proposed [B3]. This concept, termed PMHL spectroscopy, readily transfers the properties of the phase modulation method to higher harmonic light. This drastically reduces the experimental demands and provides access to phase-cycling schemes at XUV wavelengths. The principle was demonstrated for linear and nonlinear WP excitation of alkali atoms at UV wavelengths ($\sim 400\,\mathrm{nm}$). Thereby, the ability to perform simultaneous spectroscopy with multiple harmonic light was shown. A particular focus lay on pump-probe pulse-overlap effects where convoluted contributions from SHG and SFG light were readily dissected with the inherent phase-cycling scheme. An implementation in state-of-the-art coherent XUV light sources is feasible and the established method may enable the first realization of all-XUV nonlinear time-domain spectroscopy. A respective setup for an application at a seeded FEL is currently being prepared.

As a concluding remark, the presented work successfully demonstrates the feasibility for advanced state-of-the-art multidimensional spectroscopy methods, e.g. 2D electronic spectroscopy, which are now within reach to be applied to helium droplet systems or cold molecular beams. Various aspects of linear and nonlinear excitation in different systems were explored in detail with the pump-probe setup which sets the basis for an extension to multidimensional spectroscopy. The proposed combination of the latter spectroscopy method with the isolation of molecular species in helium droplets provides a very promising novel approach to study molecular dynamics and is expected to yield insightful complementary information to studies in the liquid and solid phase.

Bibliography

The publications by the author covered in this thesis are listed in a separate bibliography on page ix.

[1] S. Mukamel, *Principles of nonlinear optical spectroscopy* (Oxford University Press, 1995).

[2] A. H. Zewail, *Femtochemistry: Atomic-Scale Dynamics of the Chemical Bond*, J. Phys. Chem. A **104**, 5660 (2000).

[3] M. J. Rosker, T. S. Rose and A. H. Zewail, *Femtosecond real-time dynamics of photofragment-trapping resonances on dissociative potential energy surfaces*, Chem. Phys. Lett. **146**, 175 (1988).

[4] D. M. Jonas, *Two-Dimensional Femtosecond Spectroscopy*, Annu. Rev. Phys. Chem. **54**, 425 (2003).

[5] H.-S. Tan, *Theory and phase-cycling scheme selection principles of collinear phase coherent multi-dimensional optical spectroscopy*, J. Chem. Phys. **129**, 124501 (2008).

[6] R. M. Hochstrasser, *Two-dimensional spectroscopy at infrared and optical frequencies*, PNAS **104**, 14190 (2007).

[7] M. Cho, *Coherent Two-Dimensional Optical Spectroscopy*, Chem. Rev. **108**, 1331 (2008).

[8] T. Brixner, J. Stenger, H. M. Vaswani, M. Cho, R. E. Blankenship and G. R. Fleming, *Two-dimensional spectroscopy of electronic couplings in photosynthesis*, Nature **434**, 625 (2005).

[9] M. L. Cowan, B. D. Bruner, N. Huse, J. R. Dwyer, B. Chugh, E. T. J. Nibbering, T. Elsaesser and R. J. D. Miller, *Ultrafast memory loss and energy redistribution in the hydrogen bond network of liquid H_2O*, Nature **434**, 199 (2005).

[10] K. W. Stone, K. Gundogdu, D. B. Turner, X. Li, S. T. Cundiff and K. A. Nelson, *Two-Quantum 2D FT Electronic Spectroscopy of Biexcitons in GaAs Quantum Wells*, Science **324**, 1169 (2009).

[11] D. B. Turner and K. A. Nelson, *Coherent measurements of high-order electronic correlations in quantum wells*, Nature **466**, 1089 (2010).

[12] P. Nuernberger, S. Ruetzel and T. Brixner, *Multidimensionale elektronische Spektroskopie photochemischer Reaktionen*, Angew. Chem. **127**, 11526 (2015).

[13] B. I. Grimberg, V. V. Lozovoy, M. Dantus and S. Mukamel, *Ultrafast Nonlinear Spectroscopic Techniques in the Gas Phase and Their Density Matrix Representation*, J. Phys. Chem. A **106**, 697 (2002).

[14] E. Collini, *Spectroscopic signatures of quantum-coherent energy transfer*, Chem. Soc. Rev. (2013).

[15] F. Fassioli, R. Dinshaw, P. C. Arpin and G. D. Scholes, *Photosynthetic light harvesting: excitons and coherence*, J. R. Soc. Interface **11**, 20130901 (2014).

[16] J. P. Toennies and A. F. Vilesov, *Superfluid Helium Droplets: A Uniquely Cold Nanomatrix for Molecules and Molecular Complexes*, Angew. Chem. Int. Ed. **43**, 2622 (2004).

[17] R. Lehnig and A. Slenczka, *Emission spectra of free base phthalocyanine in superfluid helium droplets*, J. Chem. Phys. **118**, 8256 (2003).

[18] M. Wewer and F. Stienkemeier, *Laser-induced fluorescence spectroscopy of 3,4,9,10-perylenetetracarboxylic-dianhydrid in helium nanodroplets*, J. Chem. Phys. **120**, 1239 (2004).

[19] F. Stienkemeier and A. F. Vilesov, *Electronic spectroscopy in He droplets*, J. Chem. Phys. **115**, 10119 (2001).

[20] F. Stienkemeier, F. Meier, A. Hägele, H. O. Lutz, E. Schreiber, C. P. Schulz and I. V. Hertel, *Coherence and Relaxation in Potassium-Doped Helium Droplets Studied by Femtosecond Pump-Probe Spectroscopy*, Phys. Rev. Lett. **83**, 2320 (1999).

[21] G. Droppelmann, O. Bünermann, C. P. Schulz and F. Stienkemeier, *Formation Times of RbHe Exciplexes on the Surface of Superfluid versus Normal Fluid Helium Nanodroplets*, Phys. Rev. Lett. **93**, 023402 (2004).

[22] M. Mudrich, F. Stienkemeier, G. Droppelmann, P. Claas and C. P. Schulz, *Quantum Interference Spectroscopy of Rubidium-Helium Exciplexes Formed on Helium Nanodroplets*, Phys. Rev. Lett. **100**, 023401 (2008).

[23] F. Stienkemeier and K. K. Lehmann, *Spectroscopy and dynamics in helium nanodroplets*, J. Phys. B: At. Mol. Opt. Phys. **39**, R127 (2006).

[24] N. F. Scherer, R. J. Carlson, A. Matro, M. Du, A. J. Ruggiero, V. Romero-Rochin, J. A. Cina, G. R. Fleming and S. A. Rice, *Fluorescence-detected wave packet interferometry: Time resolved molecular spectroscopy with sequences of femtosecond phase-locked pulses*, J. Chem. Phys. **95**, 1487 (1991).

[25] P. F. Tekavec, T. R. Dyke and A. H. Marcus, *Wave packet interferometry and quantum state reconstruction by acousto-optic phase modulation*, J. Chem. Phys. **125**, 194303 (2006).

[26] P. F. Tekavec, G. A. Lott and A. H. Marcus, *Fluorescence-detected two-dimensional electronic coherence spectroscopy by acousto-optic phase modulation*, J. Chem. Phys. **127**, 214307 (2007).

[27] G. A. Lott, A. Perdomo-Ortiz, J. K. Utterback, J. R. Widom, A. Aspuru-Guzik and A. H. Marcus, *Conformation of self-assembled porphyrin dimers in liposome vesicles by phase-modulation 2D fluorescence spectroscopy*, PNAS **108**, 16521 (2011).

[28] A. Perdomo-Ortiz, J. R. Widom, G. A. Lott, A. Aspuru-Guzik and A. H. Marcus, *Conformation and Electronic Population Transfer in Membrane-Supported Self-Assembled Porphyrin Dimers by 2D Fluorescence Spectroscopy*, J. Phys. Chem. B **116**, 10757 (2012).

[29] K. J. Karki, J. R. Widom, J. Seibt, I. Moody, M. C. Lonergan, T. Pullerits and A. H. Marcus, *Coherent two-dimensional photocurrent spectroscopy in a PbS quantum dot photocell*, Nat. Commun. **5**, 5869 (2014).

[30] E. Vella, H. Li, P. Grégoire, S. M. Tuladhar, M. S. Vezie, S. Few, C. M. Bazán, J. Nelson, C. Silva-Acuña and E. R. Bittner, *Ultrafast decoherence dynamics govern photocarrier generation efficiencies in polymer solar cells*, Sci Rep **6** (2016).

[31] J. Kim, V. M. Huxter, C. Curutchet and G. D. Scholes, *Measurement of Electron-Electron Interactions and Correlations Using Two-Dimensional Electronic Double-Quantum Coherence Spectroscopy*, J. Phys. Chem. A **113**, 12122 (2009).

[32] E. C. Fulmer, P. Mukherjee, A. T. Krummel and M. T. Zanni, *A pulse sequence for directly measuring the anharmonicities of coupled vibrations: Two-quantum two-dimensional infrared spectroscopy*, J. Chem. Phys. **120**, 8067 (2004).

[33] N. Christensson, F. Milota, A. Nemeth, I. Pugliesi, E. Riedle, J. Sperling, T. Pullerits, H. F. Kauffmann and J. Hauer, *Electronic Double-Quantum Coherences and Their Impact on Ultrafast Spectroscopy: The Example of β-Carotene*, J. Phys. Chem. Lett. **1**, 3366 (2010).

[34] X. Dai, M. Richter, H. Li, A. D. Bristow, C. Falvo, S. Mukamel and S. T. Cundiff, *Two-Dimensional Double-Quantum Spectra Reveal Collective Resonances in an Atomic Vapor*, Phys. Rev. Lett. **108**, 193201 (2012).

[35] F. Gao, S. T. Cundiff and H. Li, *Probing dipole–dipole interaction in a rubidium gas via double-quantum 2D spectroscopy*, Opt. Lett. **41**, 2954 (2016).

[36] W. Kuehn, K. Reimann, M. Woerner, T. Elsaesser and R. Hey, *Two-Dimensional Terahertz Correlation Spectra of Electronic Excitations in Semiconductor Quantum Wells*, J. Phys. Chem. B **115**, 5448 (2011).

[37] P. Hamm, M. Lim and R. M. Hochstrasser, *Structure of the Amide I Band of Peptides Measured by Femtosecond Nonlinear-Infrared Spectroscopy*, J. Phys. Chem. B **102**, 6123 (1998).

[38] J. D. Hybl, A. W. Albrecht, S. M. Gallagher Faeder and D. M. Jonas, *Two-dimensional electronic spectroscopy*, Chem. Phys. Lett. **297**, 307 (1998).

[39] U. Selig, C.-F. Schleussner, M. Foerster, F. Langhojer, P. Nuernberger and T. Brixner, *Coherent two-dimensional ultraviolet spectroscopy in fully non-collinear geometry*, Opt. Lett. **35**, 4178 (2010).

[40] S. Mukamel, D. Healion, Y. Zhang and J. D. Biggs, *Multidimensional Attosecond Resonant X-Ray Spectroscopy of Molecules: Lessons from the Optical Regime*, Annu. Rev. Phys. Chem. **64**, 101 (2013).

[41] G. Sansone, T. Pfeifer, K. Simeonidis and A. I. Kuleff, *Electron Correlation in Real Time*, ChemPhysChem **13**, 661 (2012).

[42] P. Tzallas, E. Skantzakis, L. a. A. Nikolopoulos, G. D. Tsakiris and D. Charalambidis, *Extreme-ultraviolet pump-probe studies of one-femtosecond-scale electron dynamics*, Nat Phys **7**, 781 (2011).

[43] F. Bencivenga, R. Cucini, F. Capotondi, A. Battistoni, R. Mincigrucci, E. Giangrisostomi, A. Gessini, M. Manfredda, I. P. Nikolov, E. Pedersoli, E. Principi, C. Svetina, P. Parisse, F. Casolari, M. B. Danailov, M. Kiskinova and C. Masciovecchio, *Four-wave mixing experiments with extreme ultraviolet transient gratings*, Nature **520**, 205 (2015).

[44] D. Gauthier, P. R. Ribič, G. De Ninno, E. Allaria, P. Cinquegrana, M. B. Danailov, A. Demidovich, E. Ferrari and L. Giannessi, *Generation of Phase-Locked Pulses from a Seeded Free-Electron Laser*, Phys. Rev. Lett. **116**, 024801 (2016).

[45] K. C. Prince, E. Allaria, C. Callegari, R. Cucini, G. D. Ninno, S. D. Mitri, B. Diviacco, E. Ferrari, P. Finetti, D. Gauthier, L. Giannessi, N. Mahne, G. Penco, O. Plekan, L. Raimondi, P. Rebernik, E. Roussel, C. Svetina, M. Trovò, M. Zangrando, M. Negro, P. Carpeggiani, M. Reduzzi, G. Sansone, A. N. Grum-Grzhimailo, E. V. Gryzlova, S. I. Strakhova, K. Bartschat, N. Douguet, J. Venzke, D. Iablonskyi, Y. Kumagai, T. Takanashi, K. Ueda, A. Fischer, M. Coreno, F. Stienkemeier, Y. Ovcharenko, T. Mazza and M. Meyer, *Coherent control with a short-wavelength free-electron laser*, Nat Photon **10**, 176 (2016).

[46] M. Fushitani, *Applications of pump-probe spectroscopy*, Annu. Rep. Prog. Chem., Sect. C: Phys. Chem. **104**, 272 (2008).

[47] M. Dantus, *COHERENT NONLINEAR SPECTROSCOPY: From Femtosecond Dynamics to Control*, Annu. Rev. Phys. Chem. **52**, 639 (2001).

[48] M. Dantus, M. J. Rosker and A. H. Zewail, *Real-time femtosecond probing of ''transition states'' in chemical reactions*, J. Chem. Phys. **87**, 2395 (1987).

[49] B. Grüner, M. Schlesinger, P. Heister, W. T. Strunz, F. Stienkemeier and M. Mudrich, *Vibrational relaxation and dephasing of Rb_2 attached to helium nanodroplets*, Phys. Chem. Chem. Phys. **13**, 6816 (2011).

[50] P. Hamm and M. Zanni, *Concepts and Methods of 2D Infrared Spectroscopy* (Cambridge University Press, 2011).

[51] A. D. Bristow, D. Karaiskaj, X. Dai, T. Zhang, C. Carlsson, K. R. Hagen, R. Jimenez and S. T. Cundiff, *A versatile ultrastable platform for optical multidimensional Fourier-transform spectroscopy*, Rev. Sci. Instrum. **80**, 073108 (2009).

[52] T. Brixner, T. Mancal, I. V. Stiopkin and G. R. Fleming, *Phase-stabilized two-dimensional electronic spectroscopy*, J. Chem. Phys. **121**, 4221 (2004).

[53] J. Réhault, M. Maiuri, A. Oriana and G. Cerullo, *Two-dimensional electronic spectroscopy with birefringent wedges*, Rev. Sci. Instrum. **85**, 123107 (2014).

[54] P. Tian, D. Keusters, Y. Suzaki and W. S. Warren, *Femtosecond Phase-Coherent Two-Dimensional Spectroscopy*, Science **300**, 1553 (2003).

[55] D. B. Turner, K. W. Stone, K. Gundogdu and K. A. Nelson, *Invited Article: The coherent optical laser beam recombination technique (COLBERT) spectrometer: Coherent multidimensional spectroscopy made easier*, Rev. Sci. Instrum. **82**, 081301 (2011).

[56] F. D. Fuller, D. E. Wilcox and J. P. Ogilvie, *Pulse shaping based two-dimensional electronic spectroscopy in a background free geometry*, Opt. Express **22**, 1018 (2014).

[57] S. Draeger, S. Roeding and T. Brixner, *Rapid-scan coherent 2D fluorescence spectroscopy*, Opt. Express **25**, 3259 (2017).

[58] G. Nardin, T. M. Autry, K. L. Silverman and S. T. Cundiff, *Multidimensional coherent photocurrent spectroscopy of a semiconductor nanostructure*, Opt. Express **21**, 28617 (2013).

[59] Y. R. Shen, *The Principles of Nonlinear Optics* (Wiley, 1984).

[60] F. D. Fuller and J. P. Ogilvie, *Experimental Implementations of Two-Dimensional Fourier Transform Electronic Spectroscopy*, Annu. Rev. Phys. Chem. **66**, 667 (2015).

[61] A. W. Albrecht, J. D. Hybl, S. M. G. Faeder and D. M. Jonas, *Experimental distinction between phase shifts and time delays: Implications for femtosecond spectroscopy and coherent control of chemical reactions*, J. Chem. Phys. **111**, 10934 (1999).

[62] J. A. Cina, *Wave-Packet Interferometry and Molecular State Reconstruction: Spectroscopic Adventures on the Left-Hand Side of the Schrödinger Equation*, Annu. Rev. Phys. Chem. **59**, 319 (2008).

[63] J. D. Biggs, J. A. Voll and S. Mukamel, *Coherent nonlinear optical studies of elementary processes in biological complexes: diagrammatic techniques based on the wave function versus the density matrix*, Phil. Trans. R. Soc. A **370**, 3709 (2012).

[64] L. Bruder, *Phase-Modulated Wave Packet Interferometry in the Gas Phase and Implementation of an Interlock System for the LDM End-Station*, Diplomarbeit, Universität Freibrug, Freiburg i. Br. (2013).

[65] C. L. Smallwood, T. M. Autry and S. T. Cundiff, *Analytical solutions to the finite-pulse Bloch model for multidimensional coherent spectroscopy*, J. Opt. Soc. Am. B **34**, 419 (2017).

[66] L. Yang and S. Mukamel, *Two-Dimensional Correlation Spectroscopy of Two-Exciton Resonances in Semiconductor Quantum Wells*, Phys. Rev. Lett. **100** (2008).

[67] A. Muthukrishnan, G. S. Agarwal and M. O. Scully, *Inducing Disallowed Two-Atom Transitions with Temporally Entangled Photons*, Phys. Rev. Lett. **93** (2004).

[68] V. May and O. Kühn, *Charge and Energy Transfer Dynamics in Molecular Systems* (John Wiley & Sons, 2011).

[69] D. S. Chemla and J. Shah, *Many-body and correlation effects in semiconductors*, Nature **411**, 549 (2001).

[70] T. Vogt, M. Viteau, J. Zhao, A. Chotia, D. Comparat and P. Pillet, *Dipole Blockade at Förster Resonances in High Resolution Laser Excitation of Rydberg States of Cesium Atoms*, Phys. Rev. Lett. **97**, 083003 (2006).

[71] N. Pörtner, A. F. Vilesov and M. Havenith, *The formation of heterogeneous van der Waals complexes in helium droplets*, Chemical Physics Letters **343**, 281 (2001).

[72] D. Tong, S. M. Farooqi, J. Stanojevic, S. Krishnan, Y. P. Zhang, R. Côté, E. E. Eyler and P. L. Gould, *Local Blockade of Rydberg Excitation in an Ultracold Gas*, Phys. Rev. Lett. **93**, 063001 (2004).

[73] M. Müller, A. Paulheim, A. Eisfeld and M. Sokolowski, *Finite size line broadening and superradiance of optical transitions in two dimensional long-range ordered molecular aggregates*, J. Chem. Phys. **139**, 044302 (2013).

[74] D. Schneble, Y. Torii, M. Boyd, E. W. Streed, D. E. Pritchard and W. Ketterle, *The Onset of Matter-Wave Amplification in a Superradiant Bose-Einstein Condensate*, Science **300**, 475 (2003).

[75] A. M. Brańczyk, D. B. Turner and G. D. Scholes, *Crossing disciplines - A view on two-dimensional optical spectroscopy*, ANNALEN DER PHYSIK **526**, 31 (2014).

[76] J. A. Leegwater and S. Mukamel, *Self-broadening and exciton line shifts in gases: Beyond the local-field approximation*, Phys. Rev. A **49**, 146 (1994).

[77] M. Mudrich and F. Stienkemeier, *Photoionisaton of pure and doped helium nanodroplets*, Int. Rev. Phys. Chem. **33**, 301 (2014).

[78] Kramida, A., Ralchenko, Yu., Reader, J. and NIST ASD Team, *NIST Atomic Spectra Database (ver. 5.3)* (2015).

[79] H. Buchenau, E. L. Knuth, J. Northby, J. P. Toennies and C. Winkler, *Mass spectra and time-of-flight distributions of helium cluster beams*, J. Chem. Phys. **92**, 6875 (1990).

[80] I. V. Hertel and W. Radloff, *Ultrafast dynamics in isolated molecules and molecular clusters*, Rep. Prog. Phys. **69**, 1897 (2006).

[81] E. W. Becker, R. Klingelhöfer and P. Lohse, *Notizen: Strahlen aus kondensiertem Helium im Hochvakuum*, Z. Naturforsch. A **16**, 1259 (1961).

[82] J. Harms, J. P. Toennies and F. Dalfovo, *Density of superfluid helium droplets*, Phys. Rev. B **58**, 3341 (1998).

[83] D. M. Brink and S. Stringari, *Density of states and evaporation rate of helium clusters*, Z Phys D - Atoms, Molecules and Clusters **15**, 257 (1990).

[84] O. Bünermann and F. Stienkemeier, *Modeling the formation of alkali clusters attached to helium nanodroplets and the abundance of high-spin states*, F. Eur. Phys. J. D **61**, 645 (2011).

[85] V. E. Bondybey, *Relaxation and vibrational energy redistribution processes in polyatomic molecules*, Annu. Rev. Phys. Chem. **35**, 591 (1984).

[86] O. Bünermann, G. Droppelmann, A. Hernando, R. Mayol and F. Stienkemeier, *Unraveling the Absorption Spectra of Alkali Metal Atoms Attached to Helium Nanodroplets†*, J. Phys. Chem. A **111**, 12684 (2007).

[87] C. Callegari and F. Ancilotto, *Perturbation Method to Calculate the Interaction Potentials and Electronic Excitation Spectra of Atoms in He Nanodroplets*, J. Phys. Chem. A **115**, 6789 (2011).

[88] F. Dalfovo, *Atomic and molecular impurities in ^{4}He clusters*, Z Phys D - Atoms, Molecules and Clusters **29**, 61 (1994).

[89] F. Stienkemeier, J. Higgins, C. Callegari, S. I. Kanorsky, W. E. Ernst and G. Scoles, *Spectroscopy of alkali atoms (Li, Na, K) attached to large helium clusters*, Z Phys D - Atoms, Molecules and Clusters **38**, 253 (1996).

[90] F. R. Brühl, R. A. Trasca and W. E. Ernst, *Rb–He exciplex formation on helium nanodroplets*, J. Chem. Phys. **115**, 10220 (2001).

[91] A. Hernando, M. Barranco, M. Pi, E. Loginov, M. Langlet and M. Drabbels, *Desorption of alkali atoms from ^{4}He nanodroplets* **14**, 3996 (2012).

[92] J. Reho, C. Callegari, J. Higgins, W. E. Ernst, K. K. Lehmann and G. Scoles, *Spin–orbit effects in the formation of the Na–He excimer on the surface of He clusters*, Faraday Discuss. **108**, 161 (1997).

[93] J. Reho, J. Higgins, K. K. Lehmann and G. Scoles, *Alkali-helium exciplex formation on the surface of helium nanodroplets. II. A time-resolved study*, J. Chem. Phys. **113**, 9694 (2000).

[94] C. P. Schulz, P. Claas and F. Stienkemeier, *Formation of K*He Exciplexes on the Surface of Helium Nanodroplets Studied in Real Time*, Phys. Rev. Lett. **87**, 153401 (2001).

[95] C. Giese, T. Mullins, B. Grüner, M. Weidemüller, F. Stienkemeier and M. Mudrich, *Formation and relaxation of RbHe exciplexes on He nanodroplets studied by femtosecond pump and picosecond probe spectroscopy*, J. Chem. Phys. **137**, 244307 (2012).

[96] P. Claas, G. Droppelmann, C. P. Schulz, M. Mudrich and F. Stienkemeier, *Wave packet dynamics of K_2 attached to helium nanodroplets*, J. Phys. B: At. Mol. Opt. Phys. **39**, S1151 (2006).

[97] P. Claas, G. Droppelmann, C. P. Schulz, M. Mudrich and F. Stienkemeier, *Wave Packet Dynamics in Triplet States of Na_2 Attached to Helium Nanodroplets*, J. Phys. Chem. A **111**, 7537 (2007).

[98] M. Mudrich, P. Heister, T. Hippler, C. Giese, O. Dulieu and F. Stienkemeier, *Spectroscopy of triplet states of Rb_2 by femtosecond pump-probe photoionization of doped helium nanodroplets*, Phys. Rev. A **80**, 042512 (2009).

[99] C. Giese, F. Stienkemeier, M. Mudrich, A. W. Hauser and W. E. Ernst, *Homo- and heteronuclear alkali metal trimers formed on helium nanodroplets. Part II. Femtosecond spectroscopy and spectra assignments*, Phys. Chem. Chem. Phys. **13**, 18769 (2011).

[100] M. Schlesinger, M. Mudrich, F. Stienkemeier and W. T. Strunz, *Dissipative vibrational wave packet dynamics of alkali dimers attached to helium nanodroplets*, Chem. Phys. Lett. **490**, 245 (2010).

[101] H. Schmidt, J. von Vangerow, F. Stienkemeier, A. S. Bogomolov, A. V. Baklanov, D. M. Reich, W. Skomorowski, C. P. Koch and M. Mudrich, *Predissociation dynamics of lithium iodide*, J. Chem. Phys. **142**, 044303 (2015).

[102] M. Fushitani, M. Bargheer, M. Gühr and N. Schwentner, *Pump–probe spectroscopy with phase-locked pulses in the condensed phase: decoherence and control of vibrational wavepackets*, Phys. Chem. Chem. Phys. **7**, 3143 (2005).

[103] L. Fechner, B. Grüner, A. Sieg, C. Callegari, F. Ancilotto, F. Stienkemeier and M. Mudrich, *Photoionization and imaging spectroscopy of rubidium atoms attached to helium nanodroplets*, Phys. Chem. Chem. Phys. **14**, 3843 (2012).

[104] J. v. Vangerow, A. Sieg, F. Stienkemeier, M. Mudrich, A. Leal, D. Mateo, A. Hernando, M. Barranco and M. Pi, *Desorption Dynamics of Heavy Alkali Metal Atoms (Rb, Cs) Off the Surface of Helium Nanodroplets*, J. Phys. Chem. A **118**, 6604 (2014).

[105] J. v. Vangerow, O. John, F. Stienkemeier and M. Mudrich, *Dynamics of solvation and desolvation of rubidium attached to He nanodroplets*, J. Chem. Phys. **143**, 034302 (2015).

[106] J. v. Vangerow, F. Coppens, A. Leal, M. Pi, M. Barranco, N. Halberstadt, F. Stienkemeier and M. Mudrich, *Imaging Excited-State Dynamics of Doped He Nanodroplets in Real-Time*, J. Phys. Chem. Lett. **8**, 307 (2017).

[107] M. Leino, A. Viel and R. E. Zillich, *Electronically excited rubidium atom in helium clusters and films. II. Second excited state and absorption spectrum*, J. Chem. Phys. **134**, 024316 (2011).

[108] J. H. Reho, J. Higgins, M. Nooijen, K. K. Lehmann, G. Scoles and M. Gutowski, *Photoinduced nonadiabatic dynamics in quartet Na_3 and K_3 formed using helium nanodroplet isolation*, J. Chem. Phys. **115**, 10265 (2001).

[109] F. R. Brühl, R. A. Miron and W. E. Ernst, *Triplet states of rubidium dimers on helium nanodroplets*, J. Chem. Phys. **115**, 10275 (2001).

[110] G. Auböck, J. Nagl, C. Callegari and W. E. Ernst, *Electron Spin Pumping of Rb Atoms on He Nanodroplets via Nondestructive Optical Excitation*, Phys. Rev. Lett. **101**, 035301 (2008).

[111] C. B. Alcock, V. P. Itkin and M. K. Horrigan, *Vapour Pressure Equations for the Metallic Elements: 298–2500K*, Can Metall Quart **23**, 309 (1984).

[112] C. Giese, *Vibrational Structure and Dynamics of triatomic Alkali Molecules and RbHe Exciplexes on Helium Nanodroplets investigated with Femtosecond and Picosecond Pump-Probe Techniques*, dissertation, Universität Freiburg, Freiburg i. Br. (2012).

[113] B. U. Grüner, *Femtosekundenspektroskopie an dotierten Heliumnanotröpfchen: Dissipative Vibrationsdynamik und Charakterisierung eines Nanoplasmas*, Dissertation, Universität Freibrug, Freiburg i. Br. (2013).

[114] O. Bünermann, *Spektroskopie von Alkali- und Erdalkaliatomen, -molekülen, Alkaliclustern und Komplexen organischer Moleküle auf Heliumnanotröpfchen*, Dissertation, Universität Bielefeld, Bielefeld (2006).

[115] F. B. Dunning and R. G. Hulet, *Atomic, Molecular, and Optical Physics: Atoms and Molecules, Volume 29B*1 edition (Academic Press, San Diego, 1996).

[116] G. Scoles, D. Bassi, U. Buck, D. C. Laine, *Atomic and Molecular Beam Methods: Volume 1* (Oxford University Press, New York, 1988).

[117] M. Binz, *Improvement and Modification of a Phase-Modulated Femtosecond Spectroscopy Setup*, Masterarbeit, Universität Freibrug, Freiburg i. Br. (2015).

[118] J. Christian, B. Broers, J. Hoogenraad, W. van der Zande and L. Noordam, *Rubidium electronic wavepackets probed by a phase-sensitive pump-probe technique*, Opt. Commun. **103**, 79 (1993).

[119] V. Blanchet, M. A. Bouchene, O. Cabrol and B. Girard, *One-color coherent control in Cs2. Observation of 2.7 fs beats in the ionization signal*, Chem. Phys. Lett. **233**, 491 (1995).

[120] V. Blanchet, C. Nicole, M.-A. Bouchene and B. Girard, *Temporal Coherent Control in Two-Photon Transitions: From Optical Interferences to Quantum Interferences*, Phys. Rev. Lett. **78**, 2716 (1997).

[121] M. A. Bouchene, C. Nicole and B. Girard, *Wavepacket interferometry with chirped pulses*, J. Phys. B: At. Mol. Opt. Phys. **32**, 5167 (1999).

[122] C. Nicole, M. A. Bouchene, S. Zamith, N. Melikechi and B. Girard, *Saturation of wave-packet interferences: Direct observation of spin precession in potassium atoms*, Phys. Rev. A **60**, R1755 (1999).

[123] M. Wollenhaupt, A. Assion, D. Liese, C. Sarpe-Tudoran, T. Baumert, S. Zamith, M. A. Bouchene, B. Girard, A. Flettner, U. Weichmann and G. Gerber, *Interferences of Ultrashort Free Electron Wave Packets*, Phys. Rev. Lett. **89**, 173001 (2002).

[124] K. Ohmori, Y. Sato, E. E. Nikitin and S. A. Rice, *High-Precision Molecular Wave-Packet Interferometry with HgAr Dimers*, Phys. Rev. Lett. **91**, 243003 (2003).

[125] K. Ohmori, H. Katsuki, H. Chiba, M. Honda, Y. Hagihara, K. Fujiwara, Y. Sato and K. Ueda, *Real-Time Observation of Phase-Controlled Molecular Wave-Packet Interference*, Phys. Rev. Lett. **96**, 093002 (2006).

[126] P. Heister and M. Mudrich, *unpublished material* (2008).

[127] E. Loginov, A. Hernando, J. A. Beswick, N. Halberstadt and M. Drabbels, *Excitation of Sodium Atoms Attached to Helium Nanodroplets: The 3p ← 3s Transition Revisited*, J. Phys. Chem. A (2015).

[128] K. Hirano, K. Enomoto, M. Kumakura, Y. Takahashi and T. Yabuzaki, *Emission spectra of Rb*He$_n$ exciplexes in a cold ^{4}He gas*, Phys. Rev. A **68**, 012722 (2003).

[129] A. Chattopadhyay, *Spectroscopic properties of the low-lying electronic states of RbHe$_n$ (n = 1, 2) and their comparison with lighter alkali metal-helium systems*, J. Phys. B: At. Mol. Opt. Phys. **45**, 035101 (2012).

[130] L. Blank, D. E. Weeks and G. S. Kedziora, *M + Ng potential energy curves including spin-orbit coupling for M = K, Rb, Cs and Ng = He, Ne, Ar*, J. Chem. Phys. **136**, 124315 (2012).

[131] D. Dell'Angelo, G. Guillon and A. Viel, *Excited Li and Na in He_n: Influence of the dimer potential energy curves*, J. Chem. Phys. **136**, 114308 (2012).

[132] F. Bouhadjar, K. Alioua, M. T. Bouazza and M. Bouledroua, *Rubidium D1 and D2 atomic lines' pressure broadened by ground-state helium atoms*, J. Phys. B: At. Mol. Opt. Phys. **47**, 185201 (2014).

[133] M. Zbiri and C. Daul, *Investigating the M*He exciplexes, M={Li,Na,K,Rb,Cs,Fr}: Density functional approach*, J. Chem. Phys. **121**, 11625 (2004).

[134] M. Leino, A. Viel and R. E. Zillich, *Electronically excited rubidium atom in a helium cluster or film*, J. Chem. Phys. **129**, 184308 (2008).

[135] J. Pascale, *Use of l-dependent pseudopotentials in the study of alkali-metal-atom-He systems. The adiabatic molecular potentials*, Phys. Rev. A **28**, 632 (1983).

[136] Z. J. Jakubek and M. Takami, *Ab initio studies of AgHe exciplex*, Chem. Phys. Lett. **265**, 653 (1997).

[137] E. Loginov and M. Drabbels, *Excited State Dynamics of Ag Atoms in Helium Nanodroplets*, J. Phys. Chem. A **111**, 7504 (2007).

[138] E. Loginov and M. Drabbels, *Dynamics of Excited Sodium Atoms Attached to Helium Nanodroplets*, J. Phys. Chem. A **118**, 2738 (2014).

[139] J. R. LeRoy, *LEVEL 8.0: A Computer Program for Solving the Radial Schrödinger Equation for Bound and Quasibound Levels*, Chemical Physics Research Report CP-663, University of Waterloo (2007).

[140] E. Loginov, C. Callegari, F. Ancilotto and M. Drabbels, *Spectroscopy on Rydberg States of Sodium Atoms on the Surface of Helium Nanodroplets*, J. Phys. Chem. A **115**, 6779 (2011).

[141] N. F. Scherer, A. Matro, L. D. Ziegler, M. Du, R. J. Carlson, J. A. Cina and G. R. Fleming, *Fluorescence-detected wave packet interferometry. II. Role of rotations and determination of the susceptibility*, J. Chem. Phys. **96**, 4180 (1992).

[142] M. Schlesinger and W. T. Strunz, *Decoherence of molecular vibrational wave packets: Oscillatory decay of purity*, Phys. Rev. A **77**, 012111 (2008).

[143] J. v. Vangerow, private communication (2017).

[144] A. Nemeth, J. Sperling, J. Hauer, H. F. Kauffmann and F. Milota, *Compact phase-stable design for single- and double-quantum two-dimensional electronic spectroscopy*, Opt. Lett. **34**, 3301 (2009).

[145] D. Karaiskaj, A. D. Bristow, L. Yang, X. Dai, R. P. Mirin, S. Mukamel and S. T. Cundiff, *Two-Quantum Many-Body Coherences in Two-Dimensional Fourier-Transform Spectra of Exciton Resonances in Semiconductor Quantum Wells*, Phys. Rev. Lett. **104**, 117401 (2010).

[146] P. E. Konold and R. Jimenez, *Excited State Electronic Landscape of mPlum Revealed by Two-Dimensional Double Quantum Coherence Spectroscopy*, J. Phys. Chem. B **119**, 3414 (2015).

[147] J. Tollerud and J. A. Davis, *Two-dimensional double-quantum spectroscopy: peak shapes as a sensitive probe of carrier interactions in quantum wells*, J. Opt. Soc. Am. B **33**, C108 (2016).

[148] T. A. Gellen, L. A. Bizimana, W. P. Carbery, I. Breen and D. B. Turner, *Ultrabroadband two-quantum two-dimensional electronic spectroscopy*, J. Chem. Phys. **145**, 064201 (2016).

[149] P. Tian and W. S. Warren, *Ultrafast measurement of two-photon absorption by loss modulation*, Opt. Lett. **27**, 1634 (2002).

[150] Y.-H. Lai, S.-Y. Lee, C.-F. Chang, Y.-H. Cheng and C.-K. Sun, *Nonlinear photoacoustic microscopy via a loss modulation technique: from detection to imaging*, Opt. Express **22**, 525 (2014).

[151] K. J. Karki, L. Kringle, A. H. Marcus and T. Pullerits, *Phase-synchronous detection of coherent and incoherent nonlinear signals*, J. Opt. **18**, 015504 (2016).

[152] V. A. Osipov, X. Shang, T. Hansen, T. Pullerits and K. J. Karki, *Nature of relaxation processes revealed by the action signals of intensity-modulated light fields*, Phys. Rev. A **94**, 053845 (2016).

[153] U. Bangert, *Phase-Modulated Detection of Second Harmonic Light to Facilitate Coherent UV-Spectroscopy*, Masterarbeit, Freiburg i. Br. (2016).

[154] J. B. Asbury, T. Steinel and M. D. Fayer, *Vibrational echo correlation spectroscopy probes of hydrogen bond dynamics in water and methanol*, J. Lumin. **107**, 271 (2004).

[155] F. C. Spano and S. Mukamel, *Nonlinear susceptibilities of molecular aggregates: Enhancement of $\chi^{(3)}$ by size*, Phys. Rev. A **40**, 5783 (1989).

[156] M. Wewer and F. Stienkemeier, *Molecular versus excitonic transitions in PTCDA dimers and oligomers studied by helium nanodroplet isolation spectroscopy*, Phys. Rev. B **67** (2003).

[157] R. F. Fink, J. Seibt, V. Engel, M. Renz, M. Kaupp, S. Lochbrunner, H.-M. Zhao, J. Pfister, F. Würthner and B. Engels, *Exciton Trapping in π-Conjugated Materials: A Quantum-Chemistry-Based Protocol Applied to Perylene Bisimide Dye Aggregates*, J. Am. Chem. Soc. **130**, 12858 (2008).

[158] F. Milota, J. Sperling, A. Nemeth, T. Mancal and H. F. Kauffmann, *Two-Dimensional Electronic Spectroscopy of Molecular Excitons*, Acc. Chem. Res. **42**, 1364 (2009).

[159] H.-G. Duan, P. Nalbach, V. I. Prokhorenko, S. Mukamel and M. Thorwart, *On the origin of oscillations in two-dimensional spectra of excitonically-coupled molecular systems*, New J. Phys. **17**, 072002 (2015).

[160] S. A. Schmid, R. Abbel, A. P. H. J. Schenning, E. W. Meijer and L. M. Herz, *Energy transfer processes along a supramolecular chain of π-conjugated molecules*, Phil. Trans. R. Soc. A **370**, 3787 (2012).

[161] H. v. Amerongen, R. v. Grondelle and L. Valkunas, *Photosynthetic Excitons* (World Scientific, 2000).

[162] J. M. Womick and A. M. Moran, *Exciton Coherence and Energy Transport in the Light-Harvesting Dimers of Allophycocyanin*, J. Phys. Chem. B **113**, 15747 (2009).

[163] N. S. Ginsberg, Y.-C. Cheng and G. R. Fleming, *Two-Dimensional Electronic Spectroscopy of Molecular Aggregates*, Acc. Chem. Res. **42**, 1352 (2009).

[164] A. Ishizaki and G. R. Fleming, *Quantum Coherence in Photosynthetic Light Harvesting*, Annu. Rev. Condens. Matter Phys. **3**, 333 (2012).

[165] S. T. Cundiff, *Optical two-dimensional Fourier transform spectroscopy of semiconductor nanostructures [Invited]*, J. Opt. Soc. Am. B **29**, A69 (2012).

[166] M. Müller, S. Izadnia, S. M. Vlaming, A. Eisfeld, A. LaForge and F. Stienkemeier, *Cooperative lifetime reduction of single acene molecules attached to the surface of neon clusters*, Phys. Rev. B **92** (2015).

[167] I. Bloch, J. Dalibard and W. Zwerger, *Many-body physics with ultracold gases*, Rev. Mod. Phys. **80**, 885 (2008).

[168] K. M. Jones, E. Tiesinga, P. D. Lett and P. S. Julienne, *Ultracold photoassociation spectroscopy: Long-range molecules and atomic scattering*, Rev. Mod. Phys. **78**, 483 (2006).

[169] V. Bendkowsky, B. Butscher, J. Nipper, J. B. Balewski, J. P. Shaffer, R. Löw, T. Pfau, W. Li, J. Stanojevic, T. Pohl and J. M. Rost, *Rydberg Trimers and Excited Dimers Bound by Internal Quantum Reflection*, Phys. Rev. Lett. **105** (2010).

[170] K. Afrousheh, P. Bohlouli-Zanjani, D. Vagale, A. Mugford, M. Fedorov and J. D. D. Martin, *Spectroscopic Observation of Resonant Electric Dipole-Dipole Interactions between Cold Rydberg Atoms*, Phys. Rev. Lett. **93** (2004).

[171] I. I. Ryabtsev, D. B. Tretyakov, I. I. Beterov and V. M. Entin, *Observation of the Stark-Tuned Förster Resonance between Two Rydberg Atoms*, Phys. Rev. Lett. **104** (2010).

[172] J. H. Gurian, P. Cheinet, P. Huillery, A. Fioretti, J. Zhao, P. L. Gould, D. Comparat and P. Pillet, *Observation of a Resonant Four-Body Interaction in Cold Cesium Rydberg Atoms*, Phys. Rev. Lett. **108**, 023005 (2012).

[173] J. J. Maki, M. S. Malcuit, J. E. Sipe and R. W. Boyd, *Linear and nonlinear optical measurements of the Lorentz local field*, Phys. Rev. Lett. **67**, 972 (1991).

[174] V. A. Sautenkov, H. Van Kampen, E. R. Eliel and J. P. Woerdman, *Dipole-dipole broadened line shape in a partially excited dense atomic gas*, Phys. Rev. Lett. **77**, 3327 (1996).

[175] H. Li, V. A. Sautenkov, Y. V. Rostovtsev and M. O. Scully, *Excitation dependence of resonance line self-broadening at different atomic densities*, J. Phys. B: At. Mol. Opt. Phys. **42**, 065203 (2009).

[176] V. O. Lorenz and S. T. Cundiff, *Non-Markovian Dynamics in a Dense Potassium Vapor*, Phys. Rev. Lett. **95** (2005).

[177] V. O. Lorenz and S. T. Cundiff, *Ultrafast spectroscopy of a dense potassium vapor*, Chem. Phys. **341**, 106 (2007).

[178] V. O. Lorenz, S. Mukamel, W. Zhuang and S. T. Cundiff, *Ultrafast Optical Spectroscopy of Spectral Fluctuations in a Dense Atomic Vapor*, Phys. Rev. Lett. **100**, 013603 (2008).

[179] F. Shen, J. Gao, A. A. Senin, C. J. Zhu, J. R. Allen, Z. H. Lu, Y. Xiao and J. G. Eden, *Many-Body Dipole-Dipole Interactions between Excited Rb Atoms Probed by Wave Packets and Parametric Four-Wave Mixing*, Phys. Rev. Lett. **99** (2007).

[180] M. Richter and S. Mukamel, *Collective two-particle resonances induced by photon entanglement*, Phys. Rev. A **83** (2011).

[181] C. Perrella, P. S. Light, T. J. Milburn, D. Kielpinski, T. M. Stace and A. N. Luiten, *Anomalous two-photon spectral features in warm rubidium vapor*, Phys. Rev. A **94**, 033403 (2016).

[182] W. Demtröder, *Laser Spectroscopy: Vol. 1: Basic Principles* (Springer Science & Business Media, 2008).

[183] Steck, Daniel A., *Rubidium 85 D Line Data*, http://steck.us/alkalidata (revision 2.1.4, 23 December 2010) (2010).

[184] Steck, Daniel A., *Rubidium 87 D Line Data*, http://steck.us/alkalidata (revision 2.1.4, 23 December 2010) (2010).

[185] Steck, Daniel A., *Cesium D Line Data*, http://steck.us/alkalidata (revision 2.0.1, 2 May 2008) (2008).

[186] C. Li, W. Wagner, M. Ciocca and W. S. Warren, *Multiphoton femtosecond phase-coherent two-dimensional electronic spectroscopy*, J. Chem. Phys. **126**, 164307 (2007).

[187] V. Perlík, J. Hauer and F. Šanda, *Finite pulse effects in single and double quantum spectroscopies*, J. Opt. Soc. Am. B **34**, 430 (2017).

[188] S. Mukamel, *Communication: The origin of many-particle signals in nonlinear optical spectroscopy of non-interacting particles*, J. Chem. Phys. **145**, 041102 (2016).

[189] S. Sauer, F. Mintert, C. Gneiting and A. Buchleitner, *Entanglement resonances of driven multi-partite quantum systems*, J. Phys. B: At. Mol. Opt. Phys. **45**, 154011 (2012).

[190] K. Bennett and S. Mukamel, *Cascading and local-field effects in non-linear optics revisited: A quantum-field picture based on exchange of photons*, J. Chem. Phys. **140**, 044313 (2014).

[191] T. H. Maiman, *Stimulated Optical Radiation in Ruby*, Nature **187**, 493 (1960).

[192] M. Lewenstein, P. Balcou, M. Y. Ivanov, A. L'Huillier and P. B. Corkum, *Theory of high-harmonic generation by low-frequency laser fields*, Phys. Rev. A **49**, 2117 (1994).

[193] L. Gallmann, C. Cirelli and U. Keller, *Attosecond Science: Recent Highlights and Future Trends*, Annu. Rev. Phys. Chem. **63**, 447 (2012).

[194] A. K. Mills, T. J. Hammond, M. H. C. Lam and D. J. Jones, *XUV frequency combs via femtosecond enhancement cavities*, J. Phys. B: At. Mol. Opt. Phys. **45**, 142001 (2012).

[195] P. R. Ribic and G. Margaritondo, *Status and prospects of x-ray free-electron lasers (X-FELs): a simple presentation*, J. Phys. D: Appl. Phys. **45**, 213001 (2012).

[196] E. Allaria, R. Appio, L. Badano, W. A. Barletta, S. Bassanese, S. G. Biedron, A. Borga, E. Busetto, D. Castronovo, P. Cinquegrana, S. Cleva, D. Cocco, M. Cornacchia, P. Craievich, I. Cudin, G. D'Auria, M. Dal Forno, M. B. Danailov, R. De Monte, G. De Ninno, P. Delgiusto, A. Demidovich, S. Di Mitri, B. Diviacco, A. Fabris, R. Fabris, W. Fawley, M. Ferianis, E. Ferrari, S. Ferry, L. Froehlich, P. Furlan, G. Gaio, F. Gelmetti, L. Giannessi, M. Giannini, R. Gobessi, R. Ivanov, E. Karantzoulis, M. Lonza, A. Lutman, B. Mahieu, M. Milloch, S. V. Milton, M. Musardo, I. Nikolov, S. Noe, F. Parmigiani, G. Penco, M. Petronio, L. Pivetta, M. Predonzani, F. Rossi, L. Rumiz, A. Salom, C. Scafuri, C. Serpico, P. Sigalotti, S. Spampinati, C. Spezzani, M. Svandrlik, C. Svetina, S. Tazzari, M. Trovo, R. Umer, A. Vascotto, M. Veronese, R. Visintini, M. Zaccaria, D. Zangrando and M. Zangrando, *Highly coherent and stable pulses from the FERMI seeded free-electron laser in the extreme ultraviolet*, Nat Photon **6**, 699 (2012).

[197] P. W. Brumer and M. Shapiro, *Principles of the Quantum Control of Molecular Processes*1 (Wiley & Sons, 2003).

[198] I. V. Schweigert and S. Mukamel, *Coherent Ultrafast Core-Hole Correlation Spectroscopy: X-Ray Analogues of Multidimensional NMR*, Phys. Rev. Lett. **99**, 163001 (2007).

[199] J. D. Biggs, Y. Zhang, D. Healion and S. Mukamel, *Multidimensional x-ray spectroscopy of valence and core excitations in cysteine*, J. Chem. Phys. **138**, 144303 (2013).

[200] Y. Zhang, D. Healion, J. D. Biggs and S. Mukamel, *Double-core excitations in formamide can be probed by X-ray double-quantum-coherence spectroscopy*, J. Chem. Phys. **138**, 144301 (2013).

[201] A. Palacios, A. González-Castrillo and F. Martín, *Molecular interferometer to decode attosecond electron–nuclear dynamics*, PNAS **111**, 3973 (2014).

[202] J. Ullrich, A. Rudenko and R. Moshammer, *Free-Electron Lasers: New Avenues in Molecular Physics and Photochemistry*, Annu. Rev. Phys. Chem. **63**, 635 (2012).

[203] W. P. de Boeij, M. S. Pshenichnikov and D. A. Wiersma, *Phase-locked heterodyne-detected stimulated photon echo. A unique tool to study solute—solvent interactions*, Chem. Phys. Lett. **238**, 1 (1995).

[204] J. C. Vaughan, T. Hornung, K. W. Stone and K. A. Nelson, *Coherently Controlled Ultrafast Four-Wave Mixing Spectroscopy*, J. Phys. Chem. A **111**, 4873 (2007).

[205] Y. H. Jiang, T. Pfeifer, A. Rudenko, O. Herrwerth, L. Foucar, M. Kurka, K. U. Kühnel, M. Lezius, M. F. Kling, X. Liu, K. Ueda, S. Düsterer, R. Treusch, C. D. Schröter, R. Moshammer and J. Ullrich, *Temporal coherence effects in multiple ionization of N_2 via XUV pump-probe autocorrelation*, Phys. Rev. A **82**, 041403 (2010).

[206] F. Sorgenfrei, W. F. Schlotter, T. Beeck, M. Nagasono, S. Gieschen, H. Meyer, A. Föhlisch, M. Beye and W. Wurth, *The extreme ultraviolet split and femtosecond delay unit at the plane grating monochromator beamline PG2 at FLASH*, Rev. Sci. Instrum. **81**, 043107 (2010).

[207] T. Gebert, D. Rompotis, M. Wieland, F. Karimi, A. Azima and M. Drescher, *Michelson-type all-reflective interferometric autocorrelation in the VUV regime*, New J. Phys. **16**, 073047 (2014).

[208] C. Benko, T. K. Allison, A. Cingöz, L. Hua, F. Labaye, D. C. Yost and J. Ye, *Extreme ultraviolet radiation with coherence time greater than 1 s*, Nat Photon **8**, 530 (2014).

[209] D. Gauthier, P. R. Ribič, G. De Ninno, E. Allaria, P. Cinquegrana, M. B. Danailov, A. Demidovich, E. Ferrari, L. Giannessi, B. Mahieu and G. Penco, *Spectrotemporal Shaping of Seeded Free-Electron Laser Pulses*, Phys. Rev. Lett. **115**, 114801 (2015).

[210] R. Zerne, C. Altucci, M. Bellini, M. B. Gaarde, T. W. Hänsch, A. L'Huillier, C. Lyngå and C.-G. Wahlström, *Phase-Locked High-Order Harmonic Sources*, Phys. Rev. Lett. **79**, 1006 (1997).

[211] P. Salières, L. Le Déroff, T. Auguste, P. Monot, P. d'Oliveira, D. Campo, J.-F. Hergott, H. Merdji and B. Carré, *Frequency-Domain Interferometry in the XUV with High-Order Harmonics*, Phys. Rev. Lett. **83**, 5483 (1999).

[212] M. Kovačev, S. V. Fomichev, E. Priori, Y. Mairesse, H. Merdji, P. Monchicourt, P. Breger, J. Norin, A. Persson, A. L'Huillier, C.-G. Wahlström, B. Carré and P. Salières, *Extreme Ultraviolet Fourier-Transform Spectroscopy with High Order Harmonics*, Phys. Rev. Lett. **95**, 223903 (2005).

[213] O. Schepp, A. Baumann, D. Rompotis, T. Gebert, A. Azima, M. Wieland and M. Drescher, *Tracing few-femtosecond photodissociation dynamics on molecular oxygen with a single-color pump-probe scheme in the VUV*, Phys. Rev. A **94**, 033411 (2016).

[214] R. Bloem, S. Garrett-Roe, H. Strzalka, P. Hamm and P. Donaldson, *Enhancing signal detection and completely eliminating scattering using quasi-phase-cycling in 2D IR experiments*, Opt. Express **18**, 27067 (2010).

[215] B. P. Fingerhut, M. Richter, J.-W. Luo, A. Zunger and S. Mukamel, *Dissecting biexciton wave functions of self-assembled quantum dots by double-quantum-coherence optical spectroscopy*, Phys. Rev. B **86**, 235303 (2012).

[216] S. Izadnia, D. Schönleber, A. Eisfeld, A. Ruf, A. C. LaForge and F. Stienkemeier, *Singlet Fission in Weakly-interacting Acene Molecules*, J. Phys. Chem. Lett. (accepted) (2017).

Erklärung

Ich erkläre hiermit, dass ich die vorliegende Arbeit ohne unzulässige Hilfe Dritter und ohne Benutzung anderer als der angegebenen Hilfsmittel angefertigt habe. Die aus anderen Quellen direkt oder indirekt übernommenen Daten und Konzepte sind unter Angabe der Quelle gekennzeichnet. Insbesondere habe ich hierfür nicht die entgeltliche Hilfe von Vermittlungs- beziehungsweise Beratungsdiensten (Promotionsberater/-beraterinnen oder anderer Personen) in Anspruch genommen. Die Arbeit wurde bisher weder im In- noch im Ausland in gleicher oder ähnlicher Form einer Prüfungsbehörde vorgelegt.

Ich habe mich nicht bereits an einer in- oder ausländischen Hochschule um die Promotion beworben.

Die Bestimmungen der Promotionsordnung der Universität Freiburg für die Fakultät für Mathematik und Physik sind mir bekannt; insbesondere weißich, dass ich vor der Aushändigung der Doktorurkunde zur Führung des Doktorgrades nicht berechtigt bin.

Freiburg i. Br., den 02. Mai 2017

Lukas Bruder

Acknowledgements

In the first place, I thank Frank Stienkemeier for the supervision and proof reading of this PhD thesis, for numerous discussions and helpful advice as well as his trust and encouragement during the whole time of this thesis.

I thankfully acknowledge the work of Marcel Binz and Ulrich Bangert during their Master thesis, Daniel Uhl during his Bachelor thesis and Sam Leutheuser during his DAAD scholarship. From the MPIPKS group I thank Zeng-Zhao Li and Alexander Eisfeld for their collaboration.

I appreciate the warm and friendly atmosphere in our group and thank all group members. In particular, I acknowledge fruitful discussions and support in the lab from Johannes von Vangerow, Marcel Mudrich, Andreas Wituschek and Markus Schulz-Weiling. I thank specifically Katrin Dulitz for useful comments on the manuscript of this dissertation.

I also thank Frank Schlawin, Manuel Gessner and Shaul Mukamel for fruitful discussions about the experiments on the collective resonances.

Schließlich danke ich ganz besonders Verena für ihre ständige Unterstützung, Aufmunterung und ihr Verständnis für die langen Arbeitszeiten. Ich danke auch meiner Familie für ihren Rückhalt. Außerdem danke ich dem evangelischen Studienwerk Villigst e.V. für die finanzielle Unterstützung dieser Dissertation.